

Photocatalytic Application of Bismuth Based Semiconducting Nanoparticles and their Heterostructures towards Selective Organic Transformations and Degradation of Persistent Organic Pollutants

Yagna Prakash Bhoi



**Department of Chemistry
National Institute of Technology Rourkela**

Photocatalytic Application of Bismuth Based Semiconducting Nanoparticles and their Heterostructures towards Selective Organic Transformations and Degradation of Persistent Organic Pollutants

*A Dissertation submitted to the
National Institute of Technology Rourkela
in partial fulfillment of the requirements*

*of the degree of
Doctor of Philosophy*

*in
Chemistry*

by

Yagna Prakash Bhoi

(Roll No. 513CY1065)

under the supervision of

Prof. Braja Gopal Mishra



**Department of Chemistry
National Institute of Technology Rourkela**



Department of Chemistry
National Institute of Technology Rourkela

December 26, 2018

Certificate of Examination

Roll Number: 513CY1065

Name: Yagna Prakash Bhoi

Title of Dissertation: “Photocatalytic Application of Bismuth Based Semiconducting Nanoparticles and their Heterostructures towards Selective Organic Transformations and Degradation of Persistent Organic Pollutants”

We the below signed, after checking the dissertation mentioned above and the official record book(s) of the student, hereby state our approval of the dissertation submitted in partial fulfillment of the requirements of the degree of Doctor of Philosophy in Chemistry at National Institute of Technology, Rourkela. We are satisfied with the volume, quality, correctness, and originality of the work.

Braja Gopal Mishra
Supervisor

Supratim Giri
Member (DSC)

Sabita Patel
Member (DSC)

Japes Bera
Member (DSC)

Examiner

Garudadhvaj Hota
Chairman (DSC)



Department of Chemistry
National Institute of Technology Rourkela

December 09, 2018

Supervisor's Certificate

This is to certify that the work presented in this dissertation entitled “*Photocatalytic Application of Bismuth Based Semiconducting Nanoparticles and their Heterostructures towards Selective Organic Transformations and Degradation of Persistent Organic Pollutants*” by Yagna Prakash Bhoi, Roll No. 513CY1065 is a record of original research carried out by him under my supervision and guidance in partial fulfillment of the requirements of the degree of *Doctor of Philosophy in Chemistry*. Neither this dissertation nor any part of it has been submitted for any degree or diploma to any institute or university in India or abroad.

Braja Gopal Mishra
Supervisor

Dedicated
To
My Beloved Family

Declaration of Originality

I, Yagna Prakash Bhoi, Roll Number 513CY1065, hereby declare that this dissertation entitled “*Photocatalytic Application of Bismuth Based Semiconducting Nanoparticles and their Heterostructures towards Selective Organic Transformations and Degradation of Persistent Organic Pollutants*” represents my original work carried out as a doctoral student of NIT Rourkela and, to the best of my knowledge, it contains no material previously published or written by another person, nor any material presented for the award of any other degree or diploma of NIT Rourkela or any other institution. Any contribution made to this research by others, with whom I have worked at NIT Rourkela or elsewhere, is explicitly acknowledged in the dissertation. Works of other authors cited in this dissertation have been duly acknowledged under the section "Bibliography". I have also submitted my original research records to the scrutiny committee for evaluation of my dissertation.

I am fully aware that in case of any non-compliance detected in future, the Senate of NIT Rourkela may withdraw the degree awarded to me on the basis of the present dissertation.

December 09, 2018
NIT Rourkela

Yagna Prakash Bhoi

Acknowledgements

This thesis is the account of four and a half years of work in the field of heterogeneous photocatalysis in relation to their synthesis and application at Department of Chemistry, National Institute of Technology, Rourkela, India, which would not have been possible without the help of many. First of all, I am thankful to BRNS, Mumbai and DST-WTI, New Delhi for funding this research work.

It is with great pleasure; I express my deep sense of gratitude to Dr. Braja Gopal Mishra for his advice, guidance, suggestions, discussions, constant trust, help and encouragement throughout the course of the investigations reported in the thesis. I also express my gratefulness to him for his affectionate and friendly attitude. I deem it a binding obligation on my part to extend my boundless tributes of gratitude and heartfelt respect to him. His patience, empathy and constant encouragement contributed to my research work and stay here being most happy and memorable one. I would sincerely acknowledge him for patiently scrutinizing my thesis and making my work success and fruitful.

I am thankful to the Director, National Institute of Technology, Rourkela for providing me the necessary infrastructural facilities. I would also like to thank Dr. S. Chatterjee, Head, Department of Chemistry and Dr. N. Panda, Ex-HOD, Department of Chemistry, for providing me laboratory and instrumental facilities during my Ph.D. work.

I wish to place on record my thankfulness to my DSC members, Dr. Garudadhvaj Hota, Dr. Supratim Giri, Dr. Sabita Patel and Dr. Japes Bera, for their valuable comments and evaluation of my progress reports and seminars during the Ph. D. program. I am sincerely thankful to all the faculty members and staff of our department for their constant help, support and a memorable atmosphere. My heartfelt thanks are due to all who helped and supported me in the awful situation with their proper care and guidance during my research work. I am also gratified towards the members of my laboratory, Dr. Purabi Kar, Dr. Sagnika Pradhan, Dibyananda Majhi, Snehashree Pradhan and Krishnendu Das for their active cooperation, support and understanding during my research work.

My profound and deep feelings are towards all my near and dearest friends for their constant support, encouragement, love and care throughout time. I feel bliss with all the beautiful moments spent over here and hearty gratitude to all to have patience and constant understanding towards me throughout the time. I want to acknowledge as well as share my happiness with my companions from GDB Hostel. Thank you all my friends, for making my stay at NIT Rourkela a truly memorable and cherished one.

Last but not the least; it would not have been possible to complete this thesis without the bottomless encouragement and support of my family, whose unflinching love, faith, and moral support in my abilities helped me to overcome many obstacles and march ahead in spite of failures. I would like to dedicate this thesis to my beloved family.

December 09, 2018
NIT, Rourkela

Yagna Prakash Bhoi
Roll No-513CY1065

Abstract

In this thesis, Bi based complex oxides and sulphide semiconductor nanomaterials have been synthesized by combustion synthesis route. The Bi based materials have been coupled with low band gap metal sulphide materials to form heterojunction photocatalytic systems with improved visible light absorption and photon harvesting efficiency. The photocatalytic activity of the heterostructure systems have been studied for degradation of organic pollutants from aqueous sources and selective organic transformation reactions under visible light illumination.

Bismuth tungstate (Bi_2WO_6) nanoparticles were synthesized by combustion synthesis method using different N-containing organic compounds as fuels (urea, glycine, hexamethylenetetramine (HMTA), malonic acid dihydrazide (MDH)). Glycine as fuel was effective for synthesis of phase pure Bi_2WO_6 nanoparticles. Employing HMTA and MDH as fuel lead to mixed phase complex oxide system with $\text{Bi}_{14}\text{W}_2\text{O}_{27}$ as minor (impurity) phase. The nature of the fuel significantly influences the particle size and morphology. The Bi_2WO_6 nanoparticles were used as an efficient photocatalyst for the visible light driven chemoselective oxidation of substituted thiophenols to disulfide using air as oxidant. Structurally diverse diphenyl disulfide moieties were obtained in high yield and excellent selectivity within a time span of 6 h of visible light irradiation. The Bi_2WO_6 nanoparticles were also synthesized by amorphous citrate process and subsequently modified by dispersing CuS to form $\text{CuS}/\text{Bi}_2\text{WO}_6$ (CuSBTA) heterojunction materials. XRD study indicated the existence of hexagonal covellite CuS and orthorhombic Russellite Bi_2WO_6 phase in the heterojunction materials. During hydrothermal treatment, the Cu^{2+} ions substituted for the W^{6+} ions in the Bi_2WO_6 lattice to form a substitutional solid solution ($\text{Bi}_2\text{Cu}_x\text{W}_{1-x}\text{O}_{6-2x}$). The CuS and Bi_2WO_6 phases existed in distinct nanorod and nanosheet morphologies, respectively. During hydrothermal treatment, significant morphological reorganization of the Bi_2WO_6 phase took place leading to the formation of flower like hierarchical nanostructures. The CuSBTA materials possess characteristic features of a type-II heterojunction exhibiting narrow band gap, enhanced visible light absorption and efficient charge separation properties. The heterojunction materials were evaluated as visible light active photocatalyst for complete degradation of Congo red dye using H_2O_2 as oxidant. The CuSBTA materials exhibited higher apparent rate constant (K_{app}) and greater efficiency for Congo red degradation compared to pure Bi_2WO_6 material.

A series of type-II heterojunction nanomaterials were synthesized by coupling $\text{Bi}_2\text{W}_2\text{O}_9$ with CdS and CuS. Initially, phase pure $\text{Bi}_2\text{W}_2\text{O}_9$ with orthorhombic crystalline structure was prepared by a facile combustion synthesis route using urea as a fuel. The CuS and CdS nanoparticles were dispersed over $\text{Bi}_2\text{W}_2\text{O}_9$ matrix by using a hydrothermal route. The heterojunction materials were characterized using XRD, XPS, FTIR, UV-Vis-DRS, PL, FESEM and HRTEM study. Pure $\text{Bi}_2\text{W}_2\text{O}_9$ exhibited micron-size plate-like particles. The occurrence of ultrafine CdS nanoparticles with diameter between 8-15 nm well dispersed over $\text{Bi}_2\text{W}_2\text{O}_9$ plates is noticed for CdS/ $\text{Bi}_2\text{W}_2\text{O}_9$ materials. For CuS/ $\text{Bi}_2\text{W}_2\text{O}_9$ materials, Cu^{2+} ions replaced partially W^{6+} ions in $\text{Bi}_2\text{W}_2\text{O}_9$ lattice to form $\text{Bi}_2\text{Cu}_x\text{W}_{2-x}\text{O}_{9-2x}$ as a nonstoichiometric solid solution phase.

Under hydrothermal treatment, the desegregation of the $\text{Bi}_2\text{W}_2\text{O}_9$ plates to nanosheets and the concurrent formation of CuS nanorods were noticed leading to their hierarchical reorganisation to microspherical structures. Both the heterojunction materials, exhibited improved visible light absorption, enhanced charge carrier separation and suitable band alignment characteristic of a type-II heterojunction. The CdS/ $\text{Bi}_2\text{W}_2\text{O}_9$ heterojunctions were evaluated as visible light active photocatalyst for aerobic oxidation of amines to imines. Structurally and functionally diverse amine molecules were oxidized to the corresponding imines with excellent selectivity in a short span of time. The CuS/ $\text{Bi}_2\text{W}_2\text{O}_9$ heterojunction materials were studied as an efficient photocatalyst for the degradation of diuron pesticide under visible light irradiation achieving 95% mineralization within 3 h. Mechanistic study indicated that the mineralization of diuron occurred in a cascade manner over the catalyst surface involving dechlorination, alkyl oxidation and oxidative ring-opening steps.

A visible light promoted photocatalytic route has been developed for mineralization of alachlor pesticide using type-II CuS/ BiFeO_3 heterojunction materials. The heterojunctions were synthesized by a two-step process involving synthesis of BiFeO_3 by combustion route followed by deposition of CuS material by hydrothermal route. Microscopically, the heterojunction materials contained BiFeO_3 nanoplates and CuS nanorods. Optical property study and photocurrent measurement suggested that these materials show excellent absorption in visible region with superior charge carrier mobility and separation compared to the individual components. The CuS/ BiFeO_3 materials showed high efficiency for mineralization of alachlor pesticide under visible light illumination achieving >95% degradation within 60 min. The mechanism of alachlor degradation over the catalyst surface was elucidated using GCMS and radical scavenger experiments.

A series of $\alpha\text{-Fe}_2\text{O}_3\text{-Bi}_2\text{S}_3$ heterojunction materials were prepared by a one-step autocombustion method employing thiourea as fuel and characterized using XRD, UV-Vis-DRS, FTIR, PL, XPS, FESEM, TEM and HRTEM analytical techniques. XRD study indicated presence of rhombohedral $\alpha\text{-Fe}_2\text{O}_3$ and orthorhombic Bi_2S_3 in the heterojunction materials. The heterojunctions displayed better optical absorption in the visible region. Microscopic studies indicated presence of well dispersed $\alpha\text{-Fe}_2\text{O}_3$ nanorods in a continuous Bi_2S_3 matrix. The $\alpha\text{-Fe}_2\text{O}_3$ nanorods were typically 30–50 nm in diameter and 120–150 nm in length growing isotopically in different direction from a single nucleation point. The calculated band positions of both components indicated a facile electrons transfer from the conduction band of $\alpha\text{-Fe}_2\text{O}_3$ to Bi_2S_3 whereas migration of holes occurs in the reverse direction yielding a type-II heterojunction. The $\alpha\text{-Fe}_2\text{O}_3\text{-Bi}_2\text{S}_3$ heterojunctions materials were evaluated as selective and efficient photocatalyst for the hydrogen transfer reduction of nitroarenes under visible light illumination. Structurally diverse nitroarenes could be selectively reduced to the corresponding amines in high yield and purity using $\alpha\text{-Fe}_2\text{O}_3\text{-Bi}_2\text{S}_3$ as photocatalyst.

Keywords: Bismuth tungstate, bismuth ferrite, CuS, CdS, diuron, Alachlor, Congo red, Amine oxidation, Thiol reduction,

Contents

Certificate of Examination	iii
Supervisor's Certificate	iv
Dedication	v
Declaration of Originality	vi
Acknowledgments	vii
Abstract	ix
Contents	xi
List of Figures	xv
List of Tables	xxi
Abbreviations	xxii
Notations	xxiii

1 Introduction & Literature Survey

1.1	General introduction.....	1
1.2	Photocatalysis in selective organic transformations.....	3
1.3	Strategies to improve photocatalytic activity of semiconducting photocatalyst.	6
1.4	Photocatalysis by bismuth based semiconducting nanomaterials.....	8
1.4.1	Bi ₂ O ₃	9
1.4.2	Bi ₂ S ₃	11
1.4.3	Bismuth salts and oxyacid salts.....	13
1.4.3.1	Bismuth phosphate (BiPO ₄).....	13
1.4.3.2	Bismuth vanadate (BiVO ₄).....	13
1.4.3.3	Bismuth oxyhalides (BiOX).....	14
1.4.4	Aurivillius family of oxides.....	15
1.4.4.1	Bi ₂ WO ₆	16
1.4.4.2	Bi ₂ W ₂ O ₉	19
1.4.5	BiFeO ₃	20
1.5	Gap in literature.....	23
1.6	Objectives of the present work.....	23
	References.....	26

2 Materials and Methods

2.1	Preparation of photocatalytic materials	41
2.1.1	Synthesis of Bi ₂ WO ₆	41
2.1.2	Synthesis of Bi ₂ W ₂ O ₉ (BWO).....	42
2.1.3	Synthesis of BiFeO ₃ (BFO)	42
2.1.4	Preparation of CuS/Bi ₂ WO ₆ (CuSBTA), CuS/Bi ₂ W ₂ O ₉ (CuSBWO) and	

	CuS/BiFeO ₃ (CuSBFO) heterojunction materials	43
2.1.5	Synthesis of CdS/Bi ₂ W ₂ O ₉ (CdSBWO).....	43
2.1.6	Synthesis of α-Fe ₂ O ₃ -Bi ₂ S ₃ heterojunction material.....	44
2.2	Characterization of the photocatalyst materials	44
2.2.1	Powder X-ray diffraction (XRD).....	44
2.2.2	UV-Vis-DRS spectroscopy.....	44
2.2.3	Fourier transform infra-red spectroscopy (FTIR).....	44
2.2.4	Photoluminescence study (PL).....	44
2.2.5	Sorptometric studies.....	45
2.2.6	X-Ray photoelectron spectroscopy.....	45
2.2.7	High resolution transmission electron microscopy (HRTEM).....	45
2.2.8	Field emission scanning electron microscopy (FESEM).....	45
2.2.9	Total organic carbon analysis (TOC).....	45
2.2.10	Transient photocurrent measurement.....	45
2.2.11	Nuclear magnetic resonance (NMR) spectroscopy.....	46
2.3	Photocatalytic activity studies.....	46
2.3.1	Photocatalytic degradation of Congo red dye (CR).....	46
2.3.2	Photocatalytic degradation of diuron pesticide (DU).....	46
2.3.3	Degradation of alachlor pesticide (AL).....	46
2.3.4	Chemoselective aerobic oxidation of thiols to disulfides	47
2.3.5	Selective oxidation of amines to imines	48
2.3.6	Photocatalytic hydrogenation of nitroarenes	48
	References.....	49

3 Visible light driven photocatalytic study of Bi₂WO₆ based materials.

Section A: Chemoselective thiol oxidation catalysed by combustion synthesized Bi₂WO₆ material

3.1	Introduction.....	50
3.2	Results and discussion.....	51
3.2.1	Structural properties study	51
3.2.2	Optical properties study	54
3.2.3	Morphological study.....	56
3.2.4	Photocatalytic activity for selective oxidation of thiols to disulfides.....	57
3.2.5	Physical and spectra data of some representative disulfides.....	62

Section B: Congo red dye degradation catalyzed by CuS-Bi₂Cu_xW_{1-x}O_{6-2x} heterojunction system

3.3	Introduction.....	63
-----	-------------------	----

3.4	Results and discussion.....	64
3.4.1	XRD study.....	64
3.4.2	XPS study.....	66
3.4.3	Morphological study.....	67
3.4.4	FTIR study.....	69
3.4.5	Optical property study.....	70
3.4.6	Photocatalytic degradation of Congo red dye.....	72
3.5	Conclusions.....	79
	Reference.....	80
4	Visible light driven photocatalytic study of Bi₂W₂O₉ based materials	
	Section A: Selective aerobic oxidation of amines to imines catalyzed by CdS/Bi₂W₂O₉ heterojunction materials	
4.1	Introduction.....	84
4.2	Results and discussion.....	85
4.2.1	XRD study.....	85
4.2.2	XPS study.....	86
4.2.3	Morphological study.....	88
4.2.4	Optical properties study	91
4.2.5	FTIR study.....	93
4.2.6	Photocatalytic selective oxidation of amines to imines	94
	Section B: Photocatalytic mineralization of diuron pesticide catalyzed by CuS/Bi₂W₂O₉ heterojunction materials	
4.3	Introduction	101
4.4	Results and discussion	102
4.4.1	XRD study.....	102
4.4.2	XPS study.....	103
4.4.3	Optical properties study.....	104
4.4.4	FTIR study.....	106
4.4.5	Morphological study.....	107
4.4.6	Photocatalytic degradation of diuron pesticide.....	111
4.4.6.1	Optimization of reaction parameters.....	111
4.4.6.2	Mechanism of photocatalytic degradation of diuron over CuSBWO surface....	114
4.5	Conclusions.....	120
	References.....	120

5	Photocatalytic degradation of alachlor pesticide catalyzed by CuS/BiFeO₃ heterojunction materials	
5.1	Introduction.....	125
5.2	Results and discussion.....	126
5.2.1	XRD study.....	126
5.2.2	XPS study.....	128
5.2.3	Optical properties study.....	130
5.2.4	FTIR study	132
5.2.5	Morphological study.....	132
5.2.6	Transient photocurrent measurement	134
5.2.7	Photocatalytic degradation of alachlor.....	135
5.2.7.1	Optimization of reaction parameters	135
5.2.7.2	Plausible mechanism for photocatalytic degradation of alachlor	138
5.3	Conclusions.....	143
	References.....	144
6	Selective reduction of nitroarenes catalyzed by α-Fe₂O₃-Bi₂S₃ heterojunction materials	
6.1	Introduction.....	147
6.2	Results and discussion.....	148
6.2.1	XRD study.....	148
6.2.2	XPS study.....	150
6.2.3	Optical properties study.....	151
6.2.4	FTIR study.....	153
6.2.5	Morphological study.....	154
6.2.6	Photocatalytic hydrogenation of nitroarenes.....	157
6.2.6.1	Optimization of reaction parameters.....	157
6.2.6.2	Plausible mechanism for photocatalytic reduction of nitroarenes.....	161
6.2.7	NMR spectral data of some of the representative amines.....	162
6.3	Conclusions.....	163
	References.....	163
7	Summary & Conclusions	167
	Visible Research Output	171

List of Figures

1.1	Energy level diagram of noble metal supported semiconducting photocatalytic materials	7
1.2	Energy level diagram of different types of heterojunction photocatalysts	8
1.3	Crystal structures of (a) α -Bi ₂ O ₃ , (b) β -Bi ₂ O ₃ and (c) δ -Bi ₂ O ₃	10
1.4	Crystal structure of Bi ₂ S ₃	11
1.5	Crystal structure of Bi ₂ WO ₆	16
1.6	Crystal structure of Bi ₂ W ₂ O ₉	20
1.7	Crystal structure of BiFeO ₃	21
3.1	X-Ray diffraction patterns of (a) BTC-G, (b) BTC-U, (c) BTC-M and (d) BTC-H materials.....	52
3.2	XRD patterns of Bi ₂ WO ₆ nanoparticles synthesized using glycine as fuel at different F/O ratio (a) F/O= 0.5, (b) F/O= 1.0, (c) F/O= 1.5 and (d) F/O= 2.0...	52
3.3	Fourier line profile analysis plots for Bi ₂ WO ₆ nanomaterials	53
3.4	UV-Vis-DRS spectra of (a) BTC-G, (b) BTC-U, (c) BTC-H and (d) BTC-M (panel I) and plots of [F(R)hv] ² as a function of photon energy for the BTC materials (panel II).....	55
3.5	Photoluminescence spectra of (a) BTC-G, (b) BTC-H, (c) BTC-U and (d) BTC-M materials.....	56
3.6	Field emission scanning electron micrograph of (a) BTC-H (b) BTC-M (c) BTC-U (d) BTC-G (F/O=1.0), (e) BTC-G (F/O=1.5), (f) BTC-G (F/O=2.0) materials.....	57
3.7	Transmission electron micrograph of Bi ₂ WO ₆ -G material.....	57
3.8	Effect of irradiation time on the isolated yield of the diphenyl disulfide for different BTC catalysts.....	58
3.9	Effect of (I) catalyst weight and (II) reaction media on the photocatalytic activity of BTC-G catalyst for the synthesis of diphenyl disulfide after 6 h of irradiation time.....	59
3.10	(I) Recyclability of the BTC-G catalyst and (II) isolated yield of diphenyl disulfide in presence of various radical scavengers after 6 h in aqueous media (the photocatalytic test was conducted under identical reaction condition by adding 2 mmol of the scavenger to the reaction mixture before illumination).....	61
3.11	Probable mechanism for the selective oxidation of thiol to disulfide catalyzed by BTC-G material under visible light irradiation.....	62
3.12	XRD patterns of (a) BTA, (b) CuS5BTA, (c) CuS10BTA, (d) CuS15BTA, (e) CuS20BTA and (f) CuS materials.....	65

3.13	(I) Variation of 2θ value with CuS content for (131) peak of (a) BTA, (b) CuS5BTA, (c) CuS10BTA, (d) CuS15BTA, (e) CuS20BTA and (II) Vegard plot indicating an increase in d_{131} spacing with CuS content.....	66
3.14	XPS spectra of CuS10BTA heterojunction material.....	69
3.15	FESEM images of (a) BTA, (b, c) CuS10BTA and (d) CuS materials.....	68
3.16	(a-c) TEM images and (d) high resolution TEM image of CuS10BTA material.....	68
3.17	FTIR spectra of (a) BTA, (b) CuS5BTA, (c) CuS10BTA, (d) CuS15BTA, (e) CuS20BTA and (f) CuS materials.....	69
3.18	UV-Vis-DRS spectra of (a) BTA, (b) CuS5BTA, (c) CuS10BTA, (d) CuS15BTA, (e) CuS20BTA and (f) CuS materials.....	70
3.19	Plot of $[F(R)hv]^2$ as a function of photon energy (hv) in eV of (a) BTA and (b) CuS materials.....	71
3.20	Photoluminescence spectra of (a) BTA, (b) CuS5BTA, (c) CuS10BTA, (d) CuS15BTA and (e) CuS20BTA materials.....	72
3.21	Photocatalytic degradation of Congo red dye catalyzed by CuSBTA heterojunction materials.....	73
3.22	UV-Vis absorbance spectra of 10^{-4} M Congo red dye solution at different irradiation time using 25 Mg of CuS20BTA catalyst.....	74
3.23	(I) First order kinetics plots for the degradation of Congo red (II) apparent first order rate constant for different CuSBTA heterojunction photocatalysts.....	75
3.24	Effect of catalyst dose on the degradation efficiency of Congo red dye studied for CuS10BTA photocatalyst.....	76
3.25	(I) Degradation efficiency and (II) apparent rate constant (K_{app}) of CuS10BTA in presence of different radical scavengers.....	76
3.26	Probable mechanism for degradation of Congo red dye catalyzed by CuSBTA material under visible light irradiation.....	77
3.27	Recyclability study of CuS10BTA photocatalyst.....	79
4.1	X-ray diffraction patterns of (a) $Bi_2W_2O_9$, (b) CdS5BWO, (c) CdS10BWO, (d) CdS20BWO and (e) CdS materials.....	86
4.2	XPS spectra of CdS20BWO heterojunction material.....	87
4.3	FESEM images of (a) $Bi_2W_2O_9$, (b) CdS5BWO, (c) CdS10BWO and (d) CdS20BWO heterojunction materials.....	88
4.4	(a-c) TEM images, (d-i) EDS mapping and (j) EDX spectrum of CdS10BWO heterojunction material.....	89
4.5	Fourier line profile analysis plots for CdS and CdSBWO heterojunction materials.....	90
4.6	UV-Vis DRS (Panel I), plot of $[F(R)\times hv]^2$ as a function of photon energy (hv) in eV of $Bi_2W_2O_9$ (Panel II) and CdS (Panel III) nanomaterials.....	91

4.7	PL spectra of (a) Bi ₂ W ₂ O ₉ , (b) CdS5BWO, (c) CdS10BWO and (d) CdS20BWO heterojunction materials.....	92
4.8	(I) Transient photocurrent and (II) current (I) vs voltage (V) measurement plots for (a) BWO and (b) CdS20BWO heterojunction materials.....	93
4.9	FTIR spectra of (a) Bi ₂ W ₂ O ₉ , (b) CdS5BWO, (c) CdS10BWO and (d) CdS20BWO heterojunction materials.....	94
4.10	Photocatalytic efficiency of CdSBWO heterojunctions (Panel I) and catalyst weight variation of CdS20BWO heterojunction (Panel II) for the photocatalytic selective oxidation of benzylamine.....	95
4.11	Photocatalytic oxidation of benzylamine in presence of different radical scavengers catalyzed by CdS20BWO catalyst (benzylamine 1 mmol, catalyst 25 mg, reaction time 12 h).....	99
4.12	Plausible mechanism for the oxidation of benzylamine over CdSBWO heterojunction photocatalyst surface.....	100
4.13	Reusability of CdS20BWO heterojunction photocatalyst for the selective oxidation of benzylamine.....	100
4.14	XRD patterns of (a) BWO, (b) CuS5BWO, (c) CuS10BWO, (d) CuS15BWO, (e) CuS20BWO and (f) CuS materials.....	102
4.15	(I) Variation of peak position with CuS content for (114) peak of pure (a) BWO, (b) CuS5BWO, (c) CuS10BWO, (d) CuS15BWO, (e) CuS20BWO and (II) Vegard plot indicating an increase in d ₁₁₄ spacing with CuS content.....	103
4.16	XPS spectra of CuS20BWO heterojunction material.....	104
4.17	UV-Vis-DRS spectra of (a) BWO, (b) CuS5BWO, (c) CuS10BWO, (d)CuS15BWO, (e) CuS20BWO and (f) CuS (Panel I) and plots of [F(R)hv] ² as a function of photon energy (hv) in eV for BWO (Panel II) and CuS (Panel III).....	105
4.18	PL spectra of (a) BWO, (b) CuS5BWO, (c) CuS10BWO, (d) CuS15BWO and (e) CuS20BWO heterojunction materials.....	106
4.19	FTIR spectra of (a) BWO, (b) CuS5BWO, (c) CuS10BWO, (d) CuS15BWO and (e) CuS20BWO heterojunction materials.....	107
4.20	FESEM images of (a) BWO, (b) CuS5BWO, (c) CuS10BWO, (d) CuS15BWO and (e) CuS20BWO heterojunction materials.....	108
4.21	Different stages of formation of hierarchical CuSBWO heterojunction microspheres.....	109
4.22	(a-f) TEM images, (g,h) EDS mapping and (i) EDX spectrum of CuS20BWO heterojunction material.....	110
4.23	Degradation efficiency of CuS20BWO catalyst for diuron degradation in presence of different oxidant (O ₂ flow 30 ml/min, O ₃ flow 30 ml/min, H ₂ O ₂ 200 μl).....	111

4.24	Photocatalytic efficiency of CuSBWO catalysts for diuron degradation (10 ppm DU, 200 μ l 30 % H ₂ O ₂ , 75 mg of catalyst).....	112
4.25	(I) Pseudo first order kinetics plots and (II) apparent rate constants of CuSBWO heterojunction photocatalysts for diuron degradation.....	112
4.26	(I) Effect of catalyst dose, (II) H ₂ O ₂ concentration and (III) diuron concentration on the photocatalytic degradation activity of CuS20BWO photocatalyst.....	113
4.27	(I) Evolution of different ions and (II) TOC removal at different irradiation time.....	114
4.28	GC-MS analysis of degradation products of diuron at different reaction time (a) pure diuron, (b) 10 min, (c) 1.5 h and (d) 3 h catalyzed by CuS20BWO heterojunction materials.....	115
4.29	Photocatalytic degradation of diuron in presence of different radical scavengers catalyzed by CuS20BWO heterojunction photocatalyst	117
4.30	(I) pseudo first order kinetics plots and (II) apparent rate constants of CuS20BWO heterojunction photocatalyst in presence of different radical scavengers.....	117
4.31	Plausible mechanism for diuron degradation over CuSBWO heterojunction surface.....	118
4.32	Reusability of CuS20BWO heterojunction photocatalyst for degradation of diuron.....	119
4.33	XRD profile of CuS20BWO heterojunction photocatalyst material (a) freshly prepared, and after (b) 1 st , (c) 2 nd , (d) 3 rd and (e) 5 th catalytic cycles.....	119
5.1	XRD profiles of (a) BiFeO ₃ , (b) CuS5BFO, (c) CuS10BFO, (d) CuS20BFO, (e) CuS and (f) Bi ₂ S ₃ materials.....	127
5.2	XRD patterns of (a) BFO and (b, c) hydrothermally treated BFO in absence and in presence of thiourea.....	128
5.3	XPS spectra of CuS10BFO heterojunction material.....	129
5.4	(Panel I) UV-Vis DRS spectra of (a) BiFeO ₃ , (b) CuS5BFO, (c) CuS10BFO, (d) CuS20BFO and (e) CuS and (Panel II & III) Plot of [F(R)h ν] ² as a function of photon energy (h ν) in eV for BFO and CuS materials.....	130
5.5	PL spectra of (a) BiFeO ₃ , (b) CuS5BFO, (c) CuS10BFO, (d) CuS20BFO and (e) CuS materials.....	131
5.6	FTIR spectra of (a) BiFeO ₃ , (b) CuS5BFO, (c) CuS10BFO and (d) CuS20BFO heterojunction materials.....	132
5.7	FESEM images of (a) BFO, (b) CuS5BFO, (c) CuS10BFO, (d) CuS20BFO and (e-h) HRTEM images of CuS10BFO material.....	133
5.8	Elemental mapping study of CuS10BFO heterojunction material.....	134
5.9	(a) Transient photocurrent and (b) current (I) vs voltage (V) measurement plots for BFO and CuS10BFO heterojunction materials.....	135

5.10	Photocatalytic efficiency of CuSBFO heterojunction photocatalysts towards the degradation of alachlor pesticide (25 mg catalyst, 10 μ l H ₂ O ₂ and 5 ppm alachlor aqueous solution).....	136
5.11	(Panel I) effect of catalyst dose (CuS10BFO catalyst, 5 ppm AL, 10 μ l H ₂ O ₂ , 1 h), (Panel II) initial alachlor concentration (25 mg CuS10BFO catalyst, 10 μ l H ₂ O ₂ , 1 h) and (Panel III) study of TOC removal (CuS10BFO catalyst, 5 ppm AL, 10 μ l H ₂ O ₂) for the photocatalytic degradation of alachlor over CuS10BFO photocatalyst.....	137
5.12	Effect of different radical scavengers on the photocatalytic degradation of alachlor studied using CuS10BFO photocatalyst.....	138
5.13	Fluorescence spectra of terephthalic acid solution containing catalyst particles (25 mg) irradiated with visible light (I) CuS10BFO and (II) BFO photocatalysts.....	139
5.14	GC-MS analysis of photocatalytic degradation products of alachlor at different irradiation time.....	140
5.15	Plausible mechanism for photocatalytic degradation of alachlor over CuSBFO surface.....	142
5.16	Recyclability test of CuS10BFO heterojunction photocatalyst for the degradation of alachlor.....	143
6.1	XRD patterns of (a) Fe ₂ O ₃ as prepared, (b) Fe ₂ O ₃ calcined at 500 °C, (c) α -Fe ₂ O ₃ (25%)-Bi ₂ S ₃ , (d) α -Fe ₂ O ₃ (37%)-Bi ₂ S ₃ , (e) α -Fe ₂ O ₃ (50%)-Bi ₂ S ₃ and (f) Bi ₂ S ₃ materials.....	149
6.2	XPS spectra of α -Fe ₂ O ₃ (37%)-Bi ₂ S ₃ photocatalyst.....	151
6.3	(Panel I) UV-Vis DRS spectra of (a) Fe ₂ O ₃ , (b) α -Fe ₂ O ₃ (25%)-Bi ₂ S ₃ , (c) α -Fe ₂ O ₃ (37%)-Bi ₂ S ₃ , (d) α -Fe ₂ O ₃ (50%)-Bi ₂ S ₃ and (e) Bi ₂ S ₃ materials and (Panel II & III) plot of [F(R)hv] ² as a function of photon energy (hv) for Fe ₂ O ₃ and Bi ₂ S ₃ materials.....	152
6.4	Photoluminescence (PL) spectra of (a) Bi ₂ S ₃ , (b) α -Fe ₂ O ₃ (25%)-Bi ₂ S ₃ , (c) α -Fe ₂ O ₃ (37%)-Bi ₂ S ₃ and (d) α -Fe ₂ O ₃ (50%)-Bi ₂ S ₃ heterojunction photocatalysts (excitation wavelength 400 nm).....	153
6.5	FTIR spectra of (a) α -Fe ₂ O ₃ (25%)-Bi ₂ S ₃ , (b) α -Fe ₂ O ₃ (37%)-Bi ₂ S ₃ and (c) α -Fe ₂ O ₃ (50%)-Bi ₂ S ₃ heterojunction materials.....	154
6.6	FESEM images of (a) Bi ₂ S ₃ , (b) α -Fe ₂ O ₃ (25%)-Bi ₂ S ₃ , (c) α -Fe ₂ O ₃ (37%)-Bi ₂ S ₃ and (d) α -Fe ₂ O ₃ (50%)-Bi ₂ S ₃ heterojunction materials.....	155
6.7	(a-d) TEM images, (e-f) HRTEM images, (g) EDX spectrum and (h) EDS mapping of α -Fe ₂ O ₃ (37%)-Bi ₂ S ₃ heterojunction material.....	156
6.8	Photocatalytic hydrogen transfer reduction of nitrobenzene to aniline catalyzed by α -Fe ₂ O ₃ -Bi ₂ S ₃ heterojunction photocatalysts (reaction conditions: 50 mg of catalyst, C ₆ H ₅ -NO ₂ :N ₂ H ₄ .H ₂ O molar ratio = 2:8).....	158

6.9	Effect of nitrobenzene to hydrazine hydrate molar ratio on the photocatalytic activity of α -Fe ₂ O ₃ (37%)-Bi ₂ S ₃ catalyst (reaction conditions: 50 mg catalyst, 4 h).....	159
6.10	(Panel I) effect of catalyst dose and (Panel II) reusability study of photocatalytic hydrogen transfer reduction of nitrobenzene to aniline (reaction condition: α -Fe ₂ O ₃ (37%)-Bi ₂ S ₃ catalyst, C ₆ H ₅ -NO ₂ :N ₂ H ₄ .H ₂ O molar ratio = 2:8, 4 h).....	160
6.11	Plausible mechanism for photocatalytic hydrogen transfer reduction of nitroarenes over the α -Fe ₂ O ₃ /Bi ₂ S ₃ heterojunction photocatalyst.....	162

List of Tables

1.1	Photocatalytic application of semiconducting nanomaterials towards selective organic transformations.....	5
1.2	Photocatalytic applications of Bi ₂ O ₃ based materials.....	10
1.3	Photocatalytic applications of Bi ₂ S ₃ based materials.....	12
1.4	Photocatalytic applications of bismuth oxysalt based heterostructure materials.	15
1.5	Photocatalytic applications of Bi ₂ WO ₆ based materials.....	18
1.6	Photocatalytic applications of Bi ₂ W ₂ O ₉	20
1.7	Photocatalytic applications of BiFeO ₃ based materials.....	22
3.1	Physicochemical characteristics and photocatalytic activity of the combustion synthesized Bi ₂ WO ₆ nanoparticles.....	54
3.2	BTC-G catalyzed selective oxidation of thiols to disulfides after 6 h of reaction in aqueous media.....	60
3.3	Specific surface areas of BTA and CuSBTA heterojunction materials.....	72
4.1	Specific surface areas and crystallite size of CdS phase in CdSBWO heterojunction materials.....	90
4.2	Photocatalytic oxidation of benzylamine catalyzed by CdS20BWO heterojunction material.....	96
4.3	Selective oxidation of various amines catalyzed by CdS20BWO heterojunction material.....	97
4.4	Specific surface areas of CuSBWO heterojunction materials.....	110
5.1	Specific surface areas of the CuSBFO heterojunction materials.....	134
6.1	Specific surface areas of Bi ₂ S ₃ , Fe ₂ O ₃ and α -Fe ₂ O ₃ -Bi ₂ S ₃ heterojunction materials.....	157
6.2	Photocatalytic hydrogen transfer reduction of structurally diverse nitroarenes catalyzed by α -Fe ₂ O ₃ (37%)-Bi ₂ S ₃ heterojunction photocatalyst.....	161

Abbreviations

AR	:	Analytical Reagent
DRS	:	Diffuse Reflectance Spectroscopy
FID	:	Flame Ionization Detector
FTIR	:	Fourier Transform Infrared Spectroscopy
GC	:	Gas Chromatography
FESEM	:	Field Emission Scanning Electron Micrograph
HRTEM	:	High Resolution Transmission Electron Micrograph
XRD	:	X-Ray Diffraction
XPS	:	X-Ray Photoelectron Spectroscopy
PL	:	Photoluminescence Spectroscopy
TOC	:	Total Organic Carbon
NMR	:	Nuclear Magnetic Resonance
GC-MS	:	Gas Chromatography-Mass Spectrometry
HPLC	:	High Performed Liquid Chromatography

Notations

eV	:	Electron volt
m ² /g	:	square meter per gram
g	:	gram
Hz	:	Hertz
nm	:	nanometer
Å	:	Angstrom
d	:	Inter planner spacing
r	:	radius
cm	:	centimeter
KJ	:	kilo Joule
h	:	hour
θ	:	Bragg angle
v	:	frequency

CHAPTER 1

Introduction & Literature Survey

1.1 General Introduction

Increasing demand and shortage of clean water sources due to rapid industrialization, population growth and long-term droughts have become an issue worldwide. Various survey data indicates that around four billion people worldwide have no or little access to clean water supply and millions of people are affected by severe waterborne diseases. One of the sustainable ways to deal with water shortage is to recycle the waste water from industrial and agricultural sectors. In this context, development of low-cost and high efficiency advanced water treatment technologies to treat wastewater is highly desirable. Wastewater from industrial and agricultural sources typically contain suspended solids, heavy metal ions, water pathogens and persistent organic pollutants (POPs) such as personal care products, pharmaceuticals, dyes, pesticides, steroids, hormones and mineral oil. Among different classes of pollutants, the speciation/mineralization of POPs has received significant research focus in recent years due to their structural and functional diversity, persistency in environment and adverse effect on human health. Currently available water treatment technologies such as adsorption and coagulation merely concentrate these pollutants by transferring them to other phases [1, 2]. Other conventional water treatment methods such as sedimentation, filtration, chemical and membrane technologies involve high operating costs and could generate toxic secondary pollutants in the ecosystem. Chlorination has been the most common and widely used disinfection process. However, the disinfection by-products generated from chlorination are mutagenic and carcinogenic to human health [3]. The most recent and innovative technology employed for waste water treatment, the so called “Advanced Oxidation Process (AOP)” are based on the insitu generation of highly reactive transitory species (i.e. H_2O_2 , OH^\bullet , O_2^\bullet , O_3) for mineralization of refractory organic compounds and disinfection by-products [4-10]. The catalytic wet oxidation, one of the promising AOPs has been extensively investigated in literature. The catalytic wet oxidation process employs heterogeneous redox catalyst such as CeO_2 , CuO , MnO_2 , Mn_3O_4 and other complex oxides in conjugation with oxidants such as hydrogen peroxide, tertiary butyl hydroperoxide (TBHP) to oxidize organic pollutants under high pressure and temperature conditions [11-19]. In many studies complete degradation of the organic pollutants has been achieved using this method. However, the high operational cost and extreme reaction conditions prevent large scale utility of this technology. In recent years, heterogeneous photocatalysis employing semiconductor nanoparticles (TiO_2 , ZnO , Fe_2O_3 , CdS , ZnS , MoS_2 and Ag_3PO_4) as catalysts has been studied for degradation of a wide range of ambiguous refractory organics into innocuous products [20-26]. From the early stage of laboratory scale study, the photocatalytic method has evolved rapidly in the last few

years as a potential technology for water decontamination. Some examples of success achieved in the application of the photocatalytic technology are the heterogeneous photocatalysis plants located at the INETI (Instituto Nacional de Engenharia, Tecnologia Industrial e Inovacao, Portugal) and PSA (Plataforma Solar de Almeria, Spain) [27]. Till date TiO_2 is the most widely investigated and promising semiconductor material in photocatalytic oxidation reaction [20]. Many persistent organic substances have been degraded in TiO_2 suspensions. However, very poor response to visible light has obstructed the application of TiO_2 photocatalyst in water treatment [20]. To overcome this drawback, efforts have been devoted to modify the surface or bulk properties of TiO_2 , by doping, combining TiO_2 with another semiconductor to make hetero-junctions and dye sensitization [28-34]. Though the above methods could partly enhance the visible light photocatalytic activity of TiO_2 , their applicability in efficient visible-light-active photocatalysis remain a challenge. With advancement in the understanding of the photocatalytic process, novel visible light active semiconducting oxides, sulfides and phosphides (Fe_2O_3 , CdS , Ag_3PO_4 , SnS_2 , BiFeO_3 , ZnFe_2O_4 , WO_3 , Co_3O_4 and Bi_2O_3) photocatalysts have been designed and tested for water decontamination [22, 23, 26, 35-39]. Some of the major challenges in photocatalytic degradation of POPs using semiconductor photocatalytic materials under visible light are low photon harvesting, rapid recombination of charge carriers, generation of fewer active transient species (i.e. H_2O_2 , $\cdot\text{OH}$, $\text{O}_2^{\cdot-}$, $\text{O}_3^{\cdot-}$) and their effective utilization in photo oxidation process [40, 41]. In a typical photocatalytic process upon absorption of an incident photon, the electron (e^-) undergoes a transition from valance band to conduction band leaving behind a positively charged hole in the valance band (h^+). The extent of absorption of the light depends on the band gap, surface area and morphology of the particles [40, 41]. To absorb efficiently in visible region of electromagnetic spectrum, the band gap of the semiconductor should be less than 3 eV. A high surface area of the semiconductor implies a greater number of photon can be captured and utilized. The fate of a photochemical oxidation process depends strongly on the efficiency of utilization of the e^- and h^+ . Electrons and holes being transient species undergo rapid recombination decreasing the photocatalytic activity of the semiconductor material [40-41]. In order to efficiently separate the electrons and the holes, the photogenerated electrons can be trapped away from the active holes using heterostructure and composite systems [40-41]. The photogenerated e^- and h^+ can take part directly in the photo oxidation process or can generate the active species (i.e. H_2O_2 , $\cdot\text{OH}$, $\text{O}_2^{\cdot-}$, $\text{O}_3^{\cdot-}$) by reacting with adsorbed dioxygen or $\text{H}_2\text{O}/\text{OH}^-$ through a series of reactions [40-41]. These active species then take part in degradation of the contaminants. In this thesis, an attempt has been made to prepare Bi based semiconducting complex oxides nanomaterials (Bi_2WO_6 , $\text{Bi}_2\text{W}_2\text{O}_9$ and BiFeO_3) by combustion synthesis method. The Bi based complex materials have been subsequently modified with CuS to prepare novel heterostructure systems with improved visible light absorption, charge carrier separation and enhanced photocatalytic activity. The photocatalytic activity of the heterostructure materials have been studied for complete mineralization of recalcitrant Congo red dye and diuron and alachlor pesticides.

1.2 Photocatalysis in Selective Organic Transformations

The sustainability of the modern society relies heavily on many synthetic chemicals including drugs, cosmetics, agrochemicals, pesticides, dyes and polymers. These chemicals are consumed in bulk quantities every year. These important classes of chemicals are primarily synthesized from simple organic compounds like aldehyde/ketone, alcohols, amines and imines using oxidation, reduction and coupling processes. The conventional methods for synthesis of value added chemicals utilize homogeneous corrosive acid-base catalyst, stoichiometric reagents and harmful chemical oxidants at elevated temperature to achieve high yield of the product. However, processes involving these conventional methods are associated with problems such as catalyst handling, product purification, corrosion and generation of significant quantity of by-products [42, 43]. In recent years, several efforts have been devoted to develop greener protocol for synthesis of value added chemicals. The heterogeneous photocatalytic route is considered as a promising alternative to the conventional methods of organic synthesis. The photocatalytic route is highly sustainable, greener and economic towards synthesis of value added chemicals, as it uses renewable energy source, discourages the use of stoichiometric hazardous reagents, avoid solvent loss and uses atmospheric air as oxidant [42-45]. The use of H₂O as reaction media is another step to makes the system more eco-friendly [44, 46]. The generation of reactive $\cdot\text{OH}$ radicals by photolysis of H₂O over photocatalyst surface may lead to the generation of non-selective products in organic synthesis. For example, TiO₂ catalyzes the aerobic oxidation of benzyl alcohol under UV light giving nearly 50% conversion and 60% selectivity to benzaldehyde [47]. The low selectivity is mainly ascribed to the hydroxyl radical formation which is a non-selective oxidative species with strong oxidizing ability, resulting in a wide variety of reaction products. However, the selectivity issue has been successfully addressed by rational design of novel photocatalytic materials. Bahnemann et al have used nanoporous hierarchical Pt/Bi₂WO₆ as a highly active photocatalyst for conversion of aromatic alcohols to aldehydes under visible light irradiation [48]. The high efficiency of Bi₂WO₆ has been ascribed to nanoporous surface and hierarchical architecture whereas the Pt nanoparticles act as electron sink and prevent the recombination of exciton. The alcohol molecules compete with water and are oxidized by the VB h^+ thus minimizing the generation of $\cdot\text{OH}$ which lead to a significant improvement in selectivity [48]. Lang et al have used eosin Y sensitized TiO₂ nanoparticles coupled with TEMPO to perform selective oxidation of benzyl alcohol under visible light irradiation [49]. The working principle of the catalyst involves the transfer of photoelectrons from eosin Y to CB of TiO₂ where O₂⁻ radicals are produced by dioxygen activation. The dye radical cation formed in the process activates TEMPO to TEMPO⁺. The TEMPO⁺ undergoes nucleophilic attack by alcohol to form an intermediate which decomposes to give the benzaldehyde. The TEMPO molecules are regenerated by oxidation with O₂⁻ radicals. This photoredox cycle is highly selective to benzaldehyde formation without the involvement of $\cdot\text{OH}$ radicals [49]. Zhang et al have reported plasmonic Au

catalyst supported on oxygen deficient BiOCl for selective oxidation of benzyl alcohol to benzaldehyde with O₂ under visible light irradiation [50]. The oxygen vacancies on BiOCl trap and transfer the plasmonic hot electrons to adsorbed O₂ to produce O₂^{•-} radicals, while plasmonic hot holes on Au surface mildly oxidize benzyl alcohol to corresponding carbon-centered radicals. The concerted ring addition between these two radical species on the BiOCl surface highly favors the production of benzaldehyde [50]. In addition to above stated methods, many visible light active photocatalytic materials including PdO/WO₃, BiVO₄/g-C₃N₄, P-doped g-C₃N₄, Au/CdMoO₄, Pd@CeO₂ and layered C₃N₃S₃ Polymer/graphene hybrids have been designed for selective oxidation of aromatic alcohols to aryl aldehydes [51-57]. The oxidation of amines to imines is another important chemical transformation which has been successfully accomplished by heterogeneous photocatalytic route in an environmentally friendly way under mild condition [58-61]. Tada et al have recently demonstrated the use of visible light active Au/rutile TiO₂ photocatalyst towards aerobic oxidation of amines with excellent selectivity to imines (> 99%) [58]. The reaction proceeds through the localized surface plasmon resonance-excited electron transfer from the Au nanoparticle to the rutile TiO₂. Can Li et al have studied the photocatalytic activity of colloidal BiOCl nanosheets for aerobic oxidation of secondary amines. Compared to bulk BiOCl, the colloidal nanosheets exhibited strong absorption in the visible range which has been attributed to the high content of oxygen vacancies in the nanosheets. The BiOCl nanosheets show surface hydrophobic property and excellent photocatalytic oxidation of secondary amines [59]. The other improved photocatalytic materials developed for aerobic oxidation of amines include the WS₂ nanosheets, BiVO₄/g-C₃N₄, CuWO₄ and ZnIn₂S₄ [52, 53, 60-61]. The coupling reactions involving C-C, C-N and C-O bond formation have a special place in synthetic organic chemistry because of their application in synthesis of biologically important molecules, pharmaceuticals and fine chemicals [62-63]. Particularly, important are the Suzuki and Sonogoshira coupling reactions which have been widely used for C-C bond formation [64-69]. Conventionally, these coupling reactions are performed under homogeneous conditions using a variety of phosphine ligand/palladium catalytic complexes together with additives/co-catalysts [70-71]. However, major drawbacks such as expensive ligands, high Pd loading, difficulty in separation of the Pd complexes, palladium leaching and poor recyclability greatly limit their wide applications. In recent years, efficient photocatalytic routes have been designed for Suzuki and Sonogoshira coupling reactions [64-69]. Zhang et al have used Pd metal immobilized on conjugated microporous poly(benzoxadiazole) as a efficient, heterogeneous photocatalysts for the Suzuki coupling reactions under visible light irradiation at room temperature [65]. Excellent yield of the products are obtained for coupling of a variety of aryl halides with arylboronic acid which has been ascribed to the photoamplified Schottky effect at the metal-semiconductor interface. Yan et al have developed a plasmonic Au-Pd nanostructure composed of Au nanocrystal cores and grafted Pd nanoparticles which show excellent photocatalytic activity for Suzuki coupling reaction [66]. The Au nanocrystal core acts as a plasmonic component for efficient

light absorption, and the Pd nanoparticles act as the catalysts for Suzuki coupling reaction. Guo et al have studied the Sonogashira coupling of aryl halides with terminal alkynes using a visible-light active Pd/SiC photocatalyst under copper-, and ligand-free conditions [68]. The Mott-Schottky contact in Pd/SiC enhances the photoelectron population on the Pd nanoparticles which facilitate the cleavage of carbon-halogen bonds. In addition to the above stated organic reactions, many improved heterogeneous photocatalytic routes have been developed in recent years for reduction of nitro compounds, olefin–imine addition, radical coupling reaction, synthesis of polymer and fine chemicals [47, 72-79]. Table 1.1 presents a brief list of important photocatalytic materials studied recently for selective organic synthesis. The literature results presented above suggests the promising potential of heterogeneous photocatalytic methods in selective organic synthesis. In this thesis, we have explored the photocatalytic application of bismuth based complex oxides (Bi_2WO_6) and heterostructured photocatalytic materials ($\text{CdS}/\text{Bi}_2\text{W}_2\text{O}_9$ and $\text{Bi}_2\text{S}_3\text{-}\alpha\text{-Fe}_2\text{O}_3$) towards selective oxidation of thiols/amines and reduction of nitroarenes.

Table 1.1: Photocatalytic applications of semiconducting nanomaterials towards selective organic transformations

Catalyst	Photocatalytic reaction	Reference
Pt/ Bi_2WO_6	Benzyl alcohol oxidation	[48]
Eosin Y- TiO_2 with TEMPO	Benzyl alcohol oxidation	[49]
Au-BiOCl	Benzyl alcohol oxidation	[50]
PdO_x/WO_3	Oxidation of 2-propanol	[51]
$\text{BiVO}_4/\text{g-C}_3\text{N}_4$	Oxidation of benzyl amine and benzyl alcohol	[52]
CuWO_4	Benzyl amine oxidation	[53]
P-doped $\text{g-C}_3\text{N}_4$	Benzyl alcohol oxidation	[54]
Au/ CdMoO_4	Benzyl alcohol oxidation	[55]
Pd@CeO_2	Benzyl alcohol oxidation	[56]
$\text{C}_3\text{N}_3\text{S}_3$ Polymer/Graphene	Benzyl alcohol oxidation	[57]
Au/ TiO_2	Benzyl amine oxidation	[58]
BiOCl	Oxidation of secondary amines	[59]
WS_2	Oxidative coupling of amines	[60]
ZnIn_2S_4	Benzyl amine oxidation	[61]
Pt/ TiO_2	Benzyl alcohol oxidation	[80]
$\text{Bi}_4\text{O}_5\text{Br}_2$	Benzyl alcohol oxidation	[81]
M- TiO_2 (M = Au, Ag, Pt, and Pd)	Benzyl alcohol oxidation	[82]
$\text{g-C}_3\text{N}_4$ with N-vacancy	Benzyl alcohol oxidation	[83]
CdS-TiO_2	Benzyl alcohol oxidation	[84]
CdS@CeO_2 & CdS@TiO_2	Benzyl alcohol oxidation	[85]

M-g-C ₃ N ₄ (M= Au, Ru, Pd, Pt, Ir, Ag & Rh)	Benzyl alcohol oxidation	[86]
AgBr@Ag@TiO ₂	Benzyl alcohol oxidation	[87]
Ir/TiO ₂	Benzyl alcohol oxidation	[88]
Au-CeO ₂ -TiO ₂ /CNFs	Benzyl alcohol oxidation	[89]
AgI/AgVO ₃	Benzyl amine oxidation	[90]
g-C ₃ N ₄	Benzyl amine oxidation	[91]
Nb ₂ O ₅	Benzyl amine oxidation	[92]
TiO ₂	Oxidation of amines	[93]
TiO ₂	Benzyl amine oxidation	[94]
dye-sensitized TiO ₂	Benzyl amine oxidation	[95]
TiO ₂	Benzyl amine oxidation	[96]
TiO ₂ -silicate	Benzyl amine oxidation	[97]
CdS	Benzyl amine oxidation	[98]
Au/Al ₂ O ₃	Aldehyde to Ester	[99]
Cr/SiO ₂	Biodiesel production	[100]
TiO ₂	Esterification of acetic acid to methyl acetate	[101]
TiO ₂	Esterification of oleic acid	[102]
Pd@g-C ₃ N ₄	C-H activation and oxidative esterification	[103]
Ru@TiO ₂	esterification reaction and transfer-hydrogenation reactions	[104]
TiO ₂	Cross-coupling of methanol and formaldehyde	[105]
g-C ₃ N ₄	Esterification of benzaldehyde and alcohol	[106]
VO@g-C ₃ N ₄	Oxidative esterification	[107]
TiO ₂	Deoxygenation of epoxides	[108]
Pd-TiO ₂	Hydrogenation of alkenes to alkanes	[109]
Pd/SiC	Sonogashira coupling reaction	[110]
Ru-Pd bimetallic complex	Suzuki-Miyaura coupling reaction	[111]
Plasmonic Au-Pd	Suzuki coupling reactions	[112]
Au-Pd@ZrO ₂	Suzuki-Miyaura coupling	[113]

1.3 Strategies to Improve Photocatalytic activity of semiconducting photocatalyst

In a photocatalytic reaction, several factors including band gap, surface area, crystallinity and morphology of the semiconductor influence the photocatalytic activity. In order to develop efficient visible light active photocatalytic protocol, the semiconducting material should have

good photon harvesting efficiency and efficient separation of excitons. Several strategies have been developed in literature to reduce the recombination rate of excitons which include dispersion of plasmonic metal nanoparticles over the catalyst surface, doping of metal and non-metal and formation of heterojunction materials [40]. Dispersion of plasmonic metal nanoparticles over the photocatalyst surface significantly improves the separation of charge carriers. The metal nano particles act as both sink and reservoir of electron. Since the Fermi energy of the metal nanoparticles is lower than the semiconducting materials, the facile migration of electrons from the CB of semiconductor to metal nanoparticle takes place, resulting in efficient separation of excitons (Figure 1.1). Au, Ag, Pd and Rh noble metal have been widely used as plasmonic nanoparticle in heterogeneous photocatalysis [114]. The dispersed metal nanoparticles also act as co-catalyst and provide active sites with lower activation energy and hence improve the photocatalytic activity [114]. Doping of metal and non-metal ions is another important way to improve the photocatalytic efficiency of a photocatalyst. The doped metal and non-metal species have a tendency to capture the photo-excited electrons and holes and decrease their recombination rate. Moreover, the dopants create localized energy state at the VB or CB edge which results in a red shift the absorption edge thus reducing the band gap value and improvement in visible light absorption properties of the photocatalyst [114-116]. Several metal ions including Ag^+ , Rb^+ , Ni^{2+} , Co^{2+} , Cu^{2+} , V^{3+} , Ru^{3+} , Fe^{3+} , Os^{3+} , Y^{3+} , La^{3+} , Pt^{4+} , Pt^{2+} and Cr^{3+} have been used as dopants in heterogeneous photocatalysis in order to improve the photocatalytic activity.

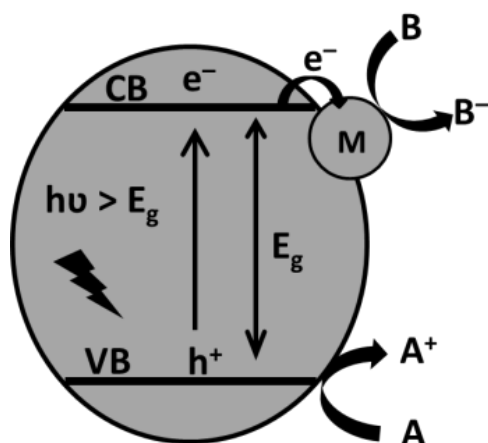


Figure 1.1: Energy level diagram of noble metal supported semiconducting photocatalytic materials.

Formation of composite and heterojunctions between semiconducting materials is one of the widely studied strategy to improve visible light absorption and charge carrier separation properties. Depending on the alignment of VB and CB of two semiconductors, the heterojunction systems are broadly divided into three categories [40-41]. Figure 1.2 schematically represents the band alignment between two semiconductors.

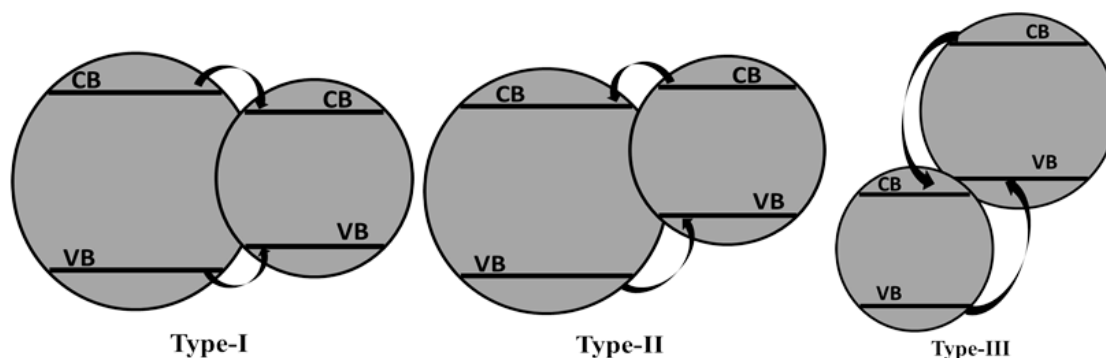


Figure 1.2: Energy level diagram of different types of heterojunction photocatalysts.

In a type I heterojunction, the movement of photo excited electrons and holes takes place from the high band gap materials to low band gap semiconducting material. This migration of excitons leads to the accumulation of electrons and holes in one of the semiconductor surface. Hence the type I heterojunction are able to separate the charge carriers to some extent. In case of type II heterojunction, the migration of photo excited electrons takes place from the CB of one semiconductor to CB of second semiconductor and the holes migrates in a reverse direction in the VB of both semiconductors. The photoelectrons reside in the CB of one semiconductor whereas the holes reside on the VB of other semiconductor leading to efficient space separation of the charge carriers. Among the heterojunction systems, the Type-II heterojunctions are highly efficient for the charge carrier separation.

1.4 Photocatalysis by Bismuth based Semiconducting Nanomaterials

There have been significant efforts by scientific community in recent years to study the application of semiconducting nanoparticles as photocatalyst for complete oxidation/mineralization of environmental pollutants and selective organic synthesis. With reference to their application under visible light/solar light irradiation, the semiconducting nanoparticles can be divided into two category ie. low band gap (< 3 eV) and wide band gap (> 3 eV). The wide band gap semiconducting materials require higher energy for electronic transition and hence poorly absorb in the visible region. The poor response to visible light significantly affects their efficiency. The low band gap semiconducting materials by virtue of their small band gap absorb significant amount of visible light and are promising candidates for visible light active environmental photocatalysis. However, these materials exhibit higher charge recombination rate and inability to oxidize $\text{H}_2\text{O}/\text{OH}^-$ to hydroxyl radicals ($\cdot\text{OH}$) which is considered as a strong oxidizing species for organic contaminant [10]. In this regard in recent years, much attention has been given to a series of visible light active Bi-based photocatalysts. Although Bi is a heavy metal, it does not show acute toxicity for humans and other higher mammals because of its low uptake into mammalian cells. Bi based compounds

are widely used in the medicinal field due to its antibacterial activity. Many Bi^{3+} containing compounds have been found to possess a narrow band gap and exhibit high visible light photocatalytic activity because of the hybridized O 2p and Bi 6s valence band [117]. The largely dispersed valence band of Bi compound facilitates charge carrier separation and their utilization in photocatalysis. The following section provides a brief review of bismuth based important photocatalytic materials studied in literature.

1.4.1 Bi_2O_3

Bismuth oxide (Bi_2O_3) is one of the promising photocatalytic material due to its relatively smaller band gap (2.4-2.8 eV), higher oxidation power of the valence band holes and non-toxic properties [118]. The $6s^2$ lone pair electrons of Bi^{3+} ions (electronic configuration: $[\text{Xe}] 4f^{14} 5d^{10} 6s^2$) induce intrinsic polarizability in Bi_2O_3 structure which favors separation of photogenerated electron-hole pairs and transfer of these charge carriers to the surface for photocatalytic applications [117]. Bi_2O_3 exists in five different polymorphic forms labeled as α - Bi_2O_3 (monoclinic), β - Bi_2O_3 (tetragonal), γ - Bi_2O_3 (body centered cubic), δ - Bi_2O_3 (cubic), and ω - Bi_2O_3 (triclinic) (Figure 1.3) [119]. Among these polymorphic forms, β - Bi_2O_3 has the strongest absorption in the visible light region because of its smallest band gap (~ 2.4 eV) [119]. The selective formation and stabilization of the tetragonal β - Bi_2O_3 which is a thermodynamically unstable phase, is a widely studied topic in literature. In recent years, there are several efforts to prepare different crystallographic phases of Bi_2O_3 with distinct morphology to maximize their catalytic efficiency. For example, α - Bi_2O_3 nanorods and nanoparticles have been synthesized by sonochemical and precipitation method, respectively [120, 121]. Similarly, the synthesis of β - Bi_2O_3 with a hierarchical flower like structure has been achieved using a solvothermal route [122]. The Bi_2O_3 based heterojunction materials have also been synthesized to enhance its visible light absorption and charge separation characteristics. The notable heterojunction systems studied include $\text{Bi}_2\text{O}_3/\text{TiO}_2$, $\text{Bi}_2\text{O}_3/\text{g-C}_3\text{N}_4$, $\text{Bi}_2\text{O}_3/\text{NaNbO}_3$, $\text{Bi}_3\text{O}_4\text{Br}/\alpha$ - Bi_2O_3 , $\text{WO}_3/\text{g-C}_3\text{N}_4/\text{Bi}_2\text{O}_3$, α - $\text{Bi}_2\text{O}_3/\text{BiOBr}$, $\text{CeO}_2/\text{Bi}_2\text{O}_3$, $\text{Bi}_2\text{O}_3/\text{BiPO}_4$ and $\text{Bi}_2\text{O}_3/\text{CeO}_2/\text{ZnO}$, respectively [123-132]. The visible light induced photocatalytic activity of the Bi_2O_3 based heterojunction materials have been studied for degradation of industrial dyes (rhodamine B, malachite green, methyl orange), chlorinated phenols (2,4,6-trichlorophenol, p-chlorophenol) and pharmaceutical products (tetracycline, acetaminophen) [123-145]. Table 1.2 presents the photocatalytic applications of some of the recently studied Bi_2O_3 based heterojunction semiconducting materials.

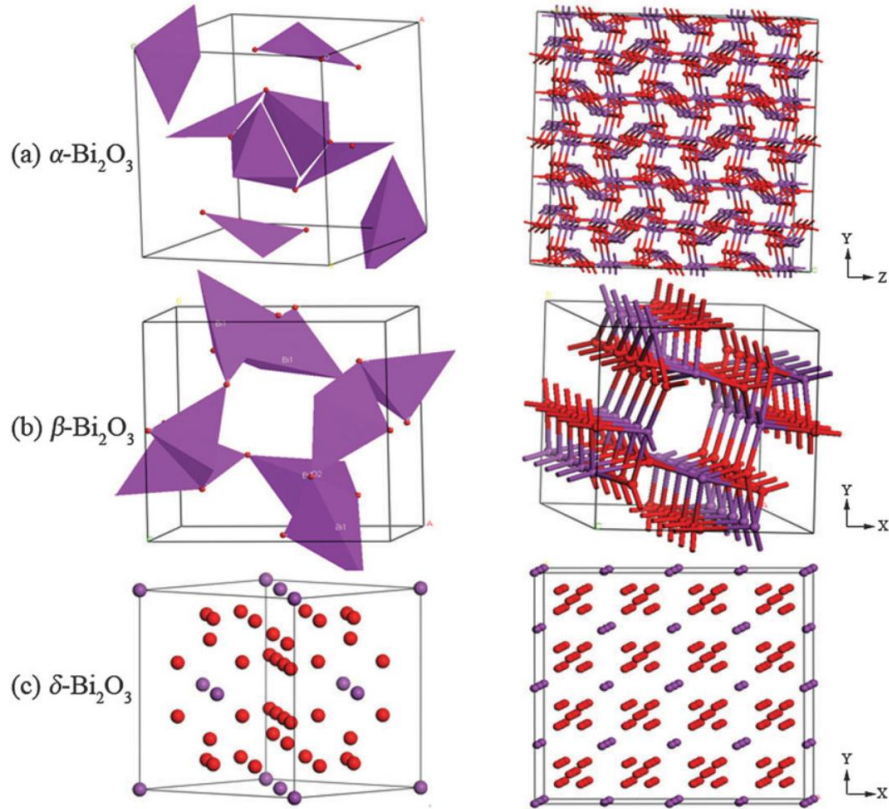


Figure 1.3: Crystal structures of (a) α - Bi_2O_3 , (b) β - Bi_2O_3 and (c) δ - Bi_2O_3 .

Table 1.2: Photocatalytic applications of Bi_2O_3 based materials.

Catalyst	Photocatalytic reactions	Reference
α - Bi_2O_3	Degradation of rhodamine B	[120]
α - Bi_2O_3 , β - Bi_2O_3 & δ - Bi_2O_3	Degradation of methyl orange and 4-chlorophenol	[121]
β - Bi_2O_3	Degradation of rhodamine B	[122]
$\text{Bi}_2\text{O}_3/\text{TiO}_2$	Degradation of ofloxacin antibiotics	[123]
β - $\text{Bi}_2\text{O}_3/\text{g-C}_3\text{N}_4$	Degradation of rhodamine B	[124]
β - $\text{Bi}_2\text{O}_3/\text{g-C}_3\text{N}_4$	Degradation of tetracycline	[125]
$\text{Bi}_2\text{O}_3/\text{NaNbO}_3$	Degradation of rhodamine B	[126]
$\text{Bi}_3\text{O}_4\text{Br}/\alpha$ - Bi_2O_3	Degradation of methyl orange and phenol	[127]
$\text{WO}_3/\text{g-C}_3\text{N}_4/\text{Bi}_2\text{O}_3$	Degradation of tetracycline hydrochloride	[128]
α - $\text{Bi}_2\text{O}_3/\text{BiOBr}$	Degradation of rhodamine B	[129]
$\text{CeO}_2/\text{Bi}_2\text{O}_3$	Degradation of orange II dye	[130]
$\text{Bi}_2\text{O}_3/\text{BiPO}_4$	Degradation of phenol and rhodamine B	[131]
Bi/α - $\text{Bi}_2\text{O}_3/\text{g-C}_3\text{N}_4$	Degradation of tetracycline and rhodamine B	[132]
α/β - Bi_2O_3	Degradation of 17α -ethynylestradiol	[134]

Pt/Bi ₂ O ₃	Degradation of rhodamine B and 2,4-dichlorophenol	[135]
BiVO ₄ /GR/Bi ₂ O ₃	Degradation of bisphenol A	[136]
Bi ₂ S ₃ /Bi ₂ O ₃ /Bi ₂ O ₂ CO ₃	Removal of HCHO	[137]
C/Fe ₃ O ₄ /Bi ₂ O ₃	Degradation of tetracycline	[138]
Au/FeVO ₄ /Bi ₂ O ₃	Degradation of malachite green	[139]
Bi ₂ O ₃ /ZnO	Degradation of alizarin red dye	[140]
α/β -Bi ₂ O ₃ heterojunction	Degradation of rhodamine B and methylene blue	[141]
g-C ₃ N ₄ /Bi ₂ O ₃ /TiO ₂	Degradation of methylene blue	[142]
α/β -Bi ₂ O ₃ -Ag-AgCl	Degradation of rhodamine B and acid orange 7	[143]
Ti-Doped- β -Bi ₂ O ₃	Degradation of pentachlorophenol	[144]
BiOCl/Bi ₂ O ₃	Degradation of gaseous isopropanol	[145]

1.4.2 Bi₂S₃

Bismuth sulfide (Bi₂S₃) is one of the widely studied material with potential applications in many advanced fields including photodiode arrays and photovoltaic converters, photo detectors, thermo-electrics, electrochemical hydrogen storage, biomolecule detection, H₂ sensing and photocatalysis [146]. The Bi₂S₃ is a narrow band gap semiconducting material with a band gap of 1.2-1.7 eV [147,148]. It exhibits a lamellar structure composed of Bi₂S₃ bands elongating along the c-axis and held together through van der Waals interactions. This unique structural characteristic could cause anisotropic growth of this material along its c-axis (Figure 1.4) [146].

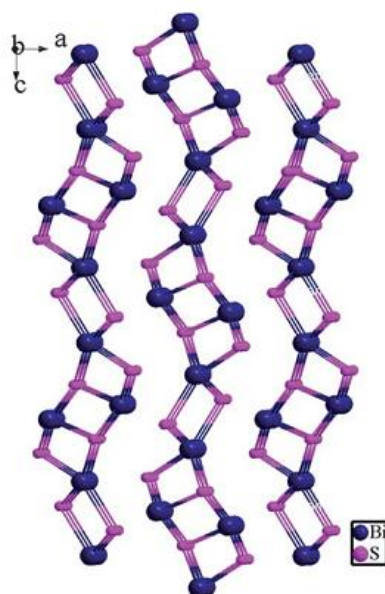


Figure 1.4: Crystal structure of Bi₂S₃.

Moreover, the synthetic methodologies, precursors and the additive are crucial in determining the morphology of the material. Y. Luo et al. have synthesized Bi_2S_3 nanorods using solvothermal synthesis and thiourea as sulphur source at $150\text{ }^\circ\text{C}$ [147]. J. H. Kim et al. have prepared Bi_2S_3 with different morphologies using 2-mercaptoethanol as sulphur precursor under solvothermal condition [148]. The morphology and aspect ratio of Bi_2S_3 crystals could be successfully controlled by changing the bismuth nitrate to 2-mercaptoethanol ratio or adding glutathione during synthesis. The reaction temperature also crucially influences the aspect ratio of the crystal [148]. By changing the sulphur source and surfactants they have successfully synthesized Bi_2S_3 crystals with hierarchical urchin like structure [148]. W. Zheng et al. prepared urchin like Bi_2S_3 by using ionic liquid assisted solvothermal synthetic route. They have also synthesized Bi_2S_3 with nanoparticle, nanorod, nanofabric, cross nanofabric and cross-nanoplate morphologies by changing the ionic liquid and reaction temperature [146]. Due to suitable band gap, the Bi_2S_3 has been extensively studied as visible light active photocatalyst towards degradation of persistent organic pollutants from aqueous sources, CO_2 reduction, reduction of Cr(VI), H_2 generation from H_2S [146-151]. In addition, the Bi_2S_3 has been coupled with many wide band gap semiconducting materials such as TiO_2 , $\text{Bi}_2\text{O}_2\text{CO}_3$, Bi_2WO_6 , BiOCl , BiOBr , BiOI , BiVO_4 and Fe_3O_4 to prepare novel visible light active heterojunction systems with enhanced photocatalytic activity [152-158]. Table 1.3 provides a list of recently studied Bi_2S_3 based heterojunction materials and their photocatalytic activities.

Table 1.3: Photocatalytic applications of Bi_2S_3 based materials.

Catalyst	Photocatalytic reaction	References
$\text{Bi}_2\text{S}_3/\text{TiO}_2$	Degradation of 2,4-dichlorophenoxyacetic acid and Cr(VI) reduction	[152]
$(\text{BiO})_2\text{CO}_3/\text{Bi}_2\text{S}_3$	Oxidation of NO	[153]
$\text{Bi}_2\text{S}_3/\text{Bi}_2\text{WO}_6$	Reduction of Cr(VI)	[154]
$\text{Bi}_2\text{S}_3/\text{BiOCl}$	Degradation of 2,4-dichlorophenol	[155]
$\text{Bi}_2\text{S}_3/\text{BiOBr}$	Degradation of methyl orange dye	[156]
$\text{Bi}_2\text{S}_3/\text{BiVO}_4$	Degradation of rhodamine B	[157]
$\text{Fe}_3\text{O}_4@\text{Bi}_2\text{S}_3$	Degradation of rhodamine B	[158]
$\text{Bi}_2\text{S}_3/\text{Bi}_2\text{O}_3/\text{Bi}_2\text{O}_2\text{CO}_3$	Degradation of methyl orange and phenol	[159]
$\text{Bi}_2\text{S}_3/\text{RGO}/\text{BiOI}$	Reduction of Cr(VI)	[160]
$\text{Bi}_2\text{S}_3/\text{CdS}$	Degradation of rhodamine B	[161]
$\text{MoS}_2/\text{Bi}_2\text{S}_3$	Reduction of Cr(VI)	[162]
$\text{Bi}_2\text{S}_3/\text{SnS}_2$	Degradation of methyl orange	[163]
$\text{Bi}_2\text{S}_3/\text{ZnS}$	Degradation of rhodamine B	[164]
$\text{Bi}_2\text{O}_3/\text{Bi}_2\text{S}_3$	Degradation of rhodamine B	[165]
$\text{CuS}/\text{Bi}_2\text{S}_3$	Degradation of rhodamine B	[166]

g-C ₃ N ₄ /Bi ₂ S ₃	Degradation of methyl orange	[167]
Bi ₂ S ₃ /ZnO	Degradation of acid black 1	[168]
Bi ₂ S ₃ /Y-zeolite	H ₂ production	[169]
Bi ₂ S ₃ @ZIF-8	Degradation of rhodamine B	[170]
Bi ₂ S ₃ /TiO ₂ /Au	Degradation of rhodamine B and reduction of 4-Nitrophenol	[171]
ZnO-ZnS-Bi ₂ S ₃ -RGO	H ₂ production	[172]
Bi ₂ S ₃ /Bi ₂ Sn ₂ O ₇	Degradation of rhodamine B	[173]
Bi ₂ S ₃ /ZnO	Degradation of methyl orange	[174]

1.4.3 Bismuth Salts and Oxyacid Salts:

The oxyacid salts of bismuth have been recently recognized as potential photocatalysts for degradation of refractory organic compounds from aqueous sources. Particularly, notable are the BiOX (X = Cl⁻, I⁻, Br⁻, CO₃²⁻), BiPO₄ and BiVO₄ salts which have been studied for degradation of industrial dyes, pharmaceutical products as well as for photocatalytic splitting of water [175-178]. The following sections provide an overview of the bismuth oxysalts studied for photochemical decontamination of water.

1.4.3.1 Bismuth Phosphate (BiPO₄)

The BiPO₄ is a wide band gap semiconductor (band gap 3.8 eV) which absorbs efficiently in the UV region [177]. This material has been found to be more active than TiO₂ for degradation of phenolic compounds under UV irradiation [179]. The BiPO₄ process certain exceptional optical and electronic properties. The conduction and valence band position of BiPO₄ are +0.42 and +4.28 eV with respect to the standard hydrogen electrode [180]. The higher oxidation potential of the valence band stimulates the generated holes to react with OH⁻ ions to produce [•]OH radicals [180]. Moreover, the inductive effect of PO₄³⁻ group plays a key role in the electron-hole separation and further accelerates the photocatalytic degradation reaction. BiPO₄ being a wide band gap semiconductor, absorbs poorly in the visible region. In order to enhance the visible light response of BiPO₄, it has been coupled with low band gap semiconductors. Particularly notable are the heterojunction systems CdS/BiPO₄, BiPO₄/g-C₃N₄, AgBr/BiPO₄, Ag₃PO₄/BiPO₄, BiOBr/BiPO₄, BiPO₄/Bi₂S₃, BiPO₄/Bi₂WO₆ and BiPO₄/BiOCl which have been used for degradation of methylene blue, benzene, acid blue 92 dye, rhodamine B and methyl orange dye [180-187].

1.4.3.2 Bismuth Vanadates (BiVO₄)

Among the bismuth salts, bismuth vanadate (BiVO₄) is so far the most useful photocatalyst material for wastewater treatment and photocatalytic water splitting under visible light irradiation [176, 178]. BiVO₄ is an n-type narrow band-gap semiconductor. BiVO₄ exists in

three crystallographic phases, i.e. tetragonal zircon (z-t), tetragonal scheelite (s-t), and monoclinic scheelite (s-m) structures. The photocatalytic activity of BiVO_4 is strongly dependent on its crystalline structure [176, 178]. Among the three crystallographic phases, the monoclinic scheelite BiVO_4 (m- BiVO_4) shows much higher photocatalytic performance than the other two tetragonal phases due to its relatively narrow band-gap energy (2.34 eV) [176]. Shang et al. has reported excellent photocatalytic activity of m- BiVO_4 hierarchical nanostructure towards degradation of organic dye under visible light irradiation [188]. However, the photocatalytic property of BiVO_4 is strongly influenced by the recombination of photogenerated electrons and poor adsorption of the contaminants on its surface. In order to suppress the charge carrier recombination, BiVO_4 has been modified by supporting metallic particles (Cu, Pt, Pd and Ag) over its surface [189-192]. The metallic particles trap the conduction band electron away from the photogenerated holes and ensure their utilization in the photocatalytic process. The formation of heterojunction with various semiconductors having suitable band positions such as Bi_2WO_6 , CeO_2 , BiOI , FeVO_4 , Cu_2O , g- C_3N_4 , BiOCl and RGO have also been studied in literature. The visible light assisted photocatalytic application of BiPO_4 based heterojunction systems have been evaluated for degradation of rhodamine B, methylene blue and metronidazole, ciprofloxacin and pesticides [193-200].

1.4.3.3 Bismuth Oxyhalides (BiOX)

The bismuth oxyhalides are an important class of oxysalts which have been studied for their interesting photocatalytic properties. Bismuth oxyhalides such as BiOCl , BiOBr and BiOI have been investigated recently for degradation of contaminants from aqueous sources [175]. These materials exhibit better performance than TiO_2 (P25, Degussa) for the photocatalytic degradation reaction [175]. Among the bismuth oxyhalides, the BiOCl typically exhibits a band gap of 3.4 eV and can only adsorb UV light [201]. However, the BiOBr and BiOI display band gap in the range of 2.5-2.6 eV and 1.7-1.9 eV, respectively [175]. Both these materials are chemically and structurally stable species which absorb significantly in the visible region of the electromagnetic spectrum. In recent years, there were efforts to synthesize bismuth oxyhalide materials with different morphology and size to enhance their photocatalytic properties. X. J. Wang et al. have synthesized hierarchical micro-spherical shaped BiOI material by a facile solvothermal method [202]. Similarly, flower-like BiOI hierarchical spheres were synthesized by using a precipitation method [203, 204]. Q. Yan et al. recently reported the synthesis of self-assembled BiOCl hierarchical nanostructure material using a solvothermal synthetic route [205]. X. Qiu and H. Q. Yu group report the synthesis of BiOCl nanosheets using solvothermal route [206, 207]. The BiOX materials have been studied as photocatalyst for the degradation of organic pollutants like methylene blue, methyl orange, phenol and rhodamine B [203-211]. Recently, several attempts have been made to improve the photocatalytic efficiency of BiOX materials by the formation of heterojunction material with other semiconducting materials with suitable band alignment. $\text{BiPO}_4/\text{BiOCl}$, $\text{BiVO}_4/\text{BiOCl}$, $\text{BiOCl}/\text{g-C}_3\text{N}_4$, $\text{BiOBr}/\text{BiPO}_4$, BiOI/CeO_2 and $\text{Bi}_2\text{O}_2\text{CO}_3/\text{BiOI}$

are examples of some of recently studied bismuth oxyhalides based heterojunction materials with enhanced photocatalytic efficiency [184, 187, 199, 200, 212-214]. In Table 1.4 the photocatalytic application of some recently studied bismuth oxyacid salts based heterojunction material are presented.

Table 1.4: Photocatalytic applications of bismuth oxysalts based heterostructure materials.

Catalyst	Photocatalytic reaction	Reference
CdS/BiPO ₄	Degradation of methylene blue	[180]
BiPO ₄ /g-C ₃ N ₄	Degradation of benzene	[181]
AgBr/BiPO ₄	Degradation of methylene blue	[182]
Ag ₃ PO ₄ /BiPO ₄	Degradation of acid blue 92	[183]
BiOBr/BiPO ₄	Degradation of rhodamine B	[184]
BiPO ₄ /Bi ₂ S ₃	Degradation of methylene blue and rhodamine B	[185]
Bi ₂ WO ₆ /BiPO ₄	Degradation of rhodamine B	[186]
BiPO ₄ /BiOCl	Degradation of methyl orange	[187]
Bi ₂ WO ₆ /BiVO ₄	Degradation of rhodamine B	[193]
CeO ₂ /BiVO ₄	Degradation of methylene blue and methyl orange	[194]
BiOI/BiVO ₄	Water splitting reaction	[195]
FeVO ₄ /BiVO ₄	Degradation of metronidazole	[196]
Cu ₂ O/BiVO ₄	Degradation of 4-chlorophenol	[197]
g-C ₃ N ₄ /BiVO ₄	Degradation of methylene blue	[198]
BiOCl/BiVO ₄	Degradation of norfloxacin	[200]
BiOCl/C ₃ N ₄	Degradation of methyl orange	[212]
BiOI/CeO ₂	Degradation methylene orange and bisphenol A	[213]
Bi ₂ O ₂ CO ₃ /BiOI	Degradation of rhodamine B, methylene blue and crystal violet	[214]

1.4.4 Aurivillius Family of Oxides:

The Aurivillius family of complex oxides are characterized by the general formula Bi₂A_{n-1}B_nO_{3n+3} (A=Ca, Sr, Ba, Pb, Bi, Na, K and B =Ti, Nb, Ta, Mo, W, Fe) [215, 216]. These materials consist of perovskite-like slabs and bismuth-oxide sheets arranged alternatively in the z-direction to yield a layered crystal structure. The Aurivillius phases have received significant attention in recent years due to their layered structure and unique properties. The acid treatment of the Aurivillius oxides results in the formation of the protonated forms of the layered perovskites. For example, the transformation of Bi₂W₂O₉ to H₂W₂O₇ by loss of [Bi₂O₂]²⁺ species upon acid treatment has been reported in literature [217, 218]. The Aurivillius oxides exhibit semiconducting properties and photocatalytic behavior, which can be exploited in environmental photocatalysis and selective organic synthesis.

1.4.4.1 Bi₂WO₆

The bismuth tungstate (Bi₂WO₆) is the simplest member of the Aurivillius family of layered perovskites. It is a “A” cation-deficient bismuth-layered compounds with n =1 in the structural formula. The structure of Bi₂WO₆ composed of alternately stacked perovskite layers (A_{n-1}B_nO_{3n+1}) with “A” cation deficiency and bismuth oxide layers (Bi₂O₂) arranged along the z- direction (Figure 1.5) [219]. The Bi₂O₂ layers are comprised of a square planar net of oxygen anions with the Bi³⁺ cations present alternatively above and below the plane.

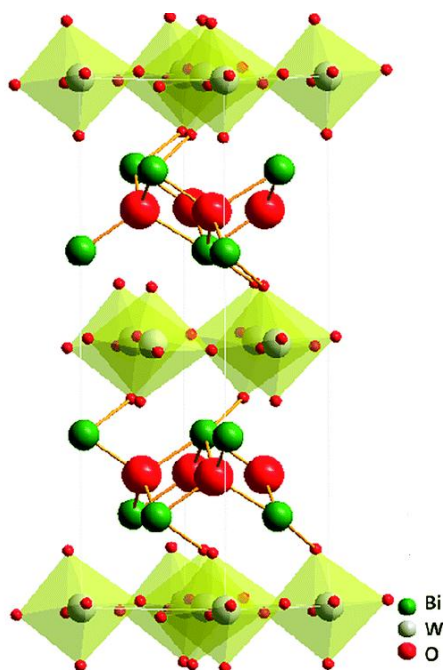


Figure 1.5: Crystal structure of Bi₂WO₆.

Bismuth tungstate has been studied widely as visible light active photocatalyst for water splitting and decomposition of organic contaminants [220, 221]. Several methods have been devised for the synthesis of this important compound which include solid state reaction [222], amorphous complex method [223], sol-gel [224], mechanochemical synthesis [225], solvothermal [219], hydrothermal [226], precipitation [227] and microwave assisted hydrothermal methods [228]. The hydrothermal method has been extensively used for synthesis of bismuth tungstate nanostructure using conventional and microwave heating. By varying the solution pH, treatment temperature, time and solvent, Bi₂WO₆ materials with different morphology and size have been obtained using hydrothermal method [220, 221]. As far as their photocatalytic activity is concerned, since the photocatalytic activity of semiconducting particles depends on the crystallite size, crystallinity, surface area and morphology of the semiconducting materials, Bi₂WO₆ materials with different morphology have been prepared. By controlling the synthetic parameters Bi₂WO₆ with different

morphologies such as nanoplates, quantum dots dispersed in nanosheets, nanofibers, Nanodiscs, micro and nanospheres, hierarchical nanostructures and mesoporous structures have been synthesized [221]. Xie et al have synthesized ultrathin (3-4 nm thickness) {001} oriented Bi_2WO_6 crystallites by a modified hydrothermal process. By controlling the pH of the precursor solution, the growth kinetics of the BWO particles is tuned to obtain the oriented specimens. The {001}-oriented Bi_2WO_6 ultrathin nanosheets exhibit higher photocatalytic activity than the nanodisks for degradation of Rhodamine B and photocatalytic water oxidation [229]. The visible-light-induced photocatalytic activity of the Bi_2WO_6 material has been studied for degradation of organic contaminants such as dyes (methylene blue, rhodamine B, methyl orange, bisphenol A, indigo Carmine), chlorinated organic compounds (chloroform, 4-chloro phenol), and aliphatic and aromatic organic compounds (formaldehyde, acetaldehyde, phenol) [219-220]. Bi_2WO_6 exhibits a band gap value of around 2.7 eV [219-220]. DFT calculation suggests that the visible-light response is due to the transition from the VB formed by the hybridization of Bi 6s and O 2p orbitals to the CB which is predominantly W 5d in character [220]. Furthermore, the hybridization of Bi 6s and O 2p levels makes the VB largely dispersed, which favors the mobility of the photogenerated holes in the valence band and is beneficial to the oxidation reaction [220]. Amano et al have studied the photocatalytic decomposition of acetaldehyde over BWO hierarchical polycrystalline particles synthesized by hydrothermal method. A linear relationship was observed between the activity and surface area of the photocatalyst [230]. Kumar and Khan have synthesized flower-like hierarchical bismuth tungstate with mesoporous structure using the non-ionic surfactant Pluronic F127. Pt particles deposited on the mesoporous Bi_2WO_6 shows excellent catalytic activity for degradation of rhodamine B under visible light radiation. The enhanced photocatalytic properties of Pt/ Bi_2WO_6 have been attributed to the efficient electron-hole separation due to electron accepting nature of Pt particles. Moreover, the Pt particles provide additional adsorption sites for rhodamine B dyes [231]. Saison et al have studied the nature of the active species involved in the photocatalytic property of Bi_2WO_6 using electron paramagnetic resonance through a spin trapping technique. It was observed that bismuth tungstate is able to generate hydroxyl radicals in aqueous aerated solution, but no superoxide radical anions are formed. Using different LED lights and TRMC experiments, these authors have demonstrated that the photocatalytic activity is correlated to the amount of photons converted into photogenerated electrons and holes and their subsequent utilization in photocatalysis without getting recombined [232]. Recently, significant effort has been directed to devise novel Bi_2WO_6 based materials with enhanced photocatalytic properties. The photogenerated surface trapped holes and electrons in Bi_2WO_6 are the prime species which facilitate photo oxidation of the organic substrates. A comparative study of the photocatalytic behavior of Bi_2WO_6 and TiO_2 reveal that fewer radicals are generated in BWO because of low photon harvesting [232]. A good way to improve the Bi_2WO_6 photocatalysts would be to trap the photogenerated electrons far from the active holes using heterostructure systems. In order to achieve this objective, different

heterojunction materials have been prepared and studied in literature. Zhang et al have synthesized graphene-Bi₂WO₆ heterojunction materials by dispersing BWO nanoparticles (30-40 nm) in the layered graphene matrix. The composite material exhibited high oxygen production rate nearly five times than the bare BWO. The enhanced activity has been ascribed to the chemical bonding between the BWO and graphene sheets which facilitate electron collection and transport and inhibit the recombination of photo-generated charge carriers [233]. Novio et al have synthesized composite material containing TiO₂ and Bi₂WO₆ nanosheets using hydrothermal method. The composite materials show improved photocatalytic activity for the degradation of rhodamine B compared to the individual photocatalytic materials [234]. The synthesis and application of Bi₂O₃/Bi₂WO₆ heterojunction photocatalyst has been studied for rhodamine B degradation. The presence of Bi₂O₃ improves the light harvesting property and reduces the recombination of the photoexcited electrons and holes during the photocatalytic reaction [235]. The photocatalytic activity of g-C₃N₄/Bi₂WO₆ hybrid catalyst has been studied for visible light induced decomposition of methylene blue. The enhanced photocatalytic activity observed for the hybrid material has been ascribed to facile transfer of the photogenerated holes from the valence band of Bi₂WO₆ to the HOMO of C₃N₄ through the interface which causes photoinduced charge separation [236]. Xiao et al have synthesized Co₃O₄/Bi₂WO₆ composites with p-n heterojunction structure using impregnation of the cobalt salt precursor. The composite material has been highly efficient for degradation of methylene blue under visible light radiation [237]. The photocatalytic applications of some of the recently studied Bi₂WO₆ based materials are presented in Table 1.5.

Table 1.5: Photocatalytic applications of Bi₂WO₆ based materials.

Catalyst	Photocatalytic reaction	References
Bi ₂ WO ₆	Degradation of ceftriaxone sodium drug	[238]
Ag/Bi ₂ WO ₆	Degradation of organic dye and antibiotics	[239]
Mo-doped Bi ₂ WO ₆	Degradation of rhodamine B	[240]
Bi ₂ WO ₆	CO ₂ reduction	[241]
Bi ₂ WO ₆	Removal of NO	[242]
Bi ₂ WO ₆	Degradation of rhodamine B, methylene blue, methyl orange and phenol	[243]
Bi ₂ WO _{6-x}	Decomposition of 2, 4-Dichlorophenol	[244]
Bi/Bi ₂ WO ₆	Degradation of rhodamine B and 4-Chlorophenol	[245]
Lu ³⁺ doped Bi ₂ WO ₆	Methylene blue degradation	[246]
Bi ₂ WO ₆	Hydrogen production and dye degradation	[247]
Bi ₂ WO ₆	Partial oxidation of methane	[248]
Bi ₂ WO ₆	Degradation of tetracycline	[249]

Bi ₂ WO ₆	Benzyl alcohol oxidation	[250]
GO/Bi ₂ WO ₆	Degradation of rhodamine B	[251]
Bi ₂ WO ₆	Photocyclization of 2-alkyl benzothiazoles and 2-alkyl benzimidazoles	[252]
Bi ₂ WO ₆	Oxidation of glycerol to dihydroxyacetone	[253]
Bi ₂ WO ₆	Oxidation of CO, n-hexane and methane	[254]
Bi ₂ WO ₆ -Cu ₃ P	Water splitting	[255]
Bi ₂ WO ₆ /Bi ₄ V ₂ O ₁₁	Cr(VI) reduction	[256]
Ag ₃ VO ₄ /Bi ₂ WO ₆	Degradation of rhodamine B, methyl orange and 4-chlorophenol	[257]
BiPO ₄ /Bi ₂ WO ₆	Degradation of methylene blue	[258]
MoS ₂ /Bi ₂ WO ₆	Degradation of rhodamine B	[259]
WO ₃ /Bi ₂ WO ₆	Degradation of rhodamine B	[260]
BiIO ₄ /Bi ₂ WO ₆	Degradation of rhodamine B	[261]
ZnO/Bi ₂ WO ₆	Degradation of rhodamine B	[262]
Bi ₂ WO ₆ /CdS	Degradation of metronidazole and methylene blue	[263]

1.4.4.2 Bi₂W₂O₉

The Bi₂W₂O₉ is a n=2 member of the homologous series [Bi₂O₂][B^{VI}_nO_{3n+1}] of cation-deficient Aurivillius phases [215-216]. The Bi₂W₂O₉ structure consists of Bi₂O₂ layers interleaved with ReO₃-like W₂O₇ sheets which are 2 octahedral layers thick (Figure 1.6). Each tungsten atom is coordinated to six oxygen atoms. The room-temperature phase is orthorhombic, space group Pna21, and the lattice parameters are a= 5.440 Å, b= 5.413 Å and c= 23.740 Å [264]. Bi₂W₂O₉ although is homologous to the Bi₂WO₆, it displays certain unique properties for which it has generated significant interest in the material science community. Bi₂W₂O₉ has been found to be highly active as photocatalyst. Kudo and Hijii have reported that the photocatalytic activity of Bi₂W₂O₉ is over ten times than Bi₂WO₆ for H₂ and O₂ evolution under UV radiation [265]. The synthesis of Bi₂W₂O₉ has been carried out primarily using solid state reaction route by calcining a stoichiometric mixture of Bi₂O₃ and WO₃ at 800°C for 48 h [264, 266]. Maczka et al have synthesized Bi₂W₂O₉ nanopowders using high energy mechanical ball milling of a stoichiometric mixture of Bi₂WO₆ with WO₃ followed by heat treatment at 750°C for 1 h. This method has yielded phase pure materials with particle size in nanodomain [267]. One of the interesting structural aspects of Bi₂W₂O₉ is its conversion to H₂W₂O₇·H₂O upon treatment with mineral acid such as HCl. In strongly (6M HCl) acidic medium, the bismuth oxide sheets are selectively leached from the layered structure and protons (2H⁺/[W₂O₇]²⁻) and water molecules are introduced to form H₂W₂O₇·H₂O. The exfoliations of the H₂W₂O₇·xH₂O material to 2D nanosheets containing double octahedral W–O layers have been studied by Mallouk et al. It has been observed that colloidal 2D tungstate nanosheets can be obtained by reaction of 25 molar excess of

tetramethyl ammonium hydroxide with $\text{H}_2\text{W}_2\text{O}_7 \cdot x\text{H}_2\text{O}$ [217]. The synthesis of colloidal double octahedral W–O nanosheets and their subsequent use in photo catalytic water splitting has been studied Osterloh et al [268]. The colloidal nanosheets shows quantum confinement and a band gap of 2.88 eV compared to the 2.81 eV and 2.68 eV band gap observed for the $\text{Bi}_2\text{W}_2\text{O}_9$ and bulk WO_3 respectively. Martinez de la Cruz et al have compared the catalytic activity of Bi_2WO_6 and $\text{Bi}_2\text{W}_2\text{O}_9$ using visible light induced Rhodamine B degradation [269]. The $\text{Bi}_2\text{W}_2\text{O}_9$ material has been synthesized by co-precipitation and calcination at 700°C shows maximum catalytic activity for the reaction. Table 1.6 presents some of the recent photocatalytic applications of $\text{Bi}_2\text{W}_2\text{O}_9$ material studied in literature.

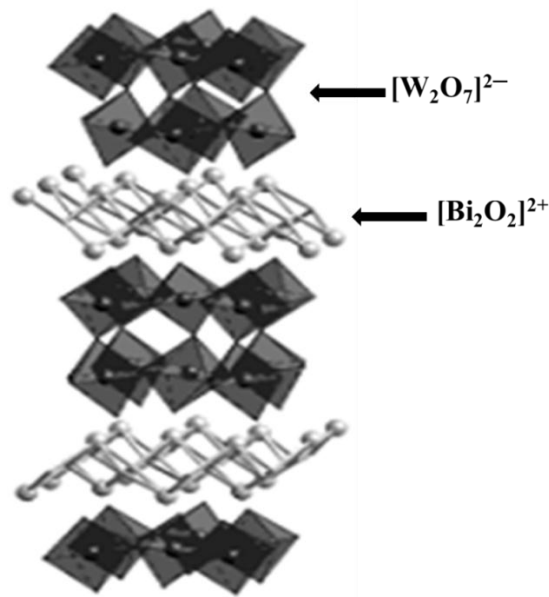


Figure 1.6: Crystal structure of $\text{Bi}_2\text{W}_2\text{O}_9$.

Table 1.6: Photocatalytic applications of $\text{Bi}_2\text{W}_2\text{O}_9$.

Catalyst	Photocatalytic reaction	Reference
$\text{Bi}_2\text{W}_2\text{O}_9$	Remove of marine plankton	[270]
$\text{Bi}_2\text{W}_2\text{O}_9$	Degradation of rhodamine B	[269]
$\text{Bi}_2\text{W}_2\text{O}_9$	H_2 evolution reaction	[271]
$\text{Bi}_2\text{W}_2\text{O}_9$	Degradation of rhodamine B	[272]
$\text{Bi}_2\text{W}_2\text{O}_9$	Degradation of ciprofloxacin drug	[273]

1.4.5 BiFeO_3

The BiFeO_3 is a promising material with potential applications in many advanced fields including magnetic, spintronics, piezoelectric devices, photovoltaics, solar cell and ion conductivity [274-279]. Beside these important applications the BFO material has been

studied as a potential material for photocatalytic applications [280, 281]. The BiFeO_3 is a narrow band gap (2.1-2.7 eV) semiconducting material [280, 281]. The polarization-induced electric field arising out its ferroelectric property has been responsible for enhanced charge carrier separation and their efficient utilization in photocatalytic processes [280, 281]. The VB of BFO material consisted of the O 2p orbitals with a small contribution from the Fe 3d orbitals whereas; the CB is constituted by the Bi 6p orbitals [280]. The ground state bulk phase of BiFeO_3 (BFO) has a rhombohedral structure with space group $R3c$ ($a = 5.58 \text{ \AA}$ and $c = 13.9$) at room temperature. The BFO perovskite structure has a general formula of ABO_3 , where 'A' corresponds to the large cation (Bi in BFO) and 'B' corresponds to the smaller cation (Fe in BFO). The structure consisted of two cation sites in the crystal lattice: the larger cation 'A' located on the corners of the unit cell and the smaller cation 'B' is in the center of the unit cell. The oxygen (O) ions are on the centers of the faces and the structure is modeled through a network of corner linked oxygen octahedron with the larger cation (A) filling the dodecahedral holes and the smaller cation (B) filling the octahedral sites (Figure 1.7) [282, 283].

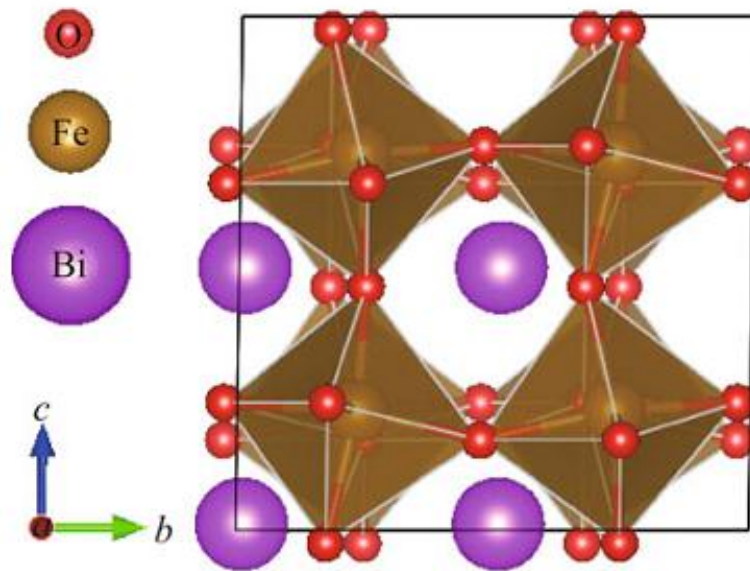


Figure 1.7: crystal structure of BiFeO_3 .

The BiFeO_3 have been synthesized by using different routes including solid state, sonochemical, sol-gel, aerosol spray, precipitation, electro spinning, hydrothermal, microwave assisted hydrothermal, combustion and chemical vapor deposition methods [284-293]. The synthetic methods employed and additives crucially decide the morphology of the BiFeO_3 nanomaterials. G. S. Armata's group have recently synthesized highly ordered mesoporous BFO using mesoporous SBA-15 silica and CMK-3 carbon as templates [294, 295]. Y. Wang et al. have successfully synthesized BFO with rod, pill and cube like morphology using a facile hydrothermal route by changing the pH of the reaction mixture [296]. The BFO materials with different morphologies and selected exposed crystal facets

have also been prepared by hydrothermal method by varying the pH of the reaction mixture without use of any additives [297, 298]. Similarly, the synthesis of rectangular BFO plates and microcubes has been accomplished by microwave assisted hydrothermal method [291, 299]. The BiFeO₃ has been studied as a light active photocatalyst for the degradation of persistent aqueous organic pollutants including dyes, pharmaceuticals and phenolic compounds from aqueous media [280, 281]. In order to improve its photocatalytic efficiency, the BFO material has been doped with La³⁺, Se⁴⁺, Ba²⁺, Gd³⁺ and Co³⁺ ions [300-303]. Further the charge separation property and photocatalytic efficiency of the BFO material has been improved by formation of composite and heterojunction with other semiconducting materials. Recently, BFO has been coupled with C₃N₄, Bi₂Fe₄O₉, CuWO₄, γ -Fe₂O₃ and TiO₂ materials and studied as photocatalyst for the degradation of organic dyes, phenolic compounds and water splitting reactions [304-310]. Table 1.7 summarizes some of the recent photocatalytic studies performed using BiFeO₃ based materials under visible light.

Table 1.7: Photocatalytic applications of BiFeO₃ based materials.

Catalyst	Photocatalytic reaction	References
Gd ³⁺ & Sn ⁴⁺ doped BiFeO ₃	Degradation of Congo red, methylene blue and methyl violet	[300]
Ba-doped BiFeO ₃	Degradation of toluene and benzene	[301]
La ³⁺ and Se ⁴⁺ doped BiFeO ₃	Degradation of Congo red	[302]
Co ³⁺ doped BiFeO ₃	Degradation of methylene blue	[303]
C ₃ N ₄ /BiFeO ₃	Degradation of rhodamine B	[304]
BiFeO ₃ /Bi ₂ Fe ₄ O ₉	H ₂ production and degradation of rhodamine B	[305]
BiFeO ₃ /CuWO ₄	Degradation of rhodamine B and methylene blue	[306]
BiFeO ₃ / γ -Fe ₂ O ₃	Degradation of rhodamine B	[307]
BiFeO ₃ /TiO ₂	H ₂ evolution reaction	[308]
BiFeO ₃ /TiO ₂	Degradation of methylene blue	[309]
TiO ₂ /BiFeO ₃	Reduction of silver cations	[310]
BiFeO ₃	Degradation of rhodamine B	[311]
BiFeO ₃	Degradation of rhodamine B	[312]
BiFeO ₃	Degradation of direct blue dye	[313]
Pt/BiFeO ₃	Degradation of methyl orange	[314]
Ca-doped BiFeO ₃	H ₂ O ₂ decomposition	[315]
BiFeO ₃	Degradation of bisphenol A	[316]
BiFeO ₃	Degradation of tetracycline	[317]

1.5 Gap in Literature

The literature studies presented in the preceding sections suggest promising photocatalytic potentials of bismuth based materials towards degradation of recalcitrant organic pollutants from aqueous sources. Moreover, the formation of heterostructure systems by combining bismuth based materials with a second semiconductor having suitable band alignment is an important strategy to improve the optical absorption and photocatalytic properties. The studies presented in section 1.2 also indicate that the development of photocatalytic route for selective organic synthesis is a promising field of research with potential application in fine chemical industries. In literature, although many methods have been used for synthesis of bismuth based materials, the use of combustion synthesis method is rarely studied. The combustion synthesis method is an effective method for the preparation of homogeneous, finely dispersed crystalline uni- and multicomponent oxides. This method is quick, straight forward and less time consuming without the involvement of any intermediate preparative steps. In this thesis an attempt has been made to synthesize bismuth based materials by combustion route. Although, there are many reports on bismuth based heterostructure materials, the use of transition metal sulfides particularly CuS and CdS to form heterostructure systems is yet to be explored. CuS and CdS are low band gap semiconducting materials which absorb significantly in visible region. Moreover, these materials possess suitable band alignment to form type II heterostructures with bismuth based materials. In this thesis, novel heterostructure materials have been prepared by combining bismuth based materials with CuS/CdS as a second semiconducting component. Although the photocatalytic application of bismuth based materials for degradation of organic pollutants including dyes, phenolic compounds and pharmaceuticals is widely studied, the applications of these materials for complete mineralization of pesticides under visible light irradiation is yet to be explored. Moreover, there are very few studies available regarding the application of bismuth based heterostructure materials towards selective organic transformation. There is a lot of scope to investigate the applicability of these important classes of photocatalytic materials towards selective organic transformation.

1.6 Objectives of the Present Work

The broad objective of this study is to prepare novel heterostructure photocatalytic systems by combining Bi based semiconducting nanomaterials and metal sulphide particles for application towards degradation of POPs from aqueous sources and selective organic transformations.

The specific objectives of this work are:

- (1) Preparation of phase pure Bi-based complex oxides and sulphide nanomaterials (Bi_2WO_6 , $\text{Bi}_2\text{W}_2\text{O}_9$, BiFeO_3 , Bi_2S_3) by combustion synthesis route using different reducible organic compounds as fuel.
- (2) To improve the visible light absorption, photon harvesting efficiency and photocatalytic properties of the Bi-based complex oxide materials by preparing novel heterostructure photocatalytic systems by coupling with metal sulfide nanoparticles (CuS, CdS).
- (3) To enhance the charge carrier separation and photocatalytic activity of Bi_2S_3 by forming heterostructure with $\alpha\text{-Fe}_2\text{O}_3$ semiconducting material.
- (4) Characterization of the synthesized heterojunction materials using XRD, XPS, PL, FESEM, HRTEM, IR, UV-Vis-DRS and other analytical techniques to understand their physicochemical characteristics, optical and photocatalytic properties.
- (5) To evaluate the photocatalytic application of the heterostructure systems towards complete mineralization of persistent organic pollutants including Congo red dye and diuron and alachlor pesticides in aqueous phase under visible light illumination.
- (6) To explore the photocatalytic potential of the Bi-based heterostructure photocatalysts for selective organic transformations (oxidation of thiols/amines and reduction of nitroarenes).

The results obtained in this investigation are described in the following chapters.

Chapter 1: This chapter briefly describes the present understanding as well as recent developments in structural and photocatalytic properties of Bi based semiconducting nanomaterials. Different strategies adopted in literature to improve the optical absorption, charge carrier separation and photocatalytic activity of the Bi based material has been described. The utility of Bi based photocatalytic materials towards mineralization of refractory organic compounds and in selective organic reactions have been highlighted with specific examples.

Chapter 2: This chapter presents the detailed experimental procedure adopted for the synthesis of phase pure Bi based nanomaterials and their nanoheterostructure systems. The instrumental techniques used for studying physicochemical characteristics of the prepared nanomaterials and the method of analysis are briefly explained. The experimental methods employed for photocatalytic mineralization of Congo red dye, diuron and alachlor pesticide are outlined. The experimental set up and reaction conditions employed for thiol/amine oxidation and nitroarene reduction are also presented. The product analysis protocols are described.

The results and discussion part of the thesis has been divided into 4 chapters.

Chapter 3: This chapter describes the photocatalytic application of Bi_2WO_6 based materials. This chapter contains two sections.

Section A: This section describes the combustion synthesis, characterization and photocatalytic application of Bi_2WO_6 nanomaterial. The effect of fuel nature and its content on the phase purity and morphology of the Bi_2WO_6 has been described. The combustion synthesized Bi_2WO_6 have been characterized using XRD, Fourier analysis, UV-Vis-DRS, PL, FESEM, HRTEM and sorptometric techniques. The photocatalytic test results for selective aerobic oxidation of thiol to disulfide are presented in this section.

Section B: This section describes the synthesis of Bi_2WO_6 by amorphous citrate method. The Bi_2WO_6 was subsequently modified with CuS to prepare $\text{CuS}/\text{Bi}_2\text{WO}_6$ heterojunction materials. The characterization study of the $\text{CuS}/\text{Bi}_2\text{WO}_6$ heterojunction system using different analytical techniques and their photocatalytic application for mineralization of Congo red dye under visible light illumination are presented in this section.

Chapter 4: The photocatalytic application of $\text{Bi}_2\text{W}_2\text{O}_9$ based materials is described in this chapter. This chapter is also divided into two sections.

Section A: In this section, the combustion synthesis of $\text{Bi}_2\text{W}_2\text{O}_9$ and its subsequent modification with CdS nanoparticles to prepare $\text{CdS}/\text{Bi}_2\text{W}_2\text{O}_9$ heterojunction materials is presented. The results obtained from the characterization study of the heterojunction materials using a variety of techniques are described. The photocatalytic test results towards selective aerobic oxidation of amine to imine are also presented and discussed.

Section B: This section describes the photocatalytic application of $\text{CuS}/\text{Bi}_2\text{W}_2\text{O}_9$ heterojunction nanomaterials for the mineralization of diuron pesticide under visible light illumination.

Chapter 5: In this chapter, the combustion synthesized BiFeO_3 is modified with CuS by using a hydrothermal method to prepare heterostructure photocatalyst. The $\text{CuS}/\text{BiFeO}_3$ heterojunction materials are characterized by using XRD, XPS, FESEM, HRTEM, PL and UV-Vis-DRS techniques. The photocatalytic application of the heterojunction materials is evaluated for the degradation of alachlor pesticide under visible light. The degradation products obtained and the detailed mechanism of the degradation of alachlor are described in this chapter.

Chapter 6: In this chapter a facile one step combustion synthesis method is described for synthesis of $\alpha\text{-Fe}_2\text{O}_3\text{-Bi}_2\text{S}_3$ heterojunction materials. The $\alpha\text{-Fe}_2\text{O}_3\text{-Bi}_2\text{S}_3$ materials have been characterized using XRD, XPS, FESEM, HRTEM, PL and UV-Vis-DRS techniques. The

photocatalytic activity of the $\alpha\text{-Fe}_2\text{O}_3\text{-Bi}_2\text{S}_3$ heterojunctions has been evaluated for the hydrogen transfer reduction of nitroarenes under visible light.

Chapter 7: The summary of results obtained from various investigations and the major conclusions drawn from these studies are presented in this chapter.

References

- [1] S. D. Gisi, G. Lofrano, M. Grassi and M. Notarnicol, *Sustainable Materials and Technologies*, 2016, 9, 10-40.
- [2] J. Akhtar, N. A. S. Amin and K. Shahzad, *Desalination and Water Treatment*, 2015, 1-19.
- [3] C. Pignata, E. Fea, R. Rovere, R. Degan, E. Lorenzi, M. de-Ceglia, T. Schiliro and G. Gilli, *Environmental Monitoring and Assessment*, 2012, 184, 2091-2103.
- [4] M. Cheng, G. Zeng, D. Huang, C. Lai, P. Xu, C. Zhang and Yang Liu, *Chemical Engineering Journal*, 2016, 284, 582-598.
- [5] G. Boczkaj and A. Fernandes, *Chemical Engineering Journal*, 2017, 320, 608–633.
- [6] J. L. Wang and L. J. Xu, *Critical Reviews in Environmental Science and Technology*, 2012, 42, 251-325.
- [7] M. A. Oturan and J. J. Aaron, *Critical Reviews in Environmental Science and Technology*, 2014, 44, 2577-2641.
- [8] Y. Deng and R. Zhao, *Current Pollution Reports*, 2015, 1,167-176.
- [9] K. E. Oshea and D. D. Dionysiou, *The Journal of Physical Chemistry Letters*, 2012, 3, 2112–2113.
- [10] R. Dewil, D. Mantzavinos, I. Poulios and M. A. Rodrigo, *Journal of Environmental Management*, 2017, 195, 93-99.
- [11] J. Levec and A. Pintar, *Catalysis Today*, 2007, 124, 172-184.
- [12] S. K. Bhargava, J. Tardio, J. Prasad, K. Foger, D. B. Akolekar and S. C. Grocott, *Industrial & Engineering Chemistry Research*, 2006, 45, 1221-1258.
- [13] S. S. Lina, D. J. Chang, C. H. Wang and C. C. Chen, *Water Research*, 2003, 37, 793-800.
- [14] L. Hua, H. Ma and L. Zhang, *Chemosphere*, 2013, 90, 143-149.
- [15] M. Parvas, M. Haghghi and S. Allahyari, *Environmental Technology*, 2014, 35, 1140–1149.
- [16] P. Liu, S. He, H. Wei, J. Wang and C. Sun, *Industrial & Engineering Chemistry Research*, 2015, 54, 130–136
- [17] Y. Liu and D. Sun, *Applied Catalysis B: Environmental*, 2007, 72, 205-211.
- [18] X. Dong, Y. Zhang, Y. Xu and M. Zhang, *RSC Advances*, 2015, 5, 47488-47497.
- [19] M. A. Wolfovich, M. V. Landau, A. Brenner and M. Herskowitz, *Industrial & Engineering Chemistry Research*, 2004, 43, 5089-5097.

- [20] M. Pelaez, N. T. Nolan, S. C. Pillai, M. K. Seery, P. Falaras, A. G. Kontos, P. S. M. Dunlop, J. W. J. Hamilton, J. A. Byrne, K. O'Shea, M. H. Entezari and D. D. Dionysiou, *Applied Catalysis B: Environmental*, 2012, 125, 331–349.
- [21] N. Tripathy, R. Ahmad, J. E. Song, H. A. Ko, Y. B. Hahn, G. Khang, *Materials Letters*, 2014, 136, 171-174.
- [22] M. Mishra and D. Man Chun, *Applied Catalysis A: General*, 2015, 498, 126–141.
- [23] L. Cheng, Q. Xiang, Y. Liao and H. Zhang, *Energy & Environmental Science*, 2018, 10.1039/C7EE03640J.
- [24] Z. Ye, L. Kong, F. Chen, Z. Chen, Y. Lin and C. Liu, *Optik*, 2018, 164, 345–354.
- [25] Z. Li, X. Meng and Z. Zhang, *Journal of Photochemistry and Photobiology C: Photochemistry Reviews*, 2018, 35, 39–55.
- [26] Y. Ma, F. Cheng, W. Liu, J. Wang and Y. Wang, *Transactions of Nonferrous Metals Society of China*, 2015, 25, 112–121.
- [27] I. Oller, P. F. Ibáñez, M. I. Maldonado, L. P. Estrada, W. Gernjak, C. Pulgarín, P. C. Passarinho and S. Malato, *Research on Chemical Intermediates*, 2007, 33, 407-420.
- [28] N. Yan, Z. Zhu, J. Zhang, Z. Zhao and Q. Liu, *Materials Research Bulletin*, 2012, 47, 1869–1873.
- [29] S. A. Ansari, M. M. Khan, M. O. Ansaric and M. H. Cho, *New Journal of Chemistry*, 2016, 40, 3000-3009.
- [30] S. Klosek and D. Raftery, *Journal of Physical Chemistry B*, 2001, 105, 2815-2819.
- [31] F. Laatar, H. Moussa, H. Alem, L. Balan, E. Girot, G. Medjahdi, H. Ezzaouia and R. Schneider, *Beilstein Journal of Nanotechnology*, 2017, 8, 2741–2752,
- [32] J. Liu, S. Yang, W. Wu, Q. Tian, S. Cui, Z. Dai, F. Ren, X. Xiao and C. Jiang, *ACS Sustainable Chemistry and Engineering*, 2015, 3, 2975–2984.
- [33] P. Chowdhury, J. Moreira, H. Goma, and A. K. Ray, *Industrial & Engineering Chemistry Research*, 2012, 51, 4523–4532.
- [34] S. K. Choi, H. S. Yang, J. H. Kim and H. Park, *Applied Catalysis B: Environmental*, 2012, 121–122, 206–213.
- [35] J. Yu, C. Y. Xu, F. X. Ma, S. P. Hu, Y. W. Zhang and L. Zhen, *ACS Applied Materials and Interfaces*, 2014, 6, 22370–22377.
- [36] S. M. Lama, J. C. Sin and A. R. Mohamed, *Materials Research Bulletin*, 2017, 90, 15–30.
- [37] H. Mehrizadeh, A. Niaei, H. H. Tseng, D. Salari and A. Khataee, *Journal of Photochemistry and Photobiology A: Chemistry*, 2017, 332, 188–195.
- [38] P. Dong, G. Hou, X. Xi, R. Shao and F. Dong, *Environmental Science: Nano*, 2017, 4, 539-557.
- [39] Y. Chen, L. Hu, M. Wang, Y. Min and Y. Zhang, *Colloids and Surfaces A: Physicochemical and Engineering Aspects*, 2009, 336, 64-68.
- [40] R. Marschall, *Advanced Functional Materials*, 2014, 24, 2421-2440.

- [41] Y. Wang, Q. Wang, X. Zhan, F. Wang, M. Safdar and J. He, *Nanoscale*, 2013, 5, 8326-8339.
- [42] G. Palmisano, E. Garcia-Lopez, G. Marc, V. Loddo, S. Yurdakal, V. Augugliaro and L. Palmisano, *Chemical Communications*, 2010, 46, 7074-7089.
- [43] D. Friedmann, A. Hakki, H. Kim, W. Choi and D. Bahnemann, *Green Chemistry*, 2016, 18, 5391-5411.
- [44] G. Palmisano, V. Augugliaro, M. Pagliaro and L. Palmisano, *Chemical Communications*, 2007, 3425-3437.
- [45] V. Augugliaro, M. Bellardita, V. Loddo, G. Palmisano, L. Palmisano and S. Yurdakal, *Journal of Photochemistry and Photobiology C: Photochemistry Reviews*, 2012, 13, 224-245.
- [46] D. Kumar, V. B. Reddy, B. G. Mishra, R. K. Rana, M. N. Nadagouda and R. S. Varma, *Tetrahedron*, 2007, 63, 3093-3097.
- [47] S. Yurdakal, G. Palmisano, V. Loddo, V. Augugliaro and L. Palmisano, *Journal of American Chemical Society*, 2008, 130, 1568-1569.
- [48] M. Qamar, R. B. Elsayed, K. R. Alhooshani, M. I. Ahmed and D. W. Bahnemann, *ACS Applied Materials & Interfaces*, 2015, 7, 1257-1269.
- [49] Y. Zhang, Z. Wang and X. Lang, *Catalysis Science & Technology*, 2017, 7, 4955-4963.
- [50] H. Li, F. Qin, Z. Yang, X. Cui, J. Wang and L. Zhang, *Journal of American Chemical Society*, 2017, 139, 3513-3521.
- [51] O. Tomita, T. Otsubo, M. Higashi, B. Ohtani and R. Abe, *ACS Catalysis*, 2016, 6, 1134-1144.
- [52] S. Samanta, S. Khilari, D. Pradhan and R. Srivastava, *ACS Sustainable Chemistry & Engineering*, 2017, 5, 2562-2577.
- [53] A. D. Proctor, S. Panuganti and B. M. Bartlett, *Chemical Communications*, 2018, 54, 1101-1104.
- [54] M. Bellardita, E. I. García-López, G. Marci, I. Krivtsov, J. R. Garcí and L. Palmisano, *Applied Catalysis B: Environmental*, 2018, 220, 222-233.
- [55] J. Bi, Z. Zhou, M. Chen, S. Liang, Y. He, Z. Zhang and L. Wu, *Applied Surface Science*, 2015, 349, 292-298.
- [56] N. Zhang, S. Liu, X. Fu and Y. J. Xu, *Journal of Physical Chemistry C*, 2011, 115, 22901-22909.
- [57] J. Xu, L. Luo, G. Xiao, Z. Zhang, H. Lin, X. Wang and J. Long, *ACS Catalysis*, 2014, 4, 3302-3306.
- [58] S. Naya, K. Kimura and H. Tada, *ACS Catalysis*, 2013, 3, 10-13.
- [59] Y. Wu, B. Yuan, M. Li, W. H. Zhang, Y. Liu and Can Li, *Chemical Science*, 2015, 6, 1873-1878.
- [60] F. Raza, J. H. Park, H. R. Lee, H. I. Kim, S. J. Jeon and J. H. Kim, *ACS Catalysis*, 2016, 6, 2754-2759.

- [61] L. Ye and Z. Li, *ChemCatChem*, 2014, 6, 2540-2543.
- [62] C. L. Sun and Z. J. Shi, *Chemical Reviews*, 2014, 114, 9219–9280.
- [63] P. Ruiz-Castillo and S. L. Buchwald, *Chemical Reviews*, 2016, 116, 12564–12649.
- [64] K. Mori, M. Kawashima and H. Yamashita, *Chemical Communications*, 2014, 50, 14501-14503.
- [65] Z. J. Wang, S. Ghasimi, K. Landfester and K. A. I. Zhang, *Chemistry of Materials*, 2015, 27, 1921-1924.
- [66] F. Wang, C. Li, H. Chen, R. Jiang, L. D. Sun, Q. Li, J. Wang, J. C. Yu and C. H. Yan, *Journal of American Chemical Society*, 2013, 135, 5588-5601.
- [67] S. Sarina, H. Zhu, E. Jaatinen, Q. Xiao, H. Liu, J. Jia, C. Chen and J. Zhao, *Journal of American Chemical Society*, 2013, 135, 5793-5801.
- [68] B. Wang, X. Guo, G. Jina and X. Guo, *Catalysis Communications*, 2017, 98, 81–84.
- [69] A. Elhage, A. E. Lanterna and J. C. Scaiano, *ACS Sustainable Chemistry & Engineering*, 2018, 6, 1717-1722.
- [70] I. Maluenda and O. Navarro, *Molecules*, 2015, 20, 7528-7557.
- [71] R. Chinchilla and C. Najera, *Chemical Society Review*, 2011, 40, 5084-5121.
- [72] G. Palmisano, M. Addamo, V. Augugliaro, T. Caronna, E. Garcia-Lopez, V. Loddo and L. Palmisano, *Chemical Communications*, 2006, 1012–1014.
- [73] M. Qamar, R. B. Elsayed, K. R. Alhooshani, M. I. Ahmed, D. W. Bahnemann, *ACS Applied Materials & Interfaces*, 2015, 7, 1257-1269.
- [74] M. Gartner, J. Ballmann, C. Damm, F. W. Heinemann, H. Kisch, *Photochemical & Photobiological Sciences*, 2007, 6, 159-164.
- [75] H. Kisch, *Accounts of Chemical Research*, 2017, 50, 1002-1010.
- [76] T. Mitkina, C. Stanglmair, W. Setzer, M. Gruber, H. Kisch and B. Konig, *Organic & Biomolecular Chemistry*, 2012, 10, 3556-3561.
- [77] A. Hakki, R. Dillert and D. Bahnemann, *Catalysis Today*, 2009, 144, 154-159.
- [78] Z. Jiao, Z. Zhai, X. Guo and X. Y. Guo, *Journal of Physical Chemistry C*, 2015, 119, 3238-3243.
- [79] N. Corrigan, S. Shanmugam, J. Xu and C. Boyer, *Chemical Society Review*, 2016, 45, 6165-6212.
- [80] Y. Shiraishi, D. Tsukamoto, Y. Sugano, A. Shiro, S. Ichikawa, S. Tanaka and T. Hirai, *ACS Catalysis*, 2012, 2, 1984-1992.
- [81] C. Zheng, G. He, X. Xiao, M. Lu, H. Zhong, X. Zuo and J. Nan, *Applied Catalysis B: Environmental*, 2017, 205, 201–210.
- [82] Y. Chen, Y. Wang, W. Li, Q. Yang, Q. Hou, L. Wei, L. Liu, F. Huang and M. Ju, *Applied Catalysis B: Environmental*, 2017, 210, 352-367.
- [83] J. Ding, W. Xu, H. Wan, D. Yuan, C. Chen, L. Wang, G. Guan and W. L. Dai, *Applied Catalysis B: Environmental*, 2018, 221, 626-634.
- [84] Y. Liu, P. Zhang, B. Tian and J. Zhang, *Catalysis Communications*, 2015, 70, 30-33.
- [85] P. Zhang, Y. Liu, B. Tian, Y. Luo and J. Zhang, *Catalysis Today*, 2017, 281, 181-188.

- [86] M. J. Lima, P. B. Tavares, A. M. T. Silva, C. G. Silva and J. L. Faria, *Catalysis Today*, 2017, 287, 70–77.
- [87] P. Zhang, P. Wu, S. Bao, Z. Wang, B. Tian and J. Zhang, *Chemical Engineering Journal*, 2016, 306, 1151-1161.
- [88] W. Feng, G. Wu, L. Li and N. Guan, *Green Chemistry*, 2011, 13, 3265-3272.
- [89] Y. Gu, C. Li, J. Bai and H. Liang, *Journal of Photochemistry and Photobiology A: Chemistry*, 2018, 351, 87-94.
- [90] X. Wang, J. Yang, S. Ma, D. Zhao, J. Dai and D. Zhang, *Catalysis Science & Technology*, 2016, 6, 243-253.
- [91] F. Su, S. C. Mathew, L. Mohlmann, M. Antonietti, X. Wang and S. Blechert, *Angewandte Chemie International Edition*, 2011, 50, 657-660.
- [92] S. Furukawa, Y. Ohno, T. Shishido, K. Teramura and T. Tanaka, *ACS Catalysis*, 2011, 1, 1150-1153.
- [93] N. Li, X. Lang, W. Ma, H. Ji, C. Chen and J. Zhao, *Chemical Communications*, 2013, 49, 5034-5036.
- [94] X. Lang, H. Ji, C. Chen, W. Ma and J. Zhao, *Angewandte Chemie International Edition*, 2011, 50, 3934-3937.
- [95] Zhan Wang and X. Lang, *Applied Catalysis B: Environmental*, 2018, 224, 404-409.
- [96] X. Lang, W. Ma, Y. Zhao, C. Chen, H. Ji and J. Zhao, *Chemistry: A European Journal*, 2012, 18, 2624-2631.
- [97] S. Zavarir and H. Zhu, *Molecules*, 2015, 20, 1941-1954.
- [98] W. Zhao, C. Liu, L. Cao, X. Yin, H. Xu and B. Zhang, *RSC Advances*, 2013, 3, 22944-22948.
- [99] Y. Zhang, Q. Xiao, Y. Bao, Y. Zhang, S. Bottle, S. Sarina, B. Zhaorigetu and H. Zhu, *Journal of Physical Chemistry C*, 2014, 118, 19062-19069.
- [100] G. Corro, N. Sánchez, U. Pal, S. Cebada and J. L. G. Fierro, *Applied Catalysis B: Environmental*, 2017, 203, 43-52.
- [101] P. Verma, K. Kaur, R. K. Wanchoo and A. P. Too, *Journal of Photochemistry and Photobiology A: Chemistry*, 2017, 336, 170-175.
- [102] M. C. Manique, A. P. Silva, A. K. Alves and C. P. Bergmann, *Materials Science and Engineering B*, 2016, 206, 17-21.
- [103] S. Verma, R. B. N. Baig, M. N. Nadagouda and R. S. Varma, *Catalysis Today*, 2018, 309, 248-252.
- [104] U. Mandi, N. Salam, S. K. Kundu, A. Bhaumik and Sk. M. Islam, *RSC Advances*, 2016, 6, 73440-73449.
- [105] Q. Yuan, Z. Wu, Y. Jin, L. Xu, F. Xiong, Y. Ma and W. Huang, *Journal of American Chemical Society*, 2013, 135, 5212-521.
- [106] L. Song, S. Zhang, X. Wu, H. Tian and Q. We, *Industrial & Engineering Chemistry Research*, 2012, 51, 9510-9514.

- [107] S. Verma, R. B. N. Baig, C. Han, M. N. Nadagoud and R. S. Varma, *Green Chemistry*, 2016, 18, 251–254.
- [108] Y. Shiraishi, H. Hirakawa, Y. Togawa and T. Hirai, *ACS Catalysis*, 2014, 4, 1642-1649.
- [109] K. Imamura, Y. Okubo, T. Ito, A. Tanaka, K. Hashimoto and H. Kominami, *RSC Advances*, 2014, 4, 19883-19886.
- [110] B. Wang, X. Guo, G. Jin, X. Guo, *Catalysis Communications*, 2017, 98, 81-84.
- [111] K. Mori, M. Kawashima and H. Yamashita, *Chemical Communication*, 2014, 50, 14501-14503.
- [112] F. Wang, C. Li, H. Chen, R. Jiang, L. D. Sun, Q. Li, J. Wang, J. C. Yu and C. H. Yan, *Journal of American Chemical Society*, 2013, 135, 5588-5601.
- [113] S. Sarina, H. Zhu, E. Jaatinen, Q. Xiao, H. Liu, J. Jia, C. Chen and J. Zhao, *Journal of American Chemical Society*, 2013, 135, 5793-5801.
- [114] A. Zaleska, *Recent Patents on Engineering*, 2008, 2, 157-164.
- [115] L. G. Devi and R. Kavitha, *Applied Catalysis B: Environmental*, 2013, 140-141, 559-587.
- [116] M. V. Dozzi and E. Selli, *Journal of Photochemistry and Photobiology C: Photochemistry Reviews*, 2013, 14, 13-28.
- [117] S. Sun and W. Wang, *RSC Advances*, 2014, 4, 47136-47152.
- [118] A. Hezam, K. Namratha, Q. A. Drmosh, Z. H. Yamani, K. Byrappa, *Ceramics International*, 2017, 43, 5292-5301.
- [119] H. Lu, S. Wang, L. Zhao, B. Dong, Z. Xu and J. Li, *RSC Advances*, 2012, 2, 3374-3378.
- [120] L. Zhang, W. Wang, J. Yang, Z. Chen, W. Zhang, L. Zhou and S. Liu, *Applied Catalysis A: General* 2006, 308, 105–110.
- [121] H. Cheng, B. Huang, J. Lu, Z. Wang, B. Xu, X. Qin, X. Zhang and Y. Dai, *Physical Chemistry Chemical Physics*, 2010,12, 15468–15475.
- [122] J. Wang, X. Yang, K. Zhao, P. Xu, L. Zong, R. Yu, D. Wang, J. Deng, J. Chen and X. Xing, *Journal Material Chemistry A*, 2013, 1, 9069–9074.
- [123] S. Sood, S. K. Mehta, A. S. K. Sinha, S. K. Kansal, *Chemical Engineering Journal*, 2016, 290, 45-52.
- [124] L. Zhang, G. Wang, Z. Xiong, H. Tang, C. Jiang, *Applied Surface Science*, 2018, 436, 162–171.
- [125] Y. Hong, C. Li, B. Yin, D. Li, Z. Zhang, B. Mao, W. Fan, W. Gu, W. Sh, *Chemical Engineering Journal*, 2018, 338, 137-146.
- [126] S. Chen, Y. Hu, L. Ji, X. Jiang and X. Fu, *Applied Surface Science*, 2014, 292, 357-366.
- [127] J. Guo, Y. Liu, Y. Hao, Y. Li, X. Wang, R. Liu and F. Li, *Applied Catalysis B: Environmental*, 2018, 224, 841–853.

- [128] L. Jiang, X. Yuan, G. Zeng, J. Liang, X. Chen, H. Yu, H. Wang, Z. Wu, J. Zhang and T. Xiong, *Applied Catalysis B: Environmental*, 2018, 227, 376–385.
- [129] L. Shan, Y. Liu, H. Chen, Z. Wu and Z. Han, *Dalton Transactions*, 2017, 46, 2310–2321.
- [130] S. H. Hsieh, A. Manivel, G. J. Lee, J. J. Wu, *Materials Research Bulletin*, 2013, 48, 4174–4180.
- [131] Y. Cong, J. Wang, H. Jin, X. Feng, Q. Wang, Y. Ji and Y. Zhang, *Industrial & Engineering Chemistry Research*, 2016, 55, 1221–1228.
- [132] A. Hezam, K. Namratha, Q.A. Drmosh, Z.H. Yamani and K. Byrapp, *Ceramics International*, 2017, 43, 5292–5301.
- [133] D. Chen, S. Wu, J. Fang, S. Lu, G. Y. Zhou, W. Feng, F. Yang, Y.Chen, Z. Q. Fang, *Separation and Purification Technology*, 2018, 193, 232–241.
- [134] Y. Shi, L. Luo, Y. Zhang, Y. Chen, S. Wang, L. Li, Y. Long and F. Jiang, *Ceramics International*, 2017, 43, 7627–7635.
- [135] K. Yang, J. Li, Y. Peng and J. Lin, *Physical Chemistry Chemical Physics*, 2017, 19, 251-257.
- [136] P. Qiu, B. Park, J. Choi, M. Cui, J. Kim and J. Khim, *Journal of Alloys and Compounds*, 2017, 706, 7-15.
- [137] Y. Huang, W. Fan, B. Long, H. Li, F. Zhao, Z. Liu, Y. Tong and H. Ji, *Applied Catalysis B: Environmental*, 2016, 185, 68-76.
- [138] N. Gao, Z. Lu, X. Zhao, Z. Zhu, Y. Wang, D. Wang, Z. Hua, C. Li, P. Huo and M. Song, *Chemical Engineering Journal*, 2016, 304, 351–361.
- [139] X. Liu, Y. Kang and D. Luo, *Materials Letters*, 2016, 185, 189-192.
- [140] S. Yi, X. Yue, D. Xu, Z. Liu, F. Zhao, D. Wang and Y. Lin, *New Journal of Chemistry*, 2015, 39, 2917-2924.
- [141] L. Shan, G. Wang, D. Li, X. San, L. Liu, L. Dong and Z. Wu, *Dalton Transactions*, 2015, 44, 7835–7843.
- [142] Y. Zhang, J. Lu, M. R. Hoffmann, Q. Wang, Y. Cong, Q. Wang and H. Jin, *RSC Advances*, 2015, 5, 48983–48991.
- [143] H. Cheng, J. Hou, H. Zhu and X. M. Guo, *RSC Advances*, 2014, 4, 41622–41630.
- [144] L. Yin, J. Niu, Z. Shen, A. Chen, *Environmental Science & Technology*, 2010, 44, 5581–5586.
- [145] S. Y. Chai, Y. J. Kim, M. H. Jung, A. K. Chakraborty, D. Jung and W. I. Lee, *Journal of Catalysis*, 2009, 262, 144-149.
- [146] J. Ma, Z. Liu, J. Lian, X. Duan, T. Kim, P. Peng, X. Liu, Q. Chen, G. Yao and W. Zheng, *CrystEngComm*, 2011, 13, 3072-3079.
- [147] Y. Luo, H. Chen, X. Li, Z. Gong, X. Wang, X. Peng, M. He and Z. Sheng, *Materials Letters*, 2013, 105, 12-15.
- [148] J. H. Kim, H. Park, C. H. Hsu and J. Xu, *Journal of Physical Chemistry C*, 2010, 114, 9634-9639.

- [149] L. Ma, Q. Zhao, Q. Zhang, M. Ding, J. Huang, X. Liu, Y. Liu, X. Wu and X. Xu, *RSC Advances*, 2014, 4, 41636-41641.
- [150] J. Chen, S. Qin, G. Song, T. Xiang, F. Xin and X. Yin, *Dalton Transactions*, 2013, 42, 15133-15138.
- [151] E. Hu, X. Gao, A. Etogo, Y. Xie, Y. Zhong and Y. Hu, *Journal of Alloys and Compounds*, 2014, 611, 335-340.
- [152] L. Yang, W. Sun, S. Luo and Y. Luo, *Applied Catalysis B: Environmental*, 2014, 156-157, 25-34.
- [153] F. Dong, X. Feng, Y. Zhang, C. Gao and Z. Wu, *RSC Advances*, 2015, 5, 11714-11723.
- [154] A. Rauf, Md. S. A. S. Shah, G. H. Choi, U. B. Humayoun, D. H. Yoon, J. W. Bae, J. Park, W. J. Kim, and P. J. Yoo, *ACS Sustainable Chemistry & Engineering*, 2015, 3, 2847-2855.
- [155] H. Cheng, B. Huang, X. Qin, X. Zhang and Y. Dai, *Chemical Communications*, 2012, 48, 97-99.
- [156] Y. Cui, Q. Jia, H. Li, J. Han, L. Zhu, S. Li, Y. Zou and J. Yang, *Applied Surface Science*, 2014, 290, 233-239.
- [157] D. K. Ma, M. L. Guan, S. S. Liu, Y. Q. Zhang, C.W. Zhang, Y. X. He and S. M. Huang, *Dalton Transaction*, 2012, 41, 5581-5586.
- [158] S. Luo, F. Chai, L. Zhang, C. Wang, L. Li, X. Liu and Z. Su, *Journal of Material Chemistry*, 2012, 22, 4832-4836.
- [159] Y. Huang, W. Fan, B. ong, H. Li, F. Zhao, Z. Liu, Y. Tong and H. Ji, *Applied Catalysis B: Environmental*, 2016, 185, 68-76.
- [160] A. Chen, Z. Bian, J. Xu, X. Xin and H. Wang, *Chemosphere*, 2017, 188, 659-666.
- [161] Y. Shi, Y. Chen, G. Tian, H. Fu, K. Pan, J. Zhou and H. Yan, *Dalton Transactions*, 2014, 43, 12396-12404.
- [162] B. Weng, X. Zhang, N. Zhang, Z. R. Tang and Y. J. Xu, *Langmuir*, 2015, 31, 4314-4322.
- [163] X. Gao, G. Huang, H. Gao, C. Pan, H. Wang, J. Yan, Y. Liu, H. Qiu, N. Ma and J. Gao, *Journal of Alloys and Compounds*, 2016, 674, 98-108.
- [164] Z. Wu, L. Chen, C. Xing, D. Jiang, J. Xie and M. Chen, *Dalton Transactions*, 2013, 42, 12980-12988.
- [165] L. Chen, J. He, Q. Yuan, Y. Liu, C. T. Au and S. F. Yin, *Journal of Materials Chemistry A*, 2015, 3, 1096-1102.
- [166] Z. Q. Liu, W. Y. Huang, Y. M. Zhang and Y. X. Tong, *CrystEngComm*, 2012, 14, 8261-8267.
- [167] Z. Xuan, Y. Shiyue, L. Yumei, W. Zuoshan and L. Weifeng, *Materials Letters*, 2015, 145, 23-26.
- [168] S. Balachandran and M. Swaminathan, *Dalton Transactions*, 2013, 42, 5338-5347.

- [169] A. Abdi, A. Denoyelle, N. C. Bernole and M. Trari, *International Journal of Hydrogen Energy*, 2013, 38, 2070-2078.
- [170] Y. H Ding, X. L. Zhang, N. Zhang, J. Y. Zhang, R. Zhang, Y. F. Liu and Y. Z. Fang, *Dalton Transactions*, 2018, 47, 684–692.
- [171] S. Paul, S. Ghosh, D. Barman and S. K. De, *Applied Catalysis B: Environmental*, 2017, 219, 287-300.
- [172] W. Xitao, L. Rong and W. Kang, *Journal of Material Chemistry A*, 2014, 2, 8304-8313.
- [173] W. Xu, J. Fang, Y. Chen, S. Lu, G. Zhou, X. Zhu and Z. Fang, *Materials Chemistry and Physics*, 2015, 154, 30-37.
- [174] S. Bera, S. Ghosh and R. N. Basu, *New Journal of Chemistry*, 2018, 42, 541-554.
- [175] J. Li, Y. Yu and L. Zhang, *Nanoscale*, 2014, 6, 8473-8488.
- [176] A. Malathi, J. Madhavan, M. Ashok kumar and P. Arunachalam, *Applied Catalysis A, General*, 2018, 555, 47-74.
- [177] C. Pan and Y. Zhu, *Catalysis Science & Technology*, 2015, 5, 3071–3083.
- [178] Z. F. Huang, L. Pan, J. J. Zou, X. Zhang and L. Wang, *Nanoscale*, 2014, 6, 14044-14063.
- [179] L. E. Mendes, C. Zaidan, J. M. R. Díaz, D. C. Napoleão, S. M. Montenegro, A. N. Araújo, M. Benachour and V. L. Silva, *Korean Journal of Chemical Engineering*, 2017, 34, 511-522.
- [180] D. Chen, Z. Kuang, Q. Zhu, Y. Du and H. Zhu, *Materials Research Bulletin*, 2015, 66, 262–267.
- [181] X. Zou, C. Ran, Y. Dong, Z. Chen, D. Dong, D. Hu, X. Li and Y. Cui, *RSC Advances*, 2016, 6, 20664-20670.
- [182] H. Xu, Y. Xu, H. Li, J. Xia, J. Xiong, S. Yin, C. Huang and H. Wan, *Dalton Transactions*, 2012, 41, 3387–3394.
- [183] N. Mohaghegh, M. Tasviri, E. Rahimi and M. R. Gholami, *RSC Advances*, 2015, 5, 12944-12955.
- [184] M. Gao, D. Zhang, X. Pu, H. Ma, C. Su, X. Gao and J. Dou, *Separation and Purification Technology*, 2016, 170, 183-189.
- [185] M. Lu, G. Yuan, Z. Wang, Y. Wang and J. Guo, *Nanoscale Research Letters*, 2015, 10, 385-391.
- [186] X. Lin, X. Guo, S. Zhao, X. Gao, H. Zhai, Q. Wang and L. Chang, *Chinese Journal of Chemical Physics*, 2014, 27, 725-731.
- [187] F. Duo, Y. Wang, X. Mao, X. Zhang, Y. Wang and C. Fan, *Applied Surface Science*, 2015, 340, 35-42.
- [188] M. Shang, W. Wang, J. Ren, S. Sun and L. Zhang, *CrystEngComm*, 2010, 12, 1754-1758.
- [189] X. Chen, L. Li, T. Yi, W. Z. Zhang, X. Zhang and L. Wang, *Journal of Solid State Chemistry*, 2015, 229, 141–149.

- [190] B. Zhang, J. Li, B. Zhang, R. Chong, R. Li, B. Yuan, S. M. Lu and C. Li, *Journal of Catalysis*, 2015, 332, 95–100.
- [191] L. Ge, *Materials Chemistry and Physics*, 2008, 107, 465–470.
- [192] A. Zhang and J. Zhang, *Applied Surface Science*, 2010, 256, 3224–3227.
- [193] P. Ju, P. Wang, B. Li, H. Fan, S. Ai, D. Zhang and Y. Wang, *Chemical Engineering Journal*, 2014, 236, 430–437.
- [194] N. Wetchakun, S. Chaiwichain, B. Inceesungvorn, K. Pingmuang, S. Phanichphant, A. I. Minett and J. Chen, *ACS Applied Material & Interfaces*, 2012, 4, 3718–3723.
- [195] K.-H. Ye, Z. Chai, J. Gu, X. Yu, C. Zhao, Y. Zhang, W. Mai, *Nano Energy*, 2015, 18, 222–231.
- [196] J. Li, W. Zhao, Y. Guo, Z. Wei, M. Han, H. He, S. Yang and C. Sun, *Applied Surface Science*, 2015, 351, 270–279.
- [197] E. Aguilera-Ruiz, M. Garza-Galvan, P. Zambrano-Robledo, J. C. Ballesteros-Pacheco, J. Vazquez-Arenas, J. Peral and U. M. Garcia-Perez, *RSC Advances*, 2017, 7, 45885–45895.
- [198] J. Cheng, X. Yan, Q. Mo, B. Liu, J. Wang, X. Yang and L. Li, *Ceramics International*, 2017, 43, 301–307.
- [199] X. Ma, Z. Ma, T. Liao, X. Liu, Y. Zhang, L. Li, W. Li and B. Hou, *Journal of Alloys and Compounds*, 2017, 702, 68–74.
- [200] Z. He, Y. Shi, C. Gao, L. Wen, J. Chen and S. Song, *Journal of Physical Chemistry C*, 2014, 118, 389–398.
- [201] W. Pingyu, Y. Qinglin and G. Lin, *Progress In Chemistry*, 2009, 21, 1734–1740.
- [202] X. J. Wang, Y. Q. Song, J. Y. Hou and X. N. Chen, *Crystal Research and Technology*, 2017, 52, 1700068–1700074.
- [203] X. Wang, F. Li, D. Li, R. Li and S. Liu, *Materials Science and Engineering B*, 2015, 112–120
- [204] F. Cao, J. Wang, S. Li, J. Cai, W. Tu, X. Lv, and G. Qin, *Journal of Alloys and Compounds*, 2015, 445–451.
- [205] S. Peng, L. Li, P. Zhu, Y. Wu, M. Srinivasan, S. G. Mhaisalkar, S. Ramakrishna and Q. Yan, *Chemistry-An Asian Journal*, 2013, 8, 258–268.
- [206] C. Huang, J. Hu, S. Cong, Z. Zhao and X. Qiu, *Applied Catalysis B: Environmental*, 2015, 172–174, 105–112.
- [207] C. Wang, Y. Zhang, W. Wang, D. Pei, G. X. Huang, J. J. Chen, X. Zhang and Q. Yu, *Applied Catalysis B: Environmental*, 2018, 221, 320–328.
- [208] A. Ahmad, X. Meng, N. Yun and Z. Zhang, *Journal of Nanomaterials*, 2016, 1–10.
- [209] H. Li, J. Liu, T. Hu, N. Du, S. Song, W. Hou, *Materials Research Bulletin*, 2016, 77, 171–177.
- [210] J. C. Sin, C. A. Lim, S. M. Lam and A. R. Mohamed, *Journal of Materials Science: Materials in Electronics*, 2017, 28, 13236–13246.

- [211] L. Lu, M. Zhou, L Yin, G. Zhou, T. Jiang, X. Wan and H. Shi, *Journal of Molecular Catalysis A: Chemical*, 2016, 423, 379-385.
- [212] X. Wang, Q. Wang, F. Li, W. Yang, Y. Zhao, Y. Hao and S. Liu, *Chemical Engineering Journal*, 2013, 234, 361–371.
- [213] X. Wen, C. G. Niu, and G. M. Zeng, *Dalton Transactions*, 2017, 46, 4982-4993.
- [214] L. Chen, S. F. Yin, S. L. Luo, R. Huang, Q. Zhang, T. Hong and C.T. Au, *Industrial & Engineering Chemistry Research*, 2012, 51, 6760–6768.
- [215] M. Maczka, L. Macalik and J. Hanuza, *Journal of Raman Spectroscopy*, 2009, 40, 2099–2103
- [216] M. Maczka, W. Paraguassu, P. T. C. Freire, A. G. S. Filho, J. M. Filho and J. Hanuza, *Physical Review B*, 2010, 81, 104301-104309.
- [217] R. E. Schaak and T. E. Mallouk, *Chemical Communications*, 2002, 706–707
- [218] M. Kudo, H. Ohkawa, W. Sugimoto, N. Kumada, Z. Liu, O. Terasaki and Y. Sugahar, *Inorganic Chemistry*, 2003, 42, 4479-4484.
- [219] L. Wu, J. Bi, Z. Li, X. Wang and X. Fu, *Catalysis Today*, 2008, 131, 15–20.
- [220] L. Zhang and Y. Zhu, *Catalysis Science and Technology*, 2012, 2, 694–706.
- [221] N. Zhang, R. Ciriminna, M. Pagliaro and Y. Xu, *Chemical Society Reviews*, 2014, 43, 5143-5402.
- [222] T. Zeng, X. Yu, S. Hui, Z. Zhou and X. Dong, *Materials Research Bulletin*, 2015, 68, 271–275.
- [223] S. Zhang, C. Zhang, Y. Man, Y. Zhu, *Journal of Solid State Chemistry*, 2006, 179, 62–69.
- [224] Y. Liu, H. Lv, J. Hu and Z. Li, *Materials Letters*, 2015, 139, 401–404.
- [225] M. Gancheva, R. Iordanova, Y. Dimitriev, D. Nihtianova, P. Stefanov and A. Naydenov, *Journal of Alloys and Compounds*, 2013, 570, 34-40.
- [226] Y. Li, J. Liu, X. Huang and G. Li, *Crystal Growth & Design*, 2007, 7, 1350-1355.
- [227] P. Tang, H. Chen and F. Cao, *Materials Letters*, 2012, 68, 171-173.
- [228] H. Xie, D. Shen, X. Wang and G. Shen, *Materials Chemistry and Physics*, 2007, 103, 334-339.
- [229] S. Sun, W. Wang, L. Zhang, E. Gao, D. Jiang, Y. Sun and Y. Xie, *ChemSusChem*, 2013, 6, 1873-1877.
- [230] F. Amano, K. Nogami, M. Tanaka and B. Ohtani, *Langmuir*, 2010, 26, 7174-7180.
- [231] M. Qamar and A. Khan, *RSC Advances*, 2014, 4, 9542–9550.
- [232] T. Saison, P. Gras, N. Chemin, C. Chanéac, O. Durupthy, V. Brezová, C. C. Justin and J. P. Jolitive, *Journal of Physical Chemistry C*, 2013, 117, 22656–22666.
- [233] Z. Sun, J. Guo, S. Zhu, L. Mao, J. Ma and D. Zhang, *Nanoscale*, 2014, 6, 2186-2193.
- [234] S. M. López, M. C. Hidalgo and J. A. Navío, *Applied Catalysis A: General*, 2012, 34-41.
- [235] M. S. Gui, W. De Zhang, Q. Xi and C. Chen, *Journal of Solid State Chemistry*, 2011, 184, 1977–1982

- [236] Y. Wang, X. Bai, C. Pan, J. He and Y. Zhu, *Journal of Material Chemistry*, 2012, 22, 11568-11573.
- [237] Q. Xiao, J. Zhang, C. Xiao and X. Tan, *Catalysis Communications*, 2008, 9, 247-253.
- [238] Y. Zhao, Y. Wang, E. Liu, J. Fan and X. Hu, *Applied Surface Science*, 2018, 436, 854-864.
- [239] J. Shen, J. Xue, Z. Chen, J. Ni, B. Tang, G. He and H. Chen, *Journal of Material Science*, 2018, 53, 4848-4860.
- [240] P. Dumrongrojthanath, A. Phuruangrat, S. Thongtem and T. Thongtem, *Journal of the Ceramic Society of Japan*, 2018, 126, 87-90.
- [241] Z. Jiang, X. Liang, H. Zheng, Y. Liu, Z. Wang, P. Wang, X. Zhang, X. Qin, Y. Dai, M. H. Whangbo and B. Huang, *Applied Catalysis B: Environmental*, 2017, 219, 209-215.
- [242] G. Li, D. Zhang, J. C. Yu and M. K. H. Leung, *Environmental Science & Technology*, 2010, 44, 4276-4281.
- [243] H. Huang, R. Cao, S. Yu, K. Xu, W. Hao, Y. Wang, F. Dong, T. Zhang and Y. Zhang, *Applied Catalysis B: Environmental*, 2017, 219, 526-537.
- [244] Y. Lv, W. Yao, R. Zong and Y. Zhu, *Scientific Reports*, 2015, 6, 19347.
- [245] Y. Huang, S. Kang, Y. Yang, H. Qin, Z. Ni, S. Yang and X. Li, *Applied Catalysis B: Environmental*, 2016, 196, 89-99.
- [246] H. A. Ahsaine, A. E. Jaouhari, A. Slassi, M. Ezahri, A. Benlhachemi, B. Bakiz, F. Guinneton and J.-R. Gavarri, *RSC Advances*, 2016, 6, 101105–101114.
- [247] R. P. Panmand, Y. A. Sethi, S. R. Kadam, M. S. Tamboli, L. K. Nikam, J. D. Ambekar, C. J. Park and B. B. Kale, *CrystEngComm*, 2015, 17, 107–115.
- [248] S. M. López, K. Villa, T. Andreu and J. R. Morante, *ACS Catalysis*, 2014, 4, 3013-3019.
- [249] X. Chu, G. Shan, C. Chang, Y. Fu, L. Yue and L. Zhu, *Frontiers of Environmental Science & Engineering*, 2014, DOI 10.1007/s11783-014-0753-y.
- [250] Y. Zhang and Y. J. Xu, *RSC Advances*, 2014, 4, 2904-2910.
- [251] X. Xu, F. Ming, J. Hong, Y. Xie and Z. Wang, *Materials Letters*, 2016, 179, 52–56.
- [252] A. P. Jakhade, M. V. Biware and R. C. Chikate, *ACS Omega*, 2017, 2, 7219–7229.
- [253] Y. Zhang, N. Zhang, Z. R. Tang and Y. J. Xu, *Chemical Science*, 2013, 4, 1820–1824.
- [254] M. Gancheva, R. Iordanova, Y. Dimitriev, D. Nihtianova, P. Stefanov and A. Naydenov, *Journal of Alloys and Compounds*, 2013, 570, 34–40.
- [255] A. Rauf, M. Ming, S. Kim, Md. S. A. S. Shah, C. H. Chung, J. H. Park and P. J. Yoo, *Nanoscale*, 2018, 10, 3026-3036.
- [256] C. N. Ri, K. S. Gol, J. J. Yong, S. N. Pak, S. C. Ri and J. H. Ri, *New Journal of Chemistry*, 2018, 42, 647-653.
- [257] S. Li, S. Hu, W. Jiang, Y. Liu, J. Liu and Z. Wang, *Journal of Colloid and Interface Science*, 2017, 501, 156–163.

- [258] Y. Zhu, Y. Wang, Q. Ling and Y. Zhu, *Applied Catalysis B: Environmental*, 2017, 200, 222–229.
- [259] X. Meng, Z. Li, H. Zeng, J. Chen and Z. Zhang, *Applied Catalysis B: Environmental*, 2017, 210, 160–172.
- [260] Y. Peng, Q. G. Chen, D. Wang, H. Y. Zhou and A.W. Xu, *CrystEngComm*, 2015, 17, 569–576.
- [261] H. Huang, S. Wang, N. Tian and Y. Zhang, *RSC Advances*, 2014, 4, 5561–5567.
- [262] Y. L. Min, K. Zhang, Y. C. Chen, Y. G. Zhang and W. Zhao, *Separation and Purification Technology*, 2012, 92, 115-120.
- [263] R. Rajendran, K. Varadharajan, V. Jayaraman, B. Singaram and J. Jeyaram, *Applied Nanoscience*, 2018, 8, 61-78.
- [264] J. Claude, C. Mesjard, B. Frit and A. Watanabe, *Journal of Material Chemistry*, 1999, 9, 1319-1322.
- [265] A. Kudo and S. Hijii, *Chemistry Letters*, 1999, 1103-1104.
- [266] M. Kudo, H. Ohkawa, W. Sugimoto, N. Kumada, Z. Liu, O. Terasaki and Y. Sugahara, *Inorganic Chemistry*, 2003, 42, 4479-4484.
- [267] M. Maczka, L. Kepinsk, L. Macalik and J. Hanuza, *Materials Chemistry and Physics*, 2011, 125, 93–101
- [268] M. R. Waller, T. K. Townsend, J. Zhao, E. M. Sabio, R. L. Chamousis, N. D. Browning and F. E. Osterloh, *Chemistry of Materials*, 2012, 24, 698-704.
- [269] S. O. Alfaro and A. M. Cruz, *Applied Catalysis A: General*, 2010, 383, 128-133.
- [270] S. Alfaro, A. Cruz, L. M. Martínez, S. W. Lee, *Catalysis Communications*, 2010, 11, 326-330.
- [271] J. Tang and J. Ye, *Journal of Materials Chemistry*, 2005, 15, 4246-4251.
- [272] A. Cruz, S. Alfaro, L. M. Martínez and I. J. Ramírez, *Journal of Ceramic Processing Research*, 2008, 9, 490-494.
- [273] S. Obregon, M. A. Gomez and D. B. Uresti, *Journal of Colloid and Interface Science*, 2017, 506, 111–119.
- [274] V. A. Khomchenko, D. V. Karpinsky and J. A. Paixao, *Journal of Materials Chemistry C*, 2017, 5, 3623-3629.
- [275] D. Sando, A. Agbelele, D. Rahmedov, J. Liu, P. Rovillain, Toulouse, I. C. Infante, A. P. Pyatakov, S. Fusil, E. Jacquet, C. Carrétéro, C. Deranlot, S. Lisenkov, D. Wang, J. M. L. Breton, M. Cazayous, A. Sacuto, J. Juraszek, A. K. Zvezdin, L. Bellaiche, B. Dkhil, A. Barthélémy and M. Bibes, *Nature Materials*, 2013, 1-5.
- [276] X. Ren, H. Fan, Y. Zhao and Z. Liu, *ACS Applied Materials & Interfaces*, 2016, 8, 26190–26197.
- [277] F. Zhang, M. Li, Y. Zhu, M. Zhao, S. Xie, M. Wei, Y. Li, Z. Hu and M. Li, *Journal of Alloys and Compounds*, 2017, 695, 3178-3182.
- [278] G. S. Lotey and N. K. Verma, *Chemical Physics Letters*, 2013, 574, 71-77.
- [279] N. Maso and A. R. West, *Chemistry of Materials*, 2012, 24, 2127-2132.

- [280] P. Kanhere and Z. Chen, *Molecules*, 2014, 19, 19996-20017.
- [281] S. Lam, J. Sinbana and A. R. Mohamed, *Materials Research Bulletin*, 2017, 90, 15-30.
- [282] R. Safi and H. Shokrollahi, *Progress in Solid State Chemistry*, 2012, 40, 6-15.
- [283] W. Ren, *Advanced Manufacturing*, 2013, 1, 166-175.
- [284] M. S. Bernardo, T. Jardiel, M. Peiteado, A. C. Caballero and M. Villegas, *Journal of European Ceramic Society*, 2011, 31, 3047-3053.
- [285] T. Soltani and M. H. Entezari, *Chemical Engineering Journal*, 2013, 223, 145-154.
- [286] J. K. Kim, S. S. Kim and W. J. Kim, *Materials Letters*, 2005, 59, 4006-4009.
- [287] Y. Huo, M. Miao, Y. Zhang, J. Zhu and H. Li, *Chemical Communications*, 2011, 47, 2089-2091
- [288] Y. Guo, Y. Pu, Y. Cui, C. Hui, J. Wan and C. Cui, *Materials Letters*, 2017, 196, 57-60.
- [289] S. Mohan and B. Subramanian, *RSC Advances*, 2013, 3, 23737-23744
- [290] Z. Xue, T. Wang, B. Chen, T. Malkoske, S. Yu and Y. Tang, *Materials*, 2015, 8, 6360-6378.
- [291] Z. Wang, W. Xu, H. Peng and X. Tang, *Journal of Materials Research*, 2013, 1498-1503
- [292] N. I. Ilic, A. S. Dzunuzovic, J. D. Bobic, B. S. Stojadinovic, P. Hammer, M. M. V. Petrovic, Z. D. D. Mitrovic and B. D. Stojanovic, *Ceramics International*, 2015, 41, 69-77.
- [293] S. J. A. Moniz, R. Q. Cabrer, C. S. Blackman, J. Tang, P. Southern, P. M. Weaver and C. J. Carmalt, *Journal of Materials Chemistry A*, 2014, 2, 2922-2927.
- [294] I. T. Papadas, K. S. Subrahmanyam, M. G. Kanatzidis and G. S. Armatas, *Nanoscale*, 2015, 7, 5737-5743.
- [295] I. Papadas, J. A. Christodoulides, G. Kioseoglou and G. S. Armatas, *Journal of Materials Chemistry A*, 2015, 3, 1587-1593.
- [296] L. Fei, J. Yuan, Y. Hu, C. Wu, J. Wang and Y. Wang, *Crystal Growth & Design*, 2011, 11, 1049-1053.
- [297] K. Suzuki, Y. Tokudome, H. Tsuda and M. Takahashi, *Journal of Applied Crystallography*, 2016, 49, 1-7.
- [298] L. J. Di, H. Yang, T. Xian, J. Y. Ma, H. M. Zhang, J. L. Jiang, Z. Q. Wei and W. J. Feng, *Journal of Nanomaterials*, 2015, 1-5.
- [299] X. Zhu, Y. Yang, K. He, J. Zhu, S. Ye, S. Zhou and Z. Liu, *Ferroelectrics*, 2010, 409, 204-210.
- [300] S. Irfan, S. Rizwan, Y. Shen, L. Li, Asfandiyar, S. Butt and C. W. Nan, *Nature*, 2017, 1-12.
- [301] T. Soltani and B. K. Lee, *Photochemical & Photobiological Sciences*, 2017, 16, 86-95.

- [302] S. Irfan, L. Li, A. S. Saleemi and C. W. Nan, *Journal of Materials Chemistry A*, 2017, 5, 11143-11151.
- [303] P. R. Vanga, R. V. Mangalaraja and M. Ashok, *Journal of Superconductivity and Novel Magnetism*, 2018, 31, 89–97.
- [304] X. Z. Deng, C. Song, Y. L. Tong, G. Yuan, F. Gao, D. Q. Liu and S. T. Zhang, *Physical Chemistry Chemical Physics*, 2018, 20, 3648-3657.
- [305] T. Zhang, Y. Shen, Y. Qiu, Y. Liu, R. Xiong, J. Shi and J. Wei, *ACS Sustainable Chemistry & Engineering*, 2017, 5, 4630–4636.
- [306] H. Ramezanalizadeh and F. Manteghi, *Journal of Photochemistry and Photobiology A: Chemistry*, 2017, 338, 60–71.
- [307] R. Guo, L. Fang, W. Dong, F. Zheng and M. Shen, *Journal of Material Chemistry*, 2011, 21, 18645–18652.
- [308] M. Humayun, A. Zada, Z. Li, M. Xie, X. Zhang, Y. Qu, F. Raziq and L. Jing, *Applied Catalysis B: Environmental*, 2016, 180, 219–226.
- [309] Y. C. Yang, Y. Liu, J. H. Wei, C. X. Pan, R. Xiong and J. Shi, *RSC Advances*, 2014, 4, 31941–31947.
- [310] Y. Zhang, A. M. Schultz, P. A. Salvador and G. S. Rohrer, *Journal of Material Chemistry*, 2011, 21, 4168–4174.
- [311] X. Y. Sun, Z. W. Liu, H. Y. Yu, Z.G. Zheng and D. C. Zeng, *Materials Letters*, 2018, 219, 225-228.
- [312] B. P. Reddy, V. Rajendar, M. C. Shekar and S. H. Park, *Digest Journal of Nanomaterials and Biostructures*, 2018, 13, 87-95.
- [313] C. Ponraj, D. Prabhakaran, G. Vinitha and J. Daniel, *Nano Hybrids and Composites*, 2017, 17, 194-201.
- [314] F. Niu, D. Chenn, L. Qinn, T. Gao, N. Zhang, S. Wang, Z. Chen, J. Wang, X. Sun and Y. Huang, *Solar Energy Materials & Solar Cells*, 2015, 143, 386–396.
- [315] M. I. Zaki, W. Ramadan, A. Katrib, A. I. M. Rabee, *Applied Surface Science*, 2014, 317, 929–934.
- [316] N. Wang, L. Zhu, M. Lei, Y. She, M. Cao and H. Tang, *ACS Catalysis*, 2011, 1, 1193–1202.
- [317] Z. Xue, T. Wang, B. Chen, T. Malkoske, S. Yu and Y. Tang, *Materials*, 2015, 8, 6360–6378.

CHAPTER 2

Materials and Methods

2.1 Preparation of Photocatalytic Materials

All the chemicals used in this study were of analytical reagent grade and used directly without further purification. Iron nitrate [$\text{Fe}(\text{NO}_3)_3 \cdot 9\text{H}_2\text{O}$] (99%), bismuth nitrate [$\text{Bi}(\text{NO}_3)_3 \cdot 5\text{H}_2\text{O}$] (99%), copper nitrate [$\text{Cu}(\text{NO}_3)_2 \cdot 3\text{H}_2\text{O}$] (99%), ammonium tungstate [$(\text{NH}_4)_{10}\text{W}_{12}\text{O}_{41}$] (66.5 %W), bismuth carbonate [$(\text{BiO})_2\text{CO}_3$] (98%), substituted thiols, urea [$\text{N}_2\text{H}_4\text{CO}$] (99.5%), thiourea [$\text{N}_2\text{H}_4\text{CS}$] (99%), hexamethylenetetramine [$\text{C}_6\text{H}_{12}\text{N}_4$] (99%), glycine [$\text{C}_2\text{H}_5\text{NO}_2$] (99%), citric acid [$\text{C}_6\text{H}_8\text{O}_7$] (99%) and congo red [$\text{C}_{32}\text{H}_{22}\text{N}_6\text{Na}_2\text{O}_6\text{S}_2$] were procured from Himedia and Merck Ltd., India. Diuron and alachlor pesticides were procured from Sigma Aldrich Ltd., India. Benzylamine was procured from Avra synthesis India Ltd. Malonic acid dihydrazide was synthesized using the literature reported procedure [1]. Double distilled water prepared in the laboratory was used in all preparation process.

2.1.1 Synthesis of Bi_2WO_6

Solution combustion synthesis of Bi_2WO_6 (BTC): The Bi_2WO_6 (BTC) nanoparticles were synthesized by solution combustion synthesis (SCS) method using ammonium tungstate and bismuth carbonate as precursor salt and hexamethylenetetramine (HMTA), malonic acid dihydrazide (MDH), urea (U) and glycine (G) as fuel. Combustion synthesis method is described as a quick, straightforward preparation process to produce homogeneous, well crystalline and agglomerated multicomponent oxide/sulfide ceramic powders, without the intermediate decomposition and/or calcination step. The combustion synthesis is a versatile, simple and rapid process, which allows effective synthesis of a variety of nanosize materials. This process involves a self-sustained reaction in homogeneous solution of different oxidizers (O) (e.g., metal nitrates) and fuels (F) (e.g., urea, glycine). Depending on the type of the precursors, as well as on conditions used, the combustion synthesis may occur as either volume or layer-by-layer propagating combustion modes. This process not only yields nanosize oxide materials but also allows uniform (homogeneous) doping of trace amounts impurity ions in a single step. In our study, we have varied the F/O between 0.5 to 2 in order to study the effect of the fuel nature and content on the crystallinity, phase purity and morphology of the synthesized nano materials. In a typical preparation procedure, 0.545 g ammonium tungstate, 0.549 g bismuth carbonate and 0.312 g of glycine was dissolved in minimum amount of double distilled water and the mixture was kept in a furnace, preheated to 400 °C. The mixture ignited instantaneously producing a foamy material, simultaneously releasing a lot of gaseous products. The combustion mixture was maintained at 400°C for 30 minutes. After 30 minutes of incubation at 400°C, the evolution of gaseous products stopped

completely and the final combustion residue was obtained. This observation suggests the completion of the combustion reaction. After completion of the combustion process, the solid material was collected, grinded for 30 minutes and then calcined at 500°C for 6 h to obtain the Bi₂WO₆ (BTC) materials. The fuel to oxidizer ratio (F/O) was calculated by using the method described by Jain et al. [2]. The F/O ratio was varied between 0.5-2.0 in order to study the effect of fuel content on the physicochemical characteristics of the Bi₂WO₆ complex oxides. The Bi₂WO₆ materials prepared using different fuels are referred to as BTC-F in the subsequent text where F is the fuel employed (Urea-U, Glycine-G, hexamethylenetetramine-H and malonic acid dihydrazide-M) for synthesis.

Synthesis of Bi₂WO₆ by amorphous citrate method (BTA): The Bi₂WO₆ (BTA) nanoparticles were also synthesized by amorphous citrate method. In a typical procedure, 0.545 g ammonium tungstate, 0.549 g bismuth carbonate and equimolar quantity (with respect to total metal ions) of citric acid (0.262 g) were dissolved in minimum amount of water to make a thick paste. The paste was then heated in an oil bath at 60°C to obtain a transparent gel. The gel was evacuated at the same temperature until it formed an expanded spongy solid material. This material was immediately transferred to a hot air oven preheated at 160 °C. The temperature of the oven was maintained at 160 °C for 2 h which yielded the amorphous citrate precursor. The amorphous precursor was then grinded and calcined at 500 °C for 6 h to obtain the Bi₂WO₆ (BTA) materials.

2.1.2 Synthesis of Bi₂W₂O₉ (BWO)

The Bi₂W₂O₉ was synthesized by solution combustion method taking ammonium tungstate, bismuth nitrate as precursor salts and urea as fuel. The fuel to oxidizer ratio was maintained at 1 [2]. In a typical synthesis, 1.04 g Bi(NO₃)₃.5H₂O, 0.53 g (NH₄)₁₀W₁₂O₄₁ and 0.069 g of urea were mixed well and made a paste by dropwise addition of distilled water. The mixture was transferred to a furnace pre-heated at 400 °C. The mixture instantaneously got ignited producing lot of gaseous product and a foamy solid. The combustion mixture was maintained at 400 °C for 30 minutes which was subsequently cooled, grinded to fine powder and calcined at 800 °C for 6 h to obtain the Bi₂W₂O₉ (BWO) material.

2.1.3. Synthesis of BiFeO₃ (BFO)

The BiFeO₃ was synthesized by a facile solution combustion method by using iron nitrate and bismuth nitrate as salt precursor and urea as fuel at F/O ratio of 1. Similar procedure as described in section 2.1.2 was used for the BiFeO₃ (BFO) synthesis. In brief, 1.55 g iron nitrate, 1.291 g bismuth nitrate and 0.383 g of urea were dissolved in minimum amount of distilled water to make a thick paste. It was then transferred to a preheated furnace maintained at 400 °C. After maintaining 30 minutes at that temperature, the combustion mixture was cooled, grinded and calcined at 500 °C for 2 h to get the BFO material.

2.1.4 Preparation of CuS/Bi₂WO₆ (CuSBTA), CuS/Bi₂W₂O₉ (CuSBWO) and CuS/BiFeO₃ (CuSBFO) heterojunction materials

The Bi based complex oxide nanomaterials described in section 2.1.1 through 2.1.3 were subsequently modified with CuS to prepare novel heterojunction systems using a hydrothermal route. The hydrothermal method is a promising route for morphology controlled synthesis of nanomaterials. The morphology, size and hierarchical organization of nanoparticles can be achieved in hydrothermal method by controlling the reaction parameters such as solvent, pH and temperature. In a typical synthesis, required amount of copper nitrate and 2.5 molar excess of thiourea were dissolved in 50 ml distilled water. To the salt solution, 1 g of as synthesized Bi based complex oxide nanomaterial (BiFeO₃, Bi₂WO₆ (BTA), Bi₂W₂O₉) was added and stirred for 30 minutes followed by 30 minutes of sonication. The aqueous suspension was then sealed in a 100 ml Teflon lined autoclave. The hydrothermal treatment was performed under autogeneous pressure at 150 °C for 24 h. After the hydrothermal treatment, the solid residue was collected and washed with water and ethanol. The resulting material was dried in a hot air oven at 60 °C for 12 h to obtain the heterojunction nanomaterials. The CuS content was varied in the range of 2-20 wt% in the heterojunction system. The heterojunction materials are referred to as CuSyBFO, CuSyBTA, CuSyBWO in the subsequent chapters where y refers to the wt% of CuS. Pure CuS material was also prepared using hydrothermal synthetic route under similar experimental conditions.

2.1.5 Synthesis of CdS/Bi₂W₂O₉ (CdSBWO)

The Bi₂W₂O₉ was also modified with CdS nanomaterials to prepare CdS/ Bi₂W₂O₉ heterojunction system using hydrothermal method. For hydrothermal synthesis, Cd(NO₃)₂.4H₂O was taken as salt precursor and thiourea as sulphur source. In a typical synthesis, required amount of cadmium nitrate and thiourea (2.5 molar excess) were dissolved in 50 ml H₂O, to which 1 g of BWO powder was added and stirred for 30 min. The aqueous suspension was then transfer to a Teflon lined autoclave of 100 ml capacity. The hydrothermal treatment was carried at 150 °C for 12 h under autogeneous pressure. After completion of reaction, the reaction mixture was allowed to cool and the solid materials were collected by centrifugation, washed each with water and ethanol. The solid residue was dried at 110°C for 12 h to get the CdSBWO material. Using this procedure, CdS/Bi₂W₂O₉ materials containing 5, 10 and 20 wt% of CdS were prepared. The CdS/Bi₂W₂O₉ heterojunction materials are referred as CdSyBWO in the subsequent text, where 'y' represents the wt% of CdS present in the heterojunction.

2.1.6 Synthesis of α-Fe₂O₃-Bi₂S₃ Heterojunction Materials

The combustion synthesis method was employed for preparation of α-Fe₂O₃-Bi₂S₃ heterojunction material. In a typical procedure, a mixture of iron nitrate, bismuth nitrate and thiourea of required stoichiometry was taken and a thick paste was made by drop wise

addition of water. The paste was then kept in a furnace whose temperature was previously adjusted to 400 °C. The F/O ratio was fixed at 1 during the synthesis [2]. The combustion mixture was kept for 30 minutes at 400 °C to ensure complete combustion reaction. During combustion synthesis, the thiourea acted as a fuel as well as sulphur source. Using this procedure, α -Fe₂O₃-Bi₂S₃ heterojunctions containing 25, 37 and 50 mol% of α -Fe₂O₃ were synthesized.

2.2 Characterization of the Photocatalyst Materials

2.2.1 Powder X-Ray Diffraction (XRD)

The powder XRD patterns of all the synthesized materials were recorded using a Rigaku, Ultima-IV multipurpose X-ray diffraction system using Ni filtered CuK α ($\lambda = 1.5418\text{\AA}$) radiation. The XRD measurements were carried out in the 2θ range of 20–70° with a scan speed of 2 degrees per minute using Bragg-Brantano configuration.

2.2.2 UV-Vis-DRS Spectroscopy

The UV-Vis diffuse reflectance spectra of the photocatalytic materials were recorded using a Jasco V-650 spectrophotometer fitted with a BaSO₄ coated integration sphere. The diffuse reflectance spectra were recorded in the wavelength range of 200–900 nm. Initially, 100-200 mg of the powder sample was taken and made into self-supporting pellets of 12 mm diameter and 2 mm in thickness using a hydraulic press. The pellet was mounted on the integration sphere by a sample holder. The pellet can be regarded as infinitely thick as required by the Kubelka-Munk theory [3]. The selected recording parameters comprised of spectral bandwidth of 4 nm and data point distance of 1 nm. For all the spectra, PTFE was used as the reference. The spectra were recorded at ambient condition in air.

2.2.3 Fourier Transform Infra-Red Spectroscopy (FTIR)

The FTIR spectra of the photocatalyst materials (as KBr pellets) were obtained in transmittance mode by using Perkin-Elmer infrared spectrometer with a resolution of 4 cm⁻¹. Nearly, 2-3 mg of the sample was mixed thoroughly with 30 mg of oven dried IR grade KBr and made into a pellet using the hydraulic press. The pellets were stored in vacuum desiccator and exposed to IR lamp for 1 minute prior to the FTIR measurement. The FTIR spectra were recorded in the spectral range of 400 cm⁻¹ to 4000 cm⁻¹.

2.2.4 Photoluminescence Study (PL)

The photoluminescence spectra of the powder photocatalyst materials were recorded in the wavelength range of 330–800 nm using a Horiba Scientific Fluoromax-4 spectrofluorometer with different excitation wavelengths for different photocatalytic systems.

2.2.5 Sorptometric Studies

The specific surface area of the photocatalyst materials were determined by BET method using N₂ adsorption/desorption at 77K using an AUTOSORB 1 Quantachome instrument. The photocatalyst materials were degassed in the temperature range of 120-160°C for 6 h prior to the surface area measurements.

2.2.6 X-Ray Photo Electron Spectroscopy

The X-ray photoelectron spectra of the heterojunction photocatalysts were recorded using SPECS make (Germany) spectrophotometer with 150 mm hemispherical analyzer at band pass energy of 12 eV. Monochromatic Al K α radiation of 1486.74 eV was used as X-ray source. Binding energy corrections due to electrostatic charging were made relative to the C1s peak as 284.6 eV.

2.2.7 High Resolution Transmission Electron Microscopy (HRTEM)

The HRTEM images of the photocatalyst samples were obtained using TECNAI 300 kV equipment. Sample for HRTEM study was prepared by dispersing the powder sample in ethanol by sonication for 1 h and then drop drying on a carbon coated copper grid (300 mesh size).

2.2.8 Field Emission Scanning Electron Microscopy (FESEM)

The FESEM images of the photocatalyst materials were recorded using Nova Nano SEM/FEI microscope. Prior to FESEM analysis, the powder samples were mounted on a carbon tape followed by gold sputtering for three minutes.

2.2.9 Total Organic Carbon Analysis (TOC)

The total organic carbon content at different time intervals during photocatalytic degradation experiments was measured using a TOC analyzer (Analytik Jena/multi N/C 3100).

2.2.10 Transient Photocurrent Measurement

The photoconductivity measurement for the pure materials as well as the heterojunction systems was carried out in a two electrode system using a Keithley 2400 sourcemeter integrated with AM 1.5G filter fitted solar simulator without any bias voltage. The photoelectrodes were prepared by depositing the slurry of photocatalyst material over the ITO substrate. In a typical procedure, 100 mg of the photocatalyst material was dispersed in 1.5 ml of dimethylformamide (DMF) solvent by mechanical sonication for 2 h. Then the prepared dispersion was deposited over the ITO substrate by spin coating (3000 rpm for 30 sec). The prepared films were dried at 100 °C for removal of the residual solvents. The top electrodes were then fabricated by depositing silver dots (diameter ~1 mm) over the film and

baked in an oven at 100 °C for 4 h. Before depositing the sample each corner of the ITO substrate were masked using a kapton tape.

2.2.11 Nuclear Magnetic Resonance (NMR) Spectroscopy

The ^1H and ^{13}C NMR spectra of isolated pure reaction products were recorded using a Bruker 400 MHz NMR spectrometer using TMS as internal standard.

2.3 Photocatalytic Activity Studies

2.3.1 Photocatalytic Degradation of Congo red Dye (CR)

The photocatalytic activity of CuSBTA heterojunction materials was evaluated for the degradation of Congo red dye (CR) under visible light irradiation in aqueous media. In a typical experiment, 25 mg of the catalyst was dispersed in 100 mL of 10^{-4} M dye solution by sonication for 10 min under dark condition. To obtain adsorption desorption equilibrium, the dye solution containing the dispersed catalyst particles was stirred for 1 h in dark. The initial concentration (C_0) of the dye was obtained by analysing the supernatant after the adsorption desorption equilibrium was attained and just before the irradiation of light. The same procedure is followed to determine C_0 for all other photocatalytic experiments reported in this thesis. The aqueous dispersion was subsequently irradiated using a 250 W Hg vapour lamp equipped with a UV-cut off filter ($\lambda > 420$ nm). As soon as the dye solution was exposed to visible light, 30% aqueous H_2O_2 solution containing 6×10^{-4} M of H_2O_2 was added to it and stirred continuously at a speed of at 500 rpm. A 3 ml quantity of the reaction mixture was collected at regular interval of time and centrifuged at 6000 rpm for 2 minutes to remove the catalyst particles. The collected supernatant solution was analyzed for CR concentration by using UV-visible spectrometer.

2.3.2 Photocatalytic Degradation of Diuron Pesticide (DU)

The photocatalytic degradation of diuron (DU) was performed under visible light irradiation ($\lambda > 400$ nm) using CuSBWO heterojunction materials as photocatalyst. In a typical experiment, 75 mg of CuSBWO catalyst was dispersed in 100 ml of 10 ppm diuron solution and stirred for 30 minutes in dark to attend adsorption desorption equilibrium. The photocatalytic degradation was performed in an immersion well quartz photoreactor (150 ml capacity) using a 150 Watt Xe lamp. Immediately after exposure, 200 μl of H_2O_2 (30 % w/v) was added and stirred continuously at 500 rpm. At regular time interval, 3 ml of reaction mixture was taken out and analyzed using UV-HPLC [Agilent semi preparative HPLC, G1322A, C-18 column] as per the reported procedure [4]. The HPLC analysis was performed using methanol and water as mobile phase in the ratio of 7:3 (v/v). The flow rate was maintained at 1 ml/min. The diuron was detected at a wavelength of 250 nm. The concentration of the released chloride ion during the photocatalytic study was estimated using ion selective electrode (Orion, Thermo scientific). The intermediate products formed during the DU degradation were identified by GC-MS analysis [Agilent GC-MS, Model 7890B/5977A, DB-5MS capillary column, FID detector]. The oven temperature was initially

kept at 50 °C for 5 minutes, and then increased linearly at 5 °C/minutes upto 250 °C, where it was maintained for 10 minutes. The injector and detector temperatures were 270 °C and 280 °C, respectively. The total organic carbon content at different time interval was also analyzed using a TOC analyzer.

2.3.3 Degradation of Alachlor Pesticide (AL)

The photocatalytic degradation of alachlor (AL) was performed under visible light irradiation ($\lambda > 400$ nm) using the CuSBFO heterojunction material as photocatalyst. In a typical photocatalytic experiment, 25 mg of CuSBFO catalyst was dispersed in 100 ml of 5 ppm AL solution and stirred for 30 minutes in dark in order to establish the adsorption desorption equilibrium. The photocatalytic degradation of AL was performed in an immersion well quartz photo reactor (200 ml capacity) using a 150 Watt Xe lamp. Immediately after exposure to the light, 10 μ l of H₂O₂ (30 % w/v) was added and stirred continuously at 500 rpm. At regular interval of time, 3 ml of the reaction mixture was taken out and the catalyst particles were removed by centrifugation. The degradation process was monitored by analyzing the supernatant in UV-HPLC [Agilent semi preparative HPLC, G1322A, C-18 column] as per the reported procedure [5]. HPLC grade acetonitrile and water was used as mobile phase in a volume ratio of 7:3 and the flow rate was maintained at 1 ml/min. The possible intermediates formed at different time of degradation reaction were identified by GC-MS analysis [Agilent GC-MS, Model 7890B/5977A with DB-5MS capillary column with dimension 30 m \times 320 μ m \times 0.25 μ m using FID detector]. The GC oven temperature was initially kept at 60 °C for 1 min, which was raised linearly at a rate of 8 °C min⁻¹ upto 180 °C and then at 5 °C min⁻¹ to 250 °C where it was hold for 20 minutes. The injector and detector temperature was maintained at 270 °C and 280 °C, respectively. The total organic carbon content at different time interval was also analyzed using a TOC analyzer.

2.3.4 Chemoselective Aerobic Oxidation of Thiols to Disulfides

The catalytic activity of the BTC nanoparticles was evaluated for the photocatalytic selective oxidation of thiophenols to disulfides under visible light irradiation using molecular oxygen from air as oxidant. In a typical catalytic test, 2 mmol of thiophenol dispersed in 05 ml of water was taken in a two neck round bottom flask fitted with a condenser. 50 mg of BTC catalyst was added to the reaction mixture and stirred for 15 minutes under dark condition. Zero air from a compressed cylinder was passed through the reaction mixture at a flow rate of 20 ml/minute. The reaction mixture was subsequently irradiated with a 125 W mercury vapor lamp with $\lambda > 400$ nm under continuous stirring at 500 rpm. The stirring speed was varied in the range of 500-800 rpm, to examine whether the process is diffusion limited. No change in yield is noticed with stirring speed suggesting that the photocatalytic test is not diffusion limited. Small amount of reaction mixture was periodically collected and the progress of the reaction was monitored by TLC. The percentage conversion at different interval of time was analyzed using a Nucon gas chromatograph using an EC-Wax capillary column and FID detector. The GC oven temperature was initially kept at 50 °C for 2 min and then increased linearly at 5 °C min⁻¹ to 200 °C where it was hold for 20 min. The injector and

detector temperatures were kept at 280 °C and 250 °C, respectively. After completion of the reaction, 05 mL of chloroform was added to the reaction mixture and shaken well. The catalyst particles were filtered and the diphenyl disulfide was recovered from the chloroform solution and recrystallized to afford colorless crystals of the pure product. The diphenyl disulfide was identified by comparing its physical and spectral characteristics with the literature reported values [6-11]. The catalyst particles were washed three times with 10 mL portions of ethanol and dried at 80 °C for 12 h to regenerate the catalyst.

2.3.5 Selective Oxidation of Amines to Imines

The photocatalytic activity of the CdSBWO heterojunction materials was evaluated for selective aerobic oxidation of amines to imines under visible light irradiation. In a typical experiment, 1 mmol of benzylamine in 5 ml of acetonitrile was taken in a round bottom flask, to which 25 mg of CdSBWO catalyst was added and stirred for 15 min under dark condition. The reaction mixture was then exposed to a 125 W high pressure mercury vapor lamp with $\lambda > 400$ nm and stirred at 500 rpm. The stirring speed was varied in the range of 500-800 rpm, to examine whether the process is diffusion limited. No change in yield is noticed with stirring speed suggesting that the photocatalytic test is not diffusion limited. The percentage conversion at different interval of time was analyzed using gas chromatography fitted with an EC-Wax capillary column (30 m \times 0.25 mm and FID detector). The GC oven was operated in a programmable mode where the initial temperature was fixed at 60 °C for 3 min and then increased linearly to 160 °C at a heating rate of 5 °C min⁻¹. The injector and detector temperatures were maintained at 200 °C and 180 °C, respectively. After the completion of the reaction, catalyst particles were separated with a membrane filter and the N-benzylidenebenzylamine was recovered from reaction mixture and purified using column chromatography. All the molecules synthesized in this work are known compounds and are identified by comparing their physical and spectral characteristics with the literature reported values [12-16].

2.3.6 Photocatalytic Hydrogenation of Nitroarenes

The photocatalytic hydrogen transfer reduction of nitroarenes was studied under visible light irradiation using α -Fe₂O₃-Bi₂S₃ heterojunction materials as catalyst. Hydrazine hydrate was used as hydrogen source. In a typical experiment, a mixture containing 50 mg of the catalyst, 2 mmol of nitro aromatic compound and 8 mmol of hydrazine hydrate was taken in a 10 ml round bottom flask fitted with a condenser and stirred for 30 min in dark to get adsorption-desorption equilibrium. A 250 W Hg vapour lamp equipped with a UV-cut off filter ($\lambda > 400$ nm) was used as a light source and stirred continuously at 500 rpm. The stirring speed was varied in the range of 500-800 rpm, to examine whether the process is diffusion limited. No change in yield is noticed with stirring speed suggesting that the photocatalytic test is not diffusion limited. The progress of the reaction was monitored using thin layer chromatography (TLC). After completion of reaction, the product was separated and purified using a chemical work up procedure. The pure products were identified using ¹H and ¹³C NMR spectroscopy. The percentage reduction of the nitroarenes was estimated at regular

interval of time by gas chromatography (GC) using a HP-5 capillary column and a FID detector employing N₂ as carrier gas. The GC oven temperature was initially maintained at 60°C for 5 min and then heated linearly at 10 °C min⁻¹ up to 160 °C where it was held for 10 min. The injector and detector temperatures were kept at 210 °C and 200 °C, respectively. All the aromatic amines obtained in this work, are known compounds and were identified by comparing their physical and spectra characteristics with literature reports [17-20].

References

- [1] K. C. Patil, M. S. Hegde, T. Rattan and S. T. Aruna, Chemistry of nanocrystalline oxide materials: Combustion synthesis, properties and applications. *World Scientific Publishing Co. Pte. Ltd, London*, 2008.
- [2] S. R. Jain, K. C. Adiga and V. R. Verneker, *Combustion and Flame*, 1981, 40, 71-79.
- [3] B. M. Weckhuysen and R. A. Schoonheydt, *Catalysis Today*, 1999, 49, 441-451.
- [4] K. Macounova, H. Krysova, J. Ludvik and J. Jirkovsky, *Journal of Photochemistry and Photobiology A: Chemistry*, 2003, 156, 273-282.
- [5] D. Zheng, Y. Xin, D. Ma, X. Wang, J. Wu and M. Gao, *Catalysis Science & Technology*, 2016, 6, 1892-1902.
- [6] M. Hajjami, F. Sharifirad and F. Gholamian, *Applied Organometallic Chemistry*, 2017, 31, e3844.
- [7] C. Bottecchia, N. Erdmann, P. M. A. Tijssen, L.-G. Milroy, L. Brunsveld, V. Hessel and T. Noel, *ChemSusChem*, 2016, 9, 1781-1785.
- [8] Y. He, D. Hang and M. Lu, *Phosphorus, Sulfur, and Silicon and the Related Elements*, 2012, 187, 1118-1124.
- [9] P. Natarajan, H. Sharma, M. Kaur, P. Sharma, *Tetrahedron Letters*, 2015, 56, 5578-5582.
- [10] S. J. Singh, N. S. Devi, *Tetrahedron Letters*, 2016, 57, 5941-5943.
- [11] L. Bettanin, S. Saba, F. Z. Galetto, G. A. Mike, J. Rafique and A. L. Braga, *Tetrahedron Letters*, 2017, 58, 4713-4716.
- [12] B. Chen, S. Shang, L. Wang, Y. Zhang and S. Gao, *Chemical Communication*, 2016, 52, 481-484.
- [13] Y. Zhi, K. Li, H. Xia, M. Xue, Y. Mua and X. Liu, *Journal of Materials Chemistry A*, 2017, 5, 8697-8704.
- [14] T. B. Nguyen, L. Ermolenko and A. Al-Mourabit, *Green Chemistry*, 2013, 15, 2713-2717.
- [15] X. Qiu, C. Len, R. Luque and Y Li, *ChemSusChem*, 2014, 7, 1684-1688.
- [16] Y. Zhang, F. Lu, R. Huang, H. Zhang and J. Zhao, *Catalysis Communications*, 2016, 81, 10-13.
- [17] F. Raza, J. H. Park, H. -R. Lee, H. I. Kim, S. J. Jeon, and J. -H. Kim, *ACS Catalysis*, 2016, 6, 2754-2759.
- [18] J. Ye, K. Ni, J. Liu, G. Chen, M. Ikram and Y. Zhu, *ChemCatChem*, 2018, 10, 259-265.
- [19] L. Liu, S. Zhang, X. Fu and C. H. Yan, *Chemical Communications*, 2011, 47, 10148-10150.
- [20] A. E. Wendlandt and S. S. Stahl, *Organic Letters*, 2012, 14, 2850-2853.

CHAPTER 3

Visible Light Driven Photocatalytic Study of Bi_2WO_6 Based Materials

Section A

Chemoselective Thiol Oxidation Catalysed by Combustion Synthesized Bi_2WO_6 Material

3.1 Introduction

Chemoselective oxidation of organic compounds to generate specialty and value added chemicals is an important field of research with potential application in pharmaceutical and related fine chemical industries [1, 2]. Among selective oxidative transformations, the oxidative coupling of thiols to disulfide has attracted a great deal of attention in recent years because of the potential application of disulfides as anti-oxidants, pharmaceuticals, pesticides, and rubber vulcanization reagents [3, 4]. The “Merox process” involving the oxidation of thiols to disulfides using NaOH is a widely used process for removal of thiols in petroleum refinery industries. However, the Merox process generates significant quantity of caustic waste as byproduct leading to environmental and disposal problem [4]. During the oxidation of thiols often formation of over-oxidized products such as thiosulfates, thiosulfonates, and sulfonic acids has been observed due to high reactivity of S-S bonds [3, 4]. Hence, there are many efforts to develop novel catalytic protocols for selective oxidation of thiols to disulfides. Particularly, notable are the methods which involve aerobic oxidation route using atmospheric oxygen as oxidant because of the sustainability of the process. Several catalytic methods have been developed in recent past towards aerobic oxidation of thiols which include VOCl_3 , molecular I_2 , Br_2/SiO_2 , 2,6-Dicarboxypyridinium chlorochromate, $\text{Al}_2\text{O}_3/\text{KF}$, PhSeZnCl , Mn(III) Schiff bases [5-10]. However, most of the catalytic methods reported so far utilize homogeneous catalytic conditions and supported reagents which suffer from drawbacks such as stoichiometric amounts of catalysts, long reaction times, high cost, and formation of toxic byproducts as well as tedious workup steps. Hence, there is a need to develop heterogeneous catalytic method which is less expensive, environmentally benign, selective and uses oxygen as oxidant. Recently, Noel et al have developed a photocatalytic method for synthesis of disulfides from thiols by aerobic oxidation route using the Eosin Y as a visible light active photocatalyst under homogeneous conditions [3]. The Eosin Y is found to be highly active and selective for the reaction and

show better activity compared to ruthenium and iridium based organometallic complexes. T. M. McCormick et al. has used tellurorhodamine chromophore as visible light active photocatalyst for selective oxidation of thiols with excellent selectivity within a short span of reaction time [11]. The heterogeneous photocatalytic protocol developed for oxidation of thiols includes NiFe_2O_4 nanoparticles [12], iron phthalocyanine immobilized on graphene oxide [13] and $\text{TiO}_2/\text{MoS}_2$ [14]. Although these methods provided good yield and selectivity to disulfide, the oxidation process using nickel ferrite require hydrogen peroxide as oxidant whereas the iron phthalocyanine are highly costly. With an intention to develop novel and economic photocatalytic protocol for selective aerobic oxidation of thiol to disulfide under visible light irradiation, in this study, we have used solution combustion synthesized Bi_2WO_6 nanoparticles as a visible light active photocatalyst. It has been observed that, the Bi_2WO_6 possesses mild oxidizing power and does not generate the nonselective hydroxyl radical under visible light illumination [15, 16]. This property of Bi_2WO_6 has been exploited recently for efficient and selective oxidation of glycerol to dihydroxyacetone and benzylalcohol to benzaldehyde [15-17]. In this study, Bi_2WO_6 nanoparticles with different morphologies and sizes are synthesized using a facile combustion route and successfully used for the aerobic oxidation of thiols to disulfides in aqueous media.

3.2 Results and Discussion

3.2.1 Structural Properties Study

The X-ray diffraction patterns of the Bi_2WO_6 nanomaterials prepared using different fuels namely hexamethylenetetramine (HMTA), malonic acid dihydrazide (MDH), urea (U) and glycine (G) at F/O ratio of 1 are presented in Fig. 3.1. The BTC-G material exhibits well-defined and intense diffraction peaks with d values of 3.14, 2.62, 1.92, 1.64 and 1.57 Å (Fig. 3.1 a). These peaks correspond to the orthorhombic phase of Russellite Bi_2WO_6 with reflection from (131), (002), (202), (133) and (262) planes, respectively (JCPDS 79-2381). For BTC-U material, in addition to the characteristic reflections of orthorhombic Russellite Bi_2WO_6 phase, a less intense peak is observed at 2θ value of 30.3° corresponding to reflection from (008) plane of $\text{Bi}_2\text{W}_2\text{O}_9$ (Fig. 3.1b). The BTC-U material contains a mixed phase system with Bi_2WO_6 as major and $\text{Bi}_2\text{W}_2\text{O}_9$ as minor phase. When MDH and HMTA are used as fuel, in addition to the characteristic reflection from the Bi_2WO_6 phase, less intense but distinct XRD peaks are observed at 2θ value of 27.6, 31.9, 45.9, 54.3, 56.9 and 58.7 degrees (Fig. 3.1 c & d). These peaks correspond to the presence of a minor amount tetragonal $\text{Bi}_{14}\text{W}_2\text{O}_{27}$ phase (JCPDS-39-0061). The XRD study clearly indicates that the nature of the fuel in the combustion mixture is very crucial for the generation of phase pure Bi_2WO_6 material. The phase pure BTC material observed in case of glycine can be ascribed to the effective complexation capability of glycine molecule with the constituent ions [18, 19]. In order to study the effect of F/O ratio on the crystallographic phase formed, the BTC material has been prepared at different F/O ratio using glycine as fuel (Fig. 3.2).

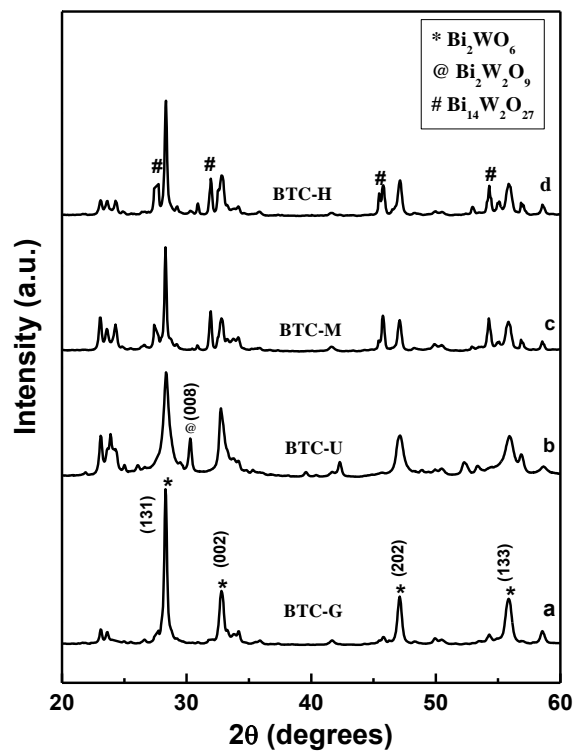


Figure 3.1: X-Ray diffraction patterns of (a) BTC-G, (b) BTC-U, (c) BTC-M and (d) BTC-H materials.

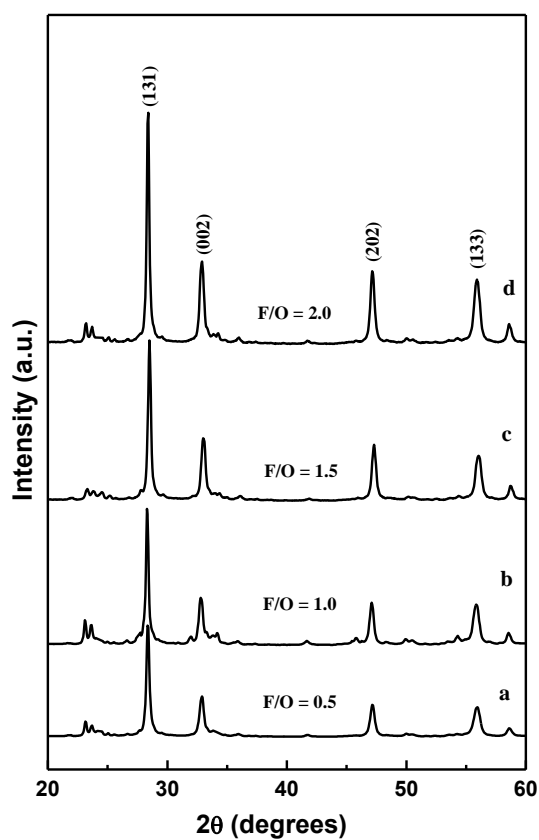


Figure 3.2: XRD patterns of Bi_2WO_6 nanoparticles synthesized using glycine as fuel at different F/O ratio (a) F/O= 0.5, (b) F/O= 1.0, (c) F/O= 1.5 and (d) F/O= 2.0.

No separate crystalline phase corresponding to either $\text{Bi}_2\text{W}_2\text{O}_9$ or $\text{Bi}_{14}\text{W}_2\text{O}_{27}$ could be detected in the XRD study. However, the XRD peak intensity increases with glycine content in the combustion mixture possibly due to increase in exothermicity of the combustion reaction leading to well crystalline materials [18]. The microstructural characteristics of the combustion synthesized BTC materials are evaluated from the Fourier line shape analysis of the XRD patterns following the Warren and Averbach method [20] using software BRAEDTH [21]. The calculated volume-weighted distributions (PV), and size coefficient (As) as function of Fourier length (L) for different BTC samples are presented in Fig. 3.3I and 3.3II, respectively. The BTC-U material exhibits a narrow distribution function (PV) in the range of 3-12 nm whereas the distribution is quite broad for the BTC-M material (Fig. 3.3I). The wide distribution function observed for the BTC-M material indicates that the material is polycrystalline in nature, contain larger grains and the distribution of the grain size is inhomogeneous.

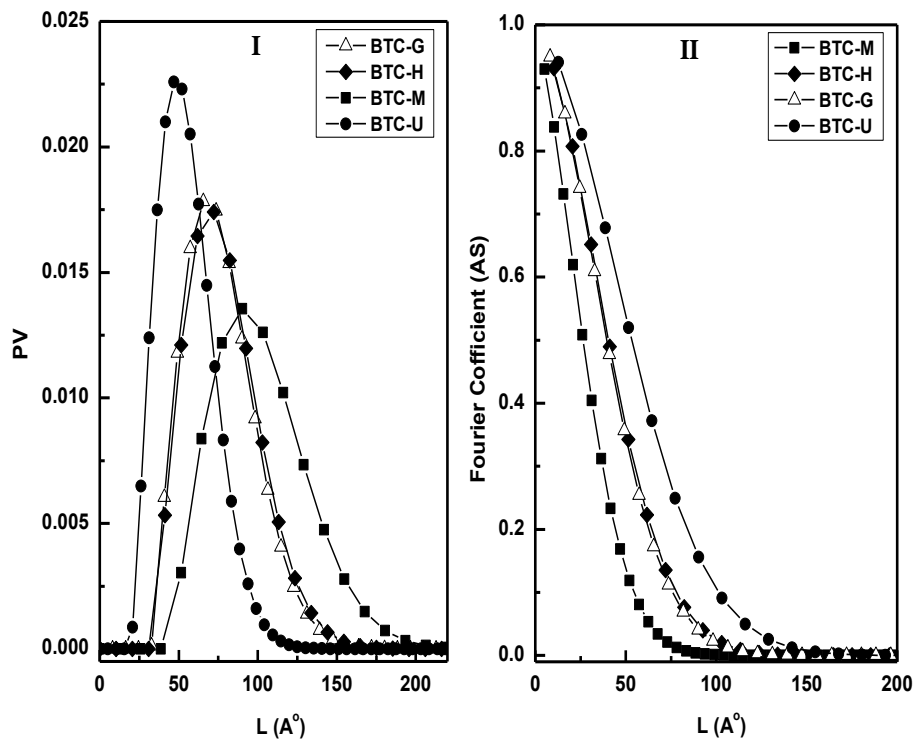


Figure 3.3: Fourier line profile analysis plots for Bi_2WO_6 nanomaterials.

The BTC-G and BTC-H materials exhibit comparable spread in distribution function (Fig. 3.3I). The volume weighted domain size calculated from the Fourier plots are presented in Table 3.1. All BWO materials contain nanoparticles with average size less than 12 nm. The crystallite size increases in the order $\text{BTC-U} < \text{BTC-G} \approx \text{BTC-H} < \text{BTC-M}$. The root mean square lattice strain calculated from the Fourier analysis for different BTC materials is presented in Table 3.1. An inverse correlation is observed between the crystallite size and the root-mean-square strain.

3.2.2 Optical Properties Study

The optical properties of the combustion synthesized BTC materials have been studied using UV-Vis-diffuse reflectance and Photoluminescence spectroscopy. Bi_2WO_6 is a semiconducting complex oxide which exhibit typical absorption edge around 450 nm with a band gap value of 2.7 eV [15, 22]. The UV-Vis-DRS spectra of the combustion synthesized BTC materials are presented in Fig. 3.4I.

Table 3.1: Physicochemical characteristics and photocatalytic activity of the combustion synthesized Bi_2WO_6 nanoparticles.

Catalyst	Band gap (eV)	Surface area (m^2/g)	Crystallite size ^a (nm)	Strain (e^2) ^{1/2}	Conversion ^a (%)	Selectivity (%)	Yield ^c (%)
BTC-G	2.86	24	7.5 ± 0.5	3.67×10^{-3}	86.0	100	83.5
BTC -H	2.82	22	9.0 ± 0.6	3.79×10^{-3}	76.2	100	73.7
BTC -M	2.70	20	11.5 ± 1.5	3.25×10^{-3}	68.4	100	64.2
BTC -U	2.90	26	5.8 ± 1.2	4.67×10^{-3}	73.0	100	68.8

a. Calculated from the Fourier line profile analysis of the XRD peaks

b. Calculated from the analysis of the reaction mixture using Gas chromatograph after 6 h of reaction time.

c. Refers to pure and isolated yield after 6 h of reaction time in aqueous media

All combustion synthesized BTC samples show strong photoabsorption properties in UV region which extend upto the visible light region. The absorption edge is in the range of 440-500 nm, which depend on the fuel used in the combustion synthesis. In case of BTC-U and BTC-G material, the absorption edges commence near 450 nm whereas for BTC-H and BTC-M materials the absorption edge is red shifted and occurs between 480-500 nm. The BTC materials show significant absorption in the visible region indicating their suitability for application as visible light active photocatalyst. The intense absorption bands with a stiff edge in the visible light region indicate that the optical absorption is due to the band gap transition rather than the transition from impurity levels [18, 23]. For Bi_2WO_6 material, the valance band is formed by hybridization of Bi 6s and O 2p orbitals whereas the conduction band is W 5d in nature [24]. The blue shift in absorption edge observed for BTC-G and BTC-U material can be ascribed to the quantum confinement effect due to the presence of ultrafine nanoparticles in these samples (Table 3.1). The band gap of the BTC materials calculated from intercept of the plot of photon energy ($h\nu$) vs $[F(R)h\nu]^2$ (Fig. 3.4II) are presented in Table 3.1. The band gap value of 2.70 eV observed for BTC-M material is typical of Bi_2WO_6 and is in agreement with earlier literature reported value [18, 23, 24]. For BTC-G, H and U materials the band gap is in the range of 2.8-2.9 eV. The higher band gap value observed for these materials is due to presence of small nanoparticles which exhibit quantum confinement effect. This is further validated from the crystallite size obtained from Fourier analysis which is in the range of 5-9 nm for these samples (Table 3.1).

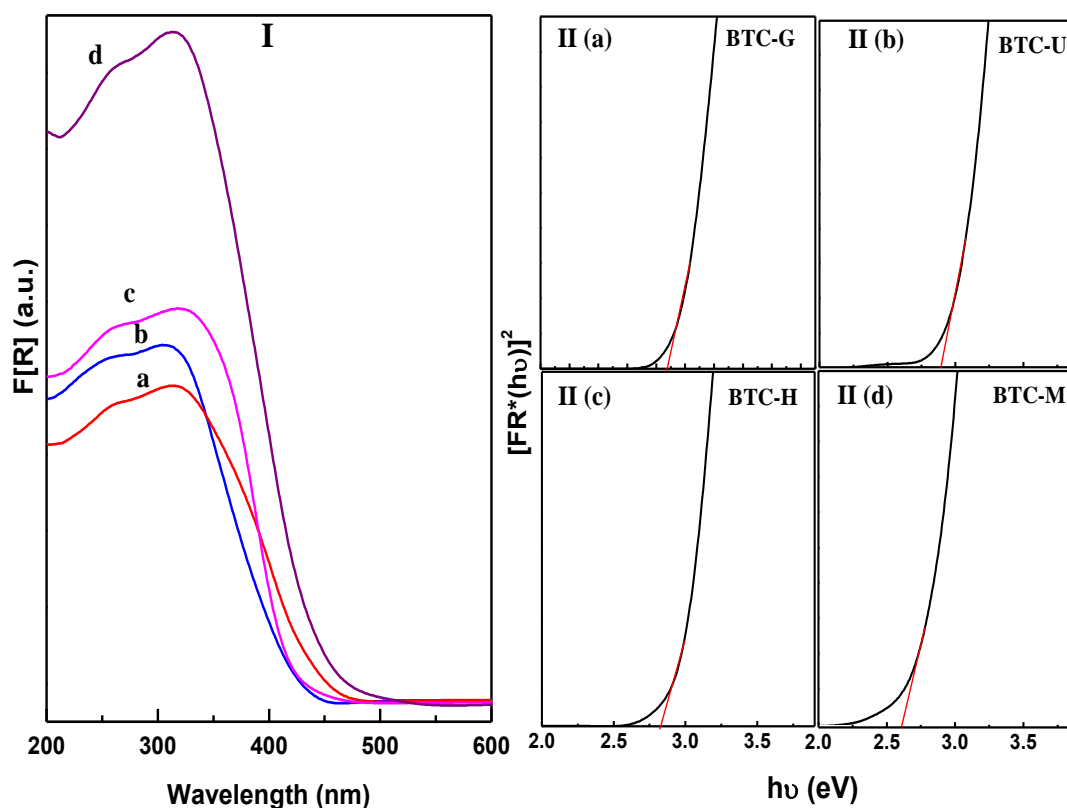


Figure 3.4: UV-Vis-DRS spectra of (a) BTC-G, (b) BTC-U, (c) BTC-H and (d) BTC-M (panel I) and plots of $[F(R)h\nu]^2$ as a function of photon energy for the BTC materials (panel II).

The PL spectra of the combustion synthesized BTC materials in the spectral region of 400-600 nm are presented in Fig. 3.5. The combustion synthesized BTC materials exhibit broad blue-green emission in the spectral region of 430-560 nm. The intense peak at 460 nm in the PL spectra can be assigned to intrinsic luminescence of Bi_2WO_6 originating from the charge transfer transition involving the valance band (hybrid orbitals of Bi 6s and O 2p) and the conductance band (W 5d) [25-27]. A weak blue emission at 435 nm is attributed to the emission due to Bi^{3+} ions from the $^3\text{P}_1$ ($6s^16p^1$) excited quantum state to the $^1\text{S}_0$ ($6s^2$) ground state [28]. The lower PL intensity observed for BTC-G material indicate that the electron-hole pair separation is more effective for this material compared to other materials. The green emission observed at 560 nm in the PL spectra is ascribed to the presence of metallic defect sites and the oxygen vacancies in the BTC nanocrystals generated due to the short time span of combustion reaction [25-28].

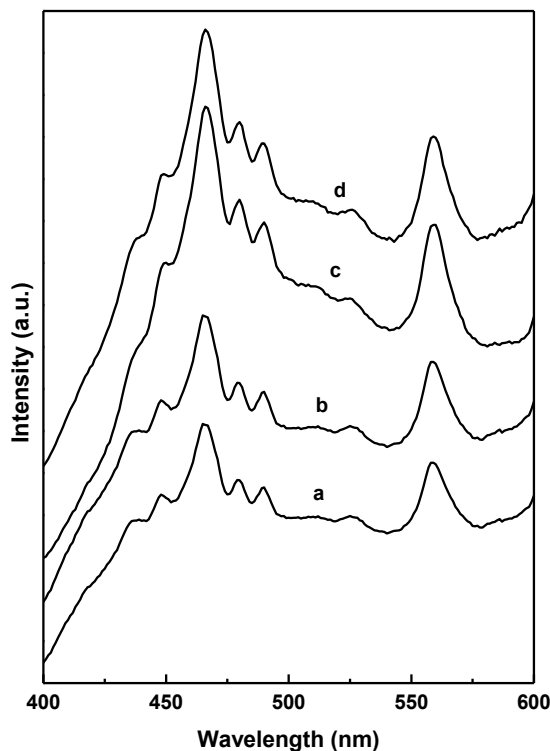


Figure 3.5: Photoluminescence spectra of (a) BTC-G, (b) BTC-H, (c) BTC-U and (d) BTC-M materials.

3.2.3 Morphological Study

The morphological features of the combustion synthesized BTC materials have been studied using field emission scanning electron microscopy. The FESEM images of different BTC materials are presented in Fig. 3.6. The BTC-G and BTC-M material contains predominantly spherical shape particles of irregular size present in an agglomerated state (Fig. 3.6 b & d). The presence of some elongated particles is also noted. Contrary to this observation, the BTC-H and BTC-U materials contain flake like or plate like particles. For BTC-G material, with increase in fuel content, the morphology gradually changes from 1D agglomerated particle to sheet shaped particles (Fig. 3. 6 d-f). The presence of polyhedral sheets with 5-7 μm width and about 100 nm thicknesses are clearly observed for BTC-G materials with F/O ratio 2, suggesting the possibility of anisotropic growth along the XY plane. The transmission electron micrograph of the BTC-G material prepared at F/O ratio of 1 is presented in Fig. 3.7. Near spherical shape particles with size in the range of 5-10 nm in an agglomerated state are observed from the TEM image (Fig. 3.7). The Fourier line shape analysis data support the TEM observation. The specific surface area of the BTC materials is found to be in the range of 18-26 m^2/g (Table 3.1).

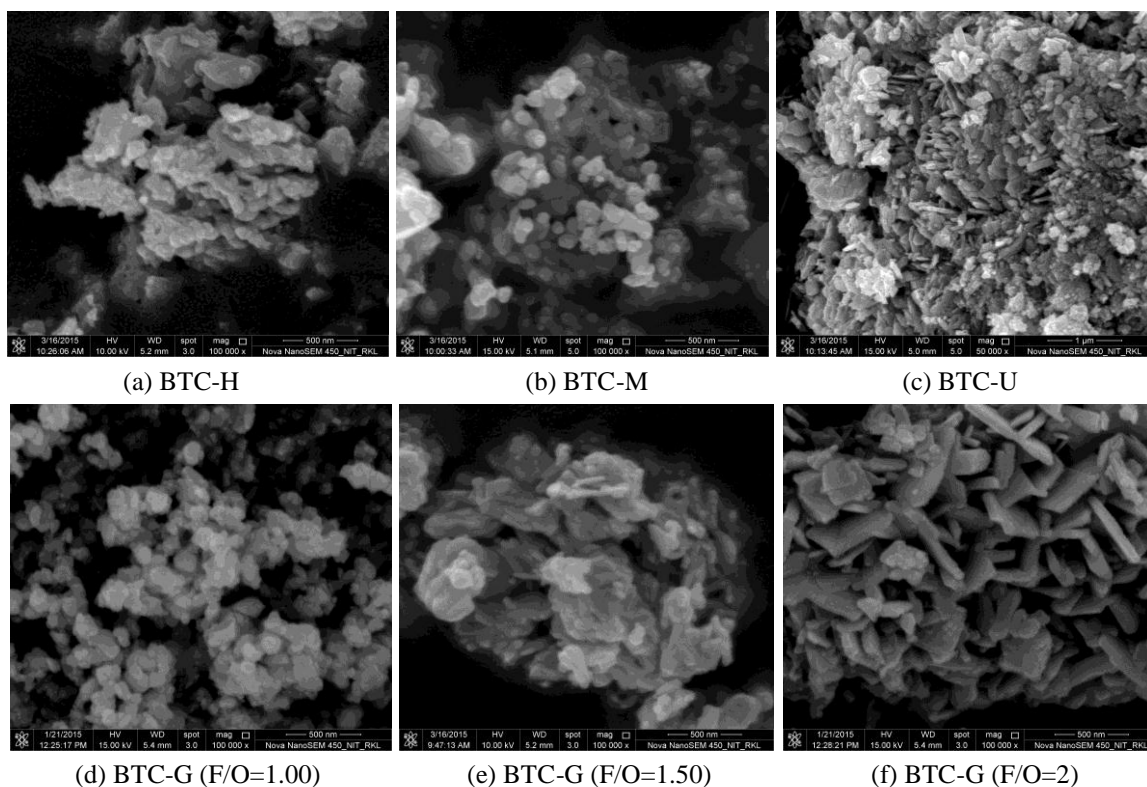


Figure 3.6: Field emission scanning electron micrographs of (a) BTC-H (b) BTC-M (c) BTC-U (d) BTC-G (F/O=1.0), (e) BTC-G (F/O=1.5), (f) BTC-G (F/O=2.0) materials.

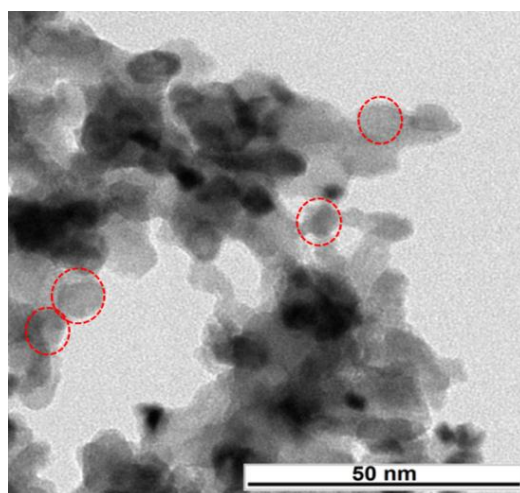
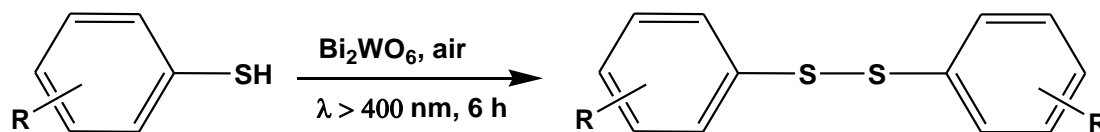


Figure 3.7: Transmission electron micrograph of $\text{Bi}_2\text{WO}_6\text{-G}$ material.

3.2.4 Photocatalytic Activity for Selective Oxidation of Thiols to Disulfides

The photocatalytic activity of the BTC nanomaterials has been evaluated for visible light driven selective oxidation of thiols to disulfide using air as oxidant. Initially, the oxidation of thiophenol is taken as a model reaction and different BTC materials are studied for their catalytic activity (Scheme 3.1). Table 1 show the percentage conversion and isolated yield of the diphenyl disulfide obtained after 6 h of irradiation time in aqueous media. The BTC materials have been found to be highly selective for diphenyl disulfides without the formation

of any over oxidized products. Among the BTC catalysts, the BTC-G material shows highest percentage conversion with maximum isolated yield of the product (Fig. 3. 8).



Scheme 3.1: Selective oxidation of thiols to disulfides catalyzed by Bi_2WO_6 nanomaterials.

The higher yield observed in case of BTC-G materials can be ascribed to the efficient separation of the e^- - h^+ pair as observed from the PL spectra and their subsequent utilization in the oxidation process. The BTC-G material has been chosen to further study the effect of various reaction parameters on photocatalytic activity. In order to establish that the reaction is truly photocatalytic in nature, different test reactions are performed under dark as well as under visible light irradiation in presence and absence of the catalyst. The reaction does not take place under dark as well as illuminated condition in absence of the catalyst. In presence of the catalyst, when the reaction is performed under dark condition the formation of product is not detected. In order to prove that the molecular oxygen from the air is the primary oxidant, the reaction is performed under nitrogen atmosphere. Only trace amount of product was detected in N_2 atmosphere (yield 5.2 %) after 6 h of reaction indicating that the molecular oxygen is the primary oxidant. In case of BTC-G material, the initial rate of diphenyl disulfide formation is quite higher than other combustion synthesized materials (Fig. 3.8)

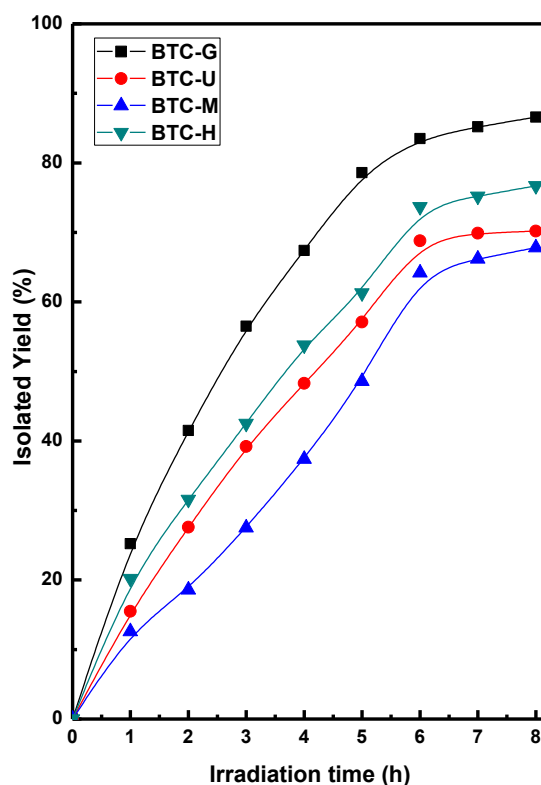


Figure 3.8: Effect of irradiation time on the isolated yield of the diphenyl disulfide for different BTC catalysts.

For a reaction involving 2 mmol of thiophenol, in order to determine optimum catalyst amount, the catalyst weight in the reaction mixture was varied between 25-100 mg. The yield of diphenyl disulfide increases with catalyst amount upto 50 mg, thereafter, further increase in catalyst quantity does not significantly impact the yield of the product (Fig. 3. 9I). At higher catalyst weight although more number of active sites are available for reaction, the scattering of light by catalyst particles also takes place leading to lower harvesting of photons. These two factors work in opposite manner and accounts for the observed trend in yield at higher catalyst weight. The effect of reaction media on the yield of the diphenyl disulfide for BTC-G catalyst after 6 h of reaction time is presented in Fig. 9 (II). For nonpolar solvent like hexane the yield of the product is very less. The photocatalytic reaction is facilitated in polar solvent. The solubility of thiophenol as well as easy accessibility of the catalyst surface is the probable reasons for the observed enhanced activity in polar solvent. After optimizing the reaction parameters, we further explored the scope of the developed photocatalytic protocol by using different substituted thiophenols. Substituted thiophenols containing electron withdrawing and donating as well as oxidizing functional groups in their structure reacted smoothly under the optimized condition to afford the corresponding diphenyl disulfides in high yield and purity (Table 3.2). The BTC-G catalyst is also found to be equally active for the conversion of aliphatic thiols to disulfides. The recyclability of the BTC-G catalyst is studied by conducting the photocatalytic tests in aqueous media for five consecutive cycles (Fig. 3.10 I).

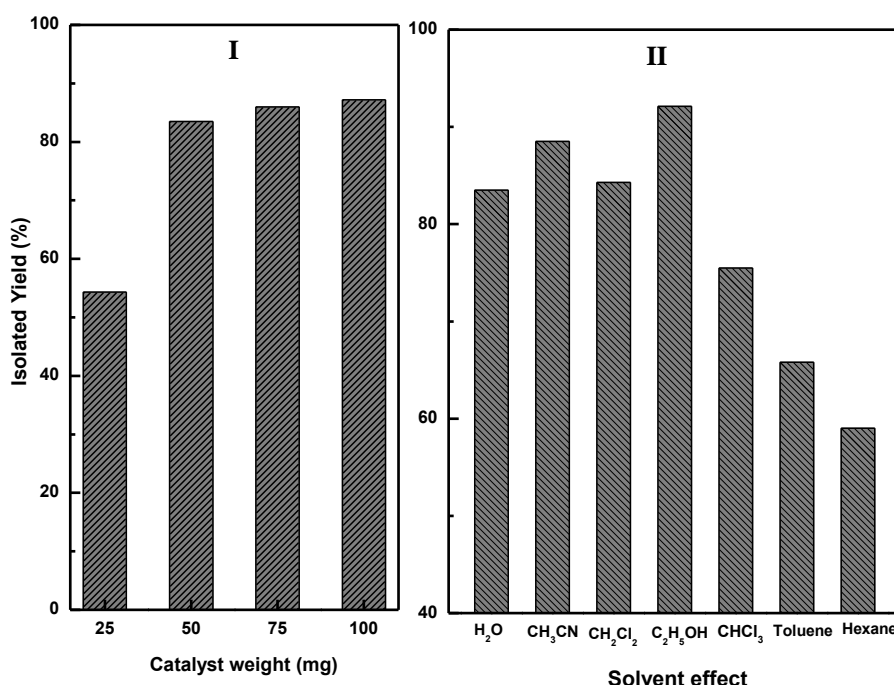
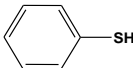
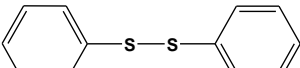

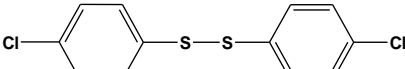
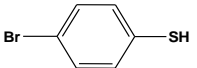
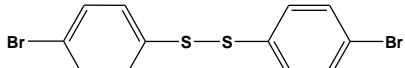
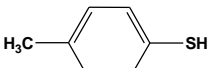
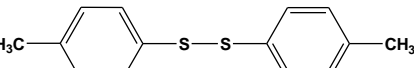
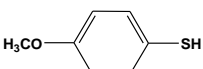
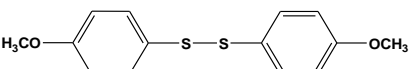
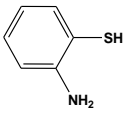
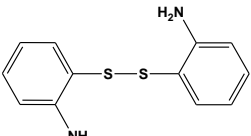
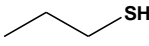
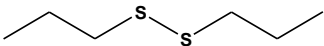
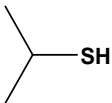
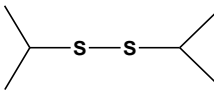


Figure 3.9: Effect of (I) catalyst weight and (II) reaction media on the photocatalytic activity of BTC-G catalyst for the synthesis of diphenyl disulfide after 6 h of irradiation time.

After completion of each cycle, the catalyst particles were filtered, dried in hot air oven and then calcined at 400 °C for 2 h to generate the catalyst. No significant difference in the yield

of the product or selectivity is observed up to five consecutive catalytic cycles indicating that BTC-G material to be highly recyclable and selective for formation of diphenyl disulfides (Fig. 3.10 D). The mechanism of photo-oxidation process over the surface of Bi_2WO_6 has been studied earlier [16, 29-32]. Upon absorption of a photon, the conduction band electrons and valence band holes are generated. The e^- and h^+ could migrate to the surface to react with the adsorbed reactants, or they could undergo recombination. The e^-h^+ recombination is divided into two categories: volume and surface recombination. The volume recombination is a dominant process in crystalline bulk semiconducting materials whereas surface recombination occurs due to entrapment and insufficient driving force for e^-h^+ pair separation [24, 30].

Table 3.2: BTC-G catalyzed selective oxidation of thiols to disulfides after 6 h of reaction in aqueous media.

Sl No.	Substrate	product	Selectivity (%)	Yield (%)
1.			100	83.5
2.			100	87.8
3.			100	82.4
4.			100	81.5
5.			100	85.0
6.			100	73.5
7.			100	87.0
8.			100	83.6

The average diffusion time for the photogenerated charge carriers from the bulk to the surface is governed by the relation $\tau = r^2/\pi^2D$ where r is the grain radius and D is the diffusion coefficient of the carrier [23]. The small grain radius of the BWO nanoparticles in the present study is quite favorable for diffusion of the charge carriers from bulk to the surface for utilization in photocatalytic process. The surface electron from the conduction band of Bi_2WO_6 can react with O_2 present in the system, reducing it to superoxide radical anion $\text{O}_2^{\bullet-}$.

The presence of superoxide radical anions in the aqueous aerated solution of Bi_2WO_6 has been detected earlier by ESR spectral analysis using spin trapping agent [16]. The formation of hydroxyl radical ($\cdot\text{OH}$) as a possible oxidizing species has been ruled out in case of Bi_2WO_6 in many studies [16, 29, 30].

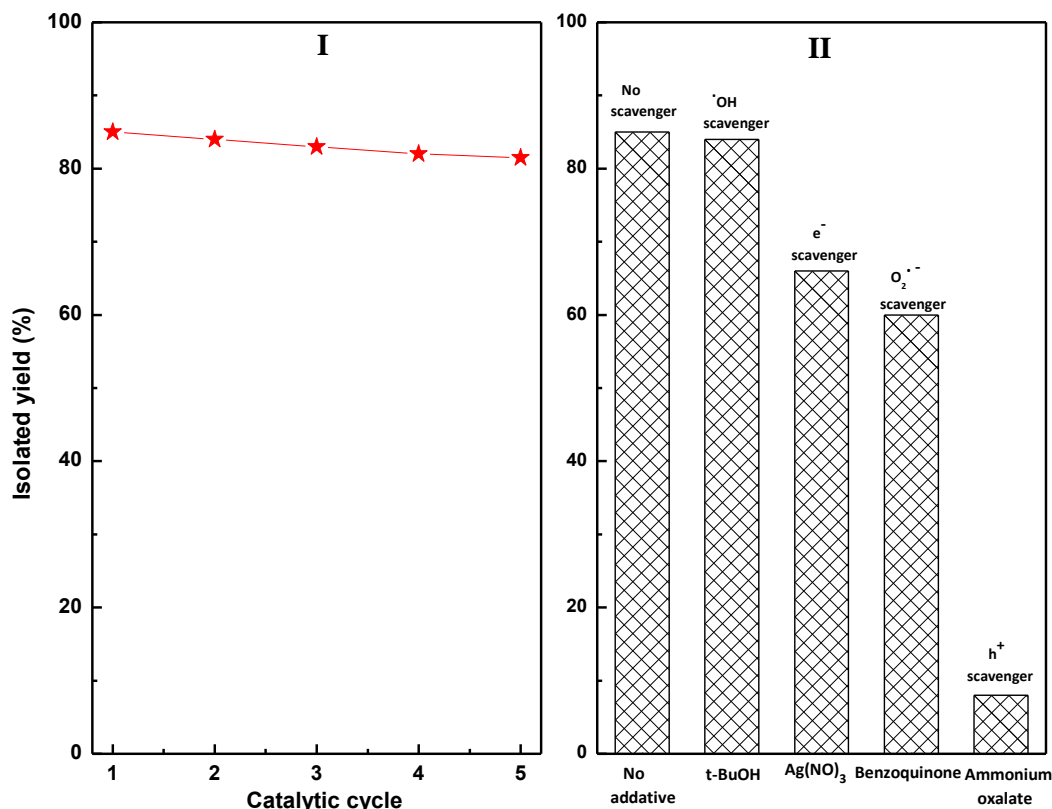


Figure 3.10: (I) Recyclability of the BTC-G catalyst and (II) isolated yield of diphenyl disulfide in presence of various radical scavengers after 6 h in aqueous media (the photocatalytic test was conducted under identical reaction condition by adding 2 mmol of the scavengers to the reaction mixture before illumination).

In the photocatalytic oxidation of thiophenol since the photogenerated holes (h^+), electrons (e^-), superoxide radical anions ($\text{O}_2^{\cdot-}$) and the hydroxyl radicals ($\cdot\text{OH}$) are the possible oxidizing species, the corresponding scavengers are used to investigate their role in the photo-oxidation process (Fig. 3.10 II) [16, 29]. The yield of disulfide decreases drastically in presence ammonium oxalate which is a hole scavenger. Similarly, considerable decrease in yield is observed in presence of benzoquinone which is a scavenger for $\text{O}_2^{\cdot-}$ radical anion. The radical scavenger experiments confirmed that the superoxide radical anions and the photogenerated holes are the predominant active species responsible for the oxidation of thiophenol to disulfide. Based on these results a plausible mechanism for the formation of disulfide is proposed (Fig. 3.11). The thiol moiety get oxidized at VB hole to give the radical cation whereas, at the CB the O_2 get reduced to $\text{O}_2^{\cdot-}$ radical anion. The radical cation and superoxide radical react with each other leading to the formation of disulfide product. Such mechanism has been proposed earlier for photocatalytic oxidation of thiol [12-14].

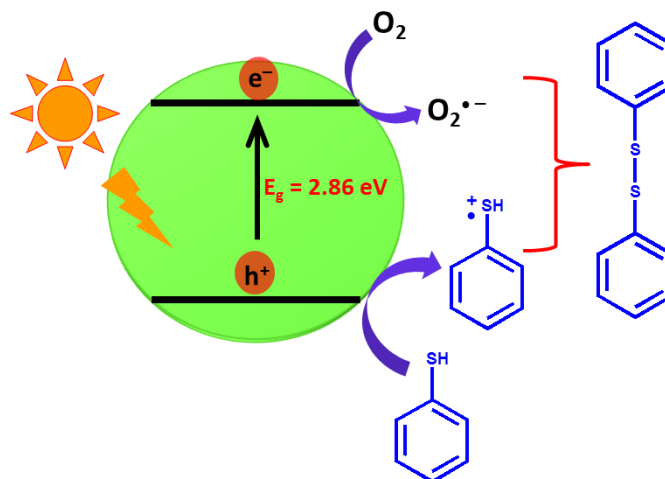
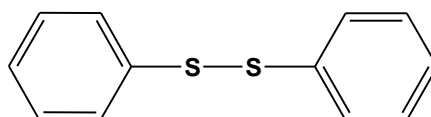


Figure 3.11: Probable mechanism for the selective oxidation of thiol to disulfide catalyzed by BTC-G material under visible light irradiation.

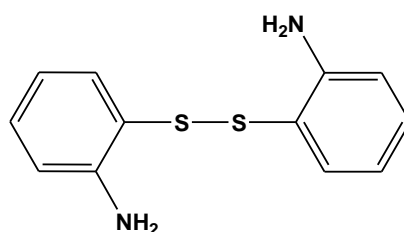
3.2.5 Physical and Spectra Data of some Representative Disulfides from Table 3.2

1,2-diphenyldisulfane (*Table 3.2, entry 1*)



Mp: 72 °C, ^1H NMR (400 MHz, CDCl_3): 7.52 (4H, d, ArH), 7.32 (4H, m, ArH), 7.22 (2H, s, ArH), ^{13}C NMR (400 MHz, CDCl_3): 137 (2 C, Ar), 129 (4 C, Ar), 127.46 (4 C, Ar), 127.15 (2 C, Ar),

2-(2-(2-aminophenyl)disulfanyl)benzenamine. (*Table 3.2, entry 6*)



Mp: 264 °C, ^1H NMR (400 MHz, CDCl_3): 7.1- 6.4 (8H, ArH), 4.25 (4H, NH_2), ^{13}C NMR (400 MHz, CDCl_3): 148.6, 136.37, 131.67, 118.31, 118.26, 115.27 (6 Ar-C)

Section B

Congo Red Dye Degradation Catalyzed by CuS- $\text{Bi}_2\text{Cu}_x\text{W}_{1-x}\text{O}_{6-2x}$ Heterojunction System

3.3 Introduction

In the previous section, we have described the combustion synthesis, characterization and photocatalytic application of Bi_2WO_6 material towards selective oxidation of thiols to disulfide under mild condition. In this section, we have synthesized CuS modified Bi_2WO_6 heterostructure system with enhanced visible light absorption and efficient charge carrier separation. We have studied the photocatalytic application of the CuS/ Bi_2WO_6 heterojunction system for the degradation of recalcitrant Congo red dye from aqueous sources.

In recent years, the use of semiconductor nanoparticles as photocatalyst for degradation of toxic chemicals from aqueous industrial effluent has emerged as the most promising technology for waste water treatment [15, 22, 33-35]. A broad spectrum of semiconducting materials has been studied for environmental clean-up using visible light as energy source [15, 34-36]. From the point of view of environmental application, the bismuth based compounds including oxides, sulfides and complex oxides are most promising and viable alternatives to TiO_2 [22, 33, 36-40]. Among Bi based photocatalytic materials, Bi_2WO_6 is one of the widely investigated system which has been studied for water splitting selective organic synthesis and decomposition of organic contaminants [36]. Although Bi_2WO_6 is an active photocatalyst, it has few limitations in terms of lower amount of visible light absorption and rapid recombination of photo generated electron and hole which significantly decrease the quantum efficiency [22, 36]. In order to overcome these limitations, Bi_2WO_6 based heterojunction systems have been widely investigated in literature [41-43]. The heterojunction systems exhibit superior visible light absorption property and photocatalytic activity than the parent Bi_2WO_6 nanomaterial.

The metal chalcogenides represent an important class of semiconducting materials which are used in many advanced technological applications [44-46]. Among the metal chalcogenides, CuS is a low band gap semiconductor (1.63-1.87 eV) which exhibits unique structural properties and finds wide application in photoelectric devices, lithium batteries, chemical sensors, solar cells, optical filters, and photocatalysis [45-47]. CuS exists in a variety of nonstoichiometric polymorphic form and exhibit composition dependent optical absorption property [48]. In recent years, morphology controlled CuS nanomaterials such as nanoflakes, nanorods, nanospheres, nanotubes, nanowires and nanoplatelets have been

synthesized by using different preparative strategies and their photocatalytic properties have been studied [46-52]. In order to increase its photocatalytic efficiency, CuS based nanohybrid and nanocomposite materials have been designed. The most notable CuS based nanocomposite materials studied for photocatalytic application include CuS/ZnO [53], CuS/ZnS p-n heterojunctions [54], CuS/Bi₂S₃ [49], CuS/RGO [55], CuS/WO₃ [56].

Congo red dye is one of the persistent organic pollutants found in the effluent water from textile, paper and plastic industries and biological labs. Congo red is carcinogenic and toxic in nature which causes severe health problems in human beings and affects all forms of aquatic life [57-63]. Benzidine a metabolite of Congo red induces cancer in the pancreas and bladder in human [57]. Due to its adverse health effect, it is highly essential to remove this toxic dye from the aqueous sources in an efficient and economical way. Several methods have been developed in recent years to remove Congo red from aqueous sources which includes adsorption, ozonation, biological treatment, sonochemical and photocatalytic degradation [58-62]. Among different methods studied so far, the photocatalytic method is one of the most effective and economical methods for complete mineralization of the dye to innocuous compounds. Recently, semiconducting nanomaterials such as titania [64], strontium doped titania [57], Zn_{1-x}Cu_xS and Zn_{1-x}Ni_xS [65], cobalt-carbon nanocomposite [58], RGO/PANI/Cu₂O composite hydrogel [66], chitosan/nano-CdS [67], and CuInSe₂-ZnO nanocomposite [68] have been studied for photocatalytic degradation of Congo red. The reported photocatalytic methods possess certain drawbacks such as incomplete degradation, slow degradation kinetics, high energy consumption (use of UV radiation), use of costly chemicals and complex synthetic steps for the photocatalyst preparation. It is highly desirable to develop novel photocatalytic protocols for efficient degradation of Congo red dye under visible light irradiation. In the present study, we have prepared CuS/Bi₂WO₆ heterojunction systems and studied their photocatalytic activity for degradation of recalcitrant Congo red dye under visible light. The Bi₂WO₆ (BTA) material was synthesized by an amorphous citrate method which was subsequently modified by CuS to form CuSBTA heterojunctions. The CuS phase is prepared by hydrothermal treatment using copper nitrate and thiourea as precursor.

3.4 Results and discussion

3.4.1 XRD Study

The XRD profiles of pure BTA together with the CuSBTA materials are shown in Fig. 3.12. Pure BTA exhibits well-defined and intense XRD peaks with d spacing values of 3.14, 2.62, 1.92, 1.64 and 1.57 Å corresponding to the orthorhombic Russellite phase of Bi₂WO₆ (JCPDS 79-2381) (Fig. 3.12a).

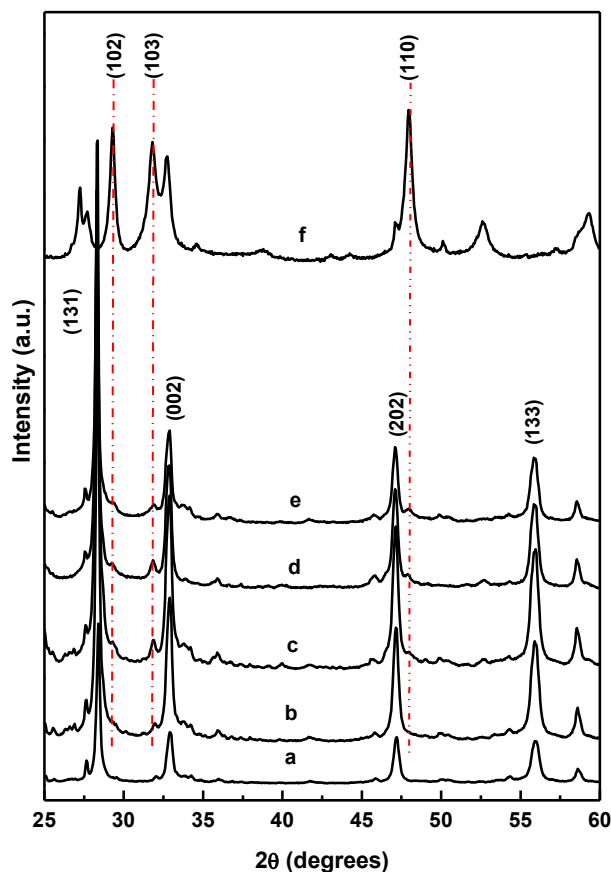


Figure 3.12: XRD patterns of (a) BTA, (b) CuS5BTA, (c) CuS10BTA, (d) CuS15BTA, (e) CuS20BTA and (f) CuS materials.

XRD pattern of pure CuS contains intense diffraction peaks with d spacing value of 3.28, 3.05, 2.80, 2.72, 1.90 and 1.73 Å corresponding to the hexagonal covellite phase (Fig. 3.12 f) (JCPDS-78-2121). The XRD profile of CuS5BTA heterojunction material exhibit reflection from the BTA phase only. The characteristic reflections corresponding to the crystalline CuS phase are absent for CuS5BTA material. As the percentage of CuS increases in the heterojunction materials, less intense but distinct XRD peaks appear at d values of 3.05, 2.80 and 1.90 Å corresponding to crystalline hexagonal CuS phase (Fig. 3.12 c-e). With increase in CuS content, the diffraction peaks of BTA phase shift gradually to lower 2θ values (Fig. 3.13 I). The variation in the d spacing for (131) peak of BTA with CuS content is presented in Fig. 3.13 II. The d spacing value increases linearly with CuS content satisfying the Vegard's law. This observation indicates an expansion in the BTA lattice due to partial substitution of W^{6+} ions (radius 0.62 Å) with Cu^{2+} ions (radius 0.73 Å) [20]. The anionic isovalent substitution of O^{2-} ions with S^{2-} ions is less likely to occur due to the large difference in ionic radii of these ionic species.

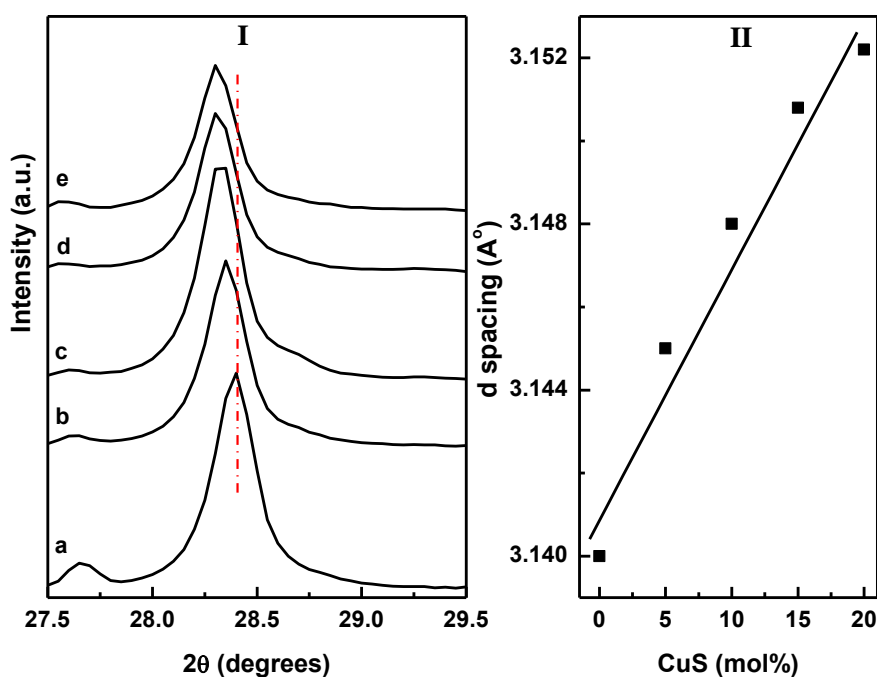


Figure 3.13: (I) Variation of 2θ value with CuS content for (131) peak of (a) BTA, (b) CuS5BTA, (c) CuS10BTA, (d) CuS15BTA, (e) CuS20BTA and (II) Vegard plot indicating an increase in d_{131} spacing with CuS content.

3.4.2 XPS Study

The chemical state of the constituent elements in the CuSBTA heterojunction material is studied using XPS. The XPS spectra of CuS10BTA composite are present in Fig. 3.14. The survey spectrum exhibits characteristic features corresponding to the presence of Bi, W, O, Cu, S species along with adventitious carbon (Fig. 3.14a). The high resolution XPS spectra for Bi, O, W, Cu and S are presented in Fig. 3.14 b-f, respectively. In the Bi 4f spectral region, the CuS10BTA material exhibits a doublet at 158.6 eV and 163.9 eV, corresponding to the Bi 4f_{7/2} and Bi 4f_{5/2} energy states. The observed doublet with a spin-orbit splitting of 5.3 eV is characteristics of Bi in a trivalent oxidation state (Bi³⁺) in Bi₂WO₆ [69-71]. In the W 4f region, two distinct peaks are noticed at 34.3 eV and 36.7 eV corresponding to the W4f_{7/2} and W4f_{5/2} energy levels of W⁶⁺ species of BT material (Fig. 3.14d) [70, 71]. The observed binding energy values are slightly lower than the binding energy reported for W⁶⁺ species of Bi₂WO₆ [70, 71]. The decrease in binding energy is ascribed to a change in the coordination environment of the W ions due to the partial substitution of Cu²⁺ species in the tungstate layer of BT material. In the O1s spectral region, a broad and asymmetric peak is observed with peak maxima at 530.5 eV. This peak can be assigned to the lattice oxygen of BTA (Fig. 3.14c) and is accordance with the earlier reported literature value [69]. Fig. 3.14e depicts the high resolution XPS spectrum of Cu in 2p region. Two distinct peaks observed at 932.3 eV and 952.3 eV correspond to the Cu2p_{3/2} and Cu2p_{1/2} signals of CuS [54].

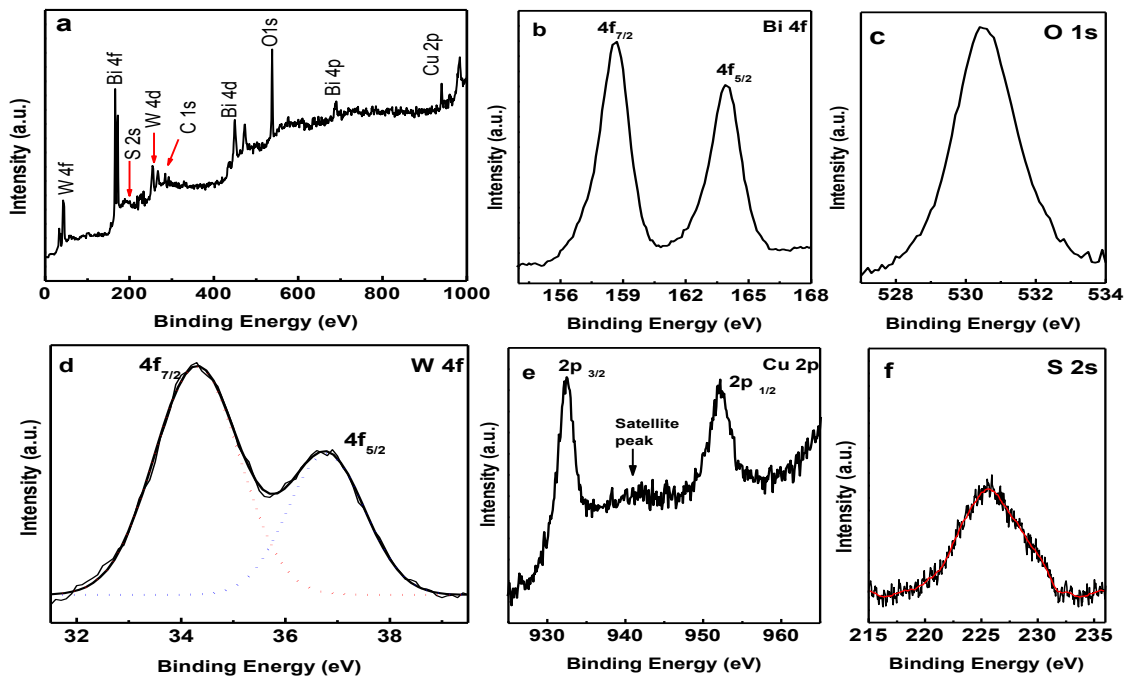


Figure 3.14: XPS spectra of CuS10BTA heterojunction material.

In addition, a broad peak is observed at 941.8 eV due to Cu^{2+} satellite peak. The S 2p region is masked by the Bi 4f peak. Hence, in order to confirm the presence of S^{2-} ions, the high resolution spectrum is recorded for the S 2s region. The presence of a broad peak centered at 225.7 eV confirms the presence of sulfide ions [49]. The XPS analysis confirmed the presence of CuS and Cu doped Bi_2WO_6 components in the heterojunction material.

3.4.3 Morphological Study

The morphological features of the CuSBTA materials have been investigated using FESEM and TEM. The FESEM images of BTA, CuS and CuS10BTA materials are presented in Fig. 3.15. The BTA material contains a mixture of polyhedral sheet shaped particles and elongated particles having size in submicron range (Fig. 3.15a). The sheet shaped particles exhibit typical length and breadth in the range of 0.3-0.4 μm and about 0.1 μm in thickness. The elongated particles have length between 0.3-0.4 μm whereas the width is less than 0.1 μm . Upon hydrothermal treatment in presence of the copper sulfide precursors, the morphology and shape of the BTA particles is significantly changed. The CuSBTA material contains BTA nanosheets which are arranged in a well-structured manner to give a flower like hierarchical structure (Fig. 3.15 b & c). Although, the hydrothermal treatment does not significantly affect the X and Y dimension, the thickness of the particles is reduced to 20-25 nm resulting in formation of nanosheets (Fig. 3.15c). The CuS phase exists in the shape of nanorods having 10-25 nm diameter and length in the range of 100-150 nm (Fig. 3.15c). The presence of CuS nanorods is observed from the FESEM study of the pure CuS material

synthesized by hydrothermal method (Fig. 3.15d). The shape and dimension of the individual components in the heterojunction material is further confirmed from TEM analysis (Fig. 3.16).

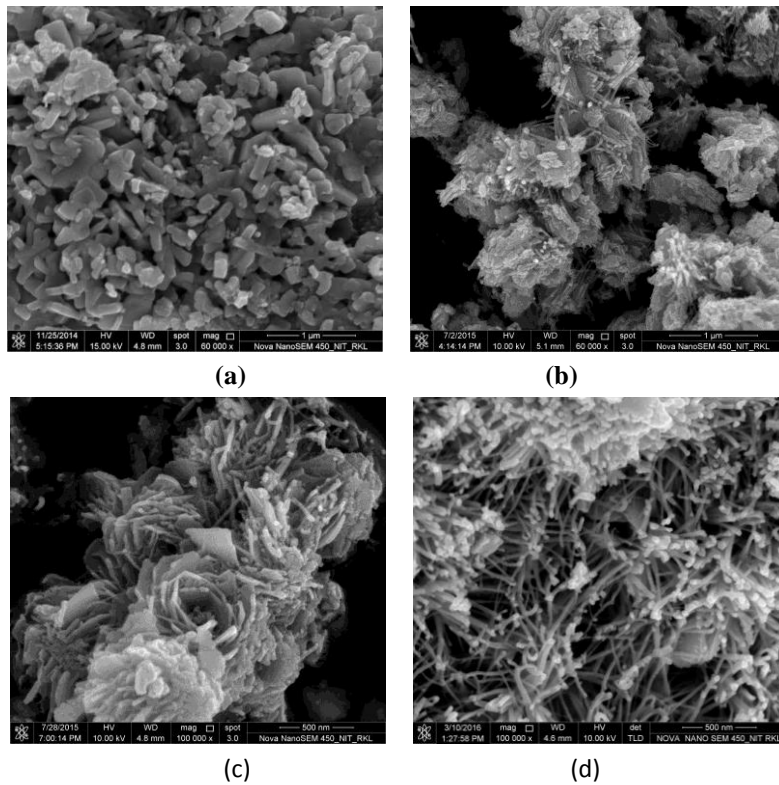


Figure 3.15: FESEM images of (a) BTA, (b, c) CuS10BTA and (d) CuS materials.

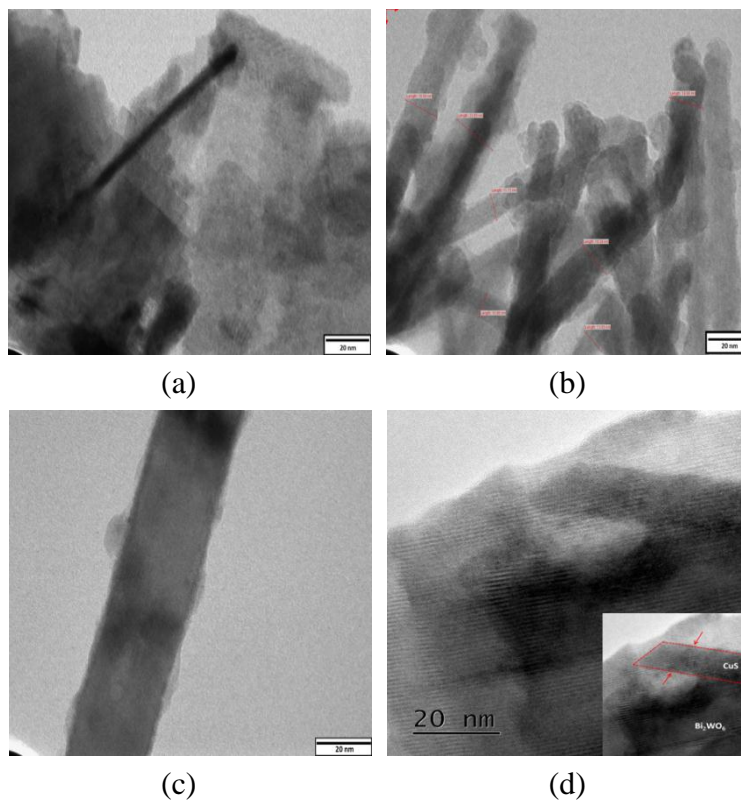


Figure 3.16: (a-c) TEM images and (d) high resolution TEM image of CuS10BTA material.

The presence of BTA nanosheets and CuS nanorods are clearly inferred from the TEM image of CuS10BTA material (Fig. 3.16a). The nanorods do not exhibit a smooth surface but rather formed by controlled directional growth of the CuS particles (Fig. 3.16 b & c). The roughness of the surface is beneficial in providing a large interface region for effective charge carrier mobility and separation. The high resolution TEM image of the CuS10BTA material is presented in Fig. 3.16d. Close microscopic contact between the CuS nanorods and BTA nanosheets is clearly noticed leading to formation of the heterojunction between the two phases.

3.4.4 FTIR Study

The FTIR spectra of pure BTA, CuS and CuSBTA heterojunction materials in the fingerprint spectral region of 400-1000 cm^{-1} are presented in Fig. 3.17. The BTA sample exhibits characteristics vibrational bands corresponding to the symmetric and asymmetric stretching vibration of W-O bond (823 and 735 cm^{-1}) and the stretching vibration of Bi-O bond (685 cm^{-1}) [26, 72].

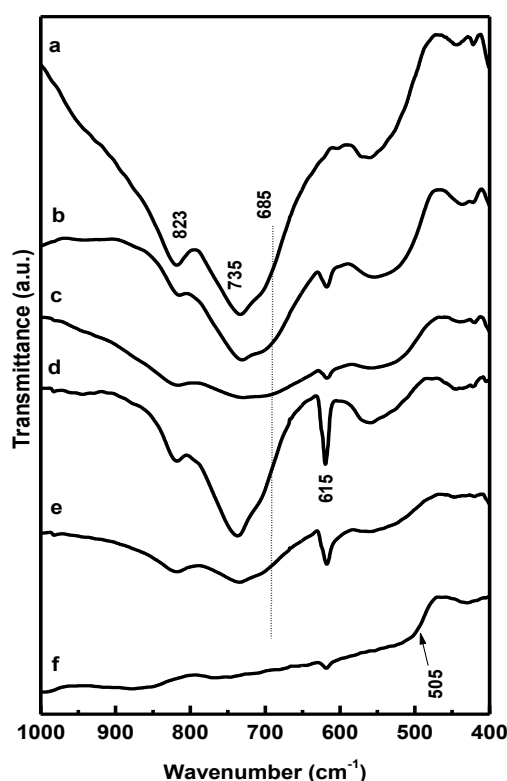


Figure 3.17: FTIR spectra of (a) BTA, (b) CuS5BTA, (c) CuS10BTA, (d) CuS15BTA, (e) CuS20BTA and (f) CuS materials.

These characteristic vibrational bands are retained in the CuSBTA materials, however, the peak position are altered. For example, for the composite materials the W-O vibrations shift by amount of 5-15 cm^{-1} towards the lower wavenumber side (Fig. 3.17 b-e). The shift in the

band position is because of the change in the W-O bond strength occurred due to the substitution of Cu^{2+} ions in the Bi_2WO_6 lattice. As described earlier, the Cu^{2+} ions substitute for the W^{6+} ions in the BTA lattice. The substitution of Cu may result in distortion of the WO_6 octahedron thereby altering the W-O bond strength. In addition to the shift in band position, new IR bands are observed at 615 and 505 cm^{-1} . These bands are assigned to the Cu-S bond stretching of the CuS component in the heterojunction materials [46, 47].

3.4.5 Optical Property Study

The optical absorption properties of pure BTA and CuSBTA heterojunction materials are studied using UV-Vis-diffuse reflectance and Photoluminescence spectroscopy. The UV-Vis-DRS spectra of BTA and CuSBTA heterojunction materials are presented in Fig. 3.18. The Bi_2WO_6 exhibits optical absorption edge around 440-450 nm with a band gap value of 2.8 eV [73]. Pure Bi_2WO_6 synthesized by amorphous citrate process display strong photo-absorption properties in UV region which extend up to the visible light region. The absorption edge commences near 440 nm (Fig. 3.18a). In addition to the strong UV absorption, the CuSBTA materials exhibit significant enhancement in visible light absorption properties. For the heterojunction materials the absorption edge starts near 750 nm. The absorption intensity in the visible region increases with increase in CuS content (Fig. 3.18 b-e).

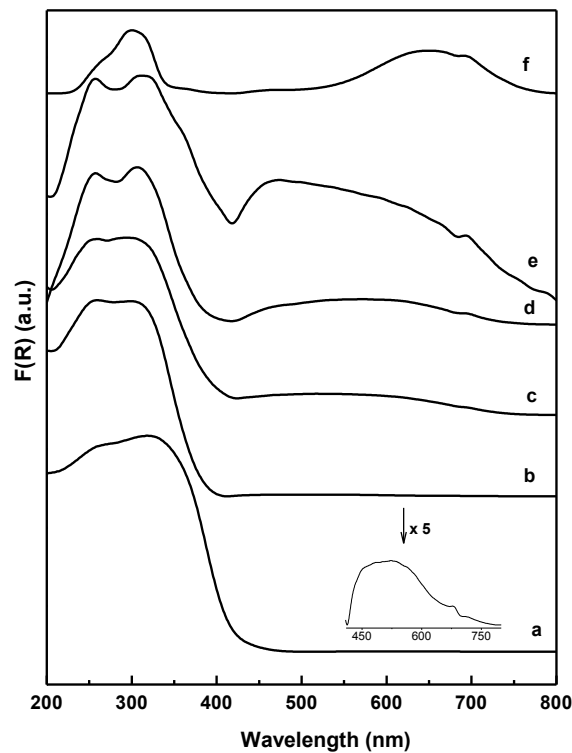


Figure 3.18: UV-Vis-DRS spectra of (a) BTA, (b) CuS5BTA, (c) CuS10BTA, (d) CuS15BTA, (e) CuS20BTA and (f) CuS materials.

The band gap of pure BTA and CuS materials are calculated from intercept of the plot of photon energy ($h\nu$) versus $[F(R)h\nu]^2$ (Fig. 3.19). Pure BTA and CuS exhibit a band gap of 2.82 eV and 1.65 eV, respectively, which is in accordance with previous reported value [73, 47]. The UV-vis study indicates that the CuSBTA materials display enhanced photo absorption in the visible region and hence suitable for application as visible light active photocatalyst.

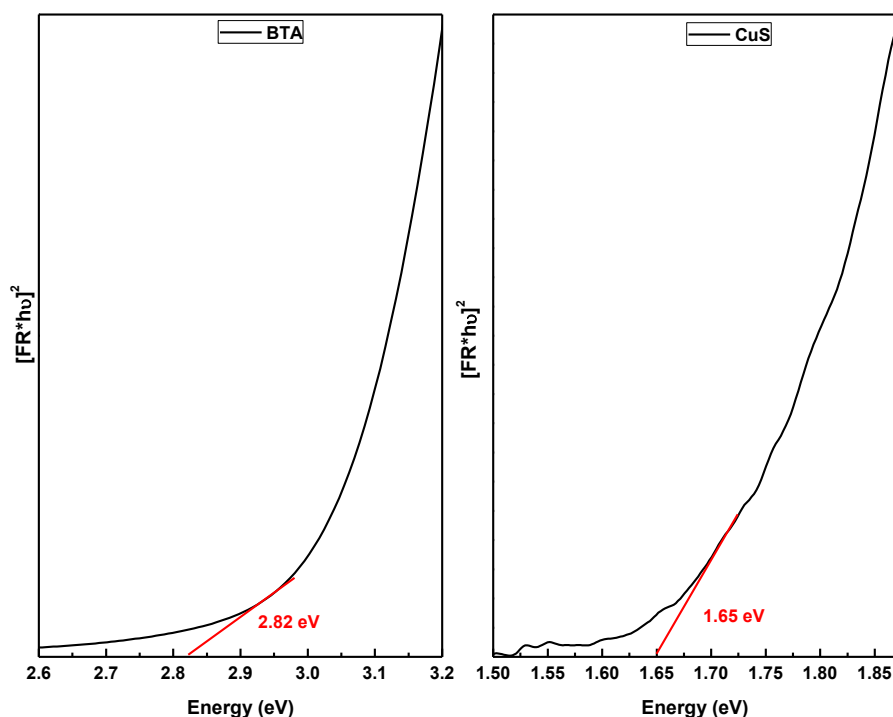


Figure 3.19: Plot of $[F(R)h\nu]^2$ as a function of photon energy ($h\nu$) in eV of (a) BTA and (b) CuS materials.

The photoluminescence (PL) spectra of BTA and CuSBTA materials are presented in Fig. 3.20. Pure BTA material exhibits broad blue-green emission in the spectral region of 450–580 nm. The intense PL band at 465 nm for Bi_2WO_6 is due to the intrinsic luminescence due to band edge transition [74]. The green emission observed at 560 nm is ascribed to the presence of defect sites and vacancy in the BTA crystal [75]. The intensity of these bands reduces significantly for the heterojunction materials. This observation indicates that the electron–hole recombination is suppressed to a large extent in the CuSBTA material. The specific surface area of the BT and CuSBTA materials is presented in Table 3.3. Pure BTA material prepared by amorphous citrate process exhibit a specific surface area of $22.2 \text{ m}^2/\text{g}$. The CuSBTA composite materials possess specific surface area in the range of $29\text{--}35 \text{ m}^2/\text{g}$. The hydrothermal treatment seems to be beneficial in terms of increase in specific surface area. The probable reason for the increase in specific surface area is the desegregation of the BTA particles during hydrothermal treatment to form nanosheets.

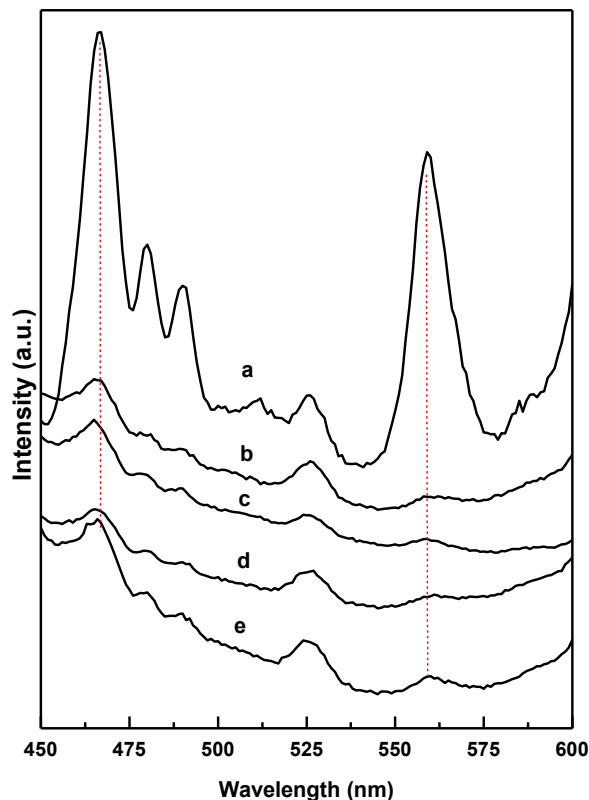


Figure 3.20: Photoluminescence spectra of (a) BTA, (b) CuS5BTA, (c) CuS10BTA, (d) CuS15BTA and (e) CuS20BTA materials.

Table 3.3: Specific surface areas of BTA and CuSBTA heterojunction materials.

Material	Specific surface area (m ² /g)
BTA	22
CuS5BTA	36
CuS10BTA	32
CuS15BTA	31
CuS20BTA	29

3.4.6 Photocatalytic Degradation of Congo red Dye

The photocatalytic activity of the CuSBTA material is evaluated for photocatalytic degradation of Congo red dye under visible light irradiation. The photocatalytic experiments are conducted by irradiating a 100 ml of 10⁻⁴ M Congo red dye solution containing 25 mg of catalyst. The degradation process is studied by monitoring the intensity of the characteristic absorption peak of congo red at 497 nm. The degradation efficiency is calculated using the expression [69, 76].

$$\begin{aligned} \text{Degradation percentage} &= [(C_0 - C) / C_0] \times 100 \\ &= [(A_0 - A) / A_0] \times 100 \dots\dots\dots (3.1) \end{aligned}$$

Where C_0 and C are the concentration and A_0 and A are the absorbance of Congo red at time 0 and t minutes, respectively. In order to confirm that the degradation process is photocatalytic in nature, the reaction is conducted in dark in presence as well as in absence of the catalyst. The degradation does not take place under dark condition indicating that the process is photocatalytic in nature. Under illuminated condition, in absence of the heterojunction photocatalyst, no significant decrease in the Congo red concentration is observed (3.6 % degraded after 4 h irradiation). When the degradation was carried out using CuS10BTA material in absence of H_2O_2 , 35% degradation is achieved after 3 h of irradiation. The degradation of Congo red dye (CR) using BTA and CuSBTA heterojunction materials in presence of H_2O_2 are compared in Fig. 3.21. The degradation process is quite sluggish for pure BT material. Nearly 50% degradation of Congo red is achieved after 1 h of irradiation (Fig. 3.21). The CuSBTA heterojunction materials on the other hand display enhanced photocatalytic activity. Upon addition of 5 wt% of CuS to BTA material, 95% degradation of Congo red is achieved within 60 minutes. As the percentage of CuS increases in the CuSBTA material, the degradation efficiency is found to increase concurrently. For CuS20BTA heterojunction material more than 95% degradation is obtained within 20 minutes of irradiation. Since the CR degradation rate is quite fast for CuS20BTA material, for kinetic reason CuS10BTA catalyst is chosen for further photocatalytic studies.

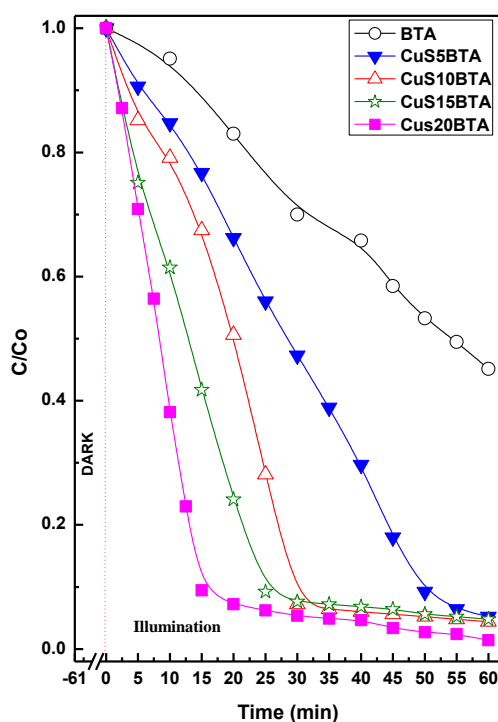


Figure 3.21: Photocatalytic degradation of Congo red dye catalyzed by CuSBTA heterojunction materials.

The UV-Vis absorbance spectra of the dye solution at different interval of irradiation time degraded using CuS20BTA material are presented in Fig. 3.22. Pure Congo red exhibits three absorption bands in the UV-Vis region. The peak at 497 is assigned to the chromophoric N=N group whereas the peaks at 343 and 237 nm have been assigned to the electronic

transition corresponding to the naphthalene and benzene moieties present in the congo red structure [68]. As observed from the absorption spectra with increase in irradiation time the peak intensity of all these peaks decreases rapidly and after 30 min of irradiation there is no significant absorption corresponding to these functionalities. This observation indicates that the CuSBTA heterojunction material is quite efficient in complete degradation of the Congo red dye.

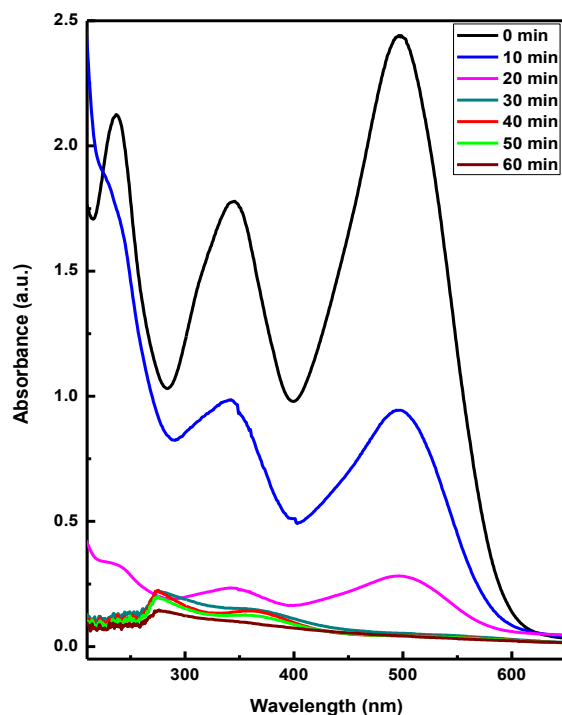


Figure 3.22: UV-Vis absorbance spectra of 10^{-4} M Congo red dye solution at different irradiation time using 25 mg of CuS20BTA catalyst.

Since, the photocatalytic degradation of dyes follows pseudo-first order kinetics [69], the apparent pseudo-first order rate constant (k_{app}) can be calculated using the equation 3.2:

$$\ln(C_0/C) = k_{app} \times t \quad \dots\dots\dots(3.2)$$

The value of k_{app} can be obtained from the gradient of the plot of $\ln(C_0/C)$ versus time (t). The plot of $\ln(C_0/C)$ vs t for different CuSBTA materials along with the k_{app} values are presented in Fig. 3.23. The pure BTA material exhibits a k_{app} value of 0.013 min^{-1} . The pseudo-first order rate constants for CuSBTA materials are significantly higher than the BTA material (Fig. 3.23II). The k_{app} for CuS20BTA material is 10 times higher than the pure BTA and nearly 5 times more than the CuS5BTA material. The k_{app} values imply that CuSBTA heterojunctions display better photocatalytic efficiency than pure BTA material. The CuS content is instrumental in influencing the photocatalytic property of the heterojunctions. Since, the CuS20BTA material exhibits high rate of degradation of Congo red, from kinetic consideration the CuS10BTA material was chosen for further photocatalytic experiments.

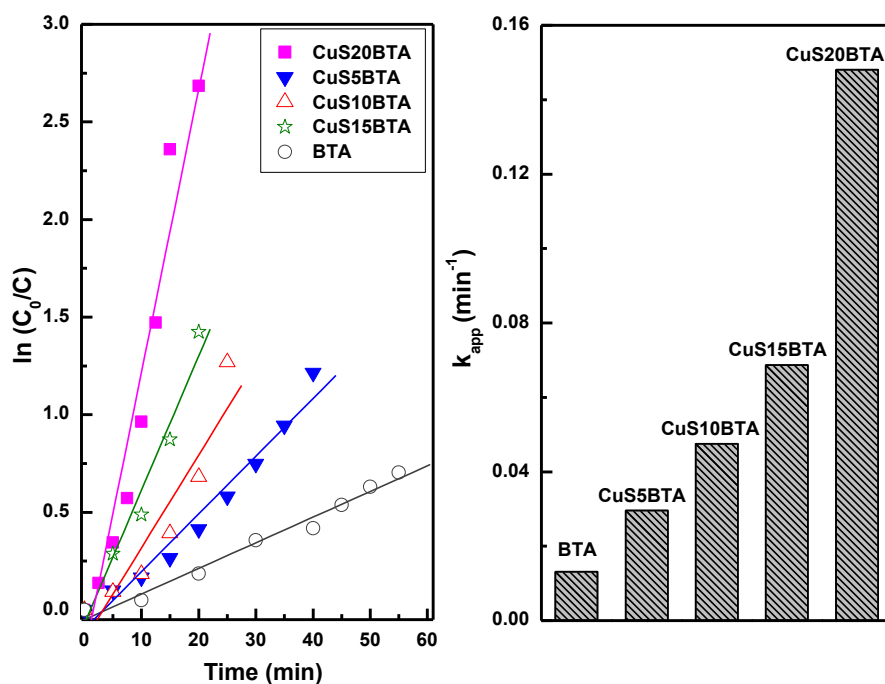


Figure 3.23: (I) First order kinetics plots for the degradation of Congo red (II) apparent first order rate constant for different CuSBTA heterojunction photocatalysts.

Catalyst dose plays a significant role in photocatalytic degradation process. In order to study the effect of catalyst dose, different weights of CuS10BTA in the range 5-30 mg are used in the photocatalytic study keeping the dye concentration fixed (100 ml of 1×10^{-4} M Congo red solution is used). The percentage degradation of the Congo red increases with increase in the catalyst weight upto 25 mg, further increase in the catalyst amount does not have a significant influence on the degradation efficiency (Fig. 3.24). The increase in degradation efficiency can be attributed to the availability of more number of active surface sites for the photo degradation process until a saturation point is reached for an optimum catalyst amount. In order to understand the possible mechanism for the degradation of Congo red, various scavengers (equimolar quantity with respect to catalyst) were added in the reaction mixture. The effect of different scavengers on the photocatalytic degradation of Congo red is presented in Fig. 3.25. The presence of electron scavenger (AgNO_3) does not influence the rate of Congo red degradation significantly. This observation indicates that the electrons are not the primary reactive species for the degradation process. Among different scavengers, significant decrease in reaction rate is observed in presence of hydroxyl radical scavenger (t-butyl alcohol) and hole scavenger (ammonium oxalate). The scavenger experiment suggests that the generated hole and the hydroxyl radicals are the prime species involved in the degradation of Congo red.

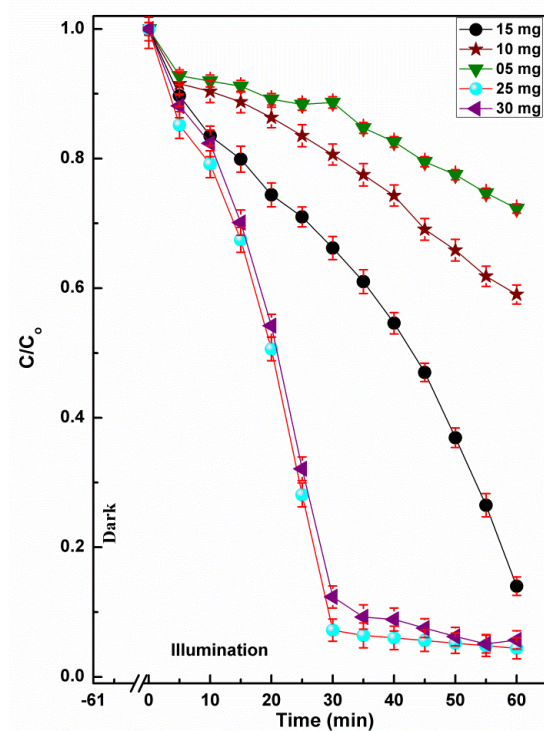


Figure 3.24: Effect of catalyst dose on the degradation efficiency of Congo red dye studied for CuS10BTA photocatalyst.

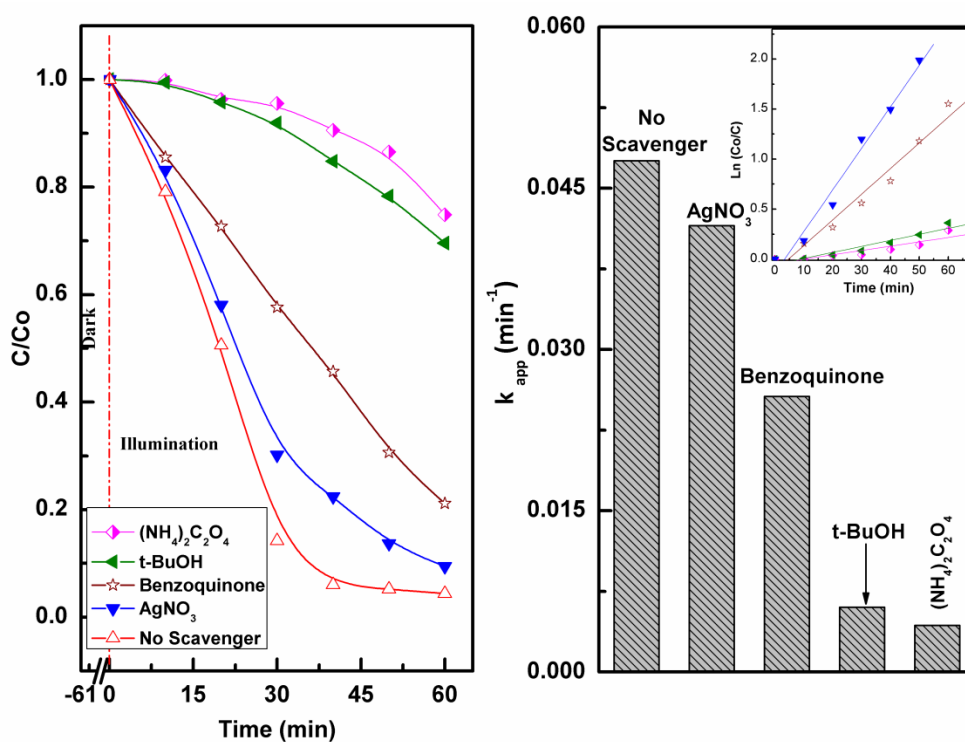


Figure 3.25: (I) Degradation efficiency and (II) apparent rate constant (K_{app}) of CuS10BTA in presence of different radical scavengers.

In a photocatalytic reaction, photo induced holes and electrons are generated due to the excitation of electrons from valence band to conduction band. The valence band and conduction band levels of the BTA and CuS material are theoretically calculated using the empirical equation 3.3 [39, 49, 56, 74].

$$E_{VB} = X_e - E_e + 0.5E_g \dots\dots\dots (3.3)$$

Where, X_e is the electronegativity of the material which is the geometric mean of the electronegativity of its constituent atoms, E_e is the energy of the free electrons on the hydrogen scale (about 4.5 eV) and E_g is the bang of the material in eV. The X_e value of Bi_2WO_6 and CuS are 6.36 eV and 5.29 eV, respectively [54, 75]. Using the measured band gap (E_g) values, the conduction and valence band levels for the pure BTA and CuS are calculated. For BTA, the VB and CB are placed at +3.27 eV and +0.45 eV, whereas the VB and CB for CuS are at +1.61 eV and -0.04 eV, respectively. The observed VB and CB levels are consistent with the literature reported values [54, 74]. Bi_2WO_6 is a known n-type semiconductor whereas CuS exhibits p-type semiconductivity [42, 49, 54]. Upon material contact between the semiconductor phases, Fermi level equilibrium leads to realignment of the band positions (Fig. 3.26). The band structures of the two components are favorably aligned for electron migration from the CB of CuS to BTA, whereas the reverse migration of holes can take place. This can result in an enhanced charge carrier separation and their efficient utilization in the photocatalytic degradation (formation of type II heterojunction). Based on the above observation a probable photocatalytic mechanism is proposed for the CR degradation on CuSBTA surface (Fig. 3.26).

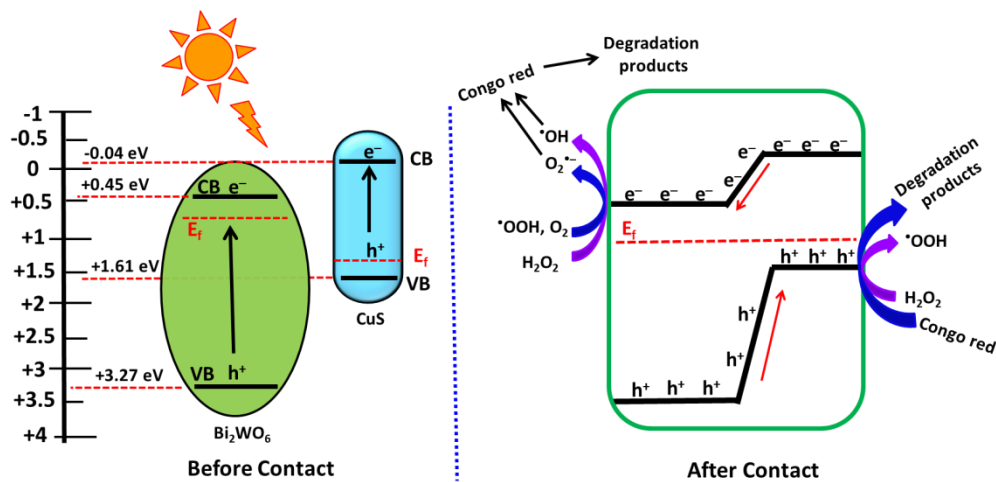


Figure 3.26: Probable mechanism for degradation of Congo red dye catalyzed by CuSBTA material under visible light irradiation.

The H_2O_2 is activated to active $*OH$ radical upon reaction with the conduction band electron. The CB electron can also react with the dissolved oxygen to form superoxide radical anion. The H_2O_2 can undergo secondary reactions through the formation of hydroperoxyl radical ($*OOH$) to produce the superoxide radicals (O_2^*). The role of superoxide radical although not substantial in the degradation process but cannot be neglected. A moderate but significant

decrease in the degradation efficiency is observed in the presence of superoxide radical scavenger. The positive hole population can increase in the VB of the CuS component due to migration of holes from the VB of BTA material. The reactive and oxidizing nature of the generated hole can oxidize Congo red. The generation of different reactive species and their use in photocatalytic degradation of Congo red is presented in equations 3.4-3.9.



In heterogeneous catalytic system for practical applicability, stability and recyclability of the catalyst is an important issue. Earlier literature study indicates that pure BT and CuS are independently very stable photocatalyst systems [47, 74]. In order to evaluate the stability and recyclability of the CuSBTA heterojunction materials, the CuS10BTA catalyst is tested for its photocatalytic activity upto five consecutive catalytic cycles (Fig. 3.27). After each cycle the catalyst particles are collected by centrifugation, washed three times with ethanol and dried for 12 h at 60°C. The recyclability experiment has been carried in a scale down manner starting with 50 mg of catalyst. In all recyclability experiments, the ratio of catalyst weight to concentration of pollutants was fixed and the experiments were conducted for 5 cycles. The catalytic data are presented as normalized data for fixed catalytic weight. The CuS10BTA material shows no significant decrease in the photocatalytic efficiency upto five repeated cycles indicating the material to be very stable and recyclable.

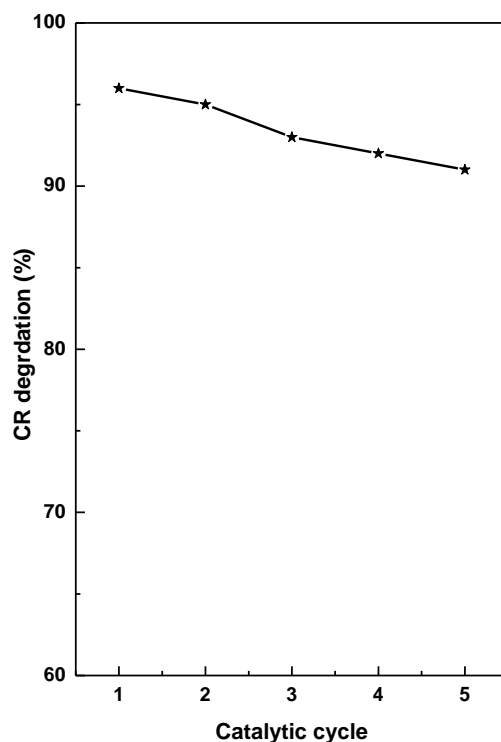


Figure 3.27: Recyclability study of CuS10BTA photocatalyst.

3.5 Conclusions

In this work, we have investigated novel photocatalytic application of Bi_2WO_6 nanomaterial towards selective organic transformation and mineralization of recalcitrant Congo red dye from aqueous sources. The Bi_2WO_6 nanoparticles are synthesized by a facile combustion route using different reducible organic compounds as fuels. Phase pure Bi_2WO_6 nanoparticles are obtained using glycine as fuel whereas formation of $\text{Bi}_2\text{W}_2\text{O}_9$ and $\text{Bi}_{14}\text{W}_2\text{O}_{27}$ as impurity phases is observed for urea, MDH and hexamethylenetetramine. Bi_2WO_6 nanoparticles with spherical, flake like and elongated polyhedral shape are obtained by varying the fuel and its content in the combustion mixture. The Bi_2WO_6 material synthesized using glycine contains uniformly distributed nanoparticles. The combustion synthesized Bi_2WO_6 material is used as an efficient photocatalyst for rapid, convenient and environmentally benign selective oxidation of thiols to disulfide in aqueous media under visible light irradiation. The Bi_2WO_6 photocatalyst is found to be highly active and selective to the formation of disulfides for a variety of substrates containing electron withdrawing and donating functional groups. The photocatalytic protocol developed in this work is advantageous in terms of its mild nature, preclusion of toxic solvent and chemicals, recyclable and stable photocatalyst, good yield and excellent selectivity for disulfide formation.

The optical and photocatalytic property of Bi_2WO_6 was further improved by heterojunction formation with CuS nanomaterial. The Bi_2WO_6 material prepared by amorphous citrate process contain orthorhombic Russellite phase. Hydrothermal

treatment in presence of copper salt precursor resulted in the incorporation of Cu^{2+} ions into the BT lattice to form the $\text{Bi}_2\text{Cu}_x\text{W}_{1-x}\text{O}_{6-2x}$ solid solution. For the heterojunction samples, the CuS and Bi_2WO_6 phases exist in distinct nanorod and nanosheet morphologies, respectively. The nanosheets are typically 20-25 nm thick and exhibit submicron length in planar dimensions. The nanorods are having 10-25 nm diameter and length in the range of 100-150 nm. The hydrothermal treatment is also responsible for the morphological reorganization of the BTA nanosheets to hierarchical flower like nanostructure. The chemical state of the individual elements in the heterojunction is confirmed from XPS analysis. The CuS and Bi_2WO_6 phases form a Type-II heterojunction which exhibit significant visible light absorption and enhanced charge carrier separation. The CuS/ Bi_2WO_6 heterojunctions are highly efficient as visible light active photocatalyst for the degradation of Congo red dye from aqueous solution. The photocatalytic protocol developed for Congo red degradation is advantageous in terms of minimum and efficient use of catalyst and oxidant, less irradiation time and its applicability for aqueous effluents containing higher concentration of the dye.

References

- [1] Z. Guo, B. Liu, Q. Zhang, W. Deng, Y. Wang and Y. Yang, *Chemical Society Review*, 2014, 43, 3480-3524.
- [2] F. Cavani, *Catalysis Today*, 2010, 157, 8-15.
- [3] A. Talla, B. Driessen, N. J. W. Straathof, L.-G. Milroy, L. Brunsveld, V. Hessel and T. Noel, *Advanced Synthesis and Catalysis*, 2015, 357, 2180-2186.
- [4] S. Dharmarathna, C. K. Kingondu, L. Pahalagedara, C. H. Kuo, Y. Zhang and S. L. Suib, *Applied Catalysis B: Environmental*, 2014, 147, 124-131.
- [5] H. Golchoubian and F. Hosseinpour, *Catalysis Communications*, 2007, 8, 697-700.
- [6] M. Kirihara, K. Okubo, T. Uchiyama, Y. Kato, Y. Ochiai, S. Matsushita, A. Hatano and K. Kanamori, *Chemical and Pharmaceutical Bulletin*, 2004, 52, 625-627.
- [7] M. Kirihara, Y. Asai, S. Ogawa, T. Noguchi, A. Hatano and Y. Hirai, *Synthesis*, 2007, 3286-3289.
- [8] M. Chakraborty, P. C. Mandal and S. Mukhopadhyay, *Polyhedron*, 2012, 45, 213-220.
- [9] M. Hayashi, K. Okunaga, S. Nishida, K. Kawamura and K. Eda, *Tetrahedron Letters*, 2010, 51, 6734-6736.
- [10] C. Tidei, M. Piroddi, F. Galli and C. Santi, *Tetrahedron Letters*, 2012, 53, 232-234.
- [11] L. V. Lutkus, H. E. Irving, K. S. Davies, J. E. Hill, J. E. Lohman, M. W. Eskew, M. R. Detty and T. M. McCormick, *Organometallics*, 2017, 36, 2588-2596.
- [12] A. M. Kulkarni, U. V. Desai, K. S. Pandit, M. A. Kulkarni and P. P. Wadgaonkar, *RSC Advances*, 2014, 4, 36702-36707.

- [13] P. Kumar, G. Singh, D. Tripathi and S. L. Jain, *RSC Advances*, 2014, 4, 50331-50337.
- [14] W. Liu, C. Wang, Y. Huang, Q. Chen, L. Wang and M. He, *Synthetic Communications*, 2016, 46, 1268-1274.
- [15] H. Tong, S. Ouyang, Y. Bi, N. Umezawa, M. Oshikiri and J. Ye, *Advanced Materials*, 2012, 24, 229-251.
- [16] Y. Zhang, N. Zhang, Z. Tang and Y. Xu, *Chemical Science*, 2013, 4, 1820-1824.
- [17] Y. Zhang and Y. J. Xu, *RSC Advances*, 2014, 4, 2904-2910.
- [18] S. Murcia-Lopez, M. C. Hidalgo and J. A. Navio, *Applied Catalysis A*, 2012, 423, 34-41.
- [19] Y. Tian, G. Hua, W. Xu, N. Li, M. Fang and L. Zhang, *Journal of Alloys and Compounds*, 2011, 509, 724-730.
- [20] B. E. Warren and B. L. Averbach, *Journal of Applied Physics*, 1950, 21, 595-598.
- [21] D. Balzar and H. Ledbetter, *Journal of Applied Crystallography*, 1993, 26, 97-103.
- [22] N. Zhang, R. Ciriminna, M. Pagliaro and Y. J. Xu, *Chemical Society Reviews*, 2014, 43, 5276-5287.
- [23] S. Sun, W. Wang, D. Jiang, Y. Sun and Y. Xie, *ChemSusChem*, 2013, 6, 1873-1877.
- [24] H. Fu, L. Zhang, W. Yao and Y. Zhu, *Applied Catalysis B: Environmental*, 2006, 66, 100-110.
- [25] D. Kim, S. Kim and M. Kang, *Bulletin of Korean Chemical Society*, 2009, 30, 630-636.
- [26] Z. Sun, J. Guo, S. Zhu, L. Mao, J. Ma and D. Zhang, *Nanoscale*, 2014, 6, 2186-2193.
- [27] F. Duan, Y. Zheng and M. Chen, *Applied Surface Science*, 2011, 257, 1972-1978.
- [28] Q. Xiao, J. Zhang, C. Xiao and X. Tan, *Catalysis Communications*, 2008, 9, 1247-1253.
- [29] H. Li, W. Hou, X. Tao and N. Du, *Applied Catalysis B: Environmental*, 2015, 172-173, 27-36.
- [30] J. Zhai, H. Yu, H. Li, L. Sun, K. Zhang and H. Yang, *Applied Surface Science*, 2015, 344, 101-106.
- [31] Z. Cui, D. Zeng, T. Tang, J. Liu and C. Xie, *Catalysis Communications*, 2010, 11, 1054-1057.
- [32] H. Fu, C. Pan, W. Yao and Y. Zhu, *Journal of Physical Chemistry B*, 2005, 109, 22432-22439.
- [33] J. Li, Y. Yu and L. Zhang, *Nanoscale*, 2014, 6, 8473-8488.
- [34] Y. Wang, Q. Wang, X. Zhan, F. Wang, M. Safdar and J. He, *Nanoscale*, 2013, 5, 8326-8339.
- [35] S. Dong, J. Feng, M. Fan, Y. Pi, L. Hu, X. Han, M. Liu and J. Sun, *RSC Advances*, 2015, 5, 14610-14630.
- [36] L. Zhang and Y. Zhu, *Catalysis Science & Technology*, 2012, 2, 694-706.

- [37] W. Liu, J. Cai and Z. Li, *ACS Sustainable Chemistry & Engineering*, 2015, 3, 277–282.
- [38] L. Sun, L. Xiang, X. Zhao, C. J. Jia, J. Yang, Z. Jin, X. Cheng and W. Fan, *ACS Catalysis*, 2015, 5, 3540-3551.
- [39] H. Huang, Y. He, X. Du, P. K. Chu and Y. Zhang, *ACS Sustainable Chemistry & Engineering*, 2015, 3, 3262–3273.
- [40] R. He, S. Cao, P. Zhou and J. Yu, *Chinese Journal of Catalysis*, 2014, 35, 989-1007.
- [41] L. Yan, Y. Wang, H. Shen, Y. Zhang, J. Li and D. Wang, *Applied Surface Science*, 2017, 393, 496-503.
- [42] X. Liu, Q. Lu, C. Zhu and S. Liu, *RSC Advances*, 2015, 5, 4077-4082.
- [43] Y. Liu, S. Liu, T. Wu, H. Lin and X. Zhang, *Journal of Sol-Gel Science and Technology*, 2017, 83, 315-323.
- [44] W. Y. Lim, and M. H. G. W. Ho, *Dalton Transactions*, 2016, 45, 552-560.
- [45] X. Rui, H. Tan, and Q. Yan, *Nanoscale*, 2014, 6, 9889-9924.
- [46] M. Saranya, C. Santhosh, R. Ramachandran, P. Kollu, P. Saravanan, M. Vinoba, S. K. Jeong and A. N. Grace, *Powder Technology*, 2014, 252, 25-32.
- [47] M. Saranyaa, R. Ramachandran, E. J. J. Samuel, S. K. Jeong and A. N. Grace, *Powder Technology*, 2015, 279, 209-220.
- [48] J. Kundu and D. Pradhan, *ACS Applied Materials & Interfaces*, 2014, 6, 1823-1834.
- [49] L. Chen, J. He, Q. Yuan, Y. W. Zhang, F. Wang, C. T. Au and S. F. Yin, *RSC Advances*, 2015, 5, 33747-33754.
- [50] M. Wang, F. Xie, W. Li, M. Chena and Y. Zhao, *Journal of Material Chemistry A*, 2013, 1, 8616-8621.
- [51] Z. Hai, J. Huang, H. Remita and J. Chen, *Material Letters*, 2013, 108, 304-307.
- [52] K. Xu and W. Ding, *Material Letters*, 2008, 62, 4437-4439.
- [53] W. Zhang, Y. Sun, Z. Xiao, W. Li, B. Li, X. Huang, X. Liu and J. Hu, *Journal of Material Chemistry A*, 2015, 3, 7304-7313.
- [54] C. Mondal, A. Singh, R. Sahoo, A. K. Sasmal, Y. Negishi and T. Pal, *New Journal of Chemistry*, 2015, 39, 5628-5635.
- [55] M. Saranya, R. Ramachandran, P. Kollu, S. K. Jeong and A. N. Grace, *RSC Advances*, 2015, 5, 15831-15840.
- [56] J. R. Theerthagiri, A. Senthil, A. Malathi, A. Selvi, J. Madhavan and A. Muthupandian, *RSC Advances*, 2015, 5, 52718-52725.
- [57] A. I. J. Joseph and S. Thiripuranthagan, *RSC Advances*, 2015, 5, 9792-9805.
- [58] J. Gong, J. Liu, X. Chen, Z. Jiang, X. Wen, E. Mijowska and T. Tang, *Journal of Material Chemistry A*, 2014, 2, 7461-7470.
- [59] Z. Hu, H. Chen, F. Ji and S. Yuan, *Journal of Hazardous Materials*, 2010, 173, 292-297.
- [60] M. Khadhraoui, H. Trabelsi, M. Ksibi, S. Bouguerra and B. Elleuch, *Journal of Hazardous Materials*, 2009, 161, 974-981.

- [61] K. P. Gopinath, H. A. M. Sahib, K. Muthukumar and M. Velan, *Bioresource Technology*, 2009, 100, 670-675.
- [62] K. P. Gopinath, K. Muthukumar and M. Velan, *Chemical Engineering Journal*, 2010, 157, 427-433.
- [63] A. T. Ojedokun and O. S. Bello, *Applied Water Science*, 2017, 7, 1965-1977.
- [64] R. K. Wahi, W. W. Yu, Y. Liu, M. L. Mejia, J. C. Falkner, W. Nolte and V. L Colvin, *Journal of Molecular Catalysis A: Chemical*, 2005, 242, 48-56.
- [65] H. R. Pouretedal and M. H. Keshavarz, *Journal of Alloys and Compounds*, 2010, 501, 130-135.
- [66] J. Miao, A. Xie, S. Li, F. Huang, J. Cao and Y. Shen, *Applied Surface Science*, 2016, 360, 594-600.
- [67] H. Zhu, R. Jiang, L. Xiao, Y. Chang, Y. Guan, X. Li and G. Zeng, *Journal of Hazardous Materials*, 2009, 169, 933-940.
- [68] M. Bagheri, A. R. Mahjoub and B. Mehri, *RSC Advances*, 2014, 4, 21757-21764.
- [69] O. Mehraj, B. M. Pirzada, N. A. Mir, S. Sultana and S. Sabir, *RSC Advances*, 2015, 5, 42910-42921.
- [70] Z. Zhang, W. Wang and E. Gao, *Journal of Materials Science*, 2014, 49, 7325-7332.
- [71] A. Kania, E. Talik, M. Szubka, W. R. Romanowski, A. Niewiadomski, S. Miga and M. Pawlik, *Journal of Alloys and Compounds*, 2016, 654, 467-474.
- [72] H. Lv, Y. Liu, J. Hu, Z. Li and Y. Lu, *RSC Advances*, 2014, 4, 63238-63245.
- [73] S. G. Kumar and K. S. R. K. Rao, *Applied Surface Science*, 2015, 355, 939-958.
- [74] Q. Xiao, J. Zhang, C. Xiao, and X. Tan, *Catalysis Communications*, 2008, 9, 1247-1253.
- [75] D. Wang, L. Guo, Y. Zhen, L. Yue, G. Xue and F. Fu, *Journal of Material Chemistry A*, 2014, 2, 11716-11727.
- [76] J. P. Dhal, B. G. Mishra and G. Hota, *RSC Advances*, 2015, 5, 58072-58083

CHAPTER 4

Visible Light Driven Photocatalytic Study of Bi₂W₂O₉ Based Materials

Section A

Selective Aerobic Oxidation of Amines to Imines Catalyzed by CdS/Bi₂W₂O₉ Heterojunction Materials

4.1 Introduction

In Chapter 3, we have described the synthesis and photocatalytic application of Bi₂WO₆ and CuS/Bi₂WO₆ heterojunction material. Bi₂WO₆ is the simplest member of the Aurivillius family of layered perovskites of general formula [Bi₂O₂][A_{n-1}B_nO_{3n+1}] (A=Ca, Sr, Ba, Pb, Bi, Na, K and B =Ti, Nb, Ta, Mo, W, Fe) [1, 2]. It is “A” cation-deficient bismuth-layered compounds with n =1 in the structural formula. In this chapter, we have presented the synthesis and photocatalytic application of Bi₂W₂O₉ based materials, which is the second member of this homologous series. Bi₂W₂O₉ although homologous to the Bi₂WO₆, it display certain unique properties for which it has generated significant interest in the material science community [1, 3-11]. Kudo and Hiji have reported that the photocatalytic activity of Bi₂W₂O₉ is over ten times than Bi₂WO₆ for H₂ and O₂ evolution under UV radiation [1]. Particularly, the Bi₂W₂O₉ is an ideal photocatalyst to carry out oxidation reactions due to its high positive valence band potential [8, 10]. The optical absorption and photocatalytic properties of Bi₂W₂O₉ can be improved significantly by coupling with suitable low band gap semiconductors with matching band potential to form heterojunction materials. With an intention to explore novel photocatalytic application of Bi₂W₂O₉ based heterostructures, in this chapter, we have described the synthesis and photocatalytic application of CdS/Bi₂W₂O₉ and CuS/Bi₂W₂O₉ heterojunction materials towards selective oxidation reaction and mineralization of potentially toxic diuron pesticide under visible light. In this section, the selective oxidation of amines to imines catalyzed by CdS/Bi₂W₂O₉ heterojunction is described. In the subsequent section, the photocatalytic application of CdS/Bi₂W₂O₉ heterojunctions toward degradation of diuron pesticide is presented.

CdS is one of the well explored narrow band gap photocatalyst with band gap energy of 2.42 eV. CdS has been successfully used as visible light active photocatalyst for oxidation of

dichloro acetic acid, few organic transformations and water splitting reaction [12-15]. Because of its narrow band gap, CdS has been coupled with many wide band gap semiconductors such as TiO₂, Bi₂MoO₆, g-C₃N₄, Bi₂PO₄ and SrS to prepare highly efficient visible light active photocatalytic systems [16-20]. The CdS based coupled semiconductor systems have been evaluated as photocatalyst for H₂ evolution and degradation of organic pollutants under visible light.

The oxidation of amines to imines is one of the important reactions since imines are used as building blocks for many pharmaceuticals and organic dyes molecules [21-23]. The conventional oxidation of amine involves the use of costly noble metal catalysts at elevated temperatures. The adverse environmental impact of oxidants, solvent wastage and unwanted by-product formation are major concerns in the conventional amine oxidation processes [21, 23]. The heterogeneous photocatalytic route is a promising alternative to the conventional method of fine chemical synthesis [24-27]. Till date, very few photocatalyst such as TiO₂, Nb₂O₅, WS₂, BiVO₄, BiOX, g-C₃N₄, AgI/AgVO₃, Au-cluster, ZnIn₂S₄, CuWO₄, and organic polymers have been studied for the oxidation of amines [21-23, 28-38]. Some of these reported photocatalytic protocols require longer time, employ photocatalyst with poor response to visible light and require molecular O₂ to carry out the oxidation reaction. Keeping in mind the advantages and disadvantages of the reported photocatalytic protocols, there is a lot of scope to develop highly efficient novel photocatalytic systems which can accomplish this oxidation reaction in aerobic condition under visible light irradiation. In this work, we have used CdS/Bi₂W₂O₉ heterojunction materials as an efficient and selective photocatalyst for oxidation of amines under mild condition.

4.2 Results and discussion

4.2.1 XRD Study

The XRD patterns of CdS/Bi₂W₂O₉ (CdSBWO) heterojunction materials together with pure Bi₂W₂O₉ and CdS are presented in Fig. 4.1. Pure Bi₂W₂O₉ material exhibits intense and sharp diffraction peaks at d-spacing values 3.95, 3.79, 3.45, 3.22, 2.98, 2.96, 2.75, 2.71, 2.42, 1.91, 1.65, 1.61 and 1.55 Å (Fig. 4.1a). These peaks correspond to diffraction from the (006), (111), (113), (114), (115), (008), (116), (020), (120), (220), (134), (228) and (229) crystallographic planes of orthorhombic bismuth tungstate (JCPDS No- 33-0221, space group- Pbn21). No impurity peaks corresponding to any analogous phase like Bi₂WO₆ could be detected from XRD indicating the high phase purity of the synthesized material.

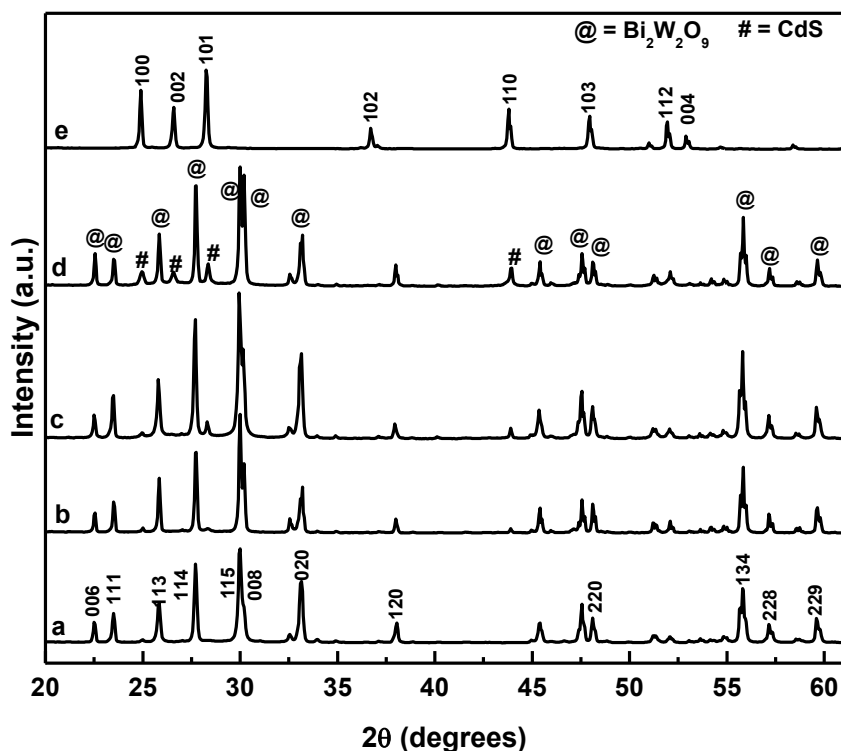


Figure 4.1: X-ray diffraction patterns of (a) $\text{Bi}_2\text{W}_2\text{O}_9$, (b) CdS_5BWO , (c) $\text{CdS}_{10}\text{BWO}$, (d) $\text{CdS}_{20}\text{BWO}$ and (e) CdS materials.

For pure CdS sharp and intense diffraction peaks are observed at d-spacing values of 3.58, 3.35, 3.16, 2.45, 2.07, 1.89, 1.76 and 1.67 Å. These peaks correspond to the diffraction from the (100), (002), (101), (102), (110), (103), (112) and (004) crystallographic planes of hexagonal cadmium sulphide phase (JCPDS No- 41-1049, space group- P63mc) (Fig. 4.1e). The CdS_5BWO heterojunction display characteristic diffraction peaks of BWO phase only (Fig. 4.1b). However, for $\text{CdS}_{10}\text{BWO}$ and $\text{CdS}_{20}\text{BWO}$ heterojunction materials low intense but distinguishable diffraction peaks for CdS phase was observed together with BWO phase (Fig. 4.1c & 4.1d). The XRD results clearly indicate the presence of both the $\text{Bi}_2\text{W}_2\text{O}_9$ and CdS crystalline phases in the CdSBWO heterojunction materials.

4.2.2 XPS Study

The oxidation state and chemical environment of the constituent elements in the heterojunction material is probed using XPS study. The XPS spectra of $\text{CdS}_{20}\text{BWO}$ heterojunction is presented in Fig. 4.2. Figure 4.2a represents the survey spectrum which confirmed the presence of Bi, W, Cd, O and S along with adventitious carbon in the sample. In the high resolution spectral region for Bi, a doublet is observed at 158.8 eV and 164 eV, respectively (Fig. 4.2b). These peaks are assigned to photoelectron emission from $\text{Bi}4f_{7/2}$ and

Bi4f_{5/2} electronic states of Bi in +3 oxidation state [8]. In this spectral region, a noticeable low intense broad peak at 162.4 eV is assigned to the S2p state [39]. Figure 4.2c presents the fine spectra of W in the 4f region. The binding energy value of 35.2 eV and 37.4 eV with a splitting factor of 2.2 eV can be attributed to W4f_{7/2} and W4f_{5/2} electronic states of W in +6 oxidation state [8]. A symmetrical doublet observed at binding energy values of 405.1 eV and 411.8 eV with a spin orbit splitting value of 6.7 eV is due to the Cd3d_{5/2} and Cd3d_{3/2} electronic states of Cd in +2 oxidation state (Fig. 4.2d) [16, 17, 39]. Figure 4.2e represents the high resolution XPS spectra for O in 1s region. A broad asymmetric peak is observed which is fitted to two peaks. These two peaks correspond to the presence of oxygen in two different electronic environments. The peaks at binding energy value of 529.7 eV is attributed to the oxygen in the (W₂O₇)²⁻ Perovskite layers while the binding energy value of 531.1 eV is due to the oxygen associated with the interlayer (Bi₂O₂)²⁺ species [8]. In the high resolution XPS spectra in the S 2s region, a broad peak with maxima at 225.7 eV is observed (Fig. 4.2f). This broad peak confirmed the presence of sulphide ions (S²⁻) [40].

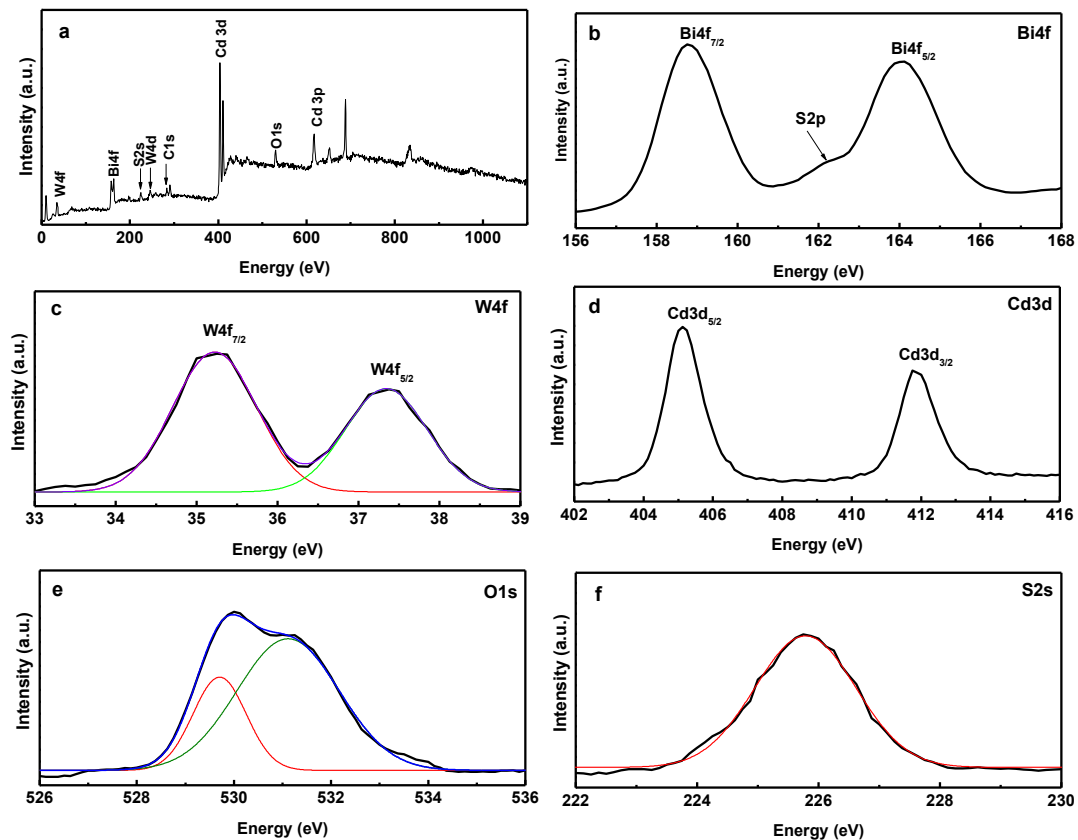


Figure 4.2: XPS spectra of CdS20BWO heterojunction material.

4.2.3 Morphological Study

The morphology of the BWO and CdSBWO heterojunction materials is studied by FESEM and HRTEM analysis. The FESEM images of BWO and CdSBWO materials are presented in Fig. 4.3. The BWO material contains micron size plates with L x B x H in the range of 0.40-2.30 μm , 0.31-1.68 μm and 0.08-0.42 μm , respectively (Fig. 4.3a). The CdSBWO heterojunction materials contain uniformly distributed spherical CdS nanoparticles grafted over the BWO plates (Fig. 4.3b-4.3d). With increase in the CdS content in the heterojunction materials the particle density of anchored CdS species increases. Moreover, local aggregation of the CdS particles is observed at higher content.

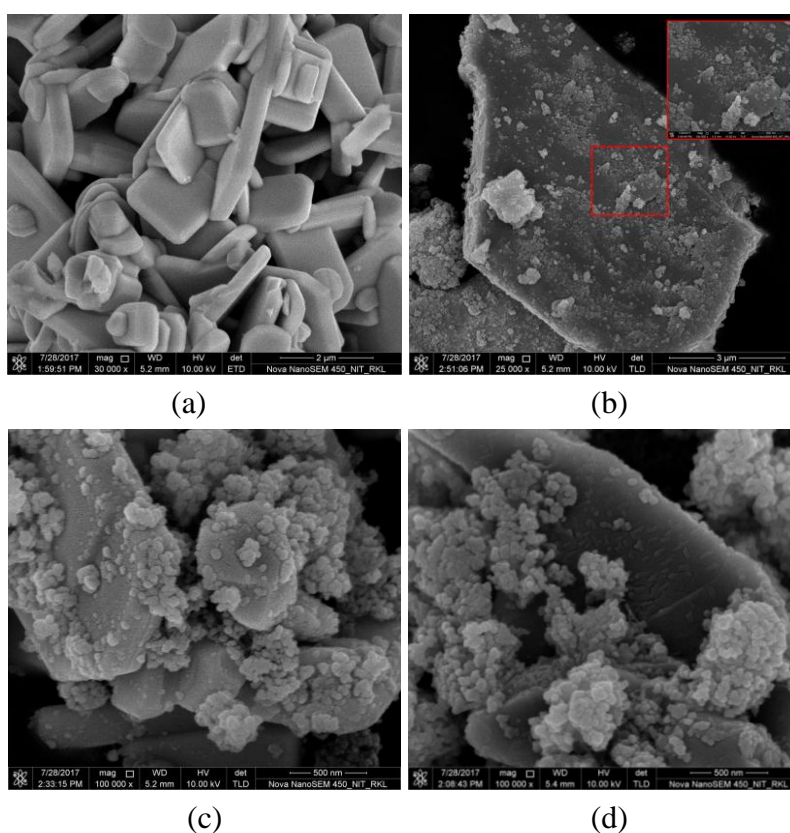


Figure 4.3: FESEM images of (a) Bi₂W₂O₉, (b) CdS₅BWO, (c) CdS₁₀BWO and (d) CdS₂₀BWO heterojunction materials.

The size and shape of CdS nanoparticles are further investigated using HRTEM analysis. Fig. 4.4 represents the TEM images of CdS₁₀BWO heterojunction material. The presence of ultrafine near spherical CdS nanoparticles with size in the range of 8-15 nm is noticed for the CdS₂₀BWO material (Fig. 4.4a & b). The CdS nanoparticles are in an agglomerated state and are attached to each other through the grain boundary (Fig. 4.4a). The high magnification TEM image of CdS₁₀BWO material revealed the formation of heterojunction between the two phases (Fig. 4.4c). The calculated inter-planar distance matches with the (113) crystallographic plane of Bi₂W₂O₉ and (002), (101) planes of CdS species (Fig. 4.4c). The elemental mapping and EDX spectrum of the heterojunction material is presented in Fig.

4.4d-4.4j. Homogeneous distribution of Bi, W, O, Cd and S elements throughout the microscopic specimen sample is observed from the elemental mapping study (Fig. 4.4 d-i). The presence CdS and Bi₂W₂O₉ in required stoichiometric quantity is inferred from the EDX study of CdS10BWO heterojunction material (Fig. 4.4j).

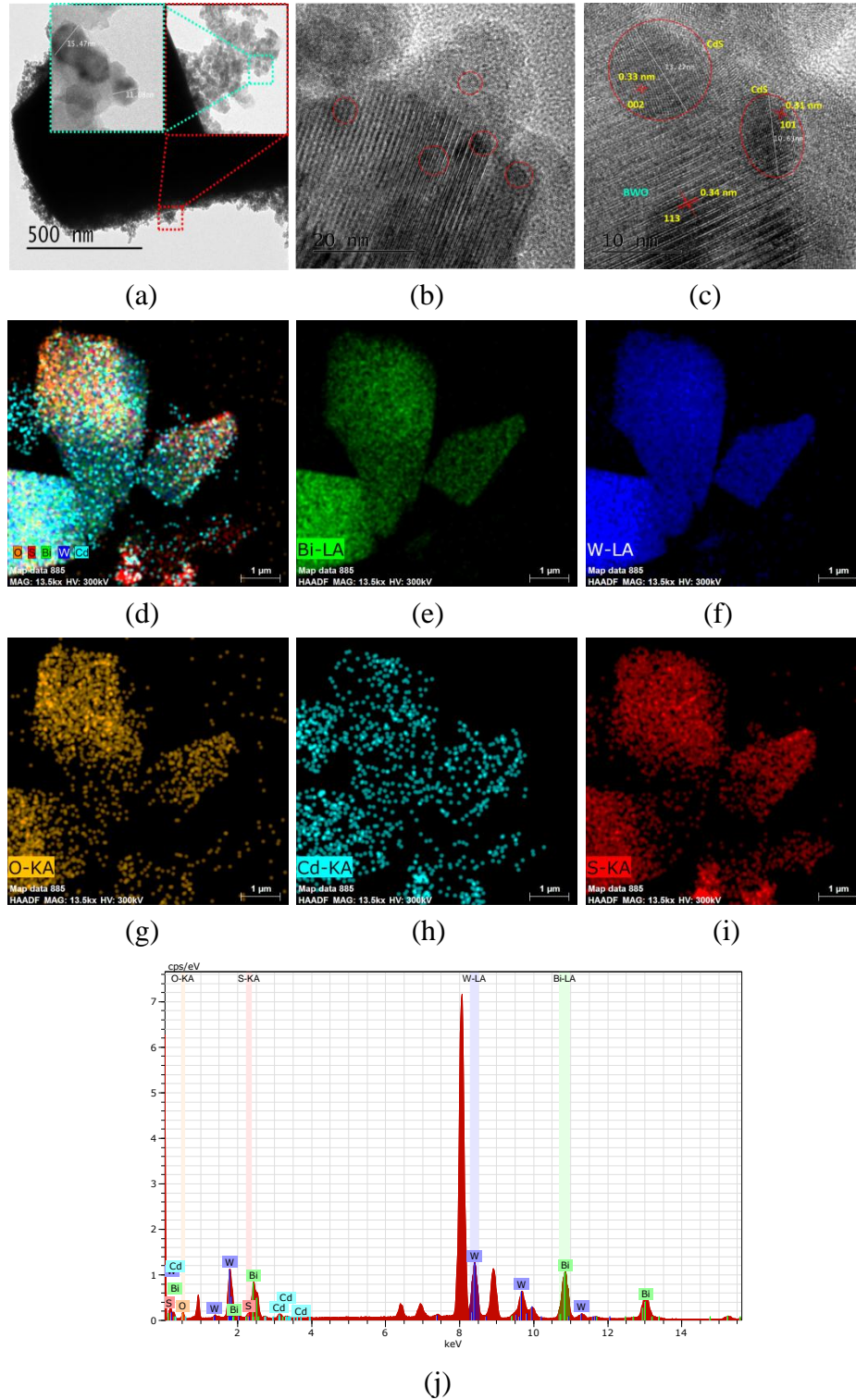


Figure 4.4: (a-c) TEM images, (d-i) EDS mapping and (j) EDX spectrum of CdS10BWO heterojunction material.

The crystallite size of the CdS phase in the CdSBWO heterojunction materials is calculated by Fourier line profile analysis of XRD peaks by Warren and Averbach method using BRAEDTH software [41]. The Fourier analysis is performed by using (101) and (110) peaks of the CdS phase. The plots of distribution function (PV) and size coefficient (AS) vs Fourier length (L) for pure CdS, CdS10BWO and CdS20BWO materials are presented in Fig. 4.5. The average crystallite sizes calculated from the initial slope of AS~L plots (Fig. 4.5I) are presented in Table 4.1. The heterojunction materials display average crystallite sizes in the range of 7-12 nm. The Fourier analysis data is found to be complimentary to the crystallite size observed from HRTEM study. The BWO and CdS materials exhibit a specific surface area of 14.3 and 32.3 m²/g. The heterojunction material exhibits surface area in the range of 24-32 m²/g (Table 4.1).

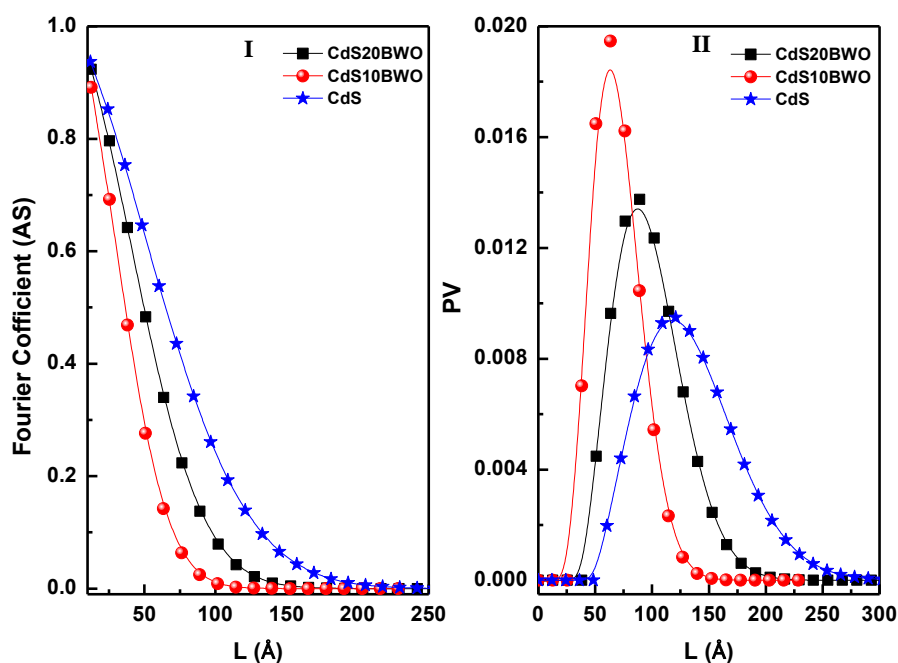


Figure 4.5: Fourier line profile analysis plots for CdS and CdSBWO heterojunction materials.

Table 4.1: Specific surface area and crystallite size of CdS phase in CdSBWO heterojunction materials.

Sl. No	Catalyst	Specific Surface area (m ² /g)	Crystallite size of CdS phase (nm) ^a
1	Bi ₂ W ₂ O ₉	14	---
2	CdS	33	14.5 ± 1.0
3	CdS5BWO	25	---
4	CdS10BWO	29	8.5 ± 1.5
5	CdS20BWO	32	10.5 ± 1.6

a. Calculated from the Fourier line profile analysis of the XRD peaks

4.2.4 Optical Properties Study

The optical property of the CdSBWO heterojunction materials is studied by UV-Vis-DRS and PL techniques. Figure 4.6I depicts the UV-Vis-DRS spectra of pure BWO and CdS together with CdSBWO heterojunction materials.

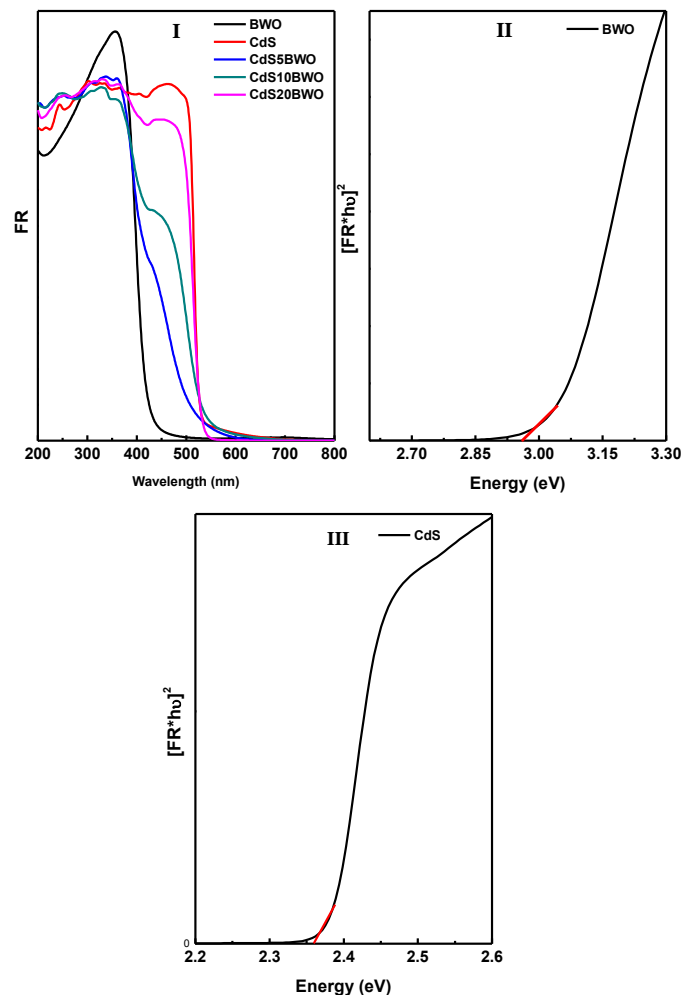


Figure 4.6: UV-Vis DRS (Panel I), plot of $[F(R) \times h\nu]^2$ as a function of photon energy ($h\nu$) in eV of $\text{Bi}_2\text{W}_2\text{O}_9$ (Panel II) and CdS (Panel III) nanomaterials.

Pure BWO shows strong absorption in the UV region, which extend up to visible region. Similarly, pure CdS shows optical absorption in the visible region with an absorption edge near 530 nm. The stiff absorption features observed for both BWO and CdS materials are due to band edge transition rather than the transition from the impurity level. Upon modification with CdS, for all the CdSBWO heterojunction materials the absorption edge shifted to the lower energy region with improved visible light absorption feature. The calculated band gap values for the pure BWO and CdS are 2.95 and 2.36 eV, respectively (Fig. 4.6 II & III). For the CdS and BWO materials the observed band gap values are consistent with the literature reported values [3, 8, 9, 16, 19].

The charge separation property of the CdSBWO heterojunction materials is studied by using PL technique and photocurrent measurement. The PL spectra of CdSBWO heterojunction materials at an excitation wavelength of 320 nm are presented in Fig. 4.7. Pure BWO material exhibits PL emission bands at 465, 480 and 490 nm, respectively (Fig. 4.7 a). The emission bands observed at 465 nm is due to the band gap transition whereas the PL bands at 480 and 490 nm are due to presence of defects and vacancies in the BWO material [10]. The intensities of these PL bands decrease significantly after modification with CdS. This observation indicates efficient charge carrier separation in the CdSBWO heterojunction materials (Fig. 4.7 b-d).

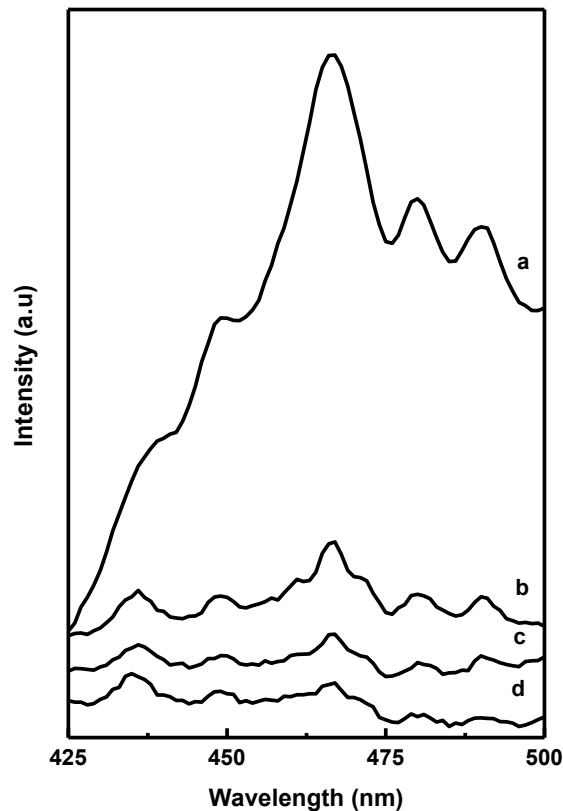


Figure 4.7: PL spectra of (a) $\text{Bi}_2\text{W}_2\text{O}_9$, (b) CdS5BWO, (c) CdS10BWO and (d) CdS20BWO heterojunction materials.

The charge carrier separation property is further studied from the photocurrent measurement of the BWO and CdS20BWO materials. The enhancement in photocurrent of CdS20BWO material over BWO material indicates an improvement in the charge carrier separation ability of the heterojunction material (Fig. 4.8I).

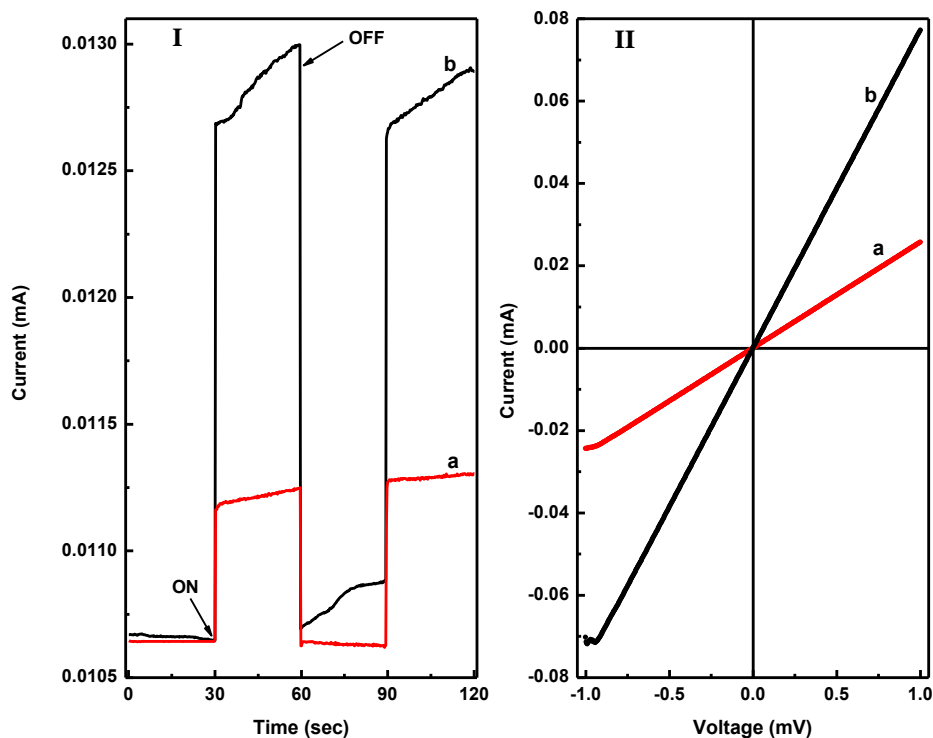


Figure 4.8: (I) Transient photocurrent and (II) current (I) vs voltage (V) measurement plots for (a) BWO and (b) CdS20BWO heterojunction materials.

The current (I) vs voltage (V) measurement for the BWO and CdS20BWO heterojunction material is presented in Fig. 4.8II. The higher slope observed in I-V plot for CdS20BWO heterojunction material indicate higher mobility of the photo excited electrons (Fig. 4.8II). The enhanced photocurrent and improved charge transport efficiency of the CdS20BWO material can be ascribed to the formation of heterojunction between the CdS and BWO components which allow facile migration of charge carriers across the grain boundary. The UV-Vis-DRS and PL study along with the calculated band gap values suggest that the CdSBWO heterojunction materials can be used as photocatalyst under visible light.

4.2.5 FTIR Study

The FTIR spectra of CdSBWO heterojunction materials along with pure BWO material are presented in Fig. 4.9. Pure BWO possesses broad bands at 437, 561, 745, 851 and 952 cm^{-1} (Fig. 4.9a). The bands at 437 and 561 cm^{-1} correspond to the Bi-O stretching vibrations whereas the 745, 851 and 952 cm^{-1} bands are assigned to the symmetric and asymmetric W-O stretching vibrations for WO_6 octahedron [42, 43]. All the CdSBWO heterojunctions display new set of IR bands at 635, 1150 and 1215 cm^{-1} along with the characteristic vibrational features of BWO (Fig. 4.9 b-d).

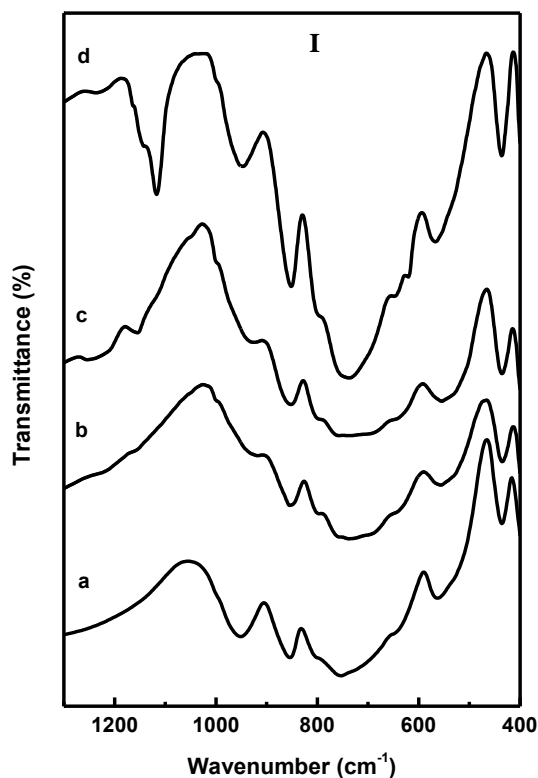
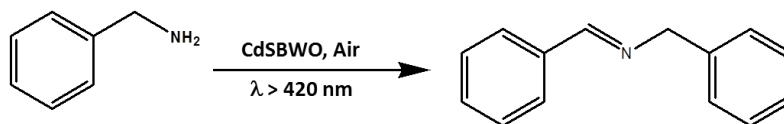


Figure 4.9: FTIR spectra of (a) $\text{Bi}_2\text{W}_2\text{O}_9$, (b) CdS5BWO, (c) CdS10BWO and (d) CdS20BWO heterojunction materials.

These bands are due to the characteristic vibrations for CdS component in the CdSBWO heterojunction materials [44]. The FTIR study revealed the presence of CdS and BWO components in the CdSBWO heterojunction materials.

4.2.6 Photocatalytic Selective Oxidation of Amines to Imines

The photocatalytic activity of the CdSBWO heterojunction materials is evaluated for the selective oxidation of benzylamine under visible light irradiation using air as oxidant (Scheme 4.1).



Scheme 4.1: Selective photocatalytic oxidation of benzylamine catalyzed by CdSBWO heterostructure photocatalyst.

As a model reaction, a mixture containing 1 mmol of benzylamine and 25 mg of CdSBWO catalyst in 5 ml CH_3CN solvent is stirred under dark condition for 30 min to achieve adsorption-desorption equilibrium. The reaction mixture was exposed to visible light under constant stirring. The progress of the reaction is monitored by gas chromatography. In absence of catalyst and under dark condition, the formation of N-Benzylidenebenzylamine

could not be detected which confirmed the photocatalytic nature of the oxidation reaction. The photocatalytic efficiency of the CdSBWO heterojunction photocatalysts together with CdS and BWO material is presented in Fig. 4.10. Although both pure CdS and BWO materials are active towards the oxidation reaction, the percentage conversion is quite low (22.5 and 40.2 % for BWO and CdS material, respectively after 12 h). In contrast to this observation, all the CdSBWO heterojunction materials exhibited higher photocatalytic efficiency with good percentage conversion and selectivity towards N-Benzylidenebenzylamine (Fig. 4.10I). Among the heterojunction materials, CdS20BWO exhibited highest photocatalytic efficiency achieving 89.3 % conversion after 8 h of reaction. Since, the surface area of CdSBWO heterojunctions increase with CdS content, the role of surface area on the photocatalytic activity is evaluated by depositing 20 wt% of CdS over BWO material by precipitation (P) and reflux (R) methods using literature reported procedure [45, 46]. The CdS20BWO-P and CdS20BWO-R materials show surface area of 20.5 m²/g and 24.3 m²/g, respectively. These materials after 8 h of reaction time exhibited 83.5 and 84.7 % conversion of benzyl amine. This observation indicates that the CdS content in the heterojunction is the primary factor responsible for higher photocatalytic activity. The presence of CdS improves the visible light absorption and charge carrier separation properties of BWO which is vital for the photocatalytic activity. Based on the results described in Fig. 4.10I, the CdS20BWO material is chosen for further study.

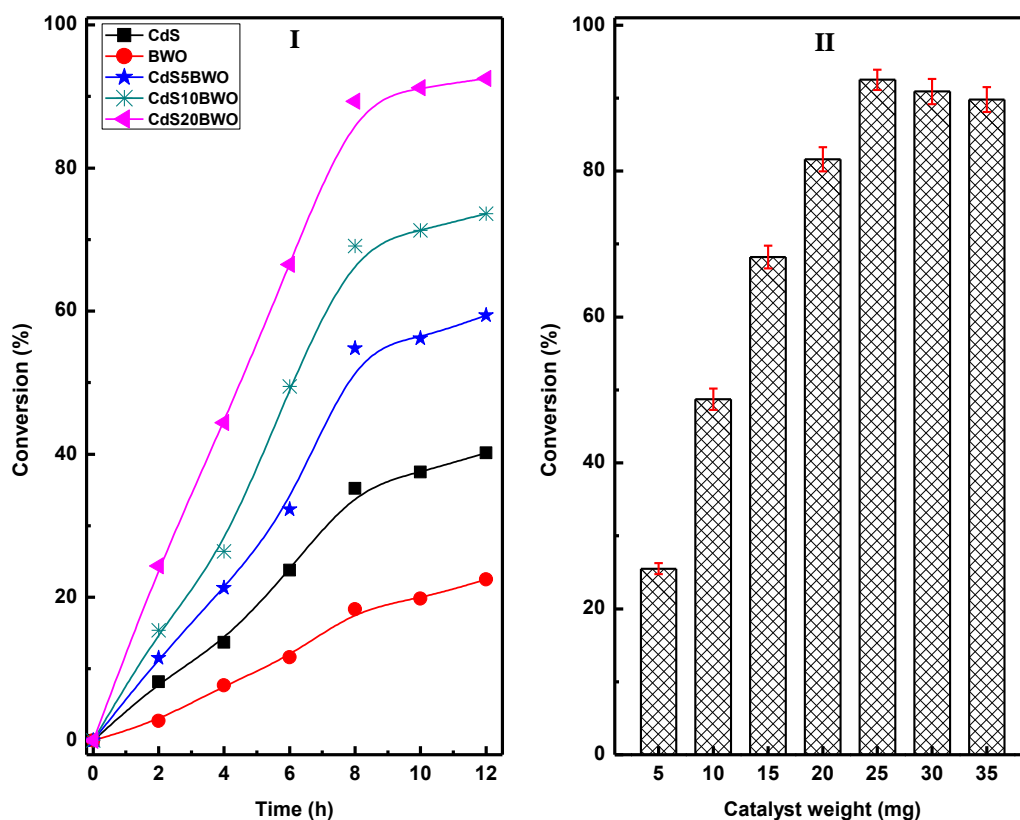


Figure 4.10: Photocatalytic efficiency of CdSBWO heterojunctions (Panel I) and catalyst weight variation of CdS20BWO heterojunction (Panel II) for the photocatalytic selective oxidation of benzylamine.

The catalyst weight is optimized by varying the catalyst amount between 5-35 mg in the reaction mixture. It is observed that, 25 mg of CdS20BWO catalyst is sufficient to carry out the oxidation of 1 mmol of the reactant with excellent conversion and selectivity (Fig. 4.10II). Further increase in catalyst amount does not have any significant impact on amine oxidation. The effect of solvent on benzylamine oxidation is studied by using different reaction media in presence of CdS20BWO photocatalyst (Table 4.2).

Table 4.2: Photocatalytic oxidation of benzylamine catalyzed by CdS20BWO heterojunction material.

Sl. No ^a	Solvent	Oxidant	Time (h)	Conversion ^b (%)	Selectivity (%)
1	CH ₃ CN	Air	12	92.5	> 99
2	CH ₃ OH	Air	12	88.4	> 99
3	C ₂ H ₅ OH	Air	12	85.8	> 99
4	H ₂ O	Air	12	26.5	45
5	CHCl ₃	Air	12	84.7	> 99
6	CH ₂ Cl ₂	Air	12	82.4	> 99
7	Hexane	Air	12	56.4	> 99
8	Toluene	Air	12	53.6	> 99
9	DMF	Air	12	81.2	> 99
10	DMSO	Air	12	83.5	> 99
11	CH ₃ CN	N ₂	24	---	---
12	CH ₃ CN	O ₂	8	93.6	> 99
13	CH ₃ CN	O ₃	6	90.2	> 99
14	CH ₃ CN	Oxone	6	92.3	> 99
15	CH ₃ CN	NaClO	6	92.7	> 99

a. Reaction conditions: benzylamine (1 mmol), solvent (5 mL), catalyst 25 mg (CdS20BWO),

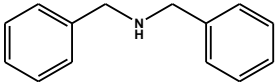
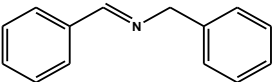
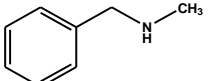
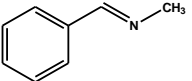
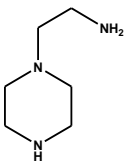
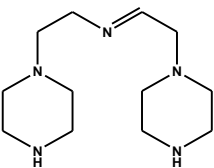
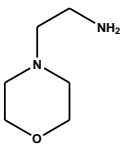
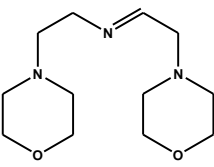
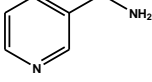
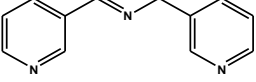
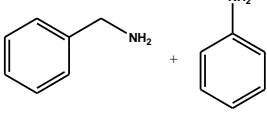
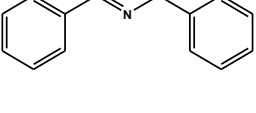
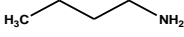
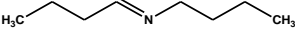
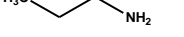
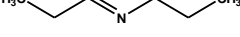
b. Determined from GC analysis

The catalytic activity is significantly higher in polar solvents in comparison to the nonpolar solvents. The higher conversion in polar organic solvent can be ascribed to better solubility of the reactant molecules and their easy accessibility to the catalyst surface. Highest conversion of benzyl amine is obtained using acetonitrile as solvent. Hence further studies are performed using acetonitrile as solvent. However in case of H₂O as solvent we observed less conversion (26.5%) with poor selectivity (45%). The low conversion in aqueous medium is due to the poor solubility of the amine molecule in H₂O in comparison to polar organic media and limited accessibility of amine molecules to the photocatalyst surface. Moreover, during the photocatalytic reactions in aqueous media the •OH radicals are generate due to oxidation in VB holes. The formation of •OH radicals leads to the formation of nonselective products, which is account for the lower selectivity of the oxidation of amine to imine in H₂O solvent. In order to study the effect of different oxidant on the oxidation of benzylamine, the oxidation

reaction is carried out in presence of 3 molar excess of different oxidants (Table 4.2, entry 13-15). It is observed that in presence of strong oxidants, the oxidation rate is expedited and > 90 % of conversion is achieved within 6 h (Table 4.2). When the reaction is conducted under N₂ atmosphere no benzylamine conversion is noticed even after 24 h of reaction (Table 4.2, entry 11). This observation suggests that under aerobic condition, the molecular O₂ present in dissolved state acts as oxidant in oxidizing the benzylamine. Although better conversion are achieved using different oxidant within a short span of time, further studies are carried out in presence of atmospheric air as oxidant in order to make the processes sustainable and greener.

After optimizing various reaction parameters, the versatility the CdS20BWO catalyzed oxidation protocol is tested by using different amines (Table 4.3). The CdS20BWO photocatalyst is highly active for selective oxidation of both the primary as well as secondary amines to the corresponding imines. However, the oxidation rate for secondary amines is relatively sluggish along with by-products formation (Table 4.3, Entry 1 & 2).

Table 4.3: Selective oxidation of various amines catalyzed by CdS20BWO heterojunction material

Entry	Reactant ^a	Product	Conversion ^b (%)	Selectivity (%)
1			81.6	> 90
2			66.4	85
3			86.4	> 90
4			88.6	> 90
5			90.3	> 90
6			89.4	85
7			18.5	70
8			14.3	68

a. Reaction conditions: amine (1 mmol), solvent (5 mL), catalyst 25 mg (CdS20BWO), reaction time 12 h

b. Determined from GC analysis

Excellent conversions are also observed for the oxidation of heterocyclic amines with very good selectivity towards imines (> 90 %) (Table 4.3, Entry 3, 4 & 5). In case of aliphatic primary amine the conversion is quite low with poor selectivity to corresponding imines (Table 4.3, Entry 7 & 8). The oxidation protocol is also extended to mixed system by taking 0.5 mmol each of benzylamine and aniline (Table 4.3, Entry 6). Formation of both N-benzylidene(phenyl)methanamine and N-benzylidenebenzenamine is noticed for this mixed amine system. However, the CdS20BWO catalyzed photocatalytic protocol is more selective towards formation of N-benzylidene(phenyl)methanamine (Selectivity 85 %). The results described in Table 4.3 suggest that the CdS20BWO catalyzed photocatalytic protocol is applicable for the oxidation of a variety of amines under visible light irradiation.

In order to understand the mechanism of photocatalytic oxidation of benzylamine, control experiments are performed in presence of equimolar quantity of different radical scavengers (Fig. 4.11). In presence of hole scavenger (ammonium oxalate), superoxide radical scavenger (benzoquinone) and electron scavenger (AgNO₃), the oxidation rate of benzylamine decreases drastically. However, presence of hydroxyl radical scavenger (t-BuOH and isopropanol) only marginally affects the oxidation reaction (Fig. 4.11). This observation rules out the active role of hydroxyl radical during the oxidation of benzylamine. Hence from scavenger experiments, the h⁺, e⁻ and O₂⁻ are identified as the primary active species responsible for the selective aerobic oxidation of benzylamine. Based on the scavenger experiment, a plausible mechanism for the amine oxidation is proposed over the CdSBWO photocatalyst surface (Fig. 4.12). Upon irradiation, the electrons get excited to the conduction band (CB) leaving behind the holes in the valence band (VB). Since the band gap of both the BWO and CdS components are < 3 eV, both the components of the heterojunction are capable to generate excitons under visible light irradiation. The valence band (VB) and conduction band (CB) potentials of the pure CdS and BWO materials are calculated theoretically using the formula in equation 4.1 [17].

$$E_{VB} = X + 0.5E_g - E_e \text{ and } E_{CB} = E_{VB} - E_g \quad \dots\dots\dots (4.1)$$

E_{VB} and E_{CB} correspond to the valence and conduction band edge potential (eV vs NHE). X is the electronegativity of the semiconductor. Whereas, E_e and E_g are the energy of free electron (4.5 eV) on hydrogen scale and band gap of the photocatalyst. The reported X value for CdS photocatalyst is 5.05 eV [17]. The X value for Bi₂W₂O₉ is calculated using equation 4.2 and 4.3 [47].

$$X_M = 1/2(A_f(M) + I_1(M)) \quad \dots\dots\dots (4.2)$$

$$X(\text{Bi}_2\text{W}_2\text{O}_9) = [(X_{\text{Bi}})^2 \times (X_{\text{W}})^2 \times (X_{\text{O}})^9]^{1/13} \quad \dots\dots\dots (4.3)$$

Where, X_M is arithmetic mean of the electron affinity (A_f) and the first ionization potential (I₁) of the constituent atoms (here Bi, W and O). The X value for Bi₂W₂O₉ is calculated to be 6.3 eV. The CB of pure CdS and BWO occur at -0.62 eV and 0.325 eV respectively, whereas the VB are placed at 1.74 eV and 3.275 eV.

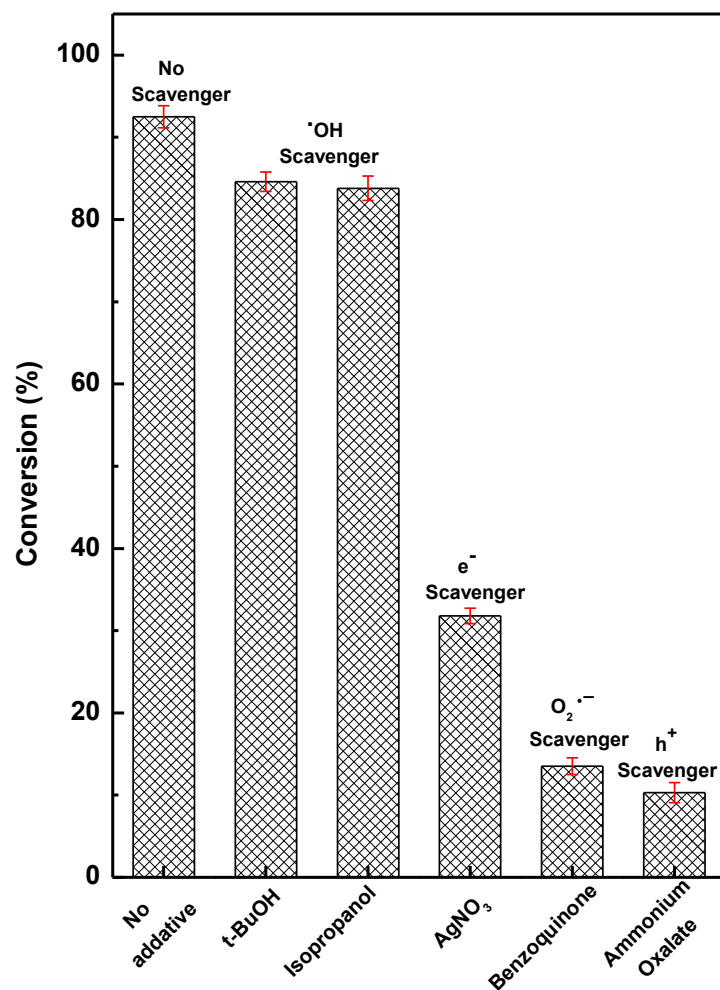


Figure 4.11: Photocatalytic oxidation of benzylamine in presence of different radical scavengers catalyzed by CdS20BWO catalyst (benzylamine 1 mmol, catalyst 25 mg, reaction time 12 h).

Upon material contact between the two semiconductor phases, there is realignment in band positions due to Fermi level equilibration. The band realignment facilitates transfer of electrons from the CB of CdS to CB of BWO. The movement of holes takes place in reverse direction in VB resulting in formation of a type II heterojunction. The VB of both CdS and BWO are placed at a sufficiently positive potential to oxidize the benzylamine. The VB holes oxidize the benzylamine to the radical cationic species I (Fig. 4.12). On the other hand, the trapping of CB electron by O_2 leads to the formation of $\text{O}_2^{\cdot-}$ radical. The $\text{O}_2^{\cdot-}$ radical react with the benzylamine radical cation to give benzylideneamine (II) by release of H_2O_2 . A second molecule of benzylamine reacts with benzylideneamine to give the final oxidized product N-benzylidene(phenyl)methanamine with the release of H_2O and NH_3 . The proposed mechanism is in line with the earlier reports for photocatalytic oxidation of amines [22, 30-33]. The practical applicability of the CdS20BWO heterojunction photocatalyst has been evaluated by checking its activity for five consecutive cycles. After each photocatalytic cycle,

the catalyst particle are collected and washed with ethanol followed by drying at 110 °C for 12 h. The CdS20BWO heterojunction material shows excellent photocatalytic efficiency for the selective oxidation of benzylamine without any appreciable loss in activity (Fig. 4.13). This observation suggests that the CdSBWO heterojunction systems are stable and recyclable photocatalysts for the oxidation of amine.

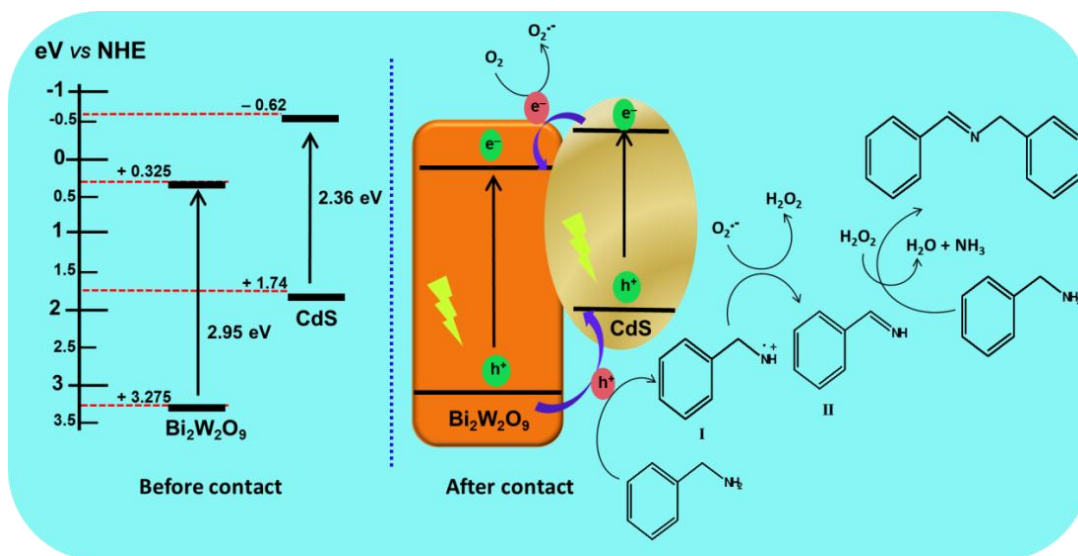


Figure 4.12: Plausible mechanism for the oxidation of benzylamine over CdSBWO heterojunction photocatalyst surface.

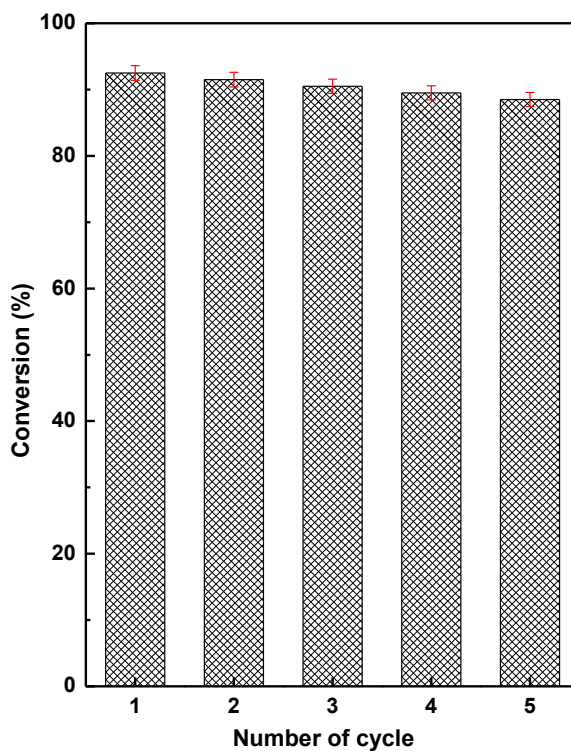


Figure 4.13: Reusability of CdS20BWO heterojunction photocatalyst for the selective oxidation of benzylamine.

Section B

Photocatalytic Mineralization of Diuron Pesticide Catalyzed by CuS/Bi₂W₂O₉ Heterojunction Materials

4.3 Introduction

Water pollution and its impact on all forms of life is a major cause of concern in present day. The industrial and agrochemical sectors are major contributors to water pollution. Wastewater from these sources contains many persistent organic pollutants like pharmaceuticals, pesticides, personal care products, surfactants, steroids, hormones and mineral oil [48-53]. Among persistent organic pollutants, pesticides are one of the major contaminant found in agricultural water due to their extensive usage. Diuron is one such widely used pesticide of halogenophenylureas family [54-56]. It is extensively used to control the broadleaf and grass weeds. Diuron is also used as an ingredient of algaecides in aquaculture [55]. Long-time exposures cause several health hazards like endocrine disorder, gastrointestinal and respiratory problems in human. It also exhibits carcinogenic and genotoxic effect [56-58]. Various methods have been adopted in literature to remove this toxic pollutant from aqueous system which include electrochemical oxidation, adsorption, biodegradation, wet air oxidation, photo Fenton oxidation and photocatalytic methods [57-70]. The photocatalytic methods have many advantages over rest of the methods in terms of the use of renewable energy source, nontoxic by-product formation, use of low cost materials and simple experimentation. So far TiO₂ based photocatalytic materials including La, Pt and N- doped TiO₂ have been studied for the degradation of diuron under UV light [58, 64-70]. The UV light active photocatalytic property of TiO₂ based materials limit their extensive application in practical field. Hence there is a need to design novel visible light active photocatalyst for the degradation of diuron pesticide. In chapter 3, we have observed that coupling of CuS with Bi₂WO₆ lead to formation of highly active visible light promoted heterojunction photocatalyst system. The CuS/Bi₂WO₆ heterojunction system was highly efficient for degradation of Congo red dye from aqueous solutions. In order to further explore the scope of bismuth tungstate based heterojunction systems in waste water treatment, in this work, we have studied the photocatalytic degradation of diuron pesticide using CuS/Bi₂W₂O₉ heterojunction material as photocatalyst under visible light.

4.4 Results and Discussion

4.4.1 XRD Study

The XRD patterns of CuSBWO heterojunction materials together with pure $\text{Bi}_2\text{W}_2\text{O}_9$ and CuS materials are presented in Fig. 4.14. Pure $\text{Bi}_2\text{W}_2\text{O}_9$ material exhibits, intense and sharp diffraction peaks corresponding to orthorhombic bismuth tungstate (JCPDS No- 33-0221, space group- Pbn21). No impurity peak corresponding to either Bi_2WO_6 or any other analogous phases could be detected indicating the high phase purity of the synthesized material (Fig. 4.14a). The XRD pattern of pure CuS corresponds to hexagonal covellite phase (JCPDS No- 78-2121, space group- P63/mmc) (Fig. 4.14f).

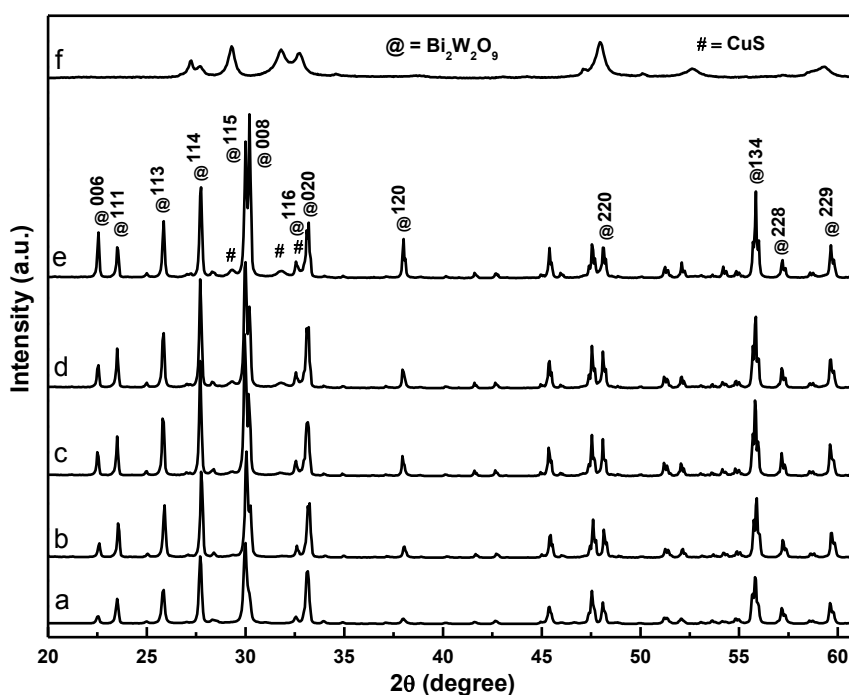


Figure 4.14: XRD patterns of (a) BWO, (b) CuS5BWO, (c) CuS10BWO, (d) CuS15BWO, (e) CuS20BWO and (f) CuS materials.

The diffraction pattern for CuS5BWO material contains characteristic peaks for $\text{Bi}_2\text{W}_2\text{O}_9$ material only (Fig. 4.14 b). In contrast to this observation, the CuS10BWO, CuS15BWO and CuS20BWO materials exhibit very low intense and broad diffraction peaks for CuS phase with d spacing values of 3.21 Å, 3.04 Å and 2.81 Å (Fig. 4.14 c-e). These materials contain crystalline biphasic system whereas for CuS5BWO material the CuS phase exist in a well dispersed state as small nanocrystallites/amorphous phase which has escaped detection by XRD. Another interesting feature of the XRD study is the gradual shift in the peak position of BWO phase to lower 2θ value with CuS content (Fig. 4.15I). A plot of d spacing values of (114) peak with CuS content shows a linear relationship satisfying Vegard's law (Fig. 4.15 II). This observation suggests partial substitution of W^{6+} ion (0.62 Å) with Cu^{2+} ion (0.73 Å)

in $\text{Bi}_2\text{W}_2\text{O}_9$ lattice to form $\text{Bi}_2\text{Cu}_x\text{W}_{2-x}\text{O}_{9-2x}$ as a nonstoichiometric substitutional solid solution.

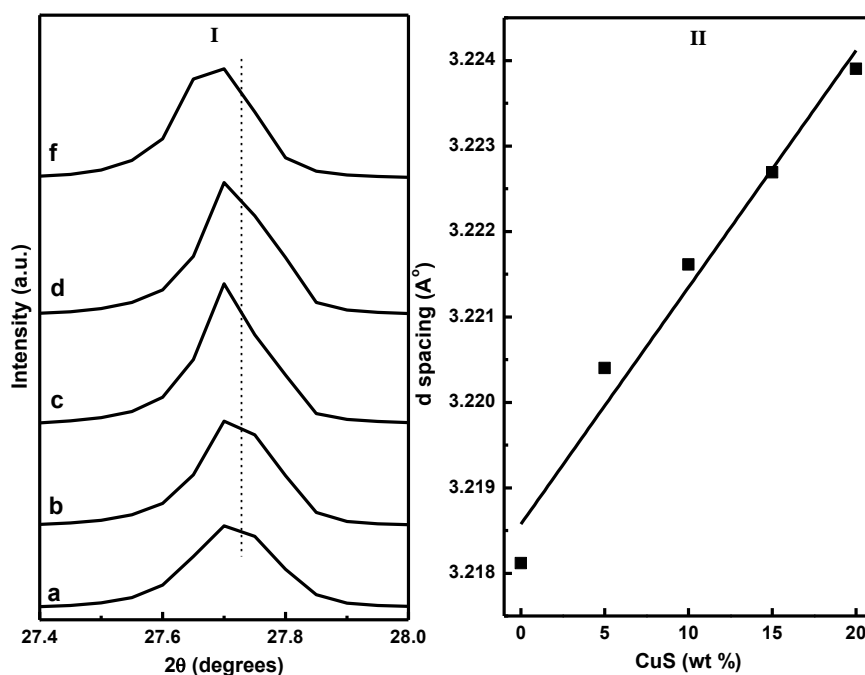


Figure 4.15: (I) Variation of peak position with CuS content for (114) peak of pure (a) BWO, (b) CuS5BWO, (c) CuS10BWO, (d) CuS15BWO, (e) CuS20BWO and (II) Vegard plot indicating an increase in d_{114} spacing with CuS content.

4.4.2 XPS Study

The XPS spectra of CuS20BWO heterojunction material are presented in Fig. 4.16. The survey spectrum shows the presence of W, Bi, O, Cu and S along with adventitious carbon (Fig. 4.16a). In the high resolution XPS spectra, a doublet is observed at 164.0 eV and 158.8 eV with a spin orbit splitting of 5.2 eV due to the $\text{Bi}4f_{5/2}$ and $\text{Bi}4f_{7/2}$ energy state of bismuth in trivalent oxidation state (Fig. 4.16b). In the W4f region, a doublet is observed at 37.1 eV and 35.0 eV, which is assigned to $\text{W}4f_{5/2}$ and $\text{W}4f_{7/2}$ states of W^{6+} species (Fig. 4.16c). For the CuS20BWO material, the observed binding energy for W^{6+} species is slightly lower than the literature reported values [8]. This lowering in binding energy value can be ascribed to the change in the electronic environment of W due to partial substitution of Cu^{2+} in the BWO lattice. In the Cu2p region a doublet is observed at 932.0 eV and 951.9 eV along with a small satellite peak at 941.9 eV. These spectral features are characteristics of Cu^{2+} species in sulphide environment (Fig. 4.16d) [71, 72].

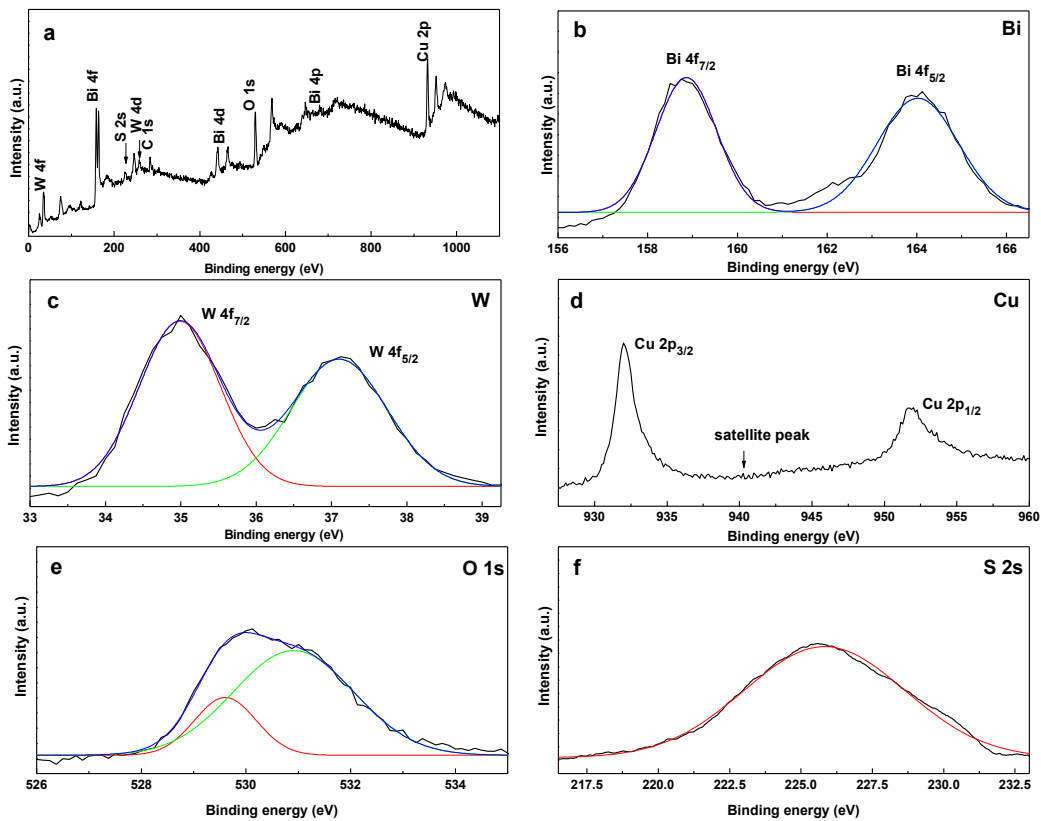


Figure 4.16: XPS spectra of CuS20BWO heterojunction material.

The O1s high resolution spectrum is broad and asymmetric due to overlapping contributions from different oxide species. The O1s spectrum can be fitted into two peaks with maxima at 529.6 and 530.9 eV corresponding to two different chemical environments. The peak at 529.6 eV can be assigned to $(W_2O_7)^{2-}$ perovskite layers while the peak at 530.9 eV is due to the interlayer oxygen of $(Bi_2O_2)^{2+}$ species (Fig. 4.16e) [8]. In the S2s region, a broad peak is noticed with binding energy value of 225.7 eV due to the S^{2-} ions of CuS phase [40]. The XPS analysis of CuS20BWO revealed the presence of CuS and Cu^{2+} substituted $Bi_2W_2O_9$ phases in the heterojunction material.

4.4.3 Optical Properties Study

The UV-Vis-DRS spectra of BWO and CuSBWO materials are presented in Fig. 4.17I. Pure BWO material shows absorption edge near 450 nm (Fig. 4.17Ia). The absorption edge for CuS commences near 890 nm (Fig. 4.17If). The CuSBWO materials show enhanced visible light absorption in comparison to pure BWO material (Fig. 4.17I b-e). For all CuSBWO materials, a new absorption feature is noticed in the visible region between 400-800 nm. The intensity of this absorption feature increases gradually with increase in CuS content. The optical band gap values of pure $Bi_2W_2O_9$ and CuS materials are calculated from Tauc's plot (Fig. 4.17II & III). Pure BWO and CuS exhibit a band gap of 2.95 eV and 1.65 eV, respectively which are consistent with reported values [8, 10, 71, 72].

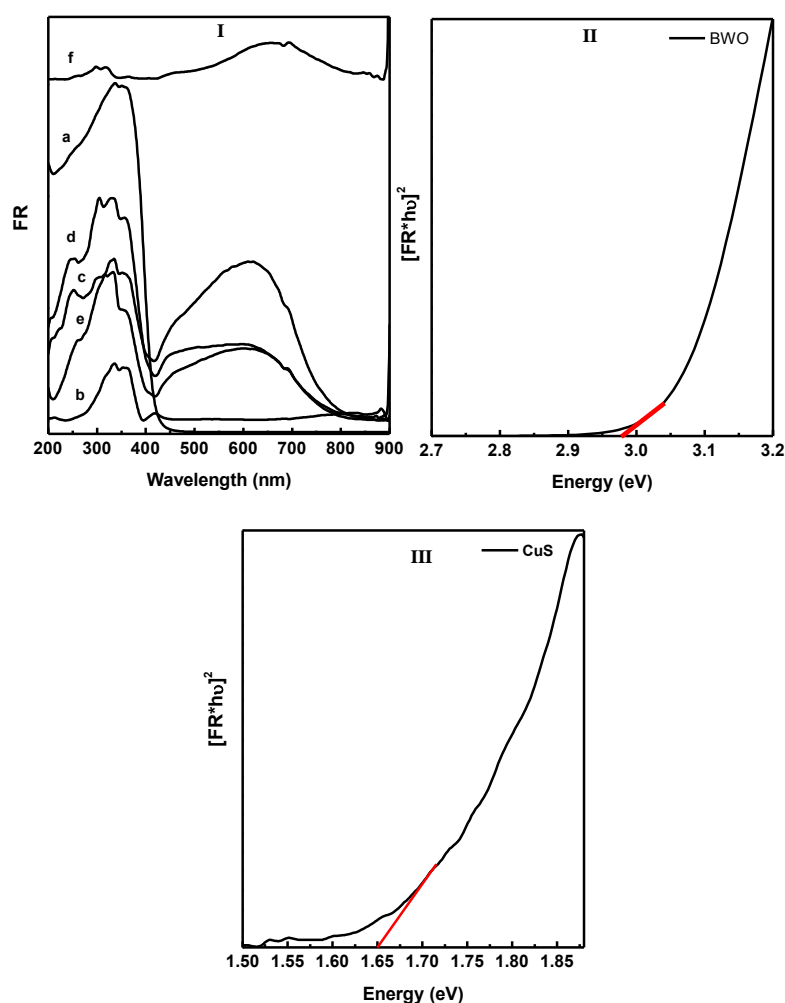


Figure 4.17: UV-Vis-DRS spectra of (a) BWO, (b) CuS5BWO, (c) CuS10BWO, (d) CuS15BWO, (e) CuS20BWO and (f) CuS (Panel I) and plots of $[F(R)hv]^2$ as a function of photon energy ($h\nu$) in eV for BWO (Panel II) and CuS (Panel III).

Figure 4.18 represents the room temperature PL spectra of BWO and CuSBWO heterojunction materials excited at 320 nm. The emission bands observed at 465 and 560 nm for BWO can be assigned to the band edge transition and presence of defect and vacancy in this material (Fig. 4.18a) [10]. Upon modification with CuS, the intensity of PL emission bands decreases significantly for all the CuSBWO heterojunction materials (Fig. 4.18 b-e). The significant decrease in PL intensities indicates efficient separation of excitons in the CuSBWO heterojunction materials. The UV-Vis-DRS and PL study suggest that these materials can be used as photocatalyst under visible light.

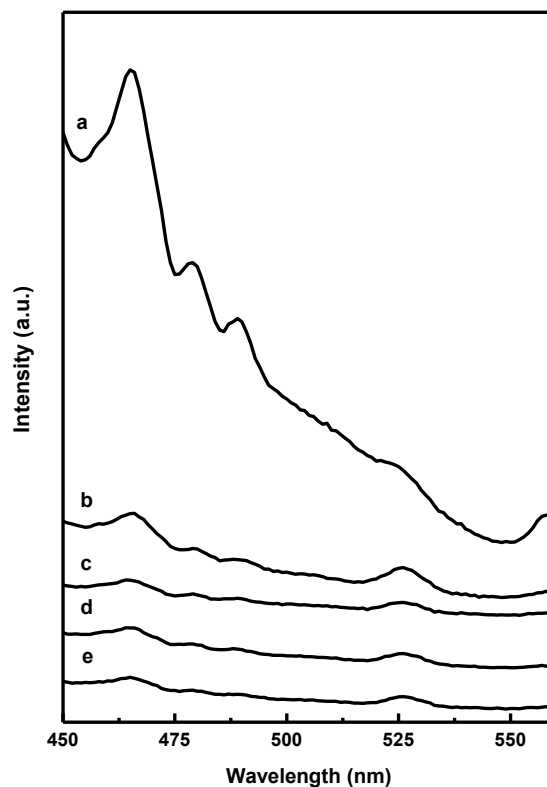


Figure 4.18: PL spectra of (a) BWO, (b) CuS5BWO, (c) CuS10BWO, (d) CuS15BWO and (e) CuS20BWO heterojunction materials.

4.4.4 FTIR Study

The FTIR spectra ($400\text{-}1000\text{ cm}^{-1}$) of BWO and CuSBWO materials are presented in Fig. 4.19. Pure $\text{Bi}_2\text{W}_2\text{O}_9$ material exhibits intense IR bands at 437 , 561 , 745 , 851 and 952 cm^{-1} corresponding to fundamental stretching vibrations of Bi-O and W-O bonds [3, 8, 9]. All the essential vibrational features of BWO are retained in the heterojunction material. However, W-O vibrational bands are shifted to lower wavenumber values by $6\text{-}8\text{ cm}^{-1}$. This observation suggests a change in the W-O bond strength upon Cu^{2+} substitution in the BWO lattice. In addition, all the CuSBWO heterojunction materials show a broad and weak IR band at 616 cm^{-1} corresponding to the Cu-S stretching vibration [73].

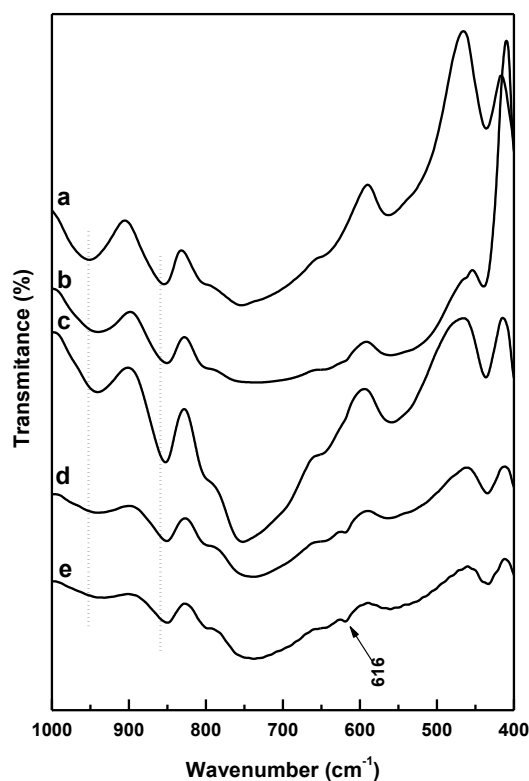


Figure 4.19: FTIR spectra of (a) BWO, (b) CuS5BWO, (c) CuS10BWO, (d) CuS15BWO and (e) CuS20BWO heterojunction materials.

4.4.5 Morphological Study

The FESEM images of BWO and CuSBWO materials are presented in Fig. 4.20. The BWO sample contains micron size plate like particles of different dimensions (Fig. 4.20a). The planar dimensions of the plates are between 4-10 μm whereas thickness is between 0.8-1.5 μm . The smooth surfaces of the BWO plates indicate uniform growth of the material in the XY direction. The red encircled highlighted areas in Fig. 4.20a displayed the different growing stages of the BWO plates. The spherical dot encircled in blue color represents the nucleation point for the growth of the BWO plates along planar directions (Fig. 4.20a). Upon hydrothermal treatment of the BWO material in presence of thiourea and copper salt precursor drastic morphological rearrangement is noticed leading to the formation of hierarchical nanostructures. All the CuSBWO heterojunction materials contain submicron size hierarchical spheres having typical diameter between 0.6-0.8 μm . The spherical particles are formed by hierarchical organization of BWO nanosheets and CuS nanorods (Fig. 4.20 b-e).

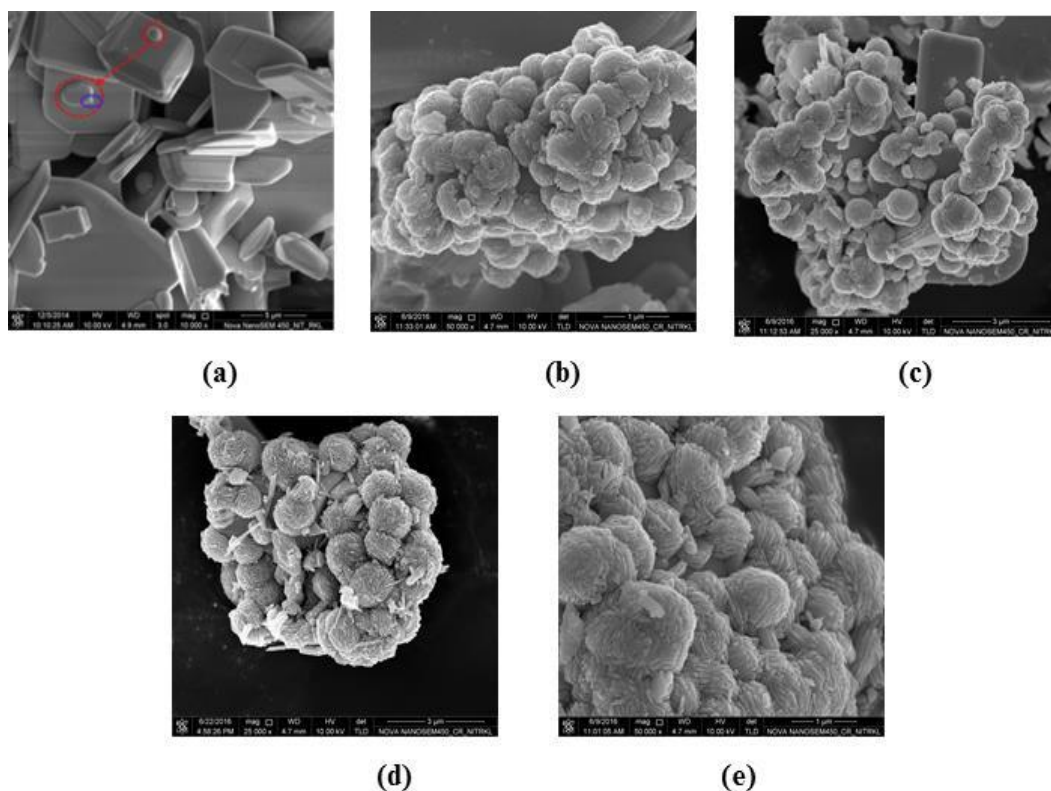


Figure 4.20: FESEM images of (a) BWO, (b) CuS5BWO, (c) CuS10BWO, (d) CuS15BWO and (e) CuS20BWO heterojunction materials.

In order to further probe different stages of formation of the spherical particles, the hydrothermally treated samples were analyzed at different time interval using FESEM (Fig. 4.21). Upon hydrothermal treatment, the BWO plates are initially desegregate to the BWO nanosheets. The lateral view of a hydrothermal treated BWO plate in Fig. 4.21b indicates its layer by layer desegregation. The BWO nanosheets subsequently arranged themselves concentrically to form spherical structure. The CuS nanorods are preferably deposited along the outer periphery and the void spaces between the nanosheets (Fig. 4.21c). Figure 4.21d depicts the top view of few partially formed hierarchical spheres. The concentric arrangement of the nanosheets can be inferred from Fig. 4.21d. The desegregated BWO nanosheets have typical length and breadth between 150-300 nm and thickness between 25-30 nm. Similarly, the CuS nanorods have typical length between 120-200 nm with diameter between of 25-35 nm.

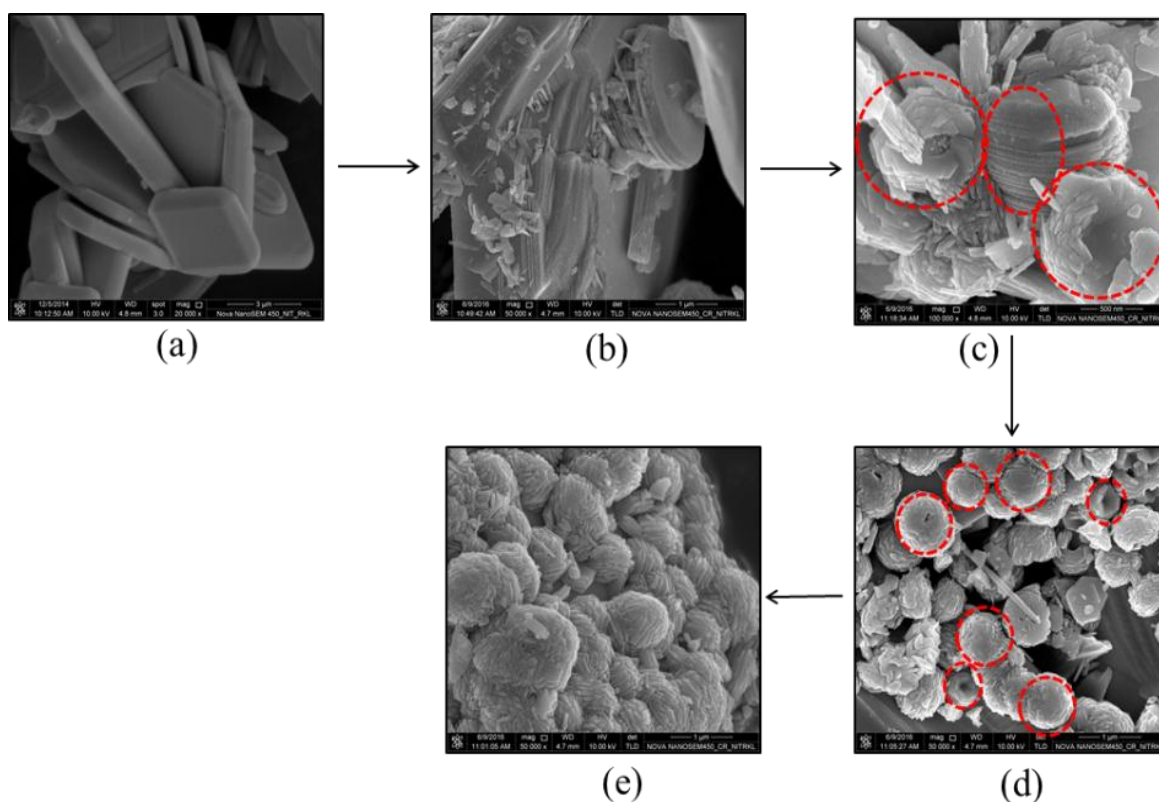


Figure 4.21: Different stages of formation of hierarchical CuSBWO heterojunction microspheres.

The morphological features, size and formation of heterojunctions are further investigated for CuS₂₀BWO material using HRTEM analysis (Fig. 4.22). The presence of spherical particles with 0.6-0.8 μm diameter is confirmed from TEM study (Fig. 4.22 a & b). Fig. 4.22c depicts the TEM image of a partially formed sphere growing towards the $-X$ direction. The hierarchical organization of BWO nanosheets and CuS nanorods are clearly observed from this image (Fig. 4.22c). The high magnification HRTEM images of CuS₂₀BWO material are presented in Fig. 4.22 d-f. In Fig. 4.22d, a single CuS nanorod with length 70 nm and diameter 30 nm can be visualized. The CuS nanorods are in intimate contact microscopically with the BWO nanosheets (Fig. 4.22e). The high resolution image in Fig. 4.22f depicts the formation of heterojunctions between BWO and CuS phases. Two different set of lattice fringes running in different directions correspond to the (105) and (106) crystallographic planes of $\text{Bi}_2\text{W}_2\text{O}_9$ and CuS, respectively (Fig. 4.22f). The EDS mapping and EDX spectrum of CuS₂₀BWO material are presented in Fig. 4.22 g-i. EDS mapping study reflects the presence of CuS nanorods in the CuSBWO sample. The presence of Bi, W, O, Cu and S with required stoichiometry is confirmed from the EDX spectrum (Fig. 4.22i). The specific surface area of the heterojunction materials are presented in Table 4.4. The CuSBWO materials show surface area in the range of 25-33 m^2/g .

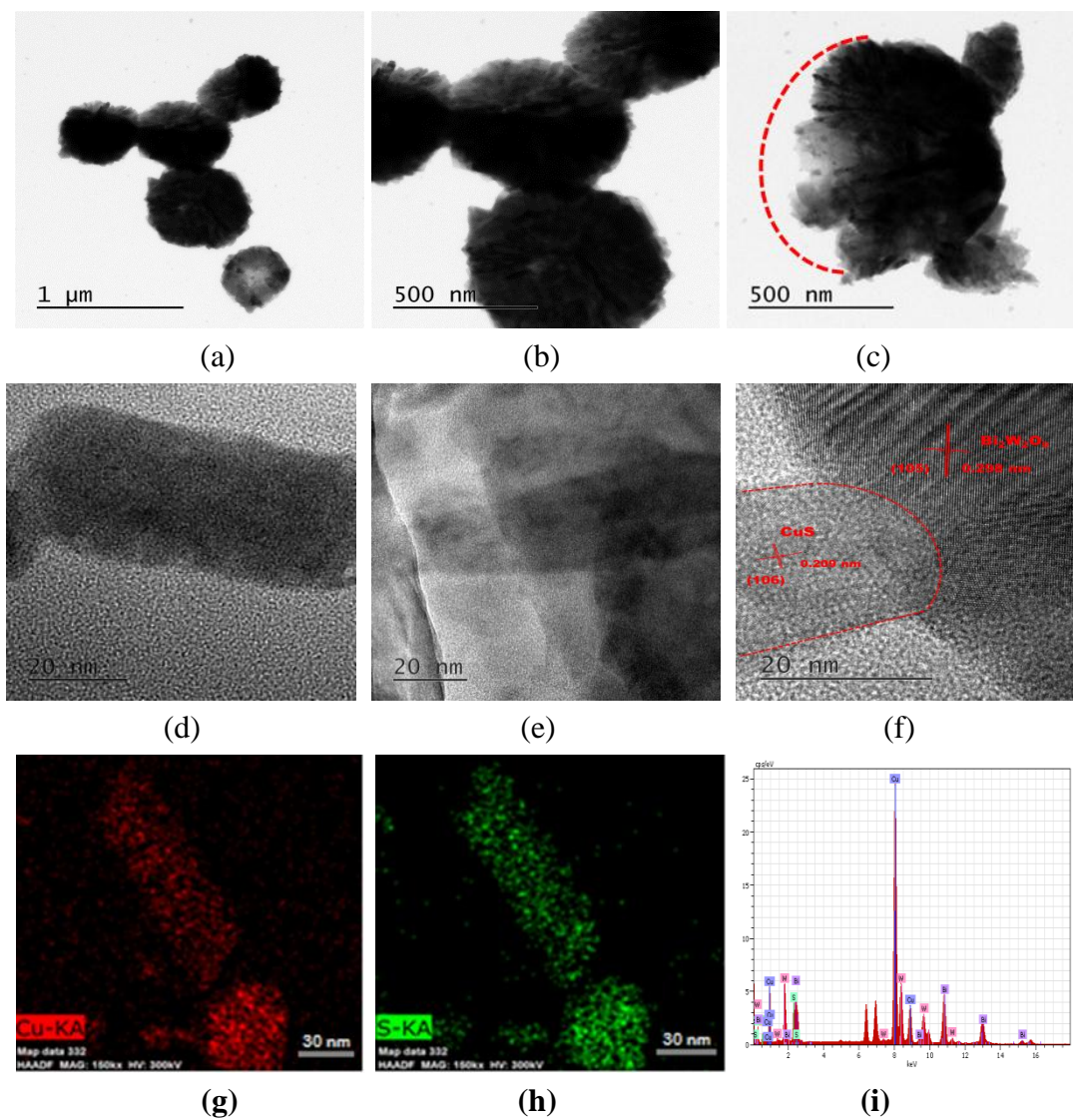


Figure 4.22: (a-f) TEM images, (g,h) EDS mapping and (i) EDX spectrum of CuS20BWO heterojunction material.

Table 4.4: Specific surface area of CuSBWO heterojunction materials.

Sl. No	Photocatalyst	Surface area (m ² /g)
1	CuS5BWO	26
2	CuS10BWO	31
3	CuS15BWO	34
4	CuS20BWO	33

4.4.6 Photocatalytic Degradation of Diuron Pesticide

4.4.6.1 Optimization of Reaction Parameters

The photocatalytic activity of CuSBWO heterojunction materials has been studied for degradation of diuron pesticide under visible light irradiation. Initially, the degradation reaction is carried out by taking 100 ml of 10 ppm diuron solution and 75 mg of CuS20BWO catalyst in presence of different oxidants (Fig. 4.23). Among different oxidants used in this study, highest degradation efficiency of 95% is achieved in presence of H_2O_2 after 3 h. Figure 4.24 represents the photocatalytic activity of different CuSBWO heterojunction photocatalysts towards degradation of 10 ppm diuron solution using H_2O_2 (200 μ l) as oxidant. In general, the heterojunction photocatalysts exhibit high initial rate and enhanced degradation efficiency than pure BWO material. The initial rate of degradation increases with increase in CuS content in the heterojunctions. Among the heterojunctions, CuS20BWO shows highest photocatalytic degradation efficiency of 95% after 3 h (Fig. 4.24). The higher photocatalytic efficiency of the CuSBWO heterojunction materials can be ascribed to their enhanced visible light absorption and improved charge carrier separation properties. Figure 4.25 represents the pseudo first order kinetic plots for diuron degradation. The K_{app} increases linearly with CuS content in the heterojunction material. The k_{app} value for CuS20BWO heterojunction is nearly 4 times higher than pure BWO material and 2 times than that of CuS5BWO heterojunction (Fig. 4.25II).

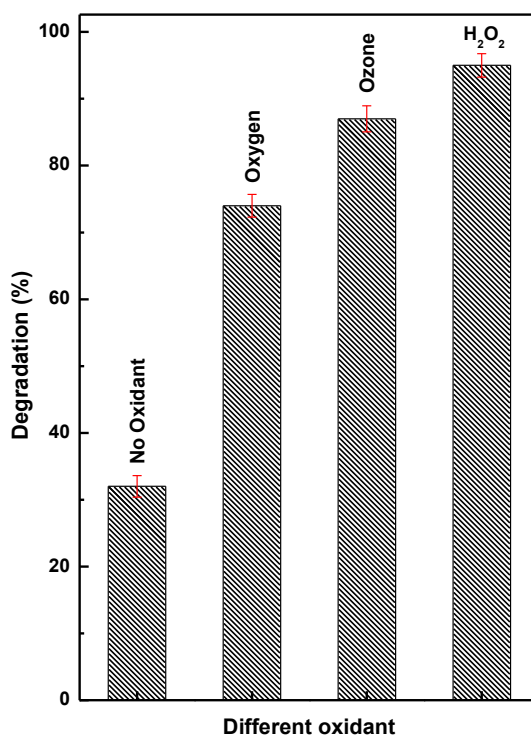


Figure 4.23: Degradation efficiency of CuS20BWO catalyst for diuron degradation in presence of different oxidant (O_2 flow 30 ml/min, O_3 flow 30 ml/min, H_2O_2 200 μ l).

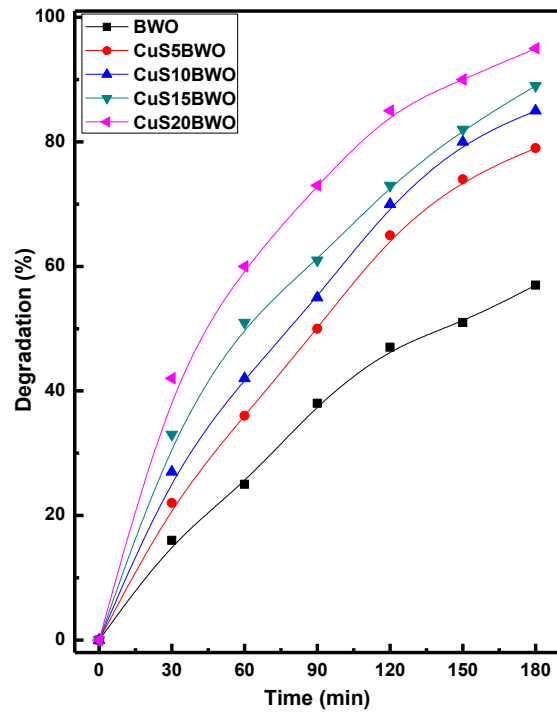


Figure 4.24: Photocatalytic efficiency of CuSBWO catalysts for diuron degradation (10 ppm DU, 200 μ l 30 % H_2O_2 , 75 mg of catalyst).

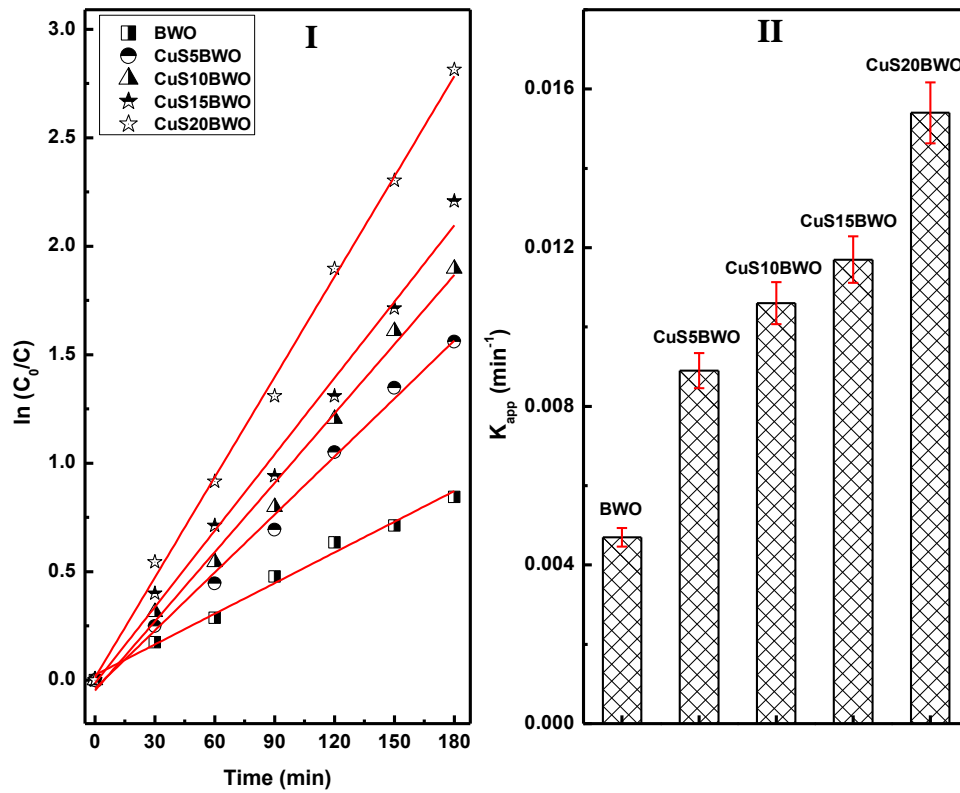


Figure 4.25: (I) Pseudo first order kinetics plots and (II) apparent rate constants of CuSBWO heterojunction photocatalysts for diuron degradation.

Figure 4.26 represents effect of various reaction parameters on the photocatalytic degradation of diuron using CuS20BWO photocatalyst. The catalyst amount is varied between 25-100 mg. The degradation rate increases with catalyst amount up to 75 mg, beyond which a marginal decrease in degradation efficiency is noticed (Fig. 4.26I). The decrease in rate at higher catalyst amount can be attributed to the scattering of incident light by the catalyst particles from the reaction mixture. The effect of H₂O₂ concentration on diuron degradation is presented in Fig. 4.26II. The diuron degradation increases with H₂O₂ concentration before attending saturation at 200 µl. Beyond this value there is a minor decrease in the degradation efficiency probably due to trapping of [•]OH radicals by excess H₂O₂ species resulting in generation of HO₂[•] radicals. The HO₂[•] radical being a weaker oxidizing agent than the [•]OH radicals is responsible for the observed decrease in degradation efficiency [74]. After optimizing various reaction parameters, the catalytic efficiency of the CuS20BWO catalyzed degradation process is further studied by varying the diuron concentration between 2-12 ppm. Up to 10 ppm diuron concentration, the degradation rate is very fast providing > 90% degradation within 3 h of irradiation time. However, for 12 ppm sample the reaction rate is relatively sluggish with 80% degradation achieved after 3 h (Fig. 4.26III). This optimization study revealed that 100 ml of 10 ppm diuron solution can be degraded efficiently using 75 mg of CuS20BWO catalyst along with 200 µl H₂O₂ as oxidant within 3 h of reaction time.

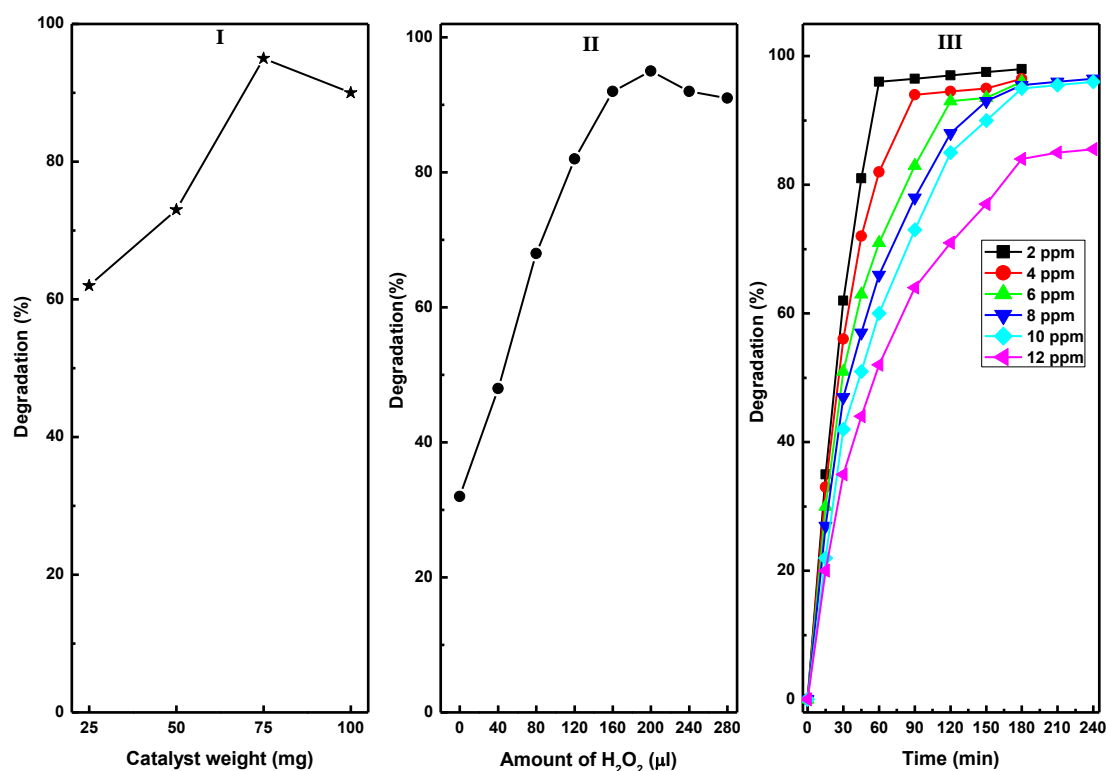


Figure 4.26: (I) Effect of catalyst dose, (II) H₂O₂ concentration and (III) diuron concentration on the photocatalytic degradation activity of CuS20BWO photocatalyst.

4.4.6.2 Mechanism of Photocatalytic Degradation of Diuron over CuSBWO Surface

The probable degradation pathway of diuron over CuS20BWO catalyst surface is probed by GC-Mass analysis as well as by monitoring the Cl^- , NH_4^+ and NO_3^- concentrations in the reaction mixture. The concentration of ammonium and nitrate ions is measured by spectrophotometric method using literature reported procedure [65]. The concentration of Cl^- ions in the reaction mixture is measured by ion selective electrode. The variation in Cl^- , NH_4^+ and NO_3^- concentrations as a function of time is presented in Fig. 4.27I. There is a rapid increase in Cl^- ion concentration with time reaching 97% removal within 90 min of irradiation. This observation suggests that the degradation of diuron proceed through an initial dechlorination step. The dechlorination step is essentially completed within 2 h of irradiation. Diuron molecule contains two N atoms in its structure which can be liberated as nitrate ion, ammonium ion and N_2 gas.

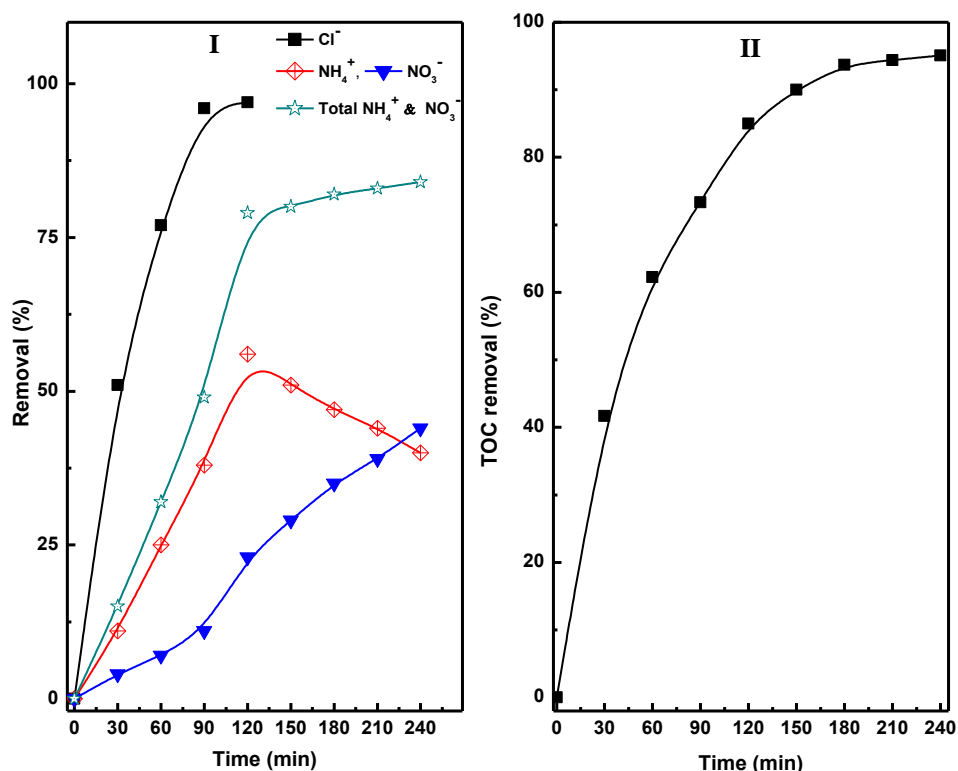


Figure 4.27: (I) Evolution of different ions and (II) TOC removal at different irradiation time.

Moreover, the formation many N containing by-products such as alkyl nitrogen, cianno derivatives, carbamic acids and amines has been detected during the photocatalytic degradation of diuron over titania surface [58]. The formation of many inorganic and organic products makes the mass balance of “N” a complex process. In the present study, the concentration of ammonium ions increases up to 2 h of reaction then shows a decreasing trend. The concentration of nitrate ions, on the other hand, increases linearly with reaction

time up to 4 h. The observed variation in NH_4^+ and NO_3^- ion concentrations suggests initial formation of ammonium ions which is further oxidized to nitrate ion upon prolong irradiation [58, 65]. After 4 h, the released ammonium and nitrate ions correspond to 84% of total nitrogen content of diuron. This observation suggests that a part of the nitrogen has either escaped as innocuous N_2 gas and/or still remain in the reaction mixture as persistent organic impurity. In order to follow the progress in mineralization of diuron, TOC analysis of the reaction mixture is carried out at regular interval of time. The TOC decreases rapidly with irradiation time and almost 90% TOC removal is noted after 2 h (Fig. 4.27II). The TOC removal after 4 h is 96.5% which suggests that a small fraction of organic carbon still remains as persistent organic impurities which are formed at intermediate stages of mineralization of diuron. These organic impurities could not be mineralized using CuSBWO catalyst.

The degradation products formed at different stages of diuron degradation are analyzed of using GCMS analysis (Fig. 4.28). Six different products are identified based on the molecular ion peaks and obtained mass fragments. Based on the GCMS data, we proposed a plausible pathway for the photocatalytic degradation of diuron (Scheme 4.2).

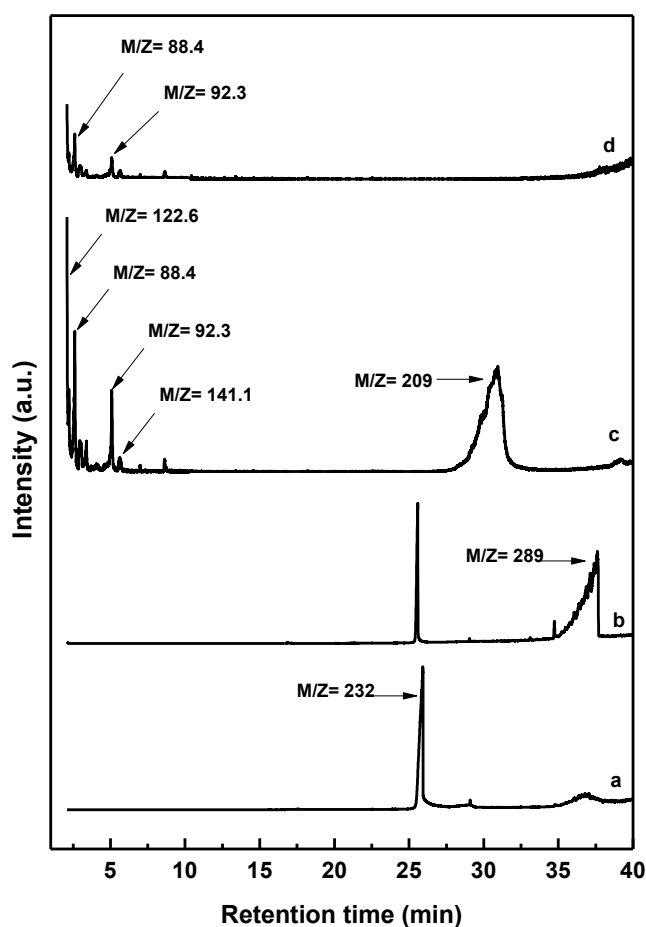
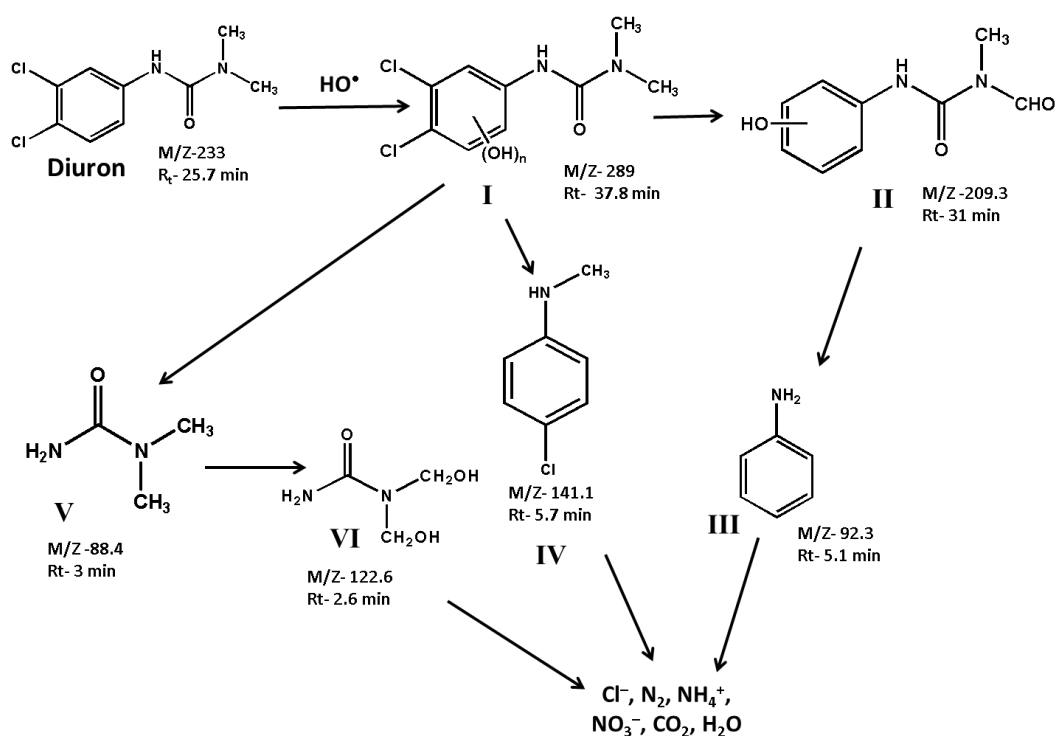


Figure 4.28: GC-MS analysis of degradation products of diuron at different reaction time (a) pure diuron, (b) 10 min, (c) 1.5 h and (d) 3 h catalyzed by CuS20BWO heterojunction material.

In the first step, the hydroxyl radicals generated on the catalyst surface attack the diuron molecule to provide a high molecular weight hydroxylated product I. The product I is formed rapidly in the reaction mixture within 10 min of irradiation. Such high molecular weight product has been observed earlier during photocatalytic degradation of diuron over TiO₂ catalyst [58]. The hydroxylated diuron species (I) undergo rapid dehalogenation reaction resulting in loss of Cl⁻ ions. Simultaneously, the alkyl groups of diuron are oxidized to form the intermediate product II [66-69]. The product I also decompose to produce N, N-dimethyl urea (product V) and N-methyl chloroaniline (product IV). The Product II undergoes further decomposition on the catalyst surface producing aniline (product III). The N, N-dimethyl urea (product V) is subsequently oxidized to bis(hydroxymethyl) urea (product VI). The intermediate products so formed are finally mineralized over the catalyst surface to give Cl⁻, NO₃⁻, NH₄⁺, CO₂ and H₂O as final product.



Scheme 4.2: Identification of different degradation products by GCMS analysis.

Scavenger experiments have been carried out to understand the role of different reactive species towards the degradation of diuron (Fig. 4.29). The scavenger experiments are conducted by irradiating a reaction mixture containing equimolar quantity of radical scavengers and CuS20BWO catalyst. In presence of hole (h⁺) scavenger (ammonium oxalate) and hydroxyl radical (•OH) scavenger (t-butyl alcohol) drastic decrease in the degradation rate is observed. The scavenger experiments confirm that the photogenerated hydroxyl radicals and hole are the primary species responsible for the diuron degradation (Fig. 4.30).

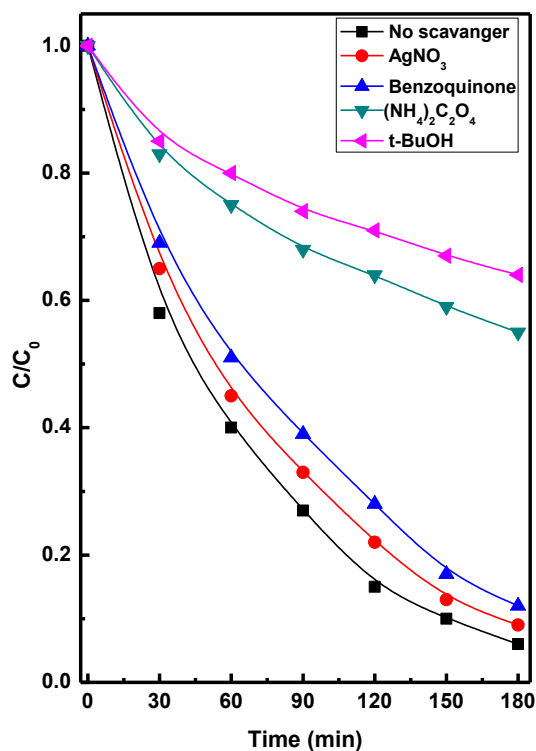


Figure 4.29: Photocatalytic degradation of diuron in presence of different radical scavengers catalyzed by CuS20BWO heterojunction photocatalyst.

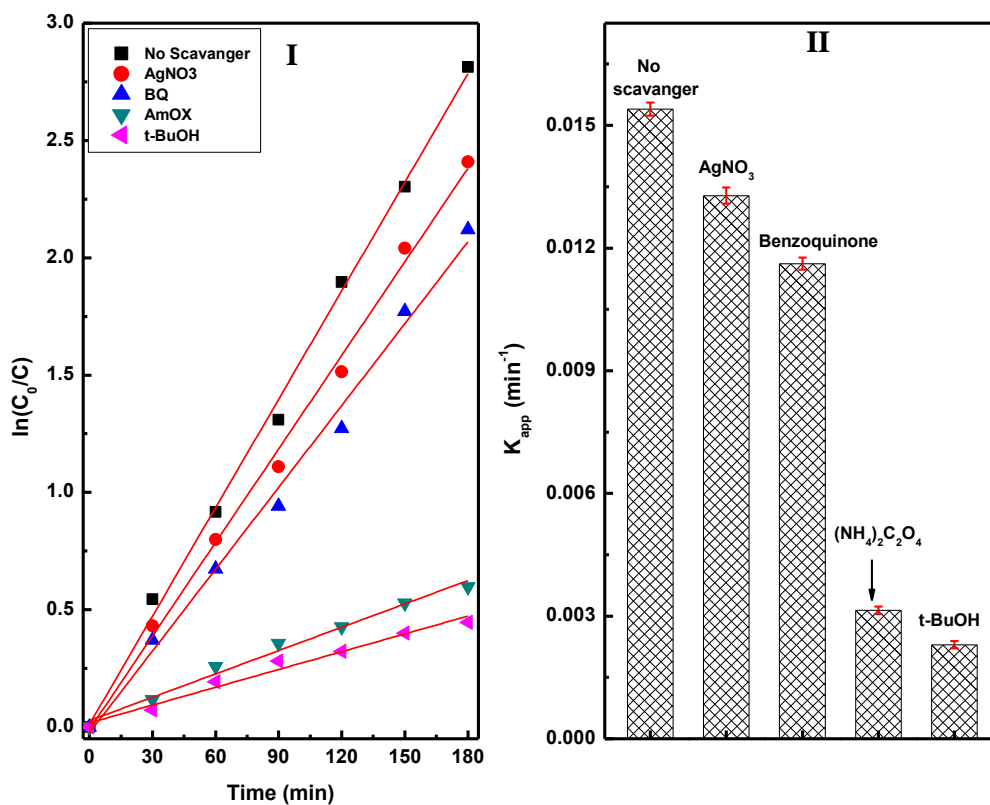


Figure 4.30: (I) Pseudo first order kinetics plots and (II) apparent rate constants of CuS20BWO heterojunction photocatalyst in presence of different radical scavengers.

The VB and CB positions for pure CuS and BWO have been presented in Chapters 3B and 4A respectively. The VB of CuS and BWO are placed at 1.61 eV and 3.275 eV whereas the CB occurred at -0.04 eV and 0.325 eV, respectively. Upon material contact, Fermi level equilibration between the semiconductor phases leads to band realignment (Fig. 4.31). The band positions of the two materials are aligned in a favourable manner for facile electron transfer from CB of CuS to CB of $\text{Bi}_2\text{W}_2\text{O}_9$. Simultaneously, the holes can migrate in opposite direction in the VB resulting in efficient charge carrier separation (Fig. 4.31). Such an arrangement of the band positions is characteristic of a type II heterojunction. A plausible mechanism for degradation of diuron on the CuSBWO surface is proposed in Fig. 4.31.

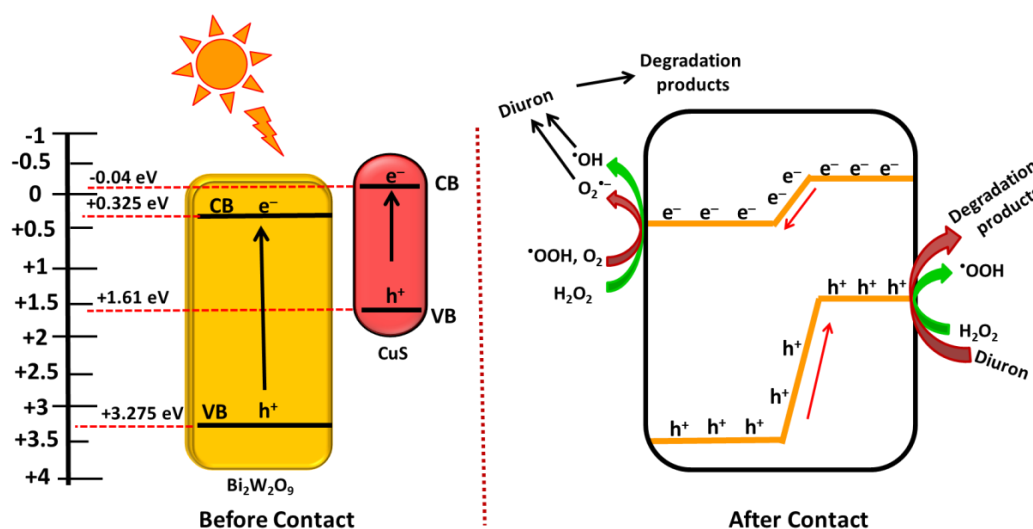


Figure 4.31: Plausible mechanism for diuron degradation over CuSBWO heterojunction surface.

Upon irradiation with visible light, the electron population increases in the CB of BWO component while the hole population increases in the VB of CuS component. The H_2O_2 is activated to hydroxyl radicals (HO^\bullet) in the CB of the heterojunction. Scavenger experiments have confirmed the participation of this transient species in the photocatalytic degradation reaction. The preferred sites for the attack of the OH^\bullet radicals are the methyl group and the aromatic ring leading to hydroxylated and subsequent oxidized products (Scheme 4.2) [58, 67-69]. In the VB of CuS, H_2O_2 is oxidized to give hydroperoxide radicals (HOO^\bullet). The hydroperoxide radicals upon reaction with diuron can generate a peroxide intermediate which can disproportionate to give product II (Scheme 4.2) [68]. Moreover, the accumulated hole species in the VB of CuS due to their oxidizing property can also contribute to the oxidative degradation of diuron. The intermediate oxidized products so formed undergo further mineralization on the catalyst surface. The stability and recyclability of the CuSBWO heterojunction photocatalyst has been checked for five consecutive cycles. The CuS20BWO heterojunction photocatalyst exhibited stable activity up to five consecutive cycles (Fig. 4.32). The XRD profiles of the CuS20BWO materials after successive catalytic cycles are

presented in Fig. 4.33. No perceivable change in the XRD patterns is noticed indicating high phase stability of the material in the photocatalytic experiments. Overall, the photocatalytic method developed in this work is advantageous in terms of use of visible light as energy source, minimum use of oxidant and catalyst and shorter reaction time.

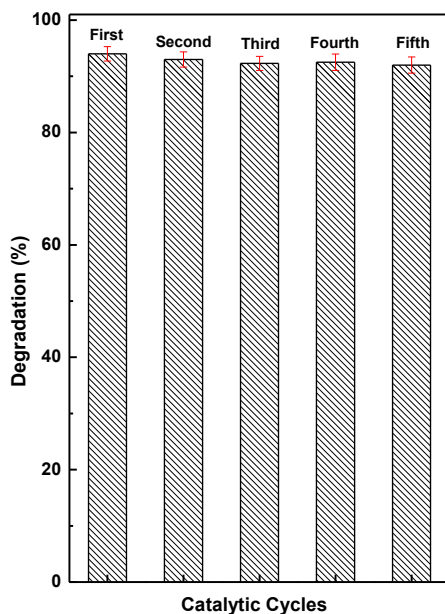


Figure 4.32: Reusability of CuS20BWO heterojunction photocatalyst for degradation of diuron.

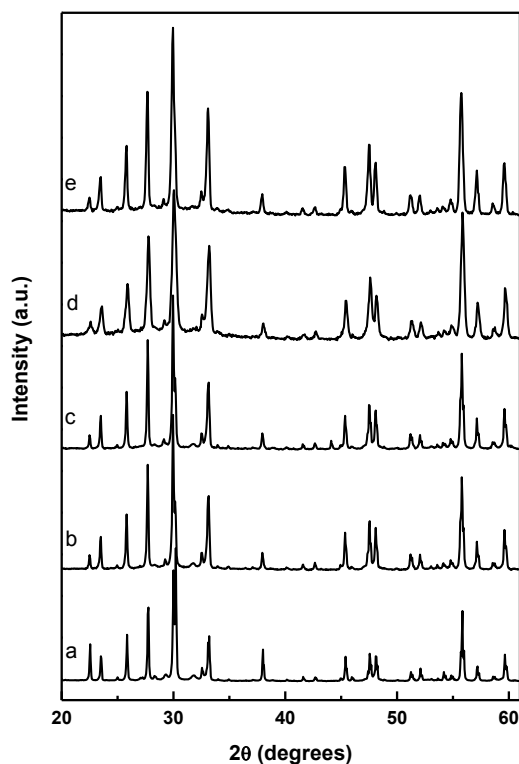


Figure 4.33: XRD profile of CuS20BWO heterojunction photocatalyst material (a) freshly prepared, and after (b) 1st, (c) 2nd, (d) 3rd and (e) 5th catalytic cycles.

4.5 Conclusions

In this study, we have developed novel $\text{Bi}_2\text{W}_2\text{O}_9$ based type-II heterostructure nanomaterials by coupling it with metal sulfide (CuS and CdS) nanoparticles. The heterojunction systems retain the crystalline phase of parent $\text{Bi}_2\text{W}_2\text{O}_9$ along with the metal sulfide phases. The microscopic close contact between the CuS/CdS and $\text{Bi}_2\text{W}_2\text{O}_9$ is established from HRTEM study. The heterostructure formation promotes migration of charge carrier across the grain boundary. The heterojunction systems exhibit improved optical absorption in the visible region and efficient separation of excitons. Microscopically, the CdS/ $\text{Bi}_2\text{W}_2\text{O}_9$ heterojunction materials contain well dispersed CdS nanoparticles over BWO plates. The $\text{Bi}_2\text{W}_2\text{O}_9$ plates have planar dimension in the range of 4-10 μm and thickness of 0.8-1.5 μm . The CdS nanoparticles have typical particle size in the range of 8-15 nm. The CdS/ $\text{Bi}_2\text{W}_2\text{O}_9$ heterojunction materials display excellent photocatalytic activity towards selective aerobic oxidation of amines to imines. A variety of primary, secondary and heterocyclic amines are oxidized to the corresponding imines using the CdSBWO material as photocatalyst. The photocatalytic protocol developed in this work is advantageous in terms of use of renewable energy source, preclusion of toxic oxidants, short reaction time, high selectivity and recyclable photocatalyst.

In case of CuS/ $\text{Bi}_2\text{W}_2\text{O}_9$ material, the partial substitution of Cu^{2+} in $\text{Bi}_2\text{W}_2\text{O}_9$ lattice leads to the formation of a non-stoichiometric solid solution phase. The $\text{Bi}_2\text{W}_2\text{O}_9$ plates desegregate to nanosheets during the hydrothermal synthesis of CuS/ $\text{Bi}_2\text{W}_2\text{O}_9$ heterojunctions. The $\text{Bi}_2\text{W}_2\text{O}_9$ nanosheets and CuS nanorods are hierarchically organised to give microspherical structure. The CuS/ $\text{Bi}_2\text{W}_2\text{O}_9$ heterojunction exhibited excellent photocatalytic activity towards visible light assisted mineralization of diuron. Mechanistic study revealed that the diuron degradation is a cascade process involving dechlorination, alkyl oxidation and oxidative ring opening leading to its complete mineralization. The CuS/ $\text{Bi}_2\text{W}_2\text{O}_9$ heterojunction photocatalyst developed in this work is stable and highly efficient for diuron degradation which can be a viable and economic alternative to TiO_2 based UV active photocatalyst.

References

- [1] A. Kudo and S. Hijji, *Chemistry Letters*, 1999, 1103-1104.
- [2] J. C. C. Mesjard, B. Frit and A. Watanabe, *Journal of Material Chemistry*, 1999, 9, 1319-1322.
- [3] S. O. Alfaro and A. M. Cruz, *Applied Catalysis A: General*, 2010, 383, 128-133.
- [4] O. M. Bordun, A. T. Stetskiv and T. M. Yaremchuk, *Journal of Applied Spectroscopy*, 2004, 71, 136-138.

- [5] O. M. Bordun, A. T. Stetskiv and T. M. Yaremchuk, *Ukrainian Journal of Physics*, 2004, 49, 991-995.
- [6] A. Feteiraw and D. C. Sinclair, *Journal of the American Ceramic Society*, 2008, 91, 1338-1341.
- [7] L. Wu, J. Xia, J. Wu and Q. Li, *Ionics*, 2015, 21, 3239-3244.
- [8] S. Obregon, M. A. R. Gomez and D. B. H. Uresti, *Journal of Colloid and Interface Science*, 2017, 506, 111-119.
- [9] S. O. Alfaro, A. M. Cruz, L. M. T. Martínez and S. W. Lee, *Catalysis Communications*, 2010, 11, 326-330.
- [10] J. Tang and J. Ye, *Journal of Material Chemistry*, 2005, 15, 4246-4251.
- [11] A. M. Cruz, S. O. Alfaro, L. M. T. Martínez and I. J. Ramírez, *Journal of Ceramic Processing Research*, 2008, 9, 490-494.
- [12] M. Gartner, J. Ballmann, C. Damm, F. W. Heinemann and H. Kisch, *Photochemical & Photobiological Sciences*, 2007, 6, 159-164.
- [13] T. Mitkina, C. Stanglmair, W. Setzer, M. Gruber, H. Kisch and B. König, *Organic & Biomolecular Chemistry*, 2012, 10, 3556-3561.
- [14] S. Sakthivel, S. U. Geissen, D. W. Bahnemann, V. Murugesan and A. Vogelpohl, *Journal of Photochemistry and Photobiology A: Chemistry*, 2002, 148, 283-293.
- [15] S. Naskar, F. Lübkemann, S. Hamid, A. Freytag, A. Wolf, J. Koch, I. Ivanova, H. Pfnür, D. Dorfs, D. W. Bahnemann and N. C. Bigall, *Advanced Functional Materials*, 2017, 27, 1604685.
- [16] Y. Huo, X. Yang, J. Zhu and H. Li, *Applied Catalysis B: Environmental*, 2011, 106, 69-75.
- [17] Y. Feng, X. Yan, C. Liu, Y. Hong, L. Zhu, M. Zhou and W. Shi, *Applied Surface Science*, 2015, 353, 87-94.
- [18] J. Fu, B. Chang, Y. Tian, F. Xi and X. Dong, *Journal of Materials Chemistry A*, 2013, 1, 3083-3090.
- [19] D. Chen, Z. Kuang, Q. Zhu, Y. Du and H. Zhu, *Materials Research Bulletin*, 2015, 66, 262-267.
- [20] Z. Khan, T. R. Chetia and M. Qureshi, *Nanoscale*, 2012, 4, 3543-3550.
- [21] Y. Wu, B. Yuan, M. Li, W. H. Zhang, Y. Liu and C. Li, *Chemical Science*, 2015, 6, 1873-1878.
- [22] A. Han, H. Zhang, G. K. Chuah and S. Jaenicke, *Applied Catalysis B: Environmental*, 2017, 219, 269-275.
- [23] S. Furukawa, Y. Ohno, T. Shishido, K. Teramura and T. Tanaka, *ACS Catalysis*, 2011, 1, 1150-1153.
- [24] G. Palmisano, E. G. -Lopez, G. Marc, V. Loddo, S. Yurdakal, V. Augugliaro and L. Palmisano, *Chemical Communications*, 2010, 46, 7074-7089.
- [25] D. Friedmann, A. Hakki, H. Kim, W. Choi and D. Bahnemann, *Green Chemistry*, 2016, 18, 5391-5411.

- [26] G. Palmisano, V. Augugliaro, M. Pagliaro and L. Palmisano, *Chemical Communications*, 2007, 3425-3437.
- [27] V. Augugliaro, M. Bellardita, V. Loddo, G. Palmisano, L. Palmisano and S. Yurdakal, *Journal of Photochemistry and Photobiology C: Photochemistry Reviews*, 2012, 13, 224-245.
- [28] Z. Wang and X. Lang, *Applied Catalysis B: Environmental*, 2018, 224, 404-409.
- [29] X. Lang, W. Ma, Y. Zhao, C. Chen, H. Ji and J. Zhao, *Chemistry: A European Journal*, 2012, 18, 2624-2631.
- [30] X. Lang, H. Ji, C. Chen, W. Ma and J. Zhao, *Angewandte Chemie International Edition*, 2011, 50, 3934-3937.
- [31] F. Raza, J. H. Park, H. R. Lee, H. I. Kim, S. J. Jeon and J. H. Kim, *ACS Catalysis*, 2016, 6, 2754-2759.
- [32] B. Yuan, R. Chong, B. Zhang, J. Li, Y. Liu and C. Li, *Chemical Communications*, 2014, 50, 15593-15596.
- [33] F. Su, S. C. Mathew, L. Mohlmann, M. Antonietti, X. Wang and S. Blechert, *Angewandte Chemie International Edition*, 2011, 50, 657-660.
- [34] X. Wang, J. Yang, S. Ma, D. Zhao, J. Dai and D. Zhang, *Catalysis Science & Technology*, 2016, 6, 243-253.
- [35] H. Chen, C. Liu, M. Wang, C. Zhang, N. Luo, Y. Wang, H. Abroshan, G. Li and F. Wang, *ACS Catalysis*, 2017, 7, 3632-3638.
- [36] L. Ye and Z. Li, *ChemCatChem*, 2014, 6, 2540-2543.
- [37] A. D. Proctor, S. Panuganti and B. M. Bartlett, *Chemical Communications*, 2018, 54, 1101-1104.
- [38] Z. J. Wang, S. Ghasimi, K. Landfester and K. A. I. Zhang, *Advanced Materials*, 2015, 27, 6265-6270.
- [39] D. Chen, Z. Kuang, Q. Zhu, Y. Du and H. Zhu, *Materials Research Bulletin*, 2015, 66, 262-267.
- [40] H. -P. Jiao, X. Yu, Z. -Q. Liu, P. -Y. Kuang and Y.-M. Zhang, *RSC Advances*, 2015, 5, 16239-16249.
- [41] D. Balzar and H. Ledbetter, *Journal of Applied Crystallography*, 1993, 26, 97-103.
- [42] M. Maczka, L. Kepinski, L. Macalik and J. Hanuza, *Materials Chemistry and Physics*, 2011, 125, 930-101.
- [43] M. Maczka, M. Ptak, L. Kepinski, P. E. Tomaszewski and J. Hanuza, *Vibrational Spectroscopy*, 2010, 53, 199-203.
- [44] Q. Wang, J. Lian, Q. Ma, Y. Bai, J. Tong, J. Zhong, R. Wang, H. Huang and B. Su, *New Journal of Chemistry*, 2015, 39, 7112-7119.
- [45] I. Zgura, N. Preda, G. Socol, C. Ghica, D. Ghica, M. Enculescu, I. Negut, L. Nedelcu, L. Frunza, C. P. Ganea and S. Frunza, *Materials Research Bulletin*, 2018, 99, 174-181.

- [46] Z. Wang, J. Peng, X. Feng, Z. Ding and Z. Li, *Catalysis Science & Technology*, 2017, 7, 2524-2530.
- [47] M. Mousavi, A. H. -Yangjeh and M. Abitorabi, *Journal of Colloid and Interface Science*, 2016, 480, 218-231.
- [48] K. N. Oviedo and D. S. Aga, *Journal of Hazardous Materials*, 2016, 316, 242-251.
- [49] G. L. Puma, B. Toepfer and A. Gora, *Catalysis Today*, 2007, 124, 124-132.
- [50] R. Andreozzi, V. Caprio, A. Insola, R. Marotta and R. Sanchirico, *Water Research*, 2000, 34, 620-628.
- [51] J. Choi, H. Lee, Y. Choi, S. Kim, S. Lee, S. Lee, W. Choi and J. Lee, *Applied Catalysis B: Environmental*, 2014, 147, 8-16.
- [52] K. Y. Foo and B. H. Hameed, *Journal of Hazardous Materials*, 2010, 175, 1-11.
- [53] M. S. Lucas, J. A. Peres and G. L. Puma, *Separation and Purification Technology*, 2010, 72, 235-241.
- [54] M. E. Madani, C. Guillard, N. Perol, J. M. Chovelon, M. E. Azzouzi, A. Zrineh and J. M. Herrmann, *Applied Catalysis B: Environmental*, 2006, 65, 70-76.
- [55] P. Sharma, V. Bhalla, S. Tuteja, M. Kukkar and C. R. Suri, *Analyst*, 2012, 137, 2495-2502.
- [56] S. Giacomazzi and N. Cochet, *Chemosphere*, 2004, 56, 1021-1032.
- [57] W. Khongthon, G. Jovanovic, A. Yokochi, P. Sangvanich and V. Pavarajarn, *Chemical Engineering Journal*, 2016, 292, 298-307.
- [58] H. Katsumata, M. Sada, Y. Nakaoka, S. Kaneco, T. Suzuki and K. Ohta, *Journal of Hazardous Materials*, 2009, 171, 1081-1087.
- [59] M. Quirantes, R. Nogales and E. Romero, *Journal of Hazardous Materials*, 2017, 331, 300-308.
- [60] J. Villaverde, M. R. Bellido, F. Merchan and E. Morillo, *Journal of Environmental Management*, 2017, 188, 379-386.
- [61] M. Carrier, M. Besson, C. Guillard and E. Gonze, *Applied Catalysis B: Environmental*, 2009, 91, 275-283.
- [62] E. C. Catalkaya and F. Kargi, *Chemosphere*, 2007, 69, 485-492.
- [63] P. Mazellier and B. Sulzberger, *Environmental Science & Technology*, 2001, 35, 3314-3320.
- [64] B. R. Saranya, V. Sathiyarayanan and S. T. Maheswari, *RSC Advances*, 2016, 6, 110970-110975.
- [65] D. Bamba, P. Atheba, D. Robert, A. Trokourey and B. Dongui, *Environmental Chemistry Letters*, 2008, 6, 163-167.
- [66] R. R. Solis, F. J. Rivas, A. M. Piernas and A. Aguera, *Chemical Engineering Journal*, 2016, 292, 72-81.
- [67] H. Krysova, J. Krysa, K. Macounova and J. Jirkovsky, *Journal of Chemical Technology & Biotechnology*, 1998, 72, 169-175.

- [68] M. Carrier, C. Guillard, M. Besson, C. Bordes and H. Chermette, *Journal of Physical Chemistry A*, 2009, 113, 6365-6374.
- [69] K. Macounova, H. Krysova, J. Ludvik and J. Jirkovsky, *Journal of Photochemistry & Photobiology A: Chemical*, 2003, 156, 273-282.
- [70] C. B. Somrani, F. Fajula, A. Finiels, P. Graffin, P. Geneste and J. L. Olive, *New Journal of Chemistry*, 2000, 24, 999-1002.
- [71] X. Meng, G. Tian, Y. Chen, R. Zhai, J. Zhou, Y. Shi, X. Cao, W. Zhoua and H. Fu, *CrystEngComm*, 2013, 15, 5144-5149.
- [72] Y. Shi, Y. Chen, G. Tian, L. Wang, Y. Xiao and H. Fu, *ChemCatChem*, 2015, 7, 1684-1690.
- [73] M. Saranya, R. Ramachandran, E J. J. Samuel, S. K. Jeong and A. N. Grace, *Powder Technology*, 2015, 279, 209-220.
- [74] C. C. Wong and W. Chu, *Environmental Science & Technology*, 2003, 37, 2310-2316.

CHAPTER 5

Photocatalytic Degradation of Alachlor Pesticide Catalyzed by CuS/BiFeO₃ Heterojunction Materials

5.1 Introduction

A variety of synthetic chemicals are used in agricultural sector as fertilizers, growth hormones and pesticides to boost productivity to cater to the need of increasing population. Among them, the pesticides are regarded as major water pollutants because of their adverse environmental and health effects. The unintended consumption of pesticides causes severe health effect like cancer, cardiovascular, reproductive and neurological disorders in non-targeted animals including humans [1, 2]. Alachlor is one of the widely used pesticides from chloroacetanilide family used to control annual grass and broadleaf weed in the crop field [3]. High chemical stability of alachlor towards photolysis and generation of numerous unwanted carcinogenic metabolites via biological and microbial degradation is a major concern [3-5]. These factors triggered for adaptation of new methodologies for the removal of alachlor from waste water in a greener, sustainable and economic way. Various methods like adsorption [6-8] and advance oxidation processes such as fenton [9, 10], sono-fenton [11], photo-fenton [12-14], direct ozonation [15], O₃/H₂O₂ [16], UV/O₃ [17], photoelectrocatalysis and photocatalysis [18-28] have been recently adopted for speciation/complete degradation of alachlor from aqueous sources. Out of these methods, the photocatalytic route is advantageous in terms of use of renewable energy source, simple and economic experimental setup which can be applied to large scale practical applications. So far TiO₂ and TiO₂ based materials such as N-doped TiO₂ [19], graphene/TiO₂ [20], TiO₂/Ti [24], Fe-TiO₂ [26, 28] are the only class of photocatalysts studied for the degradation of alachlor pesticide. TiO₂ based materials although highly active, exhibit UV light induced photocatalytic activity which is a major disadvantage in terms of the cost and sustainability of the process. Recently, thiapyrylium salts have been explored as photocatalyst for degradation of alachlor under simulated solar light [27]. There is a need to design visible light active photocatalyst which can act as a viable alternative to the TiO₂ based material. With an intention to develop novel and sustainable visible light induced photocatalytic route, in this work, we have synthesized type II CuS/BiFeO₃ heterojunction nanomaterials and studied their photocatalytic activity for degradation of alachlor pesticide from aqueous solution. The rationale behind choosing the BiFeO₃ based materials as photocatalyst originated from its narrow band gap (2.1-2.7 eV) and improved visible light absorption in comparison to other Bi based promising semiconducting material like Bi₂WO₆ and Bi₂W₂O₉. Moreover, the polarization-induced electric field arising out of its ferroelectric property has been vital for enhanced charge carrier separation and their

efficient utilization in photocatalytic processes [29]. The CuS by virtue of its higher negative conduction band potential is an ideal choice to form type-II heterojunction with BiFeO₃. Hence the combination of these materials is expected to generate efficient type-II heterojunction systems with improved photon harvesting property and higher photocatalytic activity.

5.2 Results and Discussion

5.2.1 XRD Study

The XRD patterns of BiFeO₃ (BFO) and CuS/BiFeO₃ (CuSBFO) materials are presented in Fig. 5.1. The BFO material displays characteristic XRD pattern of rhombohedral BiFeO₃ (JCPDS No-82-1254, space group- R3c) (Fig. 5.1Ia). Pure CuS and Bi₂S₃ synthesized by hydrothermal route using thiourea as precursor show characteristic patterns corresponding to the hexagonal covellite CuS (JCPDS No- 78-2121, space group- P63/mmc) and orthorhombic Bi₂S₃ (JCPDS No-75-1306, space group- Pbnm) phases, respectively (Fig. 5.1I e & f). The CuS5BFO heterojunction material exhibited characteristic peaks for BiFeO₃ only (Fig. 5.1Ib). No peaks corresponding to the crystalline CuS or any other analogues phases could be detected for this sample. The XRD pattern of CuS10BFO exhibits broad low intense features due to crystalline CuS in addition to the well-defined and intense peak of BFO phase (Fig. 5.1Ic). The CuS20BFO material, on the other hand, contains very low intense peaks with d spacing values of 2.72, 1.89, 1.73 and 1.58 Å for hexagonal CuS phase, 2.98 and 2.86 Å for Fe_{1-x}S (hexagonal Iron sulphide-JCPDS No-20-0534) and 3.55, 3.10, 2.63, 1.98, 1.87 and 1.72 Å for orthorhombic Bi₂S₃ together with the intense diffraction peaks of BiFeO₃ phase (Fig. 5.1Id). The Fe_{1-x}S and Bi₂S₃ are the minor impurity phases which occur probably due to the leaching of Bi³⁺ and Fe³⁺ ions during hydrothermal treatment of BiFeO₃ material. The leaching behaviour can be further ascertained from the observed change in the XRD peak intensities of the (104) and (110) planes of the CuS20BFO material (Fig. 5.1II). Up to 10 wt% CuS content, the relative peak intensity of these peaks remain unaltered whereas for CuS20BFO the relative intensity is found to differ.

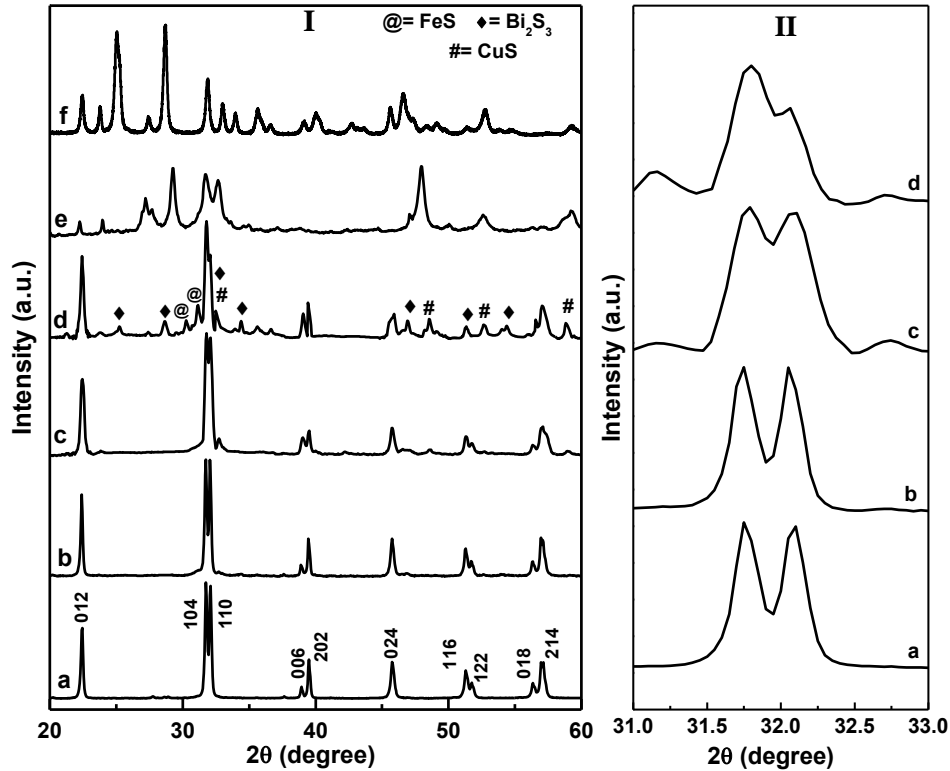


Figure 5.1: XRD profiles of (a) BiFeO₃, (b) CuS5BFO, (c) CuS10BFO, (d) CuS20BFO, (e) CuS and (f) Bi₂S₃ materials.

In order to confirm this proposition, hydrothermal treatment of BFO material is carried out in presence and absence of thiourea. The BFO structure remains unaffected in absence of thiourea (Fig. 5.2b). However, hydrothermal treatment in presence of thiourea, leads to the formation of Fe_{1-x}S and Bi₂S₃ as impurity phases due to the leaching of ions (Fig. 5.2c). The extent of leaching of the ions seems to depend on the concentration of thiourea in the solution. Up to CuS10BFO, no crystalline impurity phases could be detected, however, for CuS20BFO, the leaching of ions is more prominent leading to formation of crystalline impurity phases (Fig. 5.1Id). The XRD study suggests that thiourea is responsible for the leaching of the ions during hydrothermal treatment. Thiourea is a chelating ligand with N and S atom as coordination sites. The thiourea can effectively coordinate with Bi³⁺ and Fe³⁺ ions resulting in their partial dissolution from BFO lattice under high temperature and pressure. From XRD study, it is concluded that CuSBFO heterojunction materials up to 10 wt% CuS is a biphasic system (CuS and BFO), whereas at higher CuS content, namely CuS20BFO, Fe_{1-x}S and Bi₂S₃ appears as additional impurity phases.

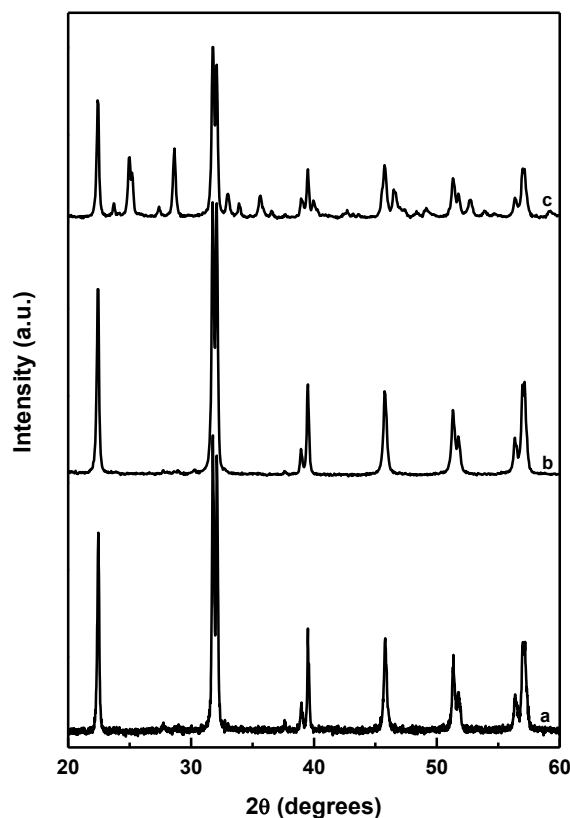


Figure 5.2: XRD patterns of (a) BFO and (b, c) hydrothermally treated BFO in absence and in presence of thiourea.

5.2.2 XPS Study

The surface chemical state of the CuSBFO heterojunction material is investigated using X-ray photoelectron spectroscopy. The XPS spectra of CuS10BFO material is presented in Fig. 5.3. The presence of Bi, Fe, Cu, O and S elements along with adventitious C are confirmed from the survey spectra (Fig. 5.3a). In the high resolution spectra, a strong doublet at 158.5 eV and 163.8 eV is observed with a splitting factor of 5.3 eV (Fig. 5.3b). These peaks correspond to the $\text{Bi}4f_{7/2}$ and $\text{Bi}4f_{5/2}$ electronic states of Bi in +3 oxidation state [30, 31, 32]. In the Fe2p region, a broad doublet peak is observed which can be fitted to four different peaks (Fig. 5.3c). The peaks at 710.5 eV and 724.0 eV can be assigned to the presence of iron in +3 oxidation state in an oxide environment [31, 33]. The peaks at 712.3 eV and 726.2 eV are due to Fe^{2+} species in sulfidic environment [34]. The Fe (II) signals accounts for the presence of a minor amount of non-stoichiometric iron sulphide impurity phase which has escaped detection by XRD. Figure 5.3d represents the high resolution XPS spectrum of Cu in 2p region. A spectral doublet with binding energies of 932.1 eV and 951.9 eV are assigned to $\text{Cu}2p_{3/2}$ and $\text{Cu}2p_{1/2}$ energy states of Cu^{2+} . Additionally, a satellite peak at 941.5 eV is noticed which confirmed the presence of copper in +2 oxidation state [35, 36].

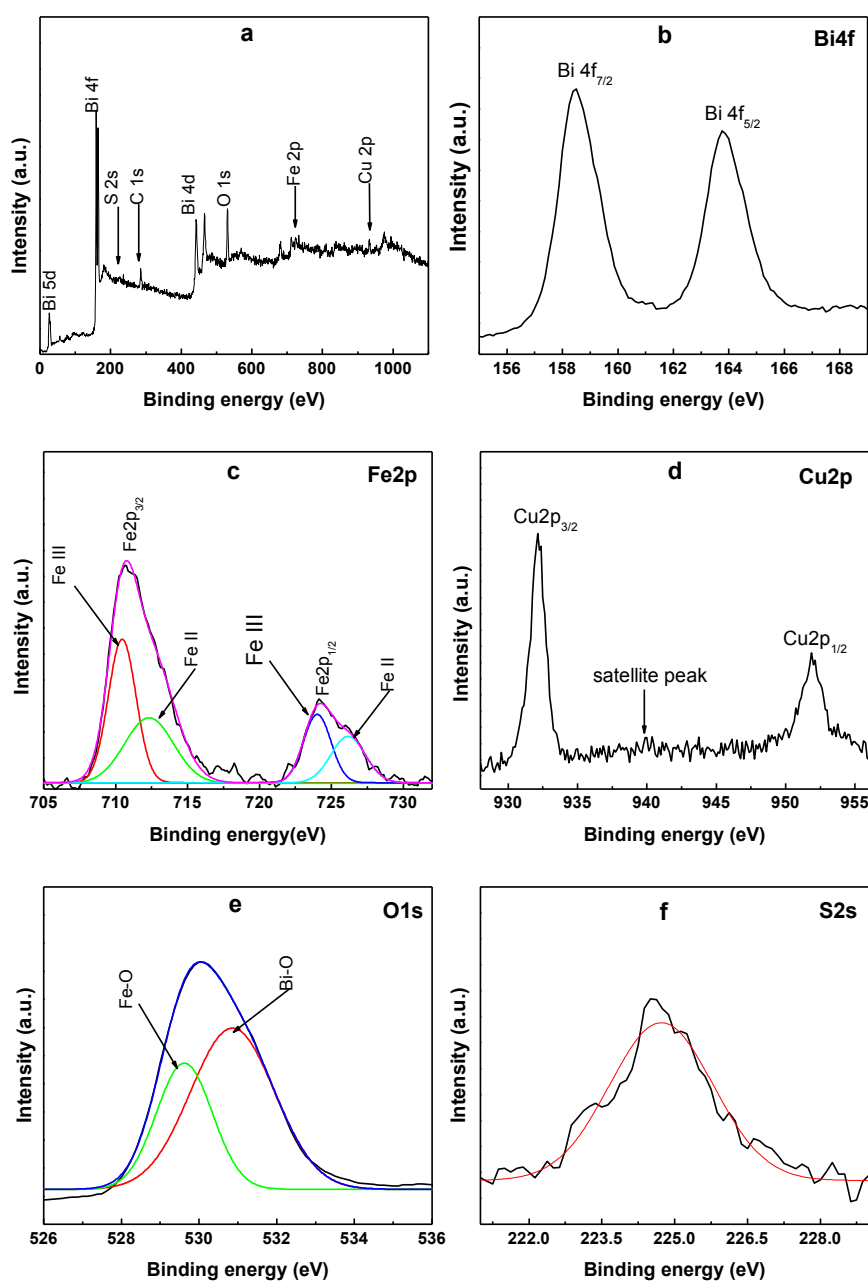


Figure 5.3: XPS spectra of CuS10BFO heterojunction material.

A broad and asymmetric peak is observed in the high resolution spectra of O1s (Fig. 5.3e). This peak is fitted to two peaks which correspond to the presence of oxygen in two different electronic environments. The peak at 530.9 eV is due to the O^{2-} ions coordinated to Bi^{+3} ions whereas the XPS peak 529.6 eV is assigned to the O^{2-} ion in Fe^{3+} environment [37]. In S2s spectral region, a broad peak is observed at 225.2 eV due S^{2-} ions of CuS phase in the heterojunction (Fig. 5.3f).

5.2.3 Optical Properties Study

The optical properties of BFO and CuSBFO heterojunction materials are studied by using UV-Vis-DRS and PL techniques. The UV-Vis-DRS spectra of BFO together with CuSBFO materials are presented in Fig. 5.4I. Pure BFO material exhibits intense absorption in visible region with absorption edge near 700 nm (Fig. 5.4Ia). Two different absorption features are noticed for the BFO material. The absorption feature between 500-700 nm is attributed to inter band transition, whereas the high energy transition in the range of 200-400 nm is due to ligand to metal charge transfer transition [38]. Pure CuS material exhibits visible light absorption with absorption edge near 850 nm (Fig. 5.4Ie).

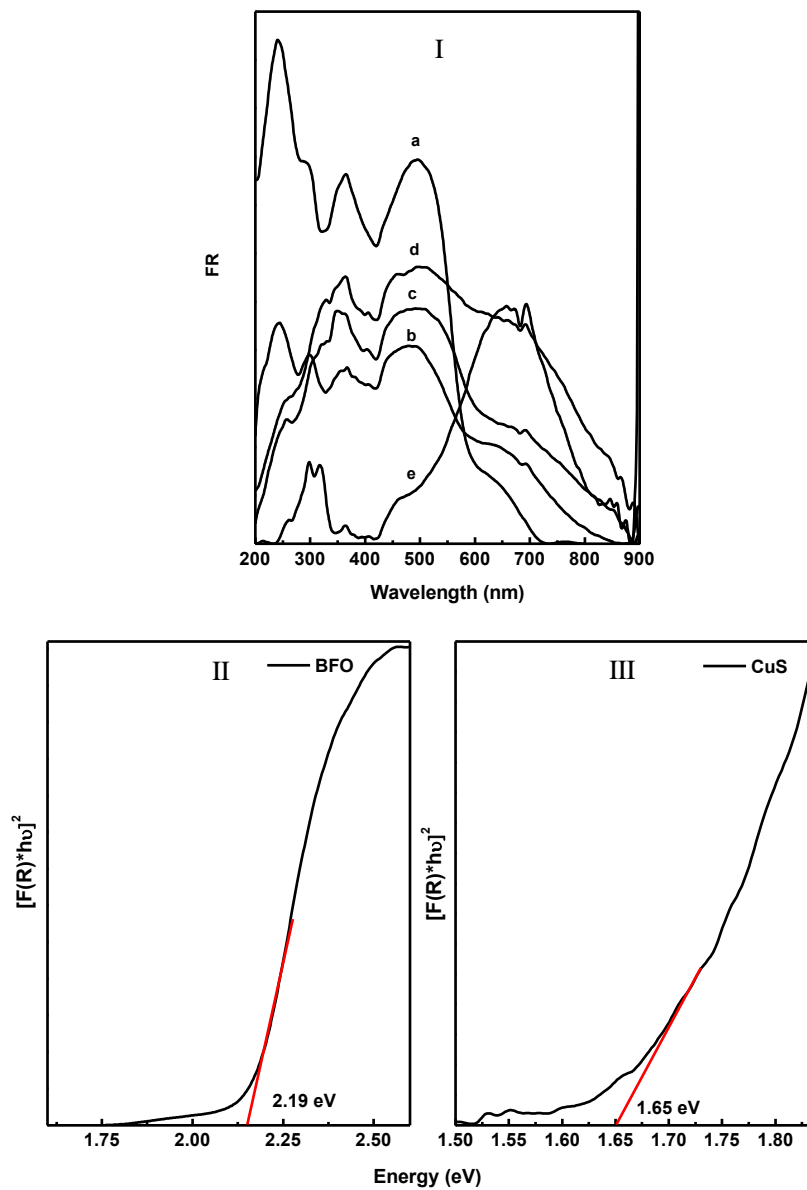


Figure 5.4: (Panel I) UV-Vis DRS spectra of (a) BiFeO₃, (b) CuS5BFO, (c) CuS10BFO, (d) CuS20BFO and (e) CuS and (Panel II & III) Plot of $[F(R)h\nu]^2$ as a function of photon energy ($h\nu$) in eV for BFO and CuS materials.

The visible light absorption properties of the CuSBFO heterojunction materials increase significantly with CuS content (Fig. 5.4I b-d). The significant enhancement in visible light absorption suggests that the CuSBFO material can be used as photocatalyst under visible light illumination. The optical band gap of the two semiconductors is calculated from Tauc's plot (Fig. 5.4 I & II). Pure BFO and CuS materials exhibit a band gap of 2.19 eV and 1.65 eV, respectively. These band gap values are quite consistent with the reported values [39, 40, 41]. The recombination rate of excitons for BFO and CuSBFO materials is accessed using photoluminescence spectroscopy (Fig. 5.5). Pure BFO material displays broad and intense PL emission bands at 448, 465 and 590 nm. The band at 590 nm is associated with the band edge transition, whereas other observed bands arise due presence of defects and impurities in the band structure [42].

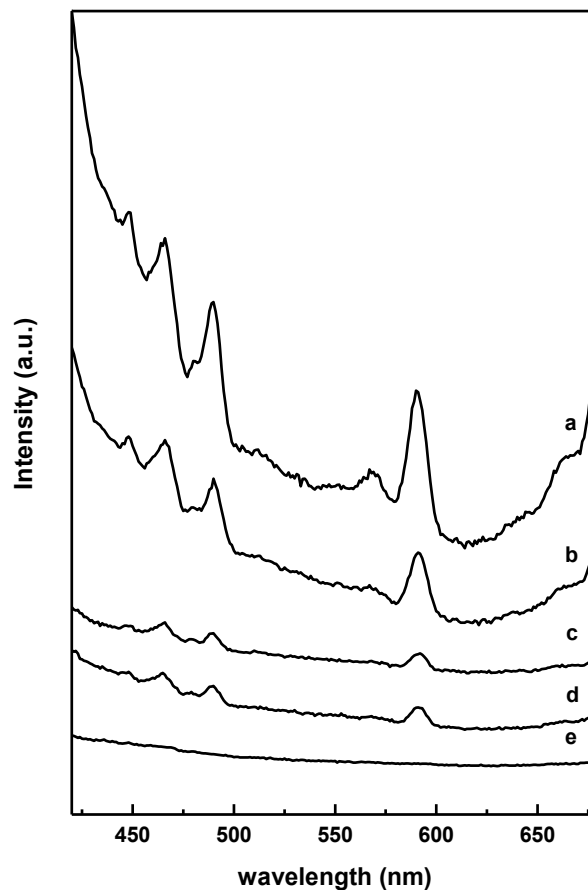


Figure 5.5: PL spectra of (a) BiFeO₃, (b) Cu₅SBFO, (c) Cu₁₀BFO, (d) Cu₂₀BFO and (e) CuS materials.

For pure CuS material no emission band could be noticed in the spectral range of 400-800 nm which is consistent with the earlier observations (Fig. 5.5e) [43, 44]. Upon modification with CuS, the PL intensity of the BFO is significantly attenuated. This decrease in PL intensity is due to efficient separation of photogenerated electron and holes in the CuSBFO materials (Fig. 5.5 b-d).

5.2.4 FTIR Study

The FTIR spectra of CuSBFO heterojunction materials are presented in Fig. 5.6. Pure BFO material shows two broad and intense IR peaks at 445 and 550 cm^{-1} (Fig. 5.6a). These IR bands are assigned to the O-Fe-O and Fe-O vibrations of FeO_6 octahedron in the perovskite structure [37, 45]. For CuSBFO materials a new set of low intense but distinguishable IR bands are observed at 616, 795, 845 and 890 cm^{-1} together with the characteristic peaks of BFO (Fig. 5.6 b-d). The IR band at 616 cm^{-1} is due to Cu-S vibrations [46]. The Cu-S vibrational band is quite weak for the CuS5BFO and CuS10BFO materials, while in case of CuS20BFO heterojunction material it is sharp and intense. The other IR bands correspond to the non-stoichiometric iron sulphide and Bi_2S_3 impurity phases present in the heterojunction materials [47, 48].

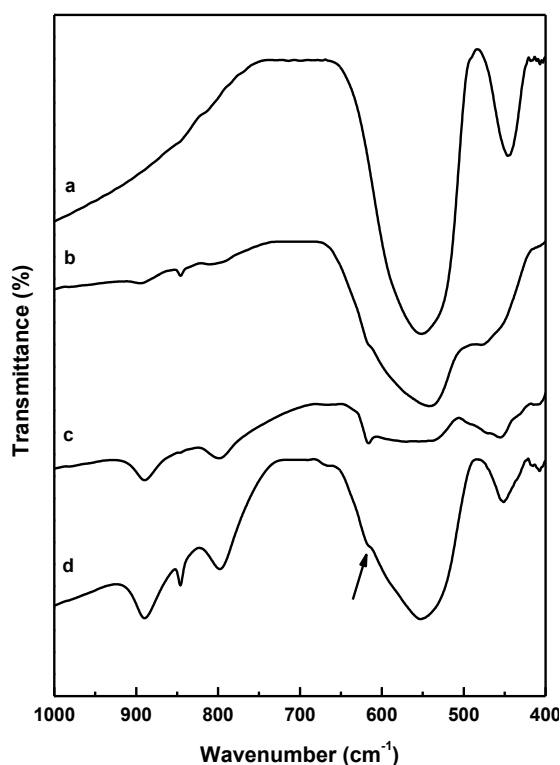


Figure 5.6: FTIR spectra of (a) BiFeO_3 , (b) CuS5BFO, (c) CuS10BFO and (d) CuS20BFO heterojunction materials.

5.2.5 Morphological Study

The microstructural properties of BFO and CuSBFO materials have been studied by using FESEM and HRTEM techniques (Fig. 5.7). The FESEM image of pure BFO material shows the presence of submicron size densely packed thin plates (Fig. 5.7a). The CuSBFO materials, on the other hand, contain uniformly distributed CuS nanorods and BFO sheets (Fig. 5.7 b-d). During hydrothermal treatment, the concurrent formation of CuS nanorods and desegregation of the densely packed BFO plates took place leading to formation of BFO

nanoplates. The BFO nanoplates show planar dimension of 0.25-0.9 μm in length and 0.15-0.8 μm in breadth. The thickness of the plates is in the range of 0.03-0.15 μm (Fig. 5.7c). The CuS nanorods have typical diameter in the range of 0.025-0.09 μm and 0.075-0.55 μm in length (Fig. 5.7c).

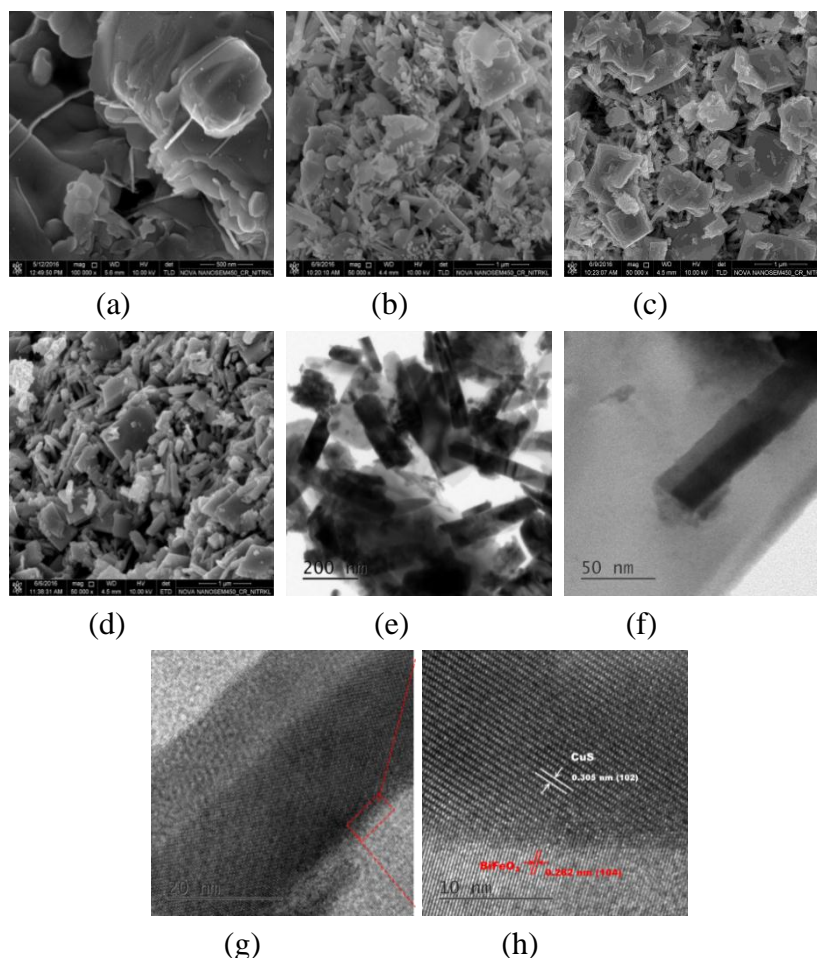


Figure 5.7: FESEM images of (a) BFO, (b) Cu5S10BFO, (c) Cu10S20BFO, (d) Cu20S40BFO and (e-h) HRTEM images of CuS10BFO material.

The density of the nanorods increases with increase in CuS content in the CuSBFO heterojunction materials. The presence of CuS nanorods and BFO plates is further confirmed from HRTEM study. The high resolution TEM image of CuS10BFO material is presented in Fig. 5.7 e-h. The presence of well dispersed CuS nanorods in a continuous matrix of BFO can be inferred from Fig. 5.7e. Figure 5.7 f-h depicts the high magnification TEM image of a CuS nanorod in contact with the BFO nanoplate. The interfacial region between CuS nanorod and BFO nanoplates is clearly observed from the high resolution image (Fig. 5.7 g-h). Microscopically close contact is established between the CuS and BFO phases which confirm the formation of heterojunction between the two phases. Two set of lattice fringes corresponding to the (102) and (104) crystallographic planes of CuS and BiFeO₃, respectively is clearly noticed in Fig. 5.7h. The formation of heterojunction is responsible for the facile migration of photo excited electrons and holes in the CuSBFO materials. The elemental

mapping images of the CuS10BFO heterojunction material is presented in Fig. 5.8. The uniform distribution of both the semiconducting materials throughout the specimen sample is confirmed from the elemental mapping study (Fig. 5.8). The BFO material exhibits a specific surface area of 18.5 m²/g. An improvement in surface area is noticed for the CuSBFO heterojunction materials (29-36 m²/g) (Table 5.1).

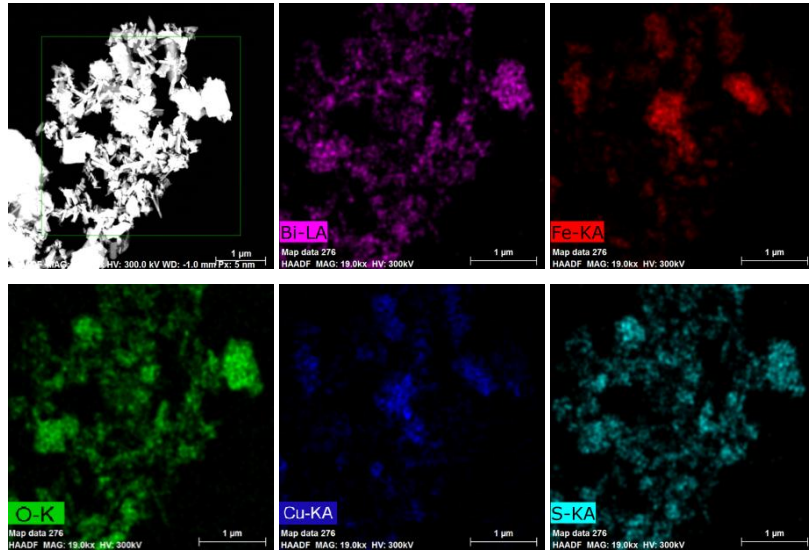


Figure 5.8: Elemental mapping study of CuS10BFO heterojunction material.

Table 5.1: Specific surface areas of the CuSBFO heterojunction materials.

Sl. No	Catalyst	Surface area (m ² /g)
1	BiFeO ₃	19
2	CuS5BFO	30
3	CuS10BFO	34
4	CuS20BFO	36

5.2.6 Transient Photocurrent Measurement

The charge separation characteristics and transport efficiency of the BFO and CuSBFO heterojunction materials is further studied by transient photocurrent measurement and current (I) vs voltage (V) plots as a function of time under visible light illumination. The CuS10BFO material exhibits higher photocurrent than pure BFO material (Fig. 5.9I). The I~V plots indicate lower resistance offered by the CuS10BFO heterojunction material towards the transport of the electrons (Fig. 5.9II) [20, 40]. These observations further suggest enhanced charge carrier separation and charge transport efficiency of the heterojunction material in comparison to pure BFO material. The enhancement in these properties is due to the

formation of heterojunction between the CuS and BFO phases, which facilitate the migration of photo induced charge carriers across grain boundaries rather than their recombination.

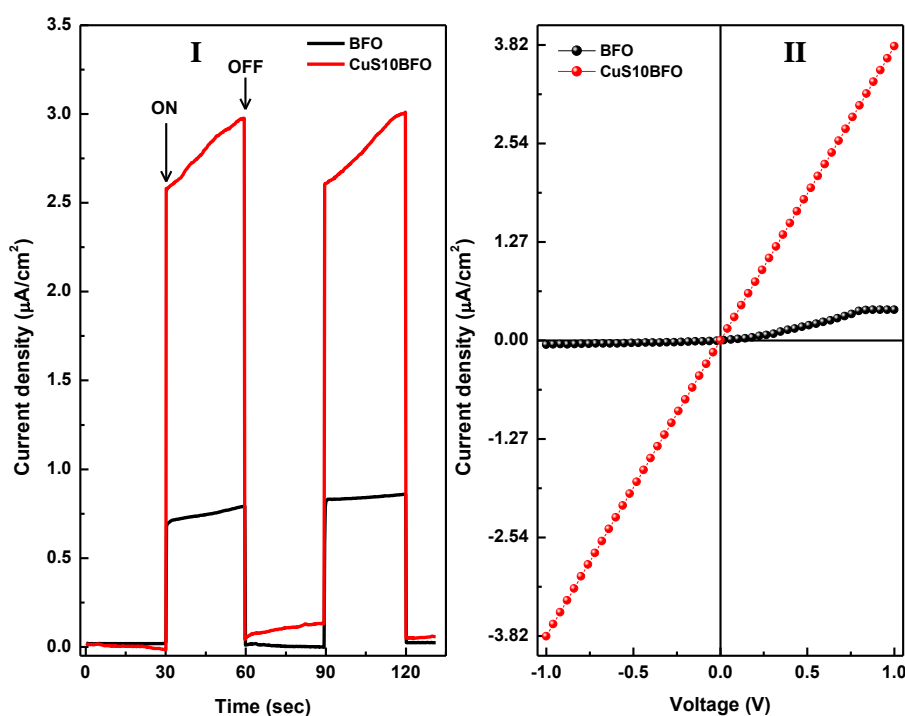


Figure 5.9: (a) Transient photocurrent and (b) current (I) vs voltage (V) measurement plots for BFO and CuS10BFO heterojunction materials.

5.2.7 Photocatalytic Degradation of Alachlor

5.2.7.1 Optimization of Reaction Parameters

The photocatalytic degradation of alachlor pesticide is studied using CuSBFO heterojunctions as catalyst. In a typical degradation reaction, 25 mg of catalyst is dispersed in a 100 ml of 5 ppm alachlor solution by sonication followed by 30 min of stirring under dark condition. The degradation reaction is initiated by adding 10 μl of 30% H₂O₂ to the aqueous suspension followed by visible light illumination. In order to establish the photocatalytic nature of the degradation, the reaction was also carried out under dark condition. After 6 h of reaction, no significant degradation of alachlor is noticed in presence as well as in absence of the catalyst. The kinetics plots for degradation of alachlor using different CuSBFO heterojunctions are presented in Fig. 5.10. Pure BFO material shows 35% alachlor degradation after 60 min of reaction (Fig. 5.10I). Significantly higher degradation rates are achieved when CuSBFO materials are used as photocatalysts. With increase in CuS content in heterojunctions the degradation efficiency increases upto 10 wt% and then decreases. The CuS20BFO material exhibited lower photocatalytic activity than the CuS10BFO probably due to the presence of higher percentage of impurity phases.

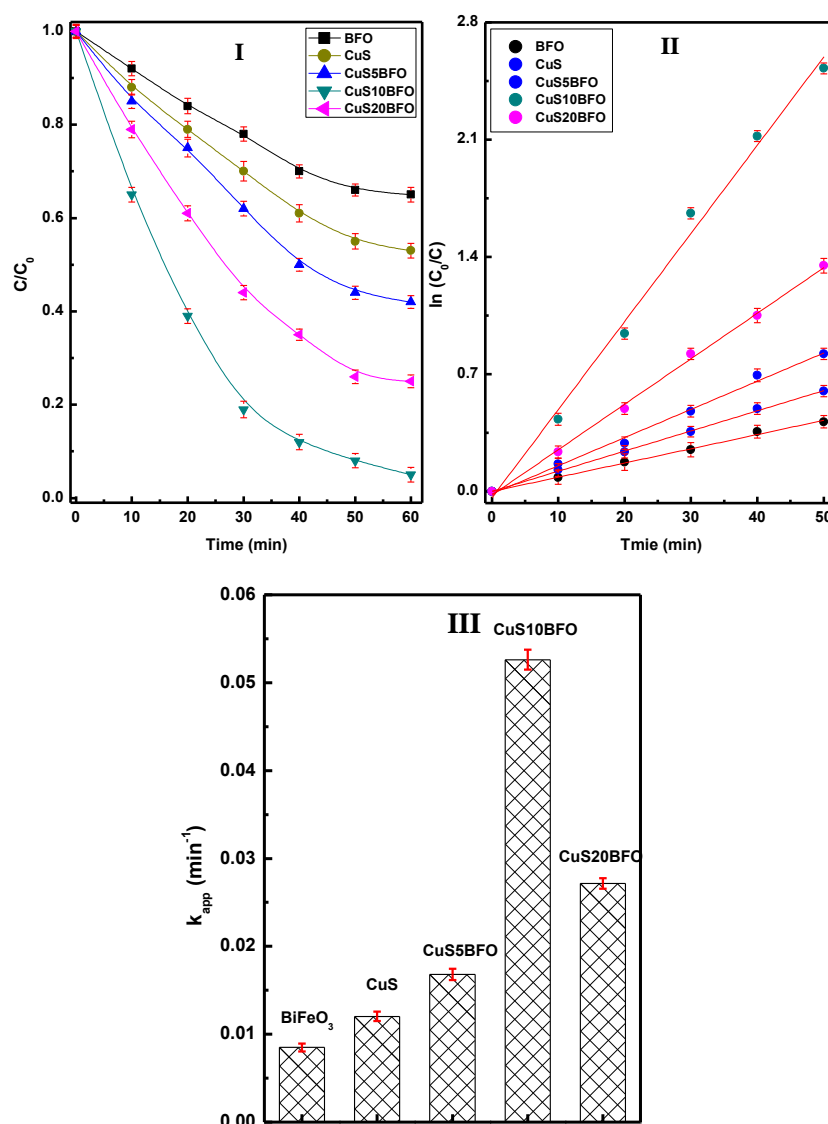


Figure 5.10: Photocatalytic efficiency of CuSBFO heterojunction photocatalysts towards the degradation of alachlor pesticide (25 mg catalyst, 10 μ l H₂O₂ and 5 ppm alachlor aqueous solution).

Using 25 mg of CuS10BFO material 95 % of alachlor is degraded within 60 min of reaction time (Fig. 5.10I). The higher degradation efficiency observed for the heterojunction materials can be ascribed to the increased visible light absorption and enhanced charge carrier separation properties. After completion of degradation reaction, the supernatant of the reaction mixture is also analyzed using AAS for leaching of ions. No appreciable concentration of Bi³⁺, Fe³⁺ and Cu²⁺ ions could be detected which rules out the possibility of Fenton or photo-Fenton type of degradation in the present study. All the heterojunction material display higher k_{app} value than the pure BFO material (Fig. 5.10 II & III). The k_{app} value for the CuS10BFO heterojunction is nearly 6 times greater than pure BFO material and 2 and 3 times that of CuS20BFO and CuS5BFO heterojunctions, respectively (Fig. 5.10III).

The degradation reaction is optimized by varying the catalyst amount and initial alachlor concentration taking the CuS10BFO heterojunction as photocatalyst. The catalyst amount is varied in the range of 5-30 mg. The degradation percentage increases with catalyst weight upto 25 mg before attending saturation (Fig. 5.11I). The initial alachlor concentration was optimized by varying the concentration between 1-6 ppm. Upto 5 ppm, 25 mg of CuS10BFO is quite efficient providing > 90% degradation within 60 min of reaction time (Fig. 5.11II). The mineralization of alachlor pesticide is also monitored by using TOC analysis of the reaction mixture at different time interval (Fig. 5.11III). The TOC removal increases with irradiation time reaching 92 % after 60 min of illumination. This observation suggests that a small fraction of degradation product remain as organic impurities which could not be mineralized by using the CuSBFO heterojunction photocatalyst.

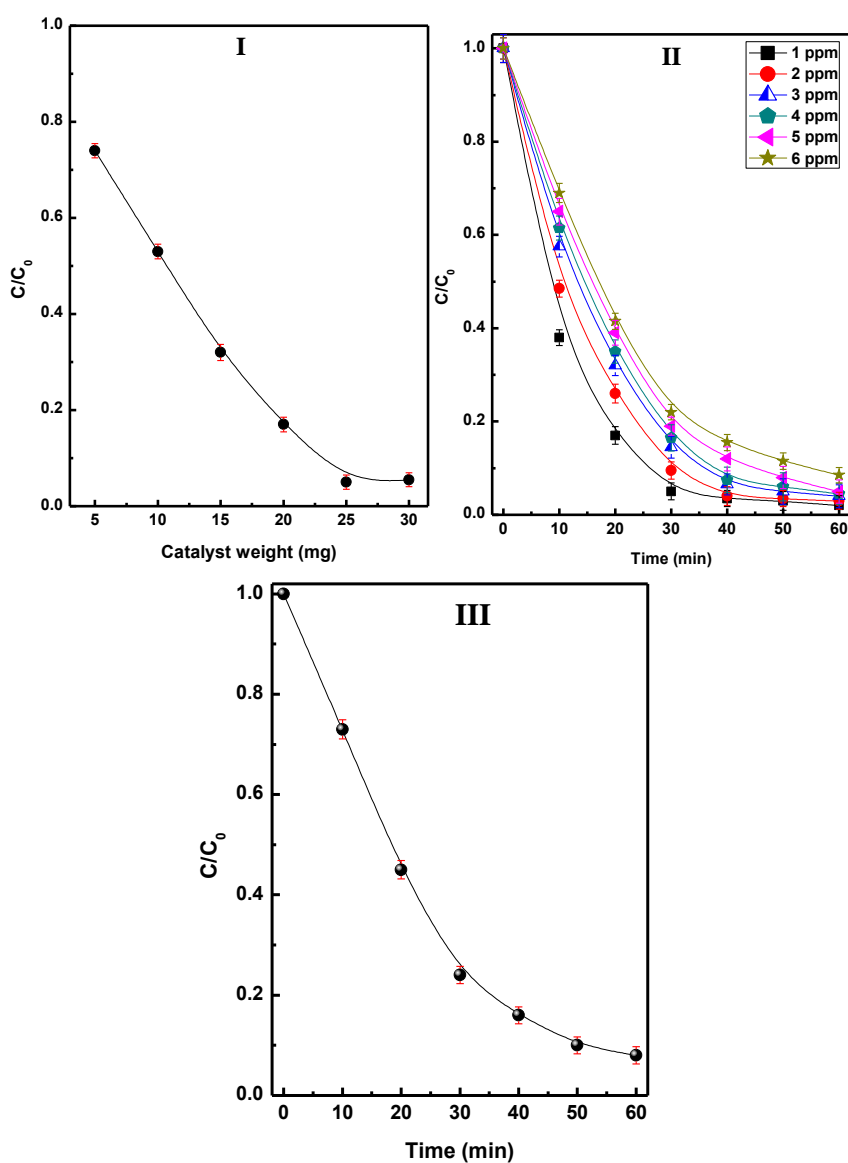


Figure 5.11: (Panel I) effect of catalyst dose (CuS10BFO catalyst, 5 ppm AL, 10 μ l H₂O₂, 1 h), (Panel II) initial alachlor concentration (25 mg CuS10BFO catalyst, 10 μ l H₂O₂, 1 h) and (Panel III) study of TOC removal (CuS10BFO catalyst, 5 ppm AL, 10 μ l H₂O₂) for the photocatalytic degradation of alachlor over CuS10BFO photocatalyst.

5.2.7.2 Plausible Mechanism for Photocatalytic Degradation of Alachlor

In order to understand the role of different radical species in the photo degradation of alachlor, degradation experiments are conducted in presence of different radical scavengers using 25 mg of CuS10BFO photocatalyst. Figure 5.12 represents the effect of different radical scavengers on the degradation of alachlor under visible light irradiation. In presence of hole and hydroxyl radical scavengers, significant decrease in degradation rate is observed.

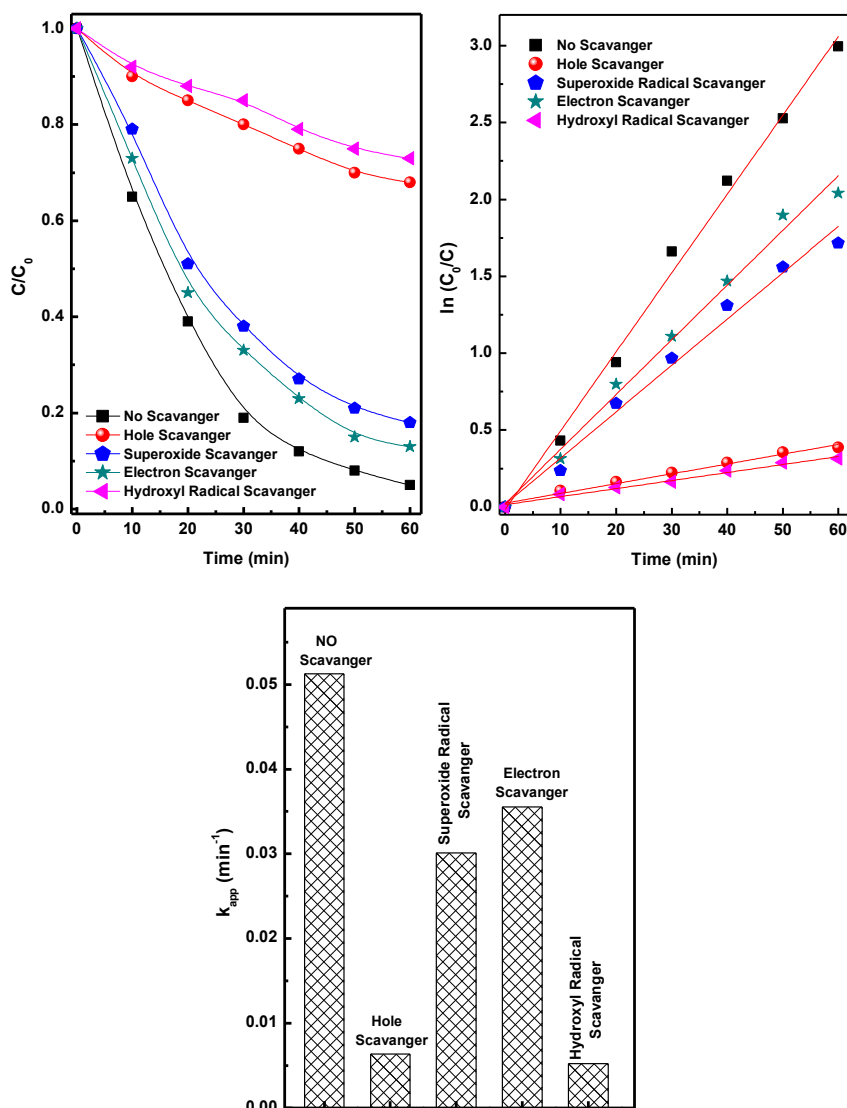


Figure 5.12: Effect of different radical scavengers on the photocatalytic degradation of alachlor studied using CuS10BFO photocatalyst.

While the superoxide radical and electron scavengers moderately decrease the rate of degradation. The scavenger experiments confirmed that the photogenerated hole and hydroxyl radicals are the primary species for the degradation of alachlor pesticide. The generation of hydroxyl radical ($\cdot\text{OH}$) on the catalyst surface is further ascertained by using terephthalic acid

(TA) as a chemical probe. TA effectively traps hydroxyl radical to generate fluorescent 2-hydroxy-terephthalic acid (HTA) [25, 40]. The fluorescence intensity can thus be correlated with the hydroxyl ions concentration in the solution. Figure 5.13 represents the fluorescence emission spectra of HTA formed in the catalyst aqueous suspension as a function of irradiation time at an excitation wavelength of 320 nm. Figure 5.13 suggests that both pure BFO and CuS10BFO heterojunctions generate hydroxyl radicals. However, the concentration of the hydroxyl radical generated over CuS10BFO (Fig. 5.13I) heterojunction material is quite high as compare to the pure BFO material (Fig. 5.13II) for a given irradiation time. This observation provides an explanation for higher photocatalytic efficiency of CuS10BFO heterojunction material which can be correlated to the generation of hydroxyl radical on the catalyst surface. In this study, 10 μl of H_2O_2 is added in the initial stage to trigger the degradation reaction of alachlor pesticide. The H_2O_2 and catalyst amount used in this study is quite less than the earlier reports on H_2O_2 assisted photocatalytic degradation of alachlor [26].

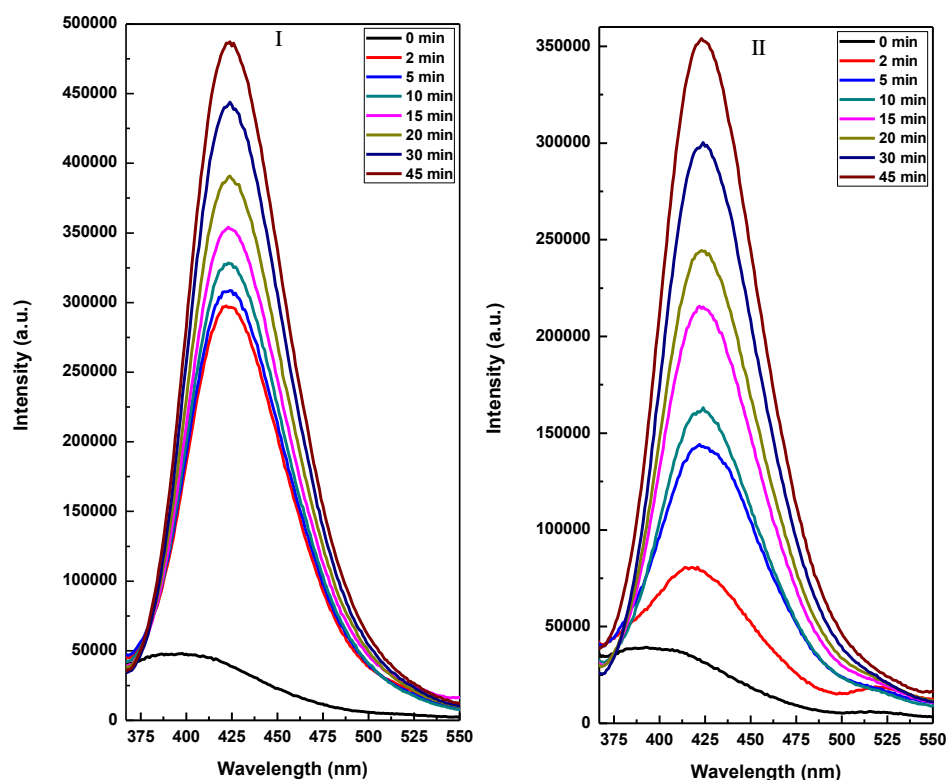


Figure 5.13: Fluorescence spectra of terephthalic acid solution containing catalyst particles (25 mg) irradiated with visible light (I) CuS10BFO and (II) BFO photocatalysts.

In order to understand the photocatalytic degradation pathway of alachlor over CuSBFO surface, GCMS analysis of reaction mixture is carried out at different irradiation time (Fig. 5.14). Seven different metabolites of alachlor are identified based on which a plausible degradation pathway on the catalyst surface is proposed (Scheme 5.1). Upon irradiation, OH^\bullet radicals are produced over the catalyst surface. The generated hydroxyl radicals attack the

aromatic ring of alachlor leading to formation of hydroxylated product II. Such intermediates have been detected earlier during TiO₂ catalyzed photocatalytic degradation of alachlor [20].

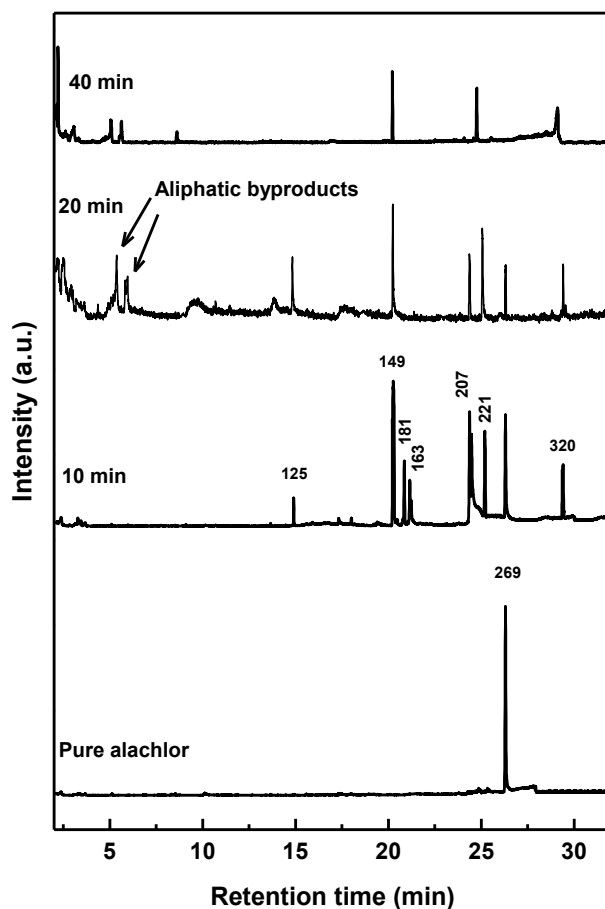
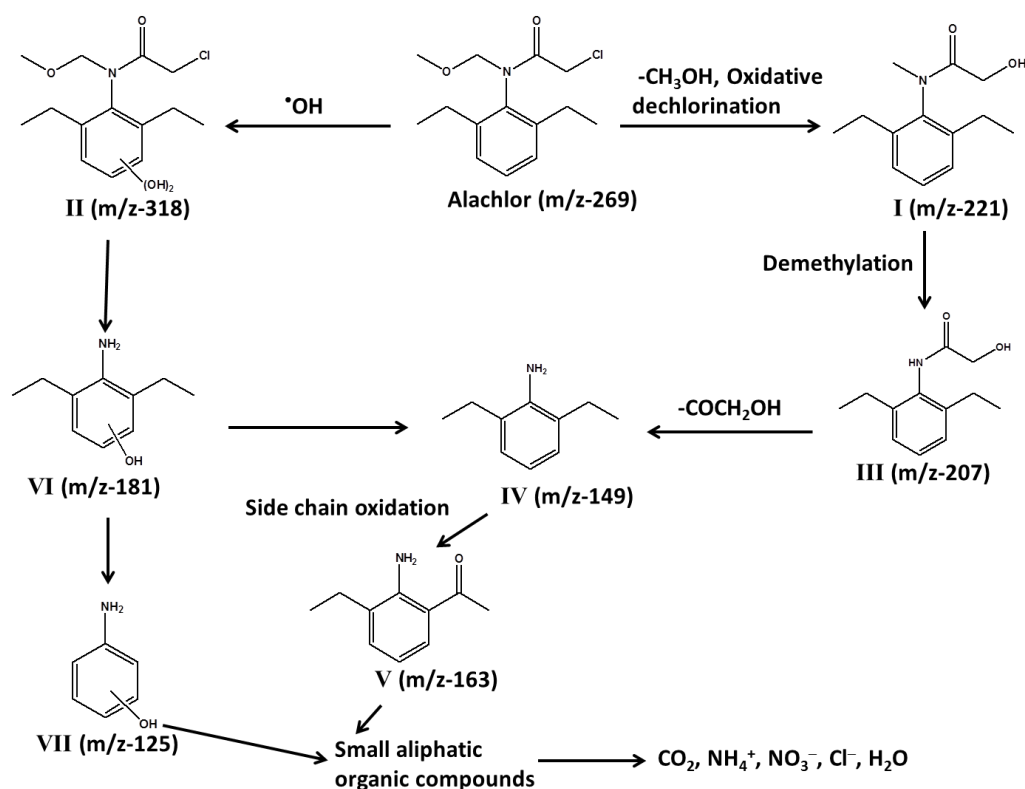


Figure 5.14: GC-MS analysis of photocatalytic degradation products of alachlor at different irradiation time.

With increase in the irradiation time the concentration of II decreases in the reaction mixture. The intermediate II can undergo further oxidation by the removal of $-\text{COCH}_2\text{Cl}$, and $-\text{CH}_2\text{OCH}_3$ groups leading to formation of VI. Simultaneously, the alachlor can react on the CuSBFO catalyst surface by loss of a methanol molecule followed by oxidative dechlorination to form the intermediate product I. Upon demethylation of I, product III is obtained which further react on the catalyst surface to afford IV (Scheme 5.1). The product VI can also undergo dehydroxylation to form product IV. The intermediates I, III and IV are common degradation products of alachlor which have been noticed in earlier studies [21, 27, 28]. The intermediate IV upon further oxidation of aliphatic side chains gives the oxidized product V [20]. Further, VI can also undergo dealkylation to afford VII. The intermediates so formed are further degraded to give small aliphatic moieties which eventually lead to the mineralization of alachlor. After 40 min of irradiation, the peak due to pure alachlor, as well as the intermediates III, V, VI and VII could not be detected in the chromatogram indicating their further oxidation during the photocatalytic process (Fig. 5.14). However, the product I, II and IV are detected in small quantities. At this time, the TOC removal corresponds to 80%

of the initial value. This observation suggests that the initial oxidation of alachlor to intermediate product I and II is relatively faster. However, the further degradation of these intermediate takes place in a cascade manner in a multi-step process leading to formation of IV which is further mineralized on the catalyst surface. The TOC removal results indicated presence of a small amount of organic carbon after 60 min, possibly due to the occurrence of small aliphatic moiety as metabolites which could not be degraded further on the catalyst surface.



Scheme 5.1: Possible degradation pathway of alachlor over the CuS10BFO photocatalyst surface.

The valance band (VB) and conduction band (CB) positions for the pure CuS and BiFeO₃ materials are calculated using the formula in equation 5.1 [49].

$$E_{\text{VB}} = X + 0.5E_{\text{g}} - 4.5 \text{ and } E_{\text{CB}} = E_{\text{VB}} - E_{\text{g}} \dots\dots\dots (5.1)$$

Where, E_{VB} and E_{CB} are the valence and conduction band potential (*wrt* NHE), X is the electronegativity of the semiconductor, E_{e} is the energy of free electron on hydrogen scale (4.5 eV), and E_{g} is the band gap of the photocatalyst. The X value for CuS and BiFeO₃ materials are 5.29 eV and 6.04 eV, respectively [50, 51]. The VB of BFO and CuS materials are placed at 2.63 eV and 1.61 eV, whereas the positions of CB are 0.445 and -0.04 eV, respectively. The band positions of both CuS and BFO materials are placed in a manner suitable for a type II heterojunction (Fig. 5.15A).

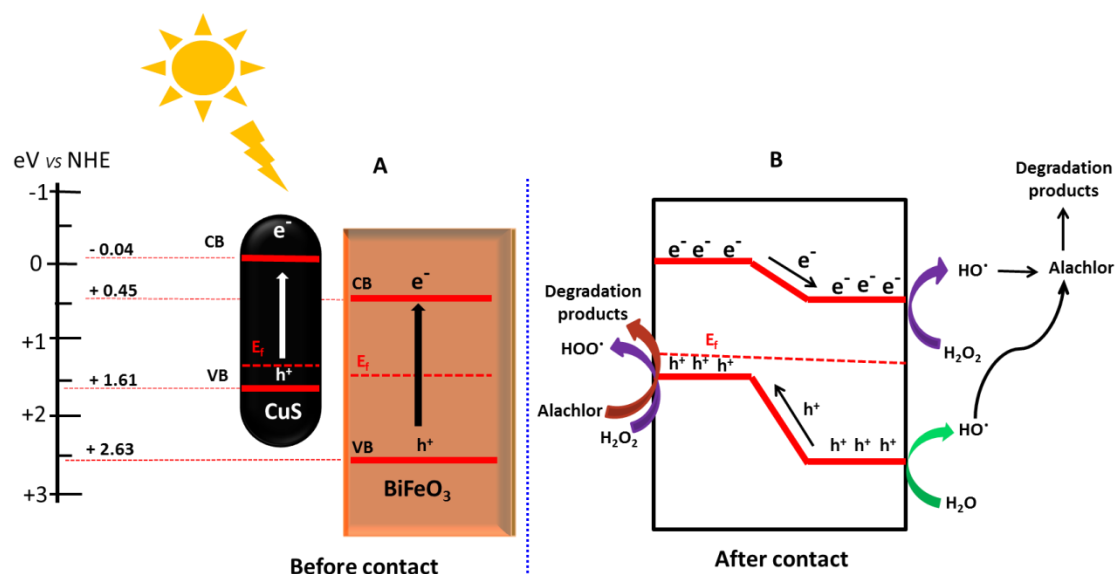


Figure 5.15: Plausible mechanism for photocatalytic degradation of alachlor over CuSBFO surface.

CuS is a known p-type semiconductor whereas un-doped BiFeO₃ exhibits intrinsic semi-conductivity with electrons and holes as the main defect species in almost equal concentrations [30, 52, 53]. After heterojunction formation, there is realignment of band positions of both semiconductors due to Fermi level equilibration (Fig. 5.15B). This band realignment facilitates the transfer of electrons from the CB of CuS to CB of BFO. Simultaneously, the holes can migrate from the VB of BFO to VB of CuS. This phenomenon leads to efficient space separation and utilization of photo generated excitons in the photocatalytic process. The hydroxyl radicals are generated at the CB of BFO by activation of H₂O₂. Simultaneously, the photocatalytic splitting of H₂O at the VB can produce •OH radicals (Fig. 5.15). The populated VB holes of CuS can also act as potential oxidizing species. These transient species can catalyze the degradation of alachlor over the CuSBFO heterojunction surface. Catalyst stability and recyclability is an important aspect of heterogeneous catalyst systems. The CuS10BFO material has been evaluated for five consecutive photocatalytic cycles for the degradation of alachlor pesticide. The heterojunction material exhibits stable catalytic activity upto five catalytic cycles without any significant decrease in the photocatalytic efficiency (Fig. 5.16).

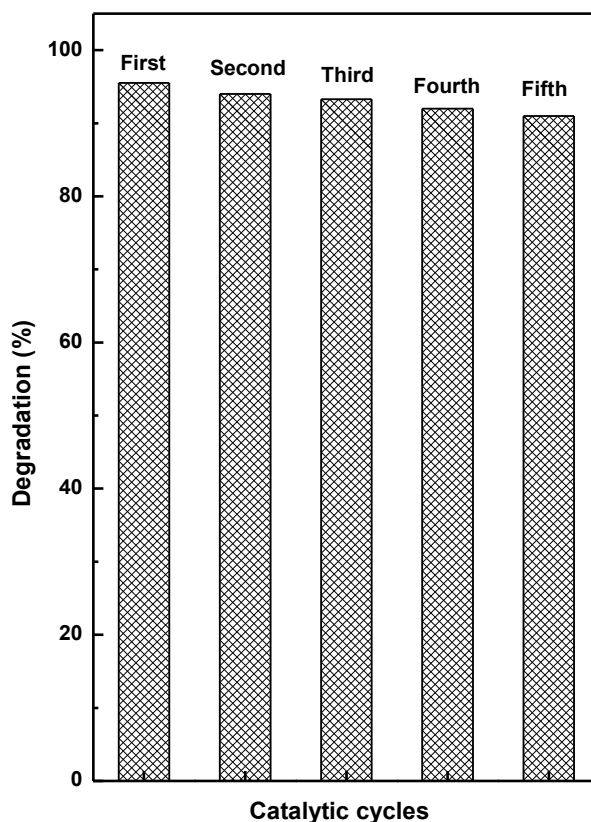


Figure 5.16: Recyclability test of CuS10BFO heterojunction photocatalyst for the degradation of alachlor.

5.3 Conclusions

In this chapter, we have described the photocatalytic application of a novel CuS/BiFeO₃ type-II heterojunction material for degradation of potentially harmful alachlor pesticide from aqueous solutions. The combustion synthesis method adopted for synthesis of BiFeO₃ species yielded phase pure material in a short time. Subsequent modification of the BiFeO₃ species with CuS by hydrothermal route leads to the formation of heterojunctions. The heterojunction materials contain crystalline covellite CuS and rhombohedral BiFeO₃ phases. Microscopic study suggested the presence of BiFeO₃ sheets with dimension of 0.25-0.9 μm in length and 0.15-0.8 μm in breadth and CuS nanorods with diameter in the range of 0.025-0.09 μm and 0.075-0.55 μm in length. The heterojunction materials exhibited enhanced visible light absorption, greater charge carrier separation and improved charge mobility, which are vital factors for their improved photocatalytic performance. The CuSBFO materials displayed excellent photocatalytic performance for mineralization of alachlor pesticides. The study of photocatalytic mechanism suggested that the degradation of alachlor occur in a series of steps over the catalyst surface with the identification of seven metabolites. The VB holes and hydroxyl radicals have been identified as the major transient species responsible for oxidation of alachlor. The photocatalytic method developed in this study is a sustainable and economic method compared to UV active photocatalytic systems.

References

- [1] C. K. Remucal, *Environmental Science: Processes & Impacts*, 2014, 16, 628-653.
- [2] D. M. Tessier and J. M. Clark, *Journal of Agricultural and Food Chemistry*, 1995, 43, 2504-2512.
- [3] P. L. Miller and Y. P. Chin, *Environmental Science & Technology*, 2005, 39, 4454-4462.
- [4] S. Chiron, J. Abian, M. Ferrer, F. Sanchez-Baeza, A. Messegueur and D. Barcelo, *Environmental Toxicology and Chemistry*, 1995, 14, 1287-1298.
- [5] J. M. Tiedje and M. L. Hagedorn, *Journal of Agricultural and Food Chemistry*, 1975, 23, 77-81.
- [6] Y. B. Kumar, N. Singh and S. B. Singh, *Journal of Environmental and Analytical Toxicology*, 2013, 3-7.
- [7] B. Paul, W. N. Martens and R. L. Frost, *Journal of Colloid and Interface Science*, 2011, 360, 132-138.
- [8] A. Leovac, E. Vasyukova, I. Ivancev-Tumbas, W. Uhl, M. Kragulj, J. Trickovic, D. Kerkez and B. Dalmacija, *RSC Advances*, 2015, 5, 8122-8133.
- [9] W. Liu, Y. Wang, Z. Ai and L. Zhang, *ACS Applied Materials & Interfaces*, 2015, 7, 28534-28544.
- [10] Y. Qin, F. Song, Z. Ai, P. Zhang and L. Zhang, *Environmental Science & Technology*, 2015, 49, 7948-7956.
- [11] C. Wang and Z. Liu, *Journal of Environmental Science and Health, Part B*, 2015, 50, 504-513.
- [12] M. I. M. Rubio, W. Gernjak, I. O. Alberola, J. B. Galvez, P. Fernandez-Ibanez and S. M. Rodriguez, *International Journal of Environment and Pollution*, 2006, 27, 135-146.
- [13] M. M. B. Martin, J. A. S. Perez, J. L. G. Sanchez, L. Montes de Oca, J. L. C. Lopez, I. Oller and S. M. Rodriguez, *Journal of Hazardous Materials*, 2008, 155, 342-349.
- [14] H. Katsumata, S. Kaneco, T. Suzuki, K. Ohta and Y. Yobiko, *Journal of Photochemistry and Photobiology A: Chemistry*, 2006, 180, 38-45.
- [15] L. Hai-yan, Q. Jiu-hui and L. Hui-juan, *Journal of Environmental Sciences*, 2007, 19, 769-775.
- [16] Z. Qiang, C. Liu, B. Dong and Y. Zhang, *Chemosphere*, 2010, 78, 517-526.
- [17] C. J. Somich, P. C. Kearney, M. T. Muldoon and S. Elsasser, *Journal of Agricultural and Food Chemistry*, 1988, 36, 1322-1326.
- [18] T. Suwannaruang and K. Wantala, *Applied Surface Science*, 2016, 380, 257-267.
- [19] D. Zheng, Y. Xin, D. Ma, X. Wang, J. Wu and M. Gao, *Catalysis Science & Technology*, 2016, 6, 1892-1902.
- [20] P. N. Moza, K. Hustert, S. Pal and P. Sukul, *Chemosphere*, 1992, 25, 1675-1682.
- [21] C. S. Ryu, M. S. Kim and B. W. Kim, *Chemosphere*, 2003, 53, 765-771.

- [22] C. C. Wong and W. Chu, *Chemosphere*, 2003, 50, 981-987.
- [23] W. Chu and C. C. Wong, *Industrial & Engineering Chemistry Research*, 2004, 43, 5027-5031.
- [24] C. L. Bahena and S. S. Martinez, *International Journal of Photoenergy*, 2006, 1-6.
- [25] Y. Xin, H. Liu, L. Han and Y. Zhou, *Journal of Hazardous Materials*, 2011, 192, 1812-1818.
- [26] K. Wantala, P. Khemthong, J. Wittayakun and N. Grisdanurak, *Korean Journal of Chemical Engineering*, 2011, 28, 2178-2183.
- [27] J. Gomis, A. Arques, A. M. Amat, M. L. Marin and M. A. Miranda, *Applied Catalysis B: Environmental*, 2012, 123-124, 208-213.
- [28] M. S. Kim, C. S. Ryu and B. W. Kim, *Water Research*, 2005, 39, 525-532.
- [29] X. Z. Deng, C. Song, Y. L. Tong, G. Yuan, F. Gao, D. Q. Liu and S. T. Zhang, *Physical Chemistry Chemical Physics*, 2018, 20, 3648-3657.
- [30] S. Chatterjee, A. Bera and A. J. Pal, *ACS Applied Materials & Interfaces*, 2014, 6, 20479-20486.
- [31] L. Lu, M. Lv, G. Liu and X. Xu, *Applied Surface Science*, 2017, 391, 535-541.
- [32] S. J. A. Moniz, D. Pugh, C. S. Blackman, J. Tang and C. J. Carmalt, *Crystal Growth & Design*, 2016, 16, 3818-3825.
- [33] D. Jiang, W. Hu, H. Wang, B. Shen and Y. Deng, *Chemical Engineering Journal*, 2012, 189-190, 443-450.
- [34] Z. Li, B. Li, Z. Liu, Z. Liu and D. Li, *RSC Advances*, 2015, 5, 106245-106251.
- [35] X. Meng, G. Tian, Y. Chen, R. Zhai, J. Zhou, Y. Shi, X. Cao, W. Zhoua and H. Fu, *CrystEngComm*, 2013, 15, 5144-5149.
- [36] Y. Shi, Y. Chen, G. Tian, L. Wang, Y. Xiao and H. Fu, *ChemCatChem*, 2015, 7, 1684-1690.
- [37] T. Soltani and B. K. Lee, *Chemical Engineering Journal*, 2016, 306, 204-213.
- [38] H. J. Feng, K. Yang, W. Deng, M. Li, M. Wang, B. Duan, F. Liu, J. Tian and X. Guo, *Physical Chemistry Chemical Physics*, 2015, 17, 26930-26936.
- [39] I. T. Papadas, K. S. Subrahmanyam, M. G. Kanatzidis and G. S. Armatas, *Nanoscale*, 2015, 7, 5737-5743.
- [40] T. Zhang, Y. Shen, Y. Qiu, Y. Liu, R. Xiong, J. Shi and J. Wei, *ACS Sustainable Chemistry & Engineering*, 2017, 5, 4630-4636.
- [41] C. Song, X. Wang, J. Zhang, X. Chen and C. Li, *Applied Surface Science*, 2017, 425, 788-795.
- [42] T. Soltani and B. K. Lee, *Photochemical and Photobiological Sciences*, 2017, 16, 86-95.
- [43] X. Jiang, Y. Xie, J. Lu, W. He, L. Zhu and Y. Qian, *Journal of Material Chemistry*, 2000, 10, 2193-2196.
- [44] P. Roy and S. K. Srivastava, *Crystal Growth & Design*, 2006, 6, 1921-1926.

- [45] H. Ramezanalizadeh and F. Manteghi, *Journal of Photochemistry and Photobiology A: Chemistry*, 2017, 338, 60-71.
- [46] M. Saranya, R. Ramachandran, E J. J. Samuel, S. K. Jeong and A. N. Grace, *Powder Technology*, 2015, 279, 209-220.
- [47] L. Chen, J. He, Q. Yuan, Y. Liu, C. T. Au and S. F. Yin, *Journal of Material Chemistry A*, 2015, 3, 1096-1102.
- [48] X. Zhang, Y. Niu, X. Meng, Y. Li and J. Zhao, *CrystEngComm*, 2013, 15, 8166-8172.
- [49] R. Guo, L. Fang, W. Dong, F. Zheng and M. Shen, *Journal of Material Chemistry*, 2011, 21, 18645-18652.
- [50] T. Fan, C. Chen and Z. Tang, *RSC Advances*, 2016, 6, 9994-10000.
- [51] C. Mondal, A. Singh, R. Sahoo, A. K. Sasmal, Y. Negishi and T. Pal, *New Journal of Chemistry*, 2015, 39, 5628–5635.
- [52] I. Vamvasakis, A. Trapali, J. Miao, B. Liu and G. S. Armatas, *Inorganic Chemistry Frontier*, 2017, 4, 433-441.
- [53] M. Schrade, N. Maso, A. Perejon, L. A. Perez-Maqueda and A. R. West, *Journal of Material Chemistry C*, 2017, 5, 10077-10086.

CHAPTER 6

Selective Reduction of Nitroarenes Catalyzed by α - Fe_2O_3 - Bi_2S_3 Heterojunction Materials

6.1 Introduction

The reduction of nitroarenes to aromatic amines is an important step in organic synthesis. The aromatic amines are valuable starting material for synthesis of amides, imines, diazonium salt and azo compounds. Amines are also used as precursors for synthesis of value added chemicals like biologically important compounds, dyes, polymers and pesticides [1, 2]. Beside above applications, the nitroarene reduction is also used as a trusted model reaction to evaluate the catalysis activity of metal and metal oxide nanocatalysts [2]. The reduction of nitro compounds to amines has been carried out using chemical reduction, catalytic hydrogenation and photocatalytic reduction methods. The chemical reduction method uses strong reducing agent like NaBH_4 and silanes [1, 3-6]. However, this method possesses limitations like nonselective intermediate formation, use of costly chemicals and metal contamination which makes the process expensive and precarious towards the environment [3, 7, 8]. The catalytic hydrogenation process employs noble metal catalyst like Pd, Pt, Ru, Rh, and Au at high H_2 pressure and temperature. Although the catalytic hydrogenation route is highly efficient, it involves use of costly metal, sophisticated instrumentation, high H_2 pressure and elevated temperature [1, 4, 9-11]. Recently, few improved metal free protocols have been designed for reduction of nitroarenes which use carbon materials like reduced graphene oxide (RGO) and N-doped mesoporous carbon as catalyst together with a reductant [12-16]. In recent years, the photocatalytic reduction method has emerged as a promising and versatile method for reduction of a variety of organic compounds containing reducible functional groups [17, 18]. The photocatalytic method offers distinct advantages in terms of renewable energy source, economy and sustainability. Till date, TiO_2 is widely investigated as a photocatalyst for reduction of nitroarenes under UV light irradiation [17, 19-22]. TiO_2 modified by composite formation with graphene, doping with transition metal and dye sensitization has been studied for nitroarenes reduction under visible light [23-26]. These modifications improve the charge carrier separation and provide good selectivity for reduction of nitroarenes. However, the reduction processes are sluggish and require longer reaction time. Besides TiO_2 based materials, CdS [27, 28], graphene [29], Bi_2MoO_6 based composite materials [30, 31], In_2S_3 -CNT [32] and Pt deposited on Ti (IV) MOF [33] have been studied for the photocatalytic reduction of nitro compounds under visible light irradiation. However, most of these reduction processes require longer time and use a sacrificial agent or solvent like ethanol or benzyl alcohol which give the corresponding

oxidized byproduct. In this work, we have developed a novel photocatalytic hydrogen transfer route for efficient reduction of nitroarenes to amines using α -Fe₂O₃-Bi₂S₃ heterojunction materials as catalyst. Hydrazine hydrate has been used as reducing agent (reduction potential = 1.15 V) which generates the innocuous N₂ as byproduct.

The Bi₂S₃ is a low band gap semiconducting material (1.2-1.7 eV) which shows promising photocatalytic activity [34-36]. Coupling of Bi₂S₃ with wide band gap semiconducting materials has been explored to prepare efficient heterostructure systems with improved photocatalytic activity towards degradation of organic contaminant from the aqueous sources [37-43]. From the point of view of applications in selective photocatalytic organic transformation, the α -Fe₂O₃-Bi₂S₃ coupled system is an ideal candidate which is yet to be investigated. Hematite (α -Fe₂O₃) is a promising visible light induced photocatalyst because of its suitable band gap (1.9-2.2 eV), plenty availability, nontoxic nature and high chemical stability [44]. Many synthetic routes like vapour phase deposition, thermal oxidation, electrochemical and solution phase synthesis have been adopted in literature to prepare α -Fe₂O₃ with improved properties [44]. By controlling preparative parameters, α -Fe₂O₃ with different morphologies such as nanorods, nanoflower, nanoflakes, nanocubes, polyhedral and rhombohedral nanoparticles have been synthesized [44, 45]. The α -Fe₂O₃ based materials have been explored as electrochemical electrode, electrocatalyst, gas sensor and photocatalyst [46-53]. In this work, we have synthesized α -Fe₂O₃-Bi₂S₃ heterojunction material by a rapid and one-step combustion synthesis route using thiourea as fuel and studied its photocatalytic application for reduction of nitroarenes.

6.2 Results and Discussion

6.2.1 XRD Study

The XRD profiles of the combustion synthesized α -Fe₂O₃-Bi₂S₃ heterojunctions along with pure components are presented in Fig. 6.1. The as-synthesized pure α -Fe₂O₃ material is amorphous in nature without any noticeable XRD peaks (Fig. 6.1a). When the combustion residue is calcined at 500 °C for 1 h, intense and sharp XRD peaks are observed at d spacing values of 3.68, 2.65, 2.51, 2.20, 1.84 and 1.69 Å (Fig. 6.1b). These peaks correspond to the reflection from the (012), (104), (110), (113), (024) and (116) planes of rhombohedral α -Fe₂O₃ (space group- R-3c, JCPDS No-72-0469). Pure Bi₂S₃ exhibits intense diffraction peaks with d-spacing values 3.95, 3.55, 3.10, 2.80, 2.70, 2.50 and 1.98 Å corresponding to reflections from (220), (130), (230), (221), (301), (240) and (002) crystallographic planes of orthorhombic Bi₂S₃ phase (space group-Pbnm, JCPDS No-75-1306) (Fig. 6.1f). For α -Fe₂O₃-Bi₂S₃ materials, peaks corresponding to both α -Fe₂O₃ and Bi₂S₃ phases are observed (Fig. 6.1 c-e). The XRD peaks at d spacing value of 2.65 and 2.50 Å arise due to the combined contribution from the α -Fe₂O₃ and Bi₂S₃ phases. With increase in the Fe₂O₃ content, these

XRD peaks gain intensity along with a concurrent decrease in the intensity of characteristic Bi_2S_3 peaks.

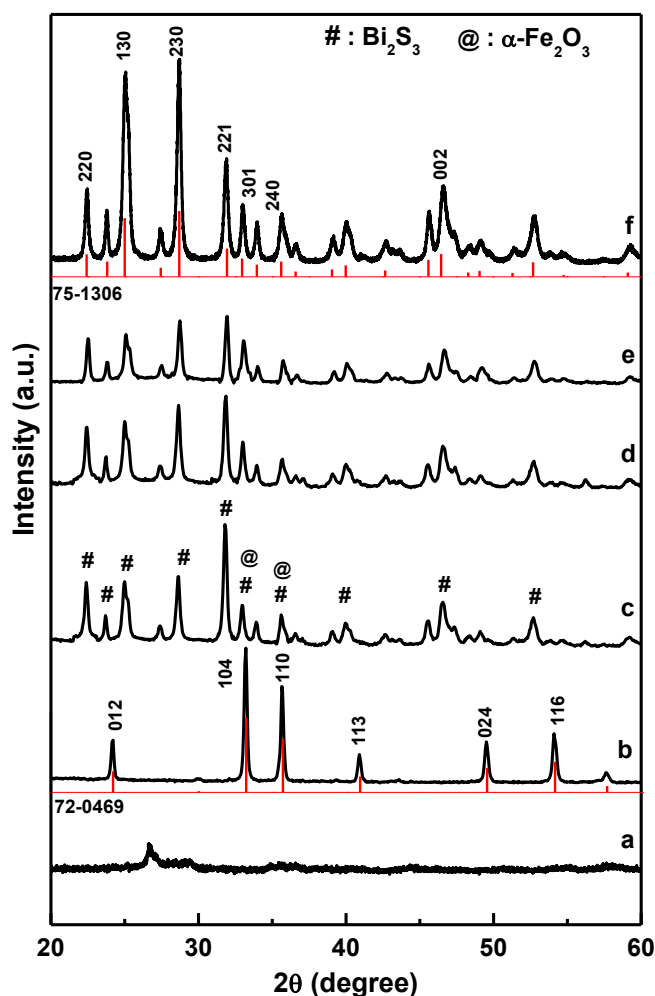


Figure 6.1: XRD patterns of (a) Fe_2O_3 as prepared, (b) Fe_2O_3 calcined at 500 °C, (c) $\alpha\text{-Fe}_2\text{O}_3(25\%)\text{-Bi}_2\text{S}_3$, (d) $\alpha\text{-Fe}_2\text{O}_3(37\%)\text{-Bi}_2\text{S}_3$, (e) $\alpha\text{-Fe}_2\text{O}_3(50\%)\text{-Bi}_2\text{S}_3$ and (f) Bi_2S_3 materials.

In general, the Bi_2S_3 phase exhibit broad diffraction patterns compared to the Fe_2O_3 phase. During combustion reaction, the thiourea acts as sulfur source as well as a fuel. The heat evolved during the exothermic combustion of thiourea ($\Delta_c H^\circ = 1472 \text{ kJ/mol}$) is utilized for transformation of the salt precursors [54]. The thermal decomposition of thiourea has been studied using theoretical and experimental methods. It has been observed that, high temperature decomposition of thiourea leads to formation of a variety of gaseous products including ammonia (NH_3), isothiocyanic acid (HSCN), hydrogen sulfide (H_2S) and carbodiimide (CN_2H_2) [55]. The H_2S and HSCN can act as sulfur source and help in the formation of Bi_2S_3 phase. Thiourea has been used as a precursor for synthesis of metal sulfides of Cu, Zn and Sn [56]. The thiourea acts as a chelating agent to form organometallic complexes with these metal ions. The metal complexes upon thermal decomposition produce the corresponding sulfides at intermediate temperatures. At higher temperature above 500 °C,

the metal oxides are formed. In the present study, we believe that the thiourea effectively coordinates with Bi^{3+} to form metal complex which undergo exothermic decomposition to produce Bi_2S_3 . The H_2S and HSCN formed as byproducts during the decomposition reaction generate an effective sulfidation environment which prevents the conversion of Bi_2S_3 to Bi_2O_3 phase. Although the formation of iron sulfides cannot be ruled out during combustion, due to the lower decomposition temperature they may be converted to oxide form. The thermal transformation behavior of Fe and Bi sulfides has been studied earlier. Bi_2S_3 is thermally stable upto 500 °C beyond which Bi_2O_3 formation has been noticed [57]. Lanjewar and Garg have observed that the thermal decomposition of iron dialkyldithiocarbamate complexes occur below 250 °C to give iron sulfide. The iron sulfides decompose beyond 250 °C leading to formation of Fe_2O_3 [58]. The temperature employed in this study is conducive for decomposition of iron sulfide to oxide. The ensuing discussion explains the formation of Bi_2S_3 and Fe_2O_3 phases which are noticed from XRD study.

6.2.2 XPS Study

The oxidation states of the constituent elements present in $\alpha\text{-Fe}_2\text{O}_3\text{-Bi}_2\text{S}_3$ heterojunction materials are studied from the XPS analysis. The XPS spectra of $\alpha\text{-Fe}_2\text{O}_3(37\%)\text{-Bi}_2\text{S}_3$ heterojunction is presented in Fig. 6.2. The survey spectrum shows characteristic spectral features corresponding to the presence of bismuth, iron, oxygen, and sulphur along with the adventitious carbon (Fig. 6.2a). In the high resolution spectra, a doublet is observed at 158.3 eV and 163.5 eV with spin-orbit splitting of 5.2 eV. These binding energies correspond to the photoelectron emission from the $\text{Bi}4f_{7/2}$ and $\text{Bi}4f_{5/2}$ energy states [37, 40, 41]. The presence of this double confirms the presence of Bi in +3 oxidation state (Fig. 6.2b). In the $\text{Fe}2p$ spectral region, the $\alpha\text{-Fe}_2\text{O}_3(37\%)\text{-Bi}_2\text{S}_3$ material exhibits a doublet at 710.5 eV and 724.5 eV along with a low intense satellite peak at 718.5 eV (Fig. 6.2c). The doublet in the high resolution spectra correspond to $\text{Fe}2p_{3/2}$ and $\text{Fe}2p_{1/2}$ energy states. The occurrence of the satellite peak at 8 eV higher than the $\text{Fe}2p_{3/2}$ along with the spectral doublet is characteristics of the Fe^{3+} ion in oxide environment [46, 47, 52]. In the $\text{O}1s$ region, a symmetric and narrow peak is observed at 530.3 eV (Fig. 6.2d). This peak corresponds to the lattice oxygen from the Fe_2O_3 component which is in agreement with the literature reported value [46, 52]. In the high resolution spectra of $\text{S}2s$ region, a broad and low intense peak is observed at 225.7 eV corresponding to the sulfide ions of Bi_2S_3 (Fig. 6.2e) [37]. The XPS analysis of the $\alpha\text{-Fe}_2\text{O}_3(37\%)\text{-Bi}_2\text{S}_3$ heterojunction confirms the presence of Bi_2S_3 and $\alpha\text{-Fe}_2\text{O}_3$ components in the heterojunction material.

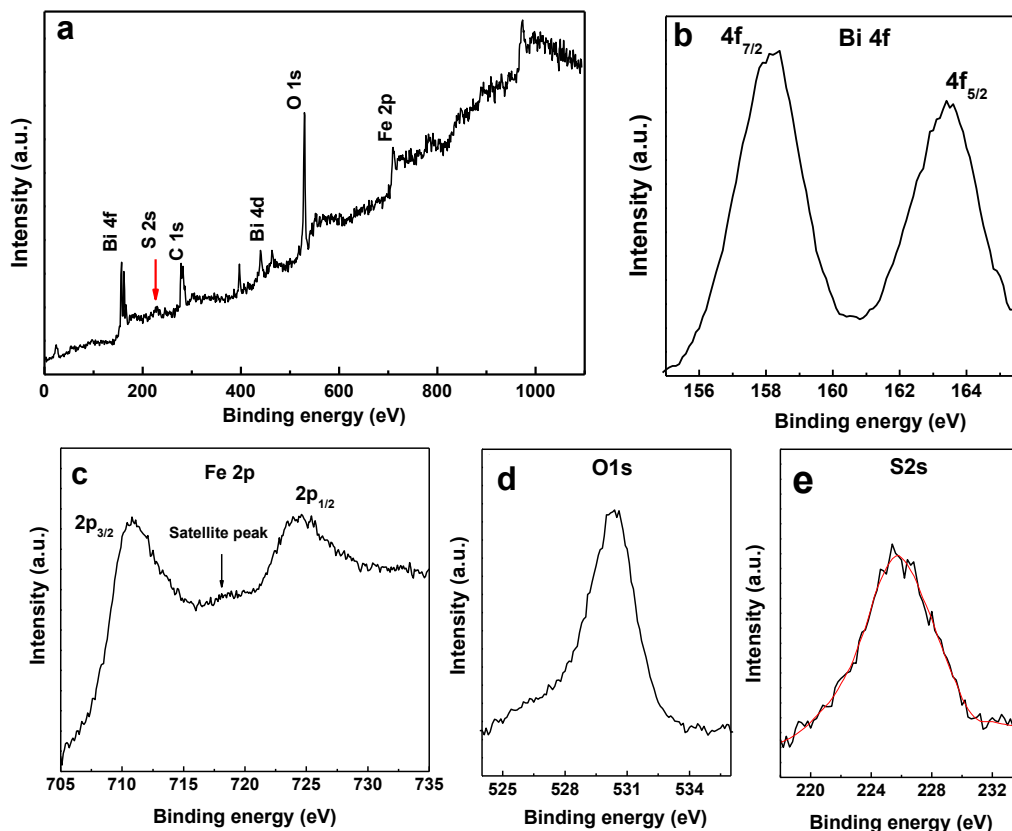


Figure 6.2: XPS spectra of α -Fe₂O₃(37%)-Bi₂S₃ photocatalyst.

6.2.3 Optical Properties Study

The UV-Vis-DRS spectra of pure Bi₂S₃, α -Fe₂O₃ and α -Fe₂O₃-Bi₂S₃ heterojunctions are presented in Fig. 6.3. Pure Fe₂O₃ exhibits significant visible light absorption with absorption edge near 600 nm (Fig. 6.3Ia). This absorption feature is attributed to the electronic transition from the oxygen to iron ($O^{2-} \rightarrow Fe^{3+}$) charge transfer transition ($6t_{1u} \rightarrow 2t_{2g}$) [53]. The absorption edge for pure Bi₂S₃ material commences near 870-880 nm (Fig. 6.3Ie). Pure Bi₂S₃ being a narrow band gap semiconductor exhibits significant visible light absorption with band gap value in the range of 1.2-1.7 eV [34, 35]. The α -Fe₂O₃-Bi₂S₃ heterojunction materials showed improved optical absorption feature in the wavelength range of 400-800 nm (Fig. 6.3I b-d). The band gap of Bi₂S₃ and Fe₂O₃ materials are calculated from the plot of photon energy ($h\nu$) versus $[FR \cdot h\nu]^2$ (Fig. 6.3 II & III). The Fe₂O₃ and Bi₂S₃ materials exhibit band gap of 2.15 eV and 1.40 eV, respectively (Fig. 6.3 II & III). The observed band gaps are consistent with the previous reports [36, 52]. The UV-Vis study and the associated band structure suggest that all heterojunction materials can be used as visible light active catalyst. The charge carrier separation characteristics of the α -Fe₂O₃-Bi₂S₃ heterojunction materials have been studied by PL technique. The PL spectra of the Bi₂S₃ and α -Fe₂O₃-Bi₂S₃ materials in the spectral region of 460-560 nm are presented in Fig. 6.3. The PL spectra are obtained by excitation at 400 nm. Pure Bi₂S₃ shows two intense PL emission bands at 465 nm and 540 nm

(Fig. 6.4a). The intense PL band observed for Bi_2S_3 material suggests rapid recombination of the e^-h^+ pair. In contrast to this observation, the $\alpha\text{-Fe}_2\text{O}_3\text{-Bi}_2\text{S}_3$ heterojunctions exhibit PL bands with a significant decrease in intensity (Fig. 6.4 b-d). The decrease in intensity is particularly more pronounced in case of the $\alpha\text{-Fe}_2\text{O}_3(37\%)\text{-Bi}_2\text{S}_3$ material (Fig. 6.4c). The decrease in the PL intensity suggests a substantial decrease in the recombination rate of photogenerated electron-hole pair leading to efficient charge carrier separation.

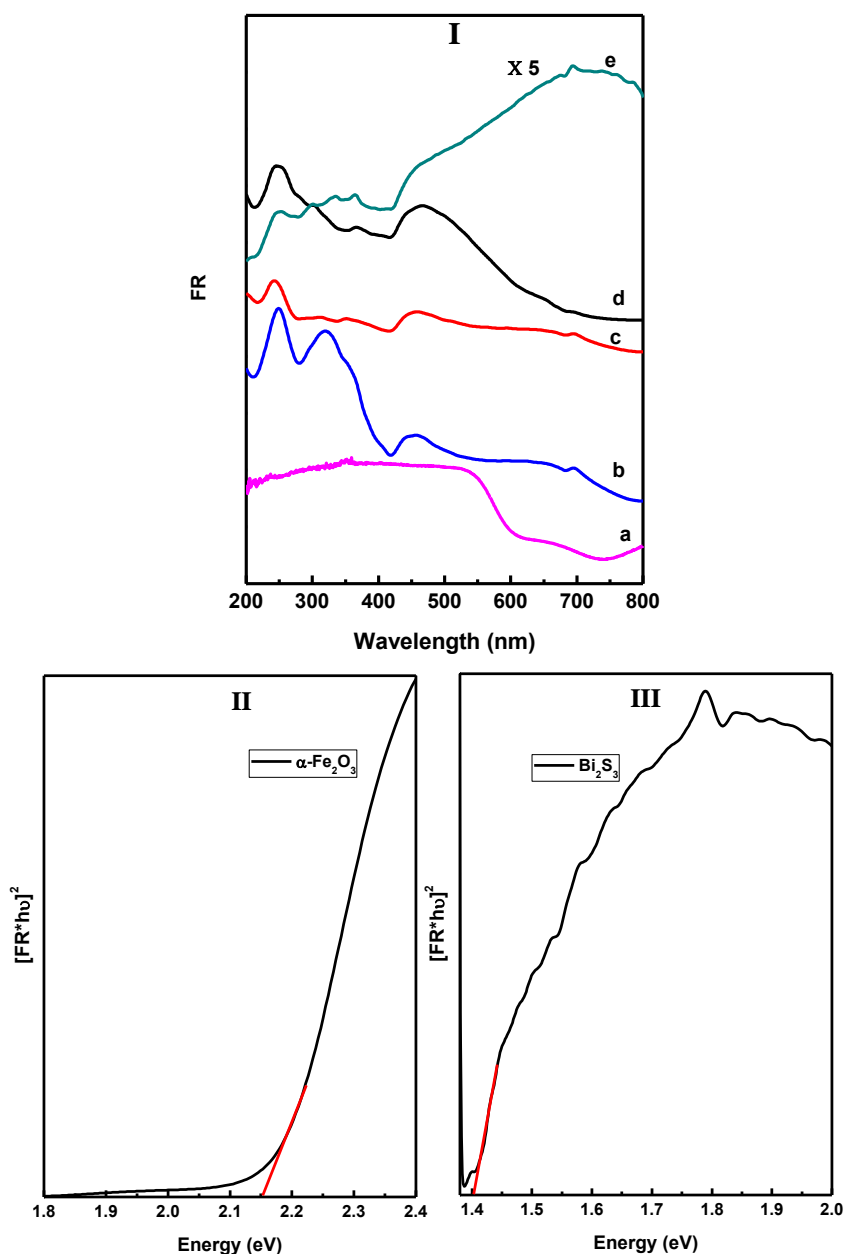


Figure 6.3: (Panel I) UV-Vis DRS spectra of (a) Fe_2O_3 , (b) $\alpha\text{-Fe}_2\text{O}_3(25\%)\text{-Bi}_2\text{S}_3$, (c) $\alpha\text{-Fe}_2\text{O}_3(37\%)\text{-Bi}_2\text{S}_3$, (d) $\alpha\text{-Fe}_2\text{O}_3(50\%)\text{-Bi}_2\text{S}_3$ and (e) Bi_2S_3 materials and (Panel II & III) plot of $[\text{F(R)hv}]^2$ as a function of photon energy ($h\nu$) for Fe_2O_3 and Bi_2S_3 materials.

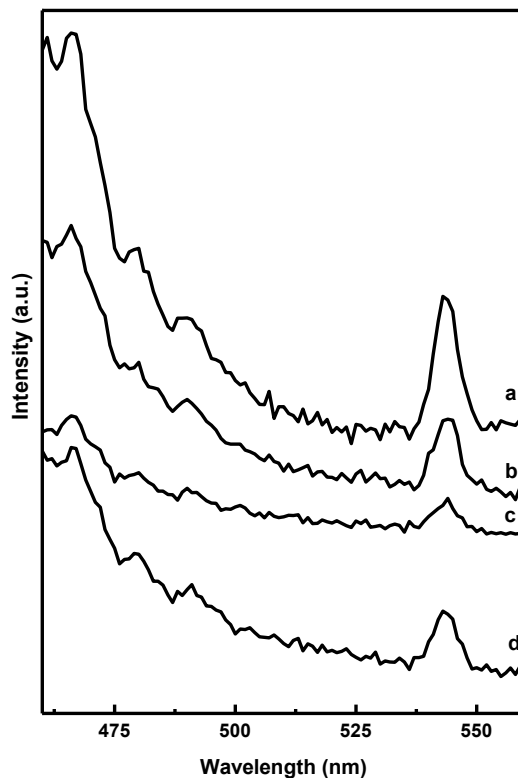


Figure 6.4: Photoluminescence (PL) spectra of (a) Bi_2S_3 , (b) $\alpha\text{-Fe}_2\text{O}_3(25\%)\text{-Bi}_2\text{S}_3$, (c) $\alpha\text{-Fe}_2\text{O}_3(37\%)\text{-Bi}_2\text{S}_3$ and (d) $\alpha\text{-Fe}_2\text{O}_3(50\%)\text{-Bi}_2\text{S}_3$ heterojunction photocatalysts (excitation wavelength 400 nm).

6.2.4 FTIR Study

The FTIR spectra of the $\alpha\text{-Fe}_2\text{O}_3\text{-Bi}_2\text{S}_3$ heterojunction materials in the fingerprint spectral region of $400\text{-}1300\text{ cm}^{-1}$ are presented in Fig. 6.5. Earlier literature studies suggest that the Bi_2S_3 and Fe_2O_3 component show characteristic stretching and bending vibration in this spectral range [43, 59]. In the present study, all the composite materials exhibit two intense and broad IR bands at 445 cm^{-1} and 550 cm^{-1} . These IR bands can be ascribed to the Fe-O vibration of the Fe_2O_3 component in the heterojunction materials [59]. In addition to the characteristics Fe_2O_3 vibration, a prominent band is observed at 1105 cm^{-1} . This band along with the less intense band observed at 615 cm^{-1} can be assigned to the Bi-S bond vibration [43]. The IR study indicates the presence of Bi_2S_3 and Fe_2O_3 component in the heterojunction material.

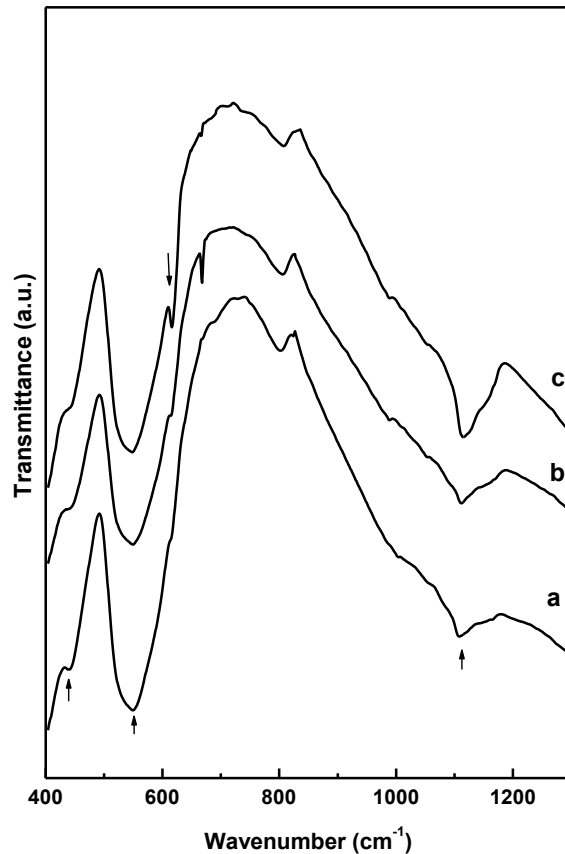


Figure 6.5: FTIR spectra of (a) $\alpha\text{-Fe}_2\text{O}_3(25\%)\text{-Bi}_2\text{S}_3$, (b) $\alpha\text{-Fe}_2\text{O}_3(37\%)\text{-Bi}_2\text{S}_3$ and (c) $\alpha\text{-Fe}_2\text{O}_3(50\%)\text{-Bi}_2\text{S}_3$ heterojunction materials.

6.2.5 Morphological Study

The surface morphology and particle size of the Bi_2S_3 and $\alpha\text{-Fe}_2\text{O}_3\text{-Bi}_2\text{S}_3$ heterojunctions have been evaluated from the FESEM and HRTEM analysis. The FESEM images of pure Bi_2S_3 along with $\alpha\text{-Fe}_2\text{O}_3\text{-Bi}_2\text{S}_3$ heterojunctions are presented in Fig. 6.6. The pure Bi_2S_3 material contains densely packed near spherical particles. These particles are connected through the grain boundary giving the structure of a continuous matrix (Fig. 6.6a). The presence of macroscopic pores can be noticed in the FESEM image. These pores originate due to the release of gaseous substances during the combustion process. In contrast to this observation, the $\alpha\text{-Fe}_2\text{O}_3\text{-Bi}_2\text{S}_3$ heterojunction materials are relatively less dense, porous and spongy in nature. All the $\alpha\text{-Fe}_2\text{O}_3\text{-Bi}_2\text{S}_3$ materials contain rod like $\alpha\text{-Fe}_2\text{O}_3$ particles of different size and dimension dispersed in a continuous Bi_2S_3 matrix (Fig. 6.6 b-d). The continuous Bi_2S_3 matrix also contains several macroscopic pores. With increase in the mol% of $\alpha\text{-Fe}_2\text{O}_3$ in the $\alpha\text{-Fe}_2\text{O}_3\text{-Bi}_2\text{S}_3$ materials, the density of the rod shaped $\alpha\text{-Fe}_2\text{O}_3$ particles are found to increase.

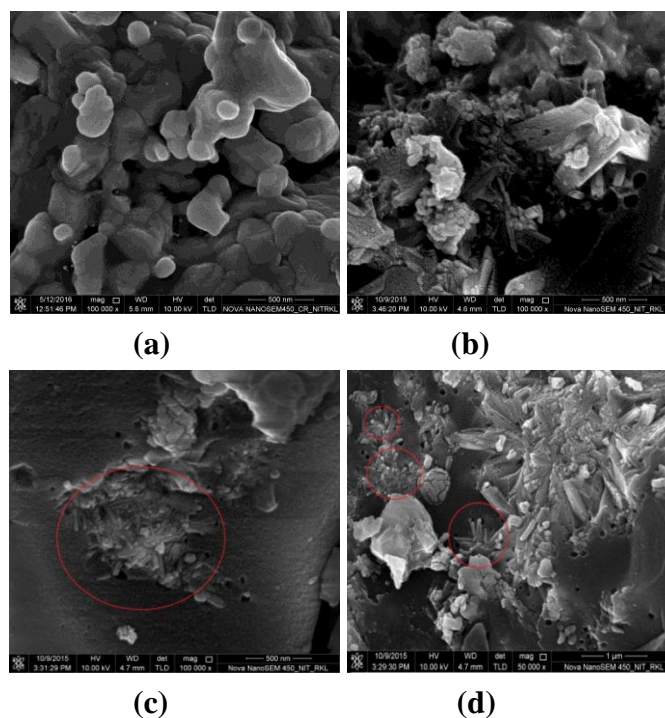


Figure 6.6: FESEM images of (a) Bi_2S_3 , (b) $\alpha\text{-Fe}_2\text{O}_3(25\%)\text{-Bi}_2\text{S}_3$, (c) $\alpha\text{-Fe}_2\text{O}_3(37\%)\text{-Bi}_2\text{S}_3$ and (d) $\alpha\text{-Fe}_2\text{O}_3(50\%)\text{-Bi}_2\text{S}_3$ heterojunction materials.

The presence of rod shaped $\alpha\text{-Fe}_2\text{O}_3$ in a continuous Bi_2S_3 matrix is further confirmed from the TEM analysis. The TEM images of $\alpha\text{-Fe}_2\text{O}_3(37\%)\text{-Bi}_2\text{S}_3$ heterojunction are presented in Fig. 6.7. The $\alpha\text{-Fe}_2\text{O}_3(37\%)\text{-Bi}_2\text{S}_3$ material contains different size $\alpha\text{-Fe}_2\text{O}_3$ rods well distributed in the continuous matrix of Bi_2S_3 (Fig 6.7a). The rods are of typically 30-50 nm in diameter and 120-150 nm in length (Fig. 6.7 b-d). The rods display a microscopically smooth surface and have originated from a nucleation point to grow in different directions. The micrograph in Fig. 6.7c shows a typical rod with its broken end. The broken end serves as the attachment point for growth of rods in different directions (Fig. 6.7c). The high resolution TEM images of $\alpha\text{-Fe}_2\text{O}_3(37\%)\text{-Bi}_2\text{S}_3$ material are presented in Fig. 6.7e and 6.7f. The formation of interface region between the Bi_2S_3 and $\alpha\text{-Fe}_2\text{O}_3$ phases can be clearly observed from the HRTEM image (Fig. 6.7f). Two different set of lattice fringes corresponding to the $\alpha\text{-Fe}_2\text{O}_3$ and Bi_2S_3 phases are observed (Fig. 6.7e). The two phases are in intimate contact leading to formation of heterojunctions which helps in facile transfer of charge carriers.

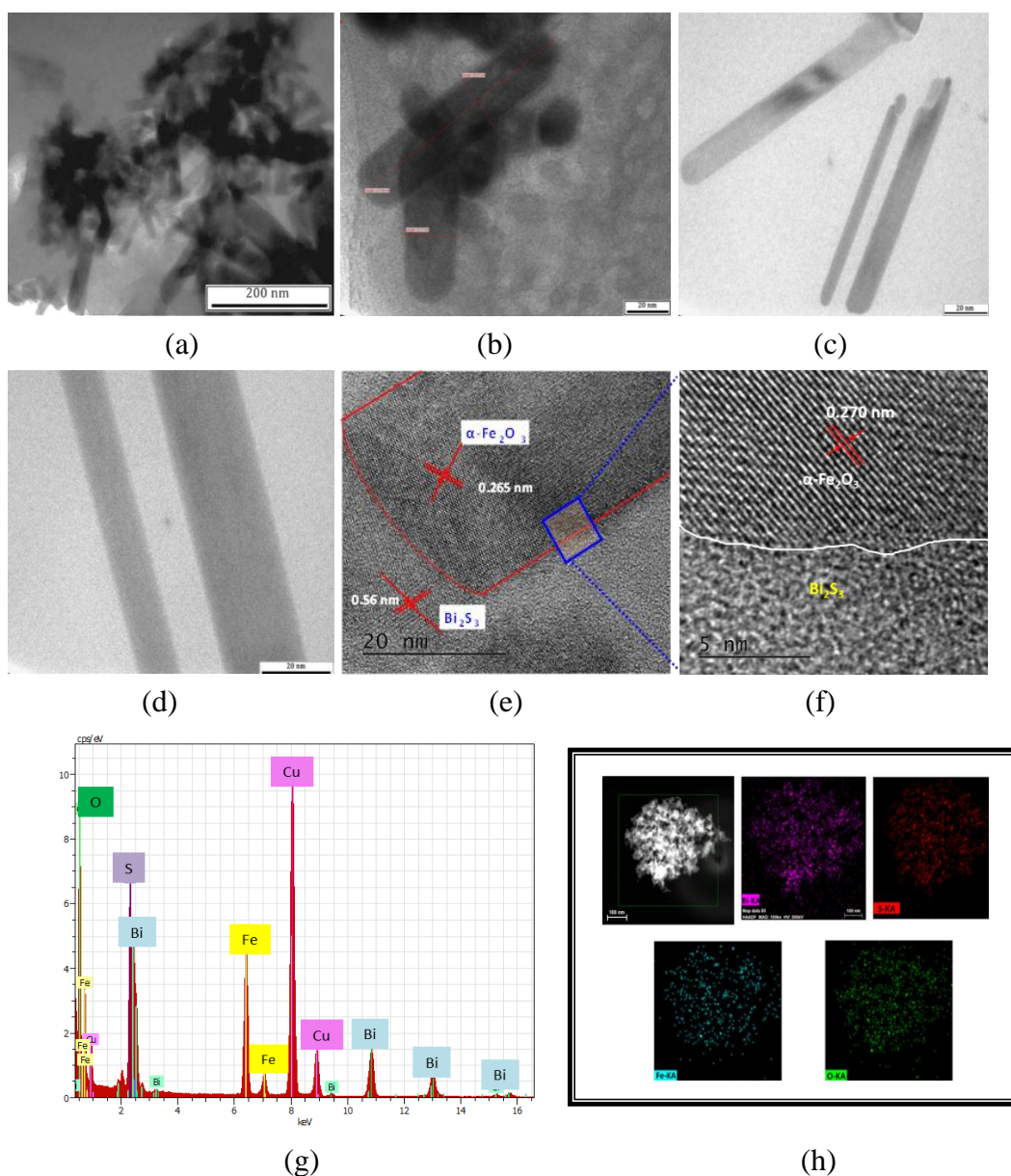


Figure 6.7: (a-d) TEM images, (e-f) HRTEM images, (g) EDX spectrum and (h) EDS mapping of $\alpha\text{-Fe}_2\text{O}_3(37\%)\text{-Bi}_2\text{S}_3$ heterojunction material.

The EDX spectrum and EDS mapping of the $\text{Fe}_2\text{O}_3(37\%)\text{-Bi}_2\text{S}_3$ material are presented in Fig. 6.7g and 6.7h, respectively. The presence of the Bi, S, Fe and O elements of required stoichiometry can be inferred from EDX spectrum. The EDS mapping images clearly indicate a uniform distribution of the elements throughout the specimen sample (Fig. 6.7h). The specific surface area of the heterojunction materials along with pure components are presented in Table 6.1. The heterojunction materials exhibit specific surface area in the range of 13-23 m^2/g .

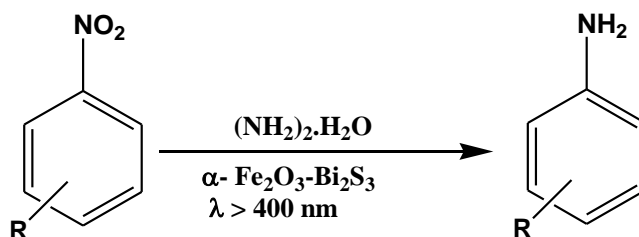
Table 6.1: Specific surface areas of Bi₂S₃, Fe₂O₃ and α -Fe₂O₃-Bi₂S₃ heterojunction materials.

Sl. No	Catalyst	Surface area (m ² /g)
1	Fe ₂ O ₃	13
2	Bi ₂ S ₃	16
3	α -Fe ₂ O ₃ (25%)-Bi ₂ S ₃	21
4	α -Fe ₂ O ₃ (37%)-Bi ₂ S ₃	23
5	α -Fe ₂ O ₃ (50%)-Bi ₂ S ₃	18

6.2.6 Photocatalytic Hydrogenation of Nitroarenes

6.2.6.1 Optimization of Reaction Parameters

The photocatalytic activity of the α -Fe₂O₃-Bi₂S₃ heterojunctions has been evaluated for the hydrogen transfer reduction of nitroarenes under visible light irradiation (Scheme 6.1).



Scheme 6.1: Photocatalytic hydrogen transfer reduction of nitroarenes to aromatic amines catalyzed by α -Fe₂O₃-Bi₂S₃ heterojunction.

Initially, the reduction of nitrobenzene is taken as a model reaction and the α -Fe₂O₃-Bi₂S₃ heterojunctions are studied for their photocatalytic activity under visible light irradiation in presence of hydrazine hydrate as hydrogen transfer agent. In order to confirm that the reaction is photocatalytic and involves hydrogen transfer, the reaction is conducted under dark and illuminated conditions in presence and absence of the α -Fe₂O₃-Bi₂S₃ catalyst and hydrazine hydrate. Under dark condition, both in presence and absence of catalyst no product could be detected indicating the photocatalytic nature of the reaction. When the reaction is carried out in absence hydrazine hydrate using α -Fe₂O₃(37%)-Bi₂S₃ catalyst, no product could be detected after an irradiation of 6 h. This observation suggests that, hydrazine hydrate as a hydrogen donor is essential for the reduction process. Figure 6.8 shows the catalytic efficiency of different α -Fe₂O₃-Bi₂S₃ catalysts for the photocatalytic hydrogen transfer reduction of nitrobenzene. Pure α -Fe₂O₃ and Bi₂S₃ catalyzed reduction process is quite sluggish with a net conversion of 53% and 36% achieved after 4 h of reaction. The α -Fe₂O₃-Bi₂S₃ heterojunction materials show enhanced photocatalytic efficiency. Among the heterojunctions, α -Fe₂O₃(37%)-Bi₂S₃ shows maximum nitrobenzene reduction ability achieving 95 % conversion of nitrobenzene with 100 % selectivity to aniline. The formation

of by-products such as imine or azo compounds is not detected in this study. Since the α - $\text{Fe}_2\text{O}_3(37\%)\text{-Bi}_2\text{S}_3$ exhibits best photocatalytic activity, this photocatalyst composition is selected for further study.

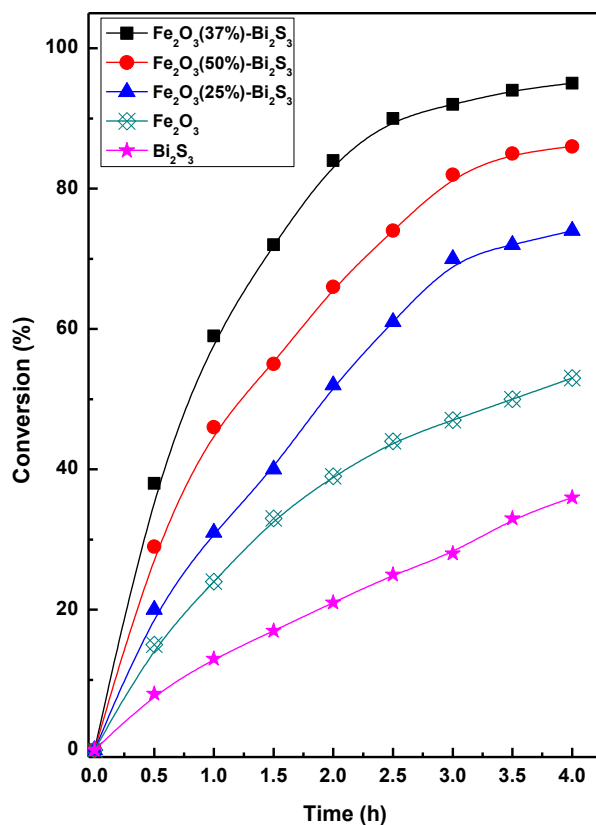


Figure 6.8: Photocatalytic hydrogen transfer reduction of nitrobenzene to aniline catalyzed by $\alpha\text{-Fe}_2\text{O}_3\text{-Bi}_2\text{S}_3$ heterojunction photocatalysts (reaction conditions: 50 mg of catalyst, $\text{C}_6\text{H}_5\text{-NO}_2\text{:N}_2\text{H}_4\cdot\text{H}_2\text{O}$ molar ratio = 2:8).

The effect of molar ratio of nitrobenzene to hydrazine hydrate on the catalytic activity of the $\alpha\text{-Fe}_2\text{O}_3(37\%)\text{-Bi}_2\text{S}_3$ catalyst is studied by varying the molar ratio of the reactants (Fig. 6.9). The reduction of nitrobenzene increases with increase in the hydrazine hydrate content in the reaction mixture and reaches to a maximum level at a molar ratio of 2:8. Further increase in the molar ratio results in a marginal decrease in the nitrobenzene reduction. This observation indicates that an optimal surface concentration of both reactants is achieved at a molar ratio of 2:8 resulting in their efficient utilization in the catalytic process. Beyond 2:8, the hydrazine hydrate adsorb to a higher extent compared to the nitrobenzene which is responsible for the marginal decrease in activity.

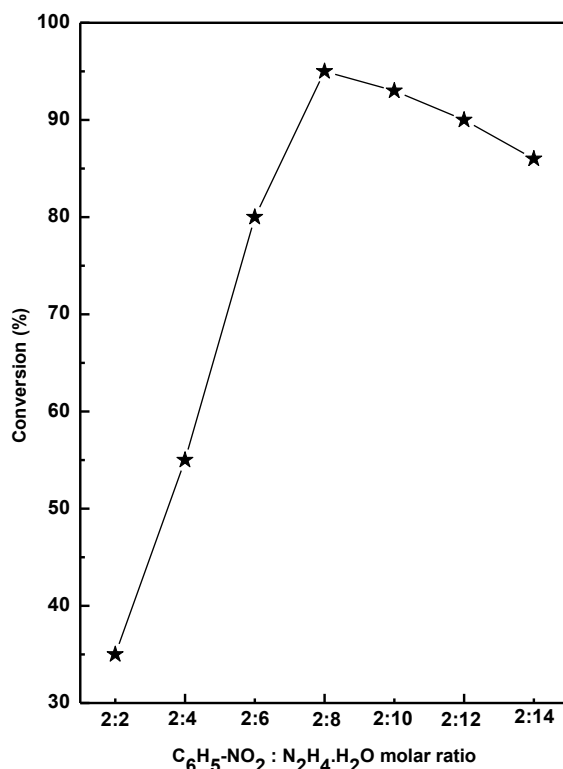


Figure 6.9: Effect of nitrobenzene to hydrazine hydrate molar ratio on the photocatalytic activity of α -Fe₂O₃(37%)-Bi₂S₃ catalyst (reaction conditions: 50 mg catalyst, 4 h).

Optimum amount of catalyst play an important role in a catalytic reaction. The catalyst amount is optimized for a 2 mmol reaction scale by using 25 mg to 100 mg of α -Fe₂O₃(37%)-Bi₂S₃ catalyst at a fixed molar ratio of the reactants (2:8) and irradiation time of 4 h (Fig. 6.10I). The reduction of nitrobenzene increases with increase in catalyst amount up to 50 mg, beyond this value there is a marginal decrease in nitrobenzene reduction. The decrease in catalytic activity at higher catalyst mass is due to increase in scattering of light from the reaction mixture, which affects the photocatalytic activity of the photocatalyst [27]. The recyclability and reusability of the α -Fe₂O₃(37%)-Bi₂S₃ has been checked for five consecutive cycles (Fig. 6.10II). After each catalytic cycle the photocatalyst is recovered, washed with ethanol, dried at 100 °C for 12 h and used for the next catalytic cycle. In the present study, up to five consecutive cycles no significant decrease in the catalytic activity of the α -Fe₂O₃(37%)-Bi₂S₃ is observed. The recyclability study indicates that the heterojunction photocatalyst is a stable and recyclable catalyst for the reduction of nitrobenzene.

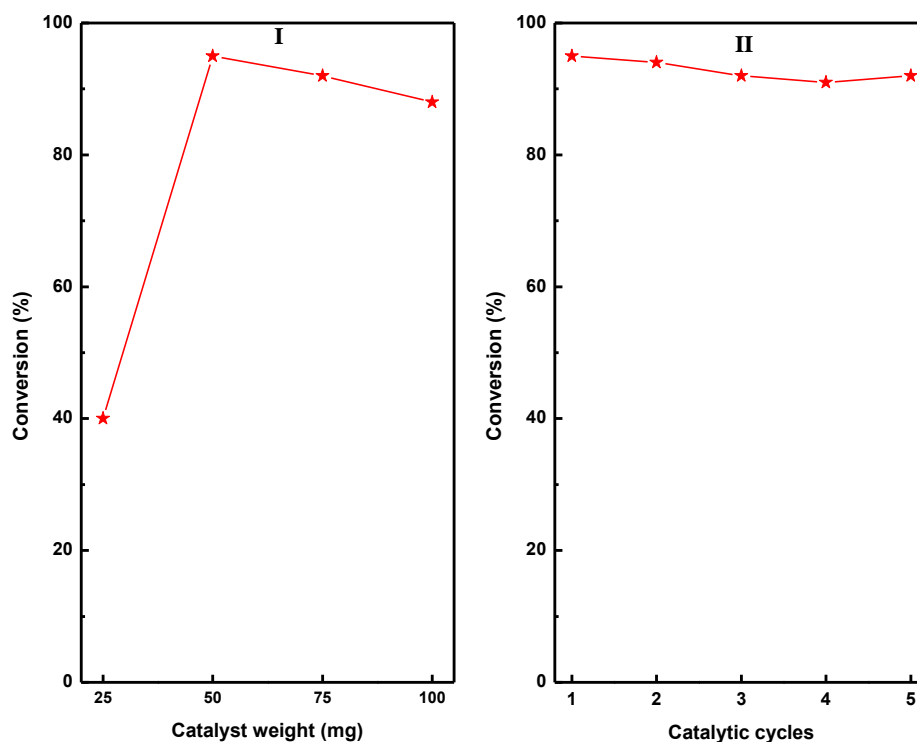


Figure 6.10: (Panel I) effect of catalyst dose and (Panel II) reusability study of photocatalytic hydrogen transfer reduction of nitrobenzene to aniline (reaction condition: α -Fe₂O₃ (37%)-Bi₂S₃ catalyst, C₆H₅-NO₂:N₂H₄.H₂O molar ratio = 2:8, 4 h).

After optimizing the reaction parameters and establishing the recyclable nature, we studied the scope and limitation of the developed photocatalytic protocol for reduction of nitroarenes containing diverse functional groups. Table 6.2 shows the photocatalytic activity of α -Fe₂O₃(37%)-Bi₂S₃ catalyst for reduction of structurally diverse nitroarenes. The heterojunction photocatalyst exhibits excellent photocatalytic efficiency for the selective hydrogen transfer reduction of substituted nitrobenzene containing both electron withdrawing and donating groups. In presence of electron withdrawing groups like -Cl, the percentage conversion is quite good with excellent yield of the corresponding amines. However, for nitrobenzene containing electron donating group like -NH₂ and -CH₃, the reduction process is slightly sluggish giving average yield of the products. An attractive feature of the developed protocol is that -Cl substituted nitrobenzene are reduced to their corresponding aniline without giving hydrodehalogenation products. Similarly, the photocatalytic reduction process is highly selective to the -NO₂ group in presence of other reducible group such as -CHO and -COOH.

Table 6.2: Photocatalytic hydrogen transfer reduction of structurally diverse nitroarenes catalyzed by α -Fe₂O₃(37%)-Bi₂S₃ heterojunction photocatalyst.

Entry	Substituent ^a (R)	Conversion ^b (%)	Yield ^c (%)
1	2-OH	91	88
2	3-OH	85	83
3	4-OH	90	87
4	3-CHO	95	92
5	4-CHO	97	93
6	2-CH ₃	80	77
7	4-CH ₃	75	71
8	4-COOH	94	91
9	3-COOH	87	83
10	2-Cl	93	90
11	4-Cl	96	91
12	2-NH ₂	75	72
13	4-NH ₂	71	67

a. reaction conditions: C₆H₅-NO₂:N₂H₂.H₂O molar ratio = 2:8, 50 mg catalyst, 4 h,

b. calculated from GC analysis,

c. refers to pure and isolated yield

6.2.6.2 Plausible Mechanism for Photocatalytic Reduction of Nitroarenes

The reduction of nitrobenzene is six protons and six electrons transfer reaction with the release of three water molecules [4, 6]. The oxidation of hydrazine to nitrogen involves the release 4 protons and 4 electrons (Eq. 6.1).



Stoichiometrically, for reduction of 2 moles nitrobenzene, 3 moles of hydrazine hydrate is needed. The positions of valence band and conduction band for α -Fe₂O₃ and Bi₂S₃ materials have been calculated using the formula in Eq. (6.2) [49].

$$E_{\text{VB}} = X_e - E_e + 0.5E_g \dots\dots\dots (6.2)$$

Where, X_e corresponds to the electronegativity of the material which is the geometric mean of the electronegativity of its constituent atoms. The E_e and E_g represents the energy of free electrons (4.5 eV) on hydrogen scale and the band gap of the material in eV, respectively. The X_e values for Bi₂S₃ and α -Fe₂O₃ are 5.27 eV and 4.78 eV, respectively [37, 48-50]. The calculated band gap values for α -Fe₂O₃ and Bi₂S₃ is 2.15 eV and 1.40 eV, respectively (Fig. 6.2). Using the above data, the position of valence band (VB) and conduction band (CB) of α -Fe₂O₃ component are calculated to be 1.355 eV and -0.795 eV respectively with respect to normal hydrogen electrode (NHE). Similarly VB and CB of Bi₂S₃ component lies at 1.47 eV and 0.07 eV with respect to NHE. Upon material contact, the Fermi level equilibration between the semiconductor phases leads to band realignment (Fig. 6.11). The CB electrons can migrate from Fe₂O₃ to Bi₂S₃, whereas the reverse migration of holes can takes place in the

VB. This cyclic movement of excitations is the characteristic feature of type-II heterojunction which reduce their recombination rate and promote the photocatalytic efficiency of the heterostructure system (Fig. 6.11). Since the reduction of nitrobenzene is a multi-electron transfer reaction, it is essential to reduce the recombination rate of photogenerated electrons and holes. This observation is further supplemented by the PL study where a significant decrease in the PL intensity has been observed (Fig. 6.4). The reduction of nitrobenzene occurs by electron transfer from CB whereas the hydrazine hydrate oxidation is carried out by holes in the VB. Based on the above discussion a plausible mechanism for the photocatalytic hydrogen transfer reduction of nitrobenzene to aniline is proposed (Fig. 6.11).

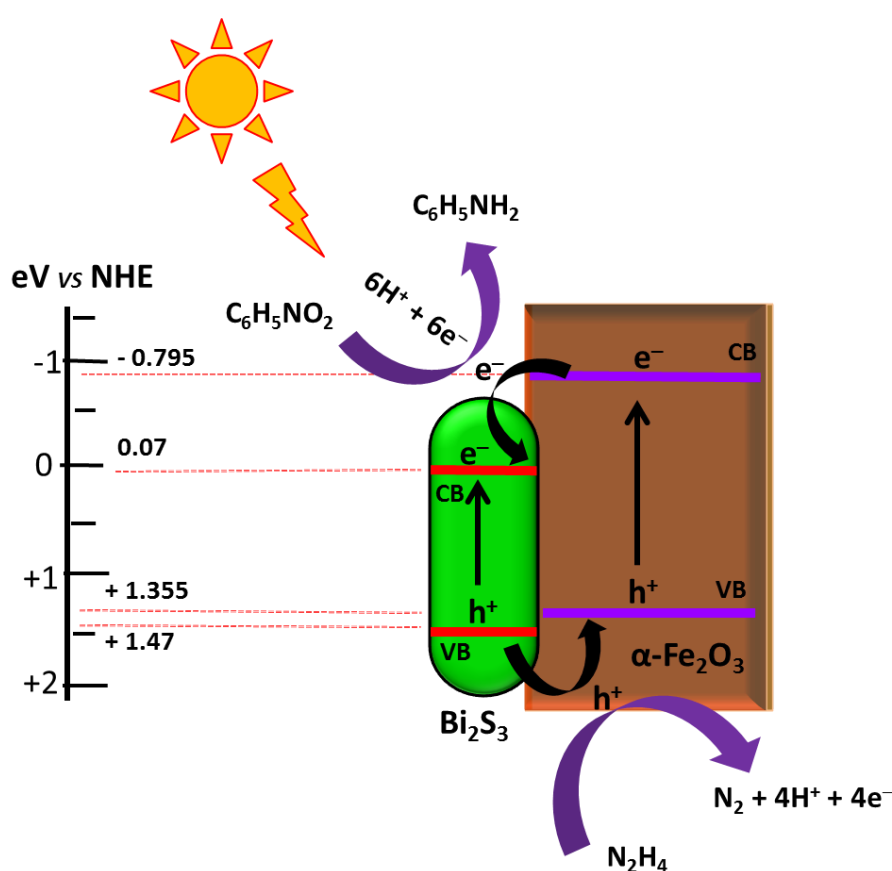


Figure 6.11: Plausible mechanism for photocatalytic hydrogen transfer reduction of nitroarenes over the α - $\text{Fe}_2\text{O}_3/\text{Bi}_2\text{S}_3$ heterojunction photocatalyst.

6.2.7 NMR Spectral Data of some of the Representative Amines (Entry in Table 6.2)

2-Aminophenol (Entry 1) ^1H NMR (400 MHz, CDCl_3) 6.68-6.81(4H, ArH), 3.64 (2H, NH_2), 4.90 (1H, OH), ^{13}C NMR (400 MHz, CDCl_3) 144.1, 134.5, 121.5, 119.5, 117.2, 115.2 (Ar-6C)

3-Aminophenol (Entry 2) ^1H NMR (400 MHz, CDCl_3) 6.8-6.9 (m, 1H), 6.13 (s, 1H), 6.15-6.17 (d, 1H), 6.19 (d, 1H), 3.67 (2H, NH_2), ^{13}C NMR (400 MHz, CDCl_3) 157.5 (1 Ar-C), 147.9 (1 Ar-C), 130.0 (1 Ar-C), 107.0 (1 Ar-C), 105.6 (1 Ar-C), 102.2 (1 Ar-C)

4-Aminophenol (Entry 3) ^1H NMR (400 MHz, CDCl_3) 6.68-6.70 (d, 2ArH), 6.61-6.63 (d, 2ArH), 4.41 (1H, OH), 3.54 (2H, NH_2), ^{13}C NMR (400 MHz, CDCl_3) 148.37 (1ArC), 139.85 (1ArC), 116.57 (2 ArC), 116.1 (2 ArC)

3-Aminobenzaldehyde (Entry 4) ^1H NMR (400 MHz, CDCl_3) 8.58 (1H, CHO), 7.17-7.28 (2 ArH), 6.79-6.82 (2 ArH), 3.97 (2H, NH_2), ^{13}C NMR (400 MHz, CDCl_3) 162.2 (1C, CHO), 146.7 (1ArC), 135.0 (1ArC), 119.6 (1ArC), 119.8 (1ArC), 118.1 (1ArC), 113.6 (1ArC)

4-Aminobenzaldehyde (Entry 5) ^1H NMR (400 MHz, CDCl_3) 8.56 (1H, CHO), 7.6 (2H, ArH), 6.7 (2H, ArH), 3.98 (2H, NH_2), ^{13}C NMR (400 MHz, CDCl_3) 156.2 (1C, CHO), 144.3 (1 ArC), 125.3 (2 ArC), 119.9 (1 ArC), 109.9 (2 ArC)

2-Aminotoluene (Entry 6) ^1H NMR (400 MHz, CDCl_3) 8.0 (m, 1H, ArH), 7.51-7.55 (d, 1H, ArH), 7.37-7.39 (m, 1H ArH), 6.7 (d, 1H, ArH), 3.63 (2H, NH_2), 2.64 (s, 3H CH_3), ^{13}C NMR (400 MHz, CDCl_3) 144.6 (1 ArC), 130.4 (1 ArC), 126.9 (1 ArC), 124.6 (1 ArC), 118.6 (1 ArC), 114.9 (1 ArC), 17.3 (1C, CH_3)

4-Aminotoluene (Entry 7) ^1H NMR (400 MHz, CDCl_3) 7.0 (2H ArH), 6.6 (2H ArH), 3.54 (2H, NH_2), 2.28 (3H, CH_3) ^{13}C NMR (400 MHz, CDCl_3) 143.8 (1 ArC), 129.7 (2 ArC), 127.8 (1 ArC), 115.2 (2 ArC), 20.5 (1C CH_3)

1,4-Diaminobenzene (Entry 13) ^1H NMR (400 MHz, CDCl_3) 6.7 (4H, ArH), 3.4 (4H, NH_2)

6.3 Conclusions

In this study, we have developed a facile one step combustion synthesis method to prepare $\alpha\text{-Fe}_2\text{O}_3\text{-Bi}_2\text{S}_3$ heterojunction nanomaterials. Thiourea used as fuel also acted as a source of sulfur. The formation of orthorhombic Bi_2S_3 and rhombohedral $\alpha\text{-Fe}_2\text{O}_3$ is confirmed from the XRD study. The heterojunction materials exhibit improved visible light absorption and enhanced charge carrier separation characteristics. The characteristic vibrational feature corresponding to both Bi_2S_3 and $\alpha\text{-Fe}_2\text{O}_3$ components are observed in the IR study. The formation of the $\alpha\text{-Fe}_2\text{O}_3\text{-Bi}_2\text{S}_3$ heterojunction is confirmed from HRTEM study. The heterojunction materials contain $\alpha\text{-Fe}_2\text{O}_3$ nanorods present in a well dispersed state in a continuous Bi_2S_3 matrix. The $\alpha\text{-Fe}_2\text{O}_3$ nanorods have typical diameter in the range of 30-50 nm and length of 120-150 nm. The $\alpha\text{-Fe}_2\text{O}_3\text{-Bi}_2\text{S}_3$ heterojunctions exhibit excellent photocatalytic activity for nitroarenes reduction under hydrogen transfer condition using hydrazine hydrate as reducing agent. Structurally diverse nitroarene moieties could be reduced to the corresponding amines in high yield and purity. The developed photocatalytic protocol is highly selective to the reduction of nitro group in presence of other reducible functional groups.

References

- [1] H. K. Kadam and S. G. Tilve, *RSC Advances*, 2015, 5, 83391-83407.
- [2] T. Aditya, A. Pal and T. Pal, *Chemical Communications*, 2015, 51, 9410-9431.

- [3] A. K. Shil, D. Sharma, N. R. Guha and P. Das, *Tetrahedron Letters*, 2012, 53, 4858-4861.
- [4] D. Cantillo, M. M. Moghaddam and C. O. Kappe, *Journal of Organic Chemistry*, 2013, 78, 4530-4542.
- [5] C. Huang, J. Hu, W. Fan,; X. Wu and X. Qiu, *Chemical Engineering Science*, 2015, 131, 155-161.
- [6] S. I. El-Hout, S. M. El-Sheikh, H. M. A. Hassan, F. A. Harraz, I. A. Ibrahim and E. A. El-Sharkawy, *Applied Catalysis A: General*, 2015, 503, 176-185.
- [7] K. Katayama, Y. Takeda, K. Shimaoka, K. Yoshida, R. Shimizu, T. Ishiwata, A. Nakamura, S. Kuwahara, A. Mase, T. Sugita and M. Mori, *Analyst*, 2014, 139, 1953-1959.
- [8] Z. Liu, Y. Huang, Q. Xiao and H. Zhu, *Green Chemistry*, 2016, 18, 817-825
- [9] Y. Zhao, H. Zhang, C. Huang, S. Chen and Z. Liu, *Journal of Colloid and Interface Science*, 2012, 374, 83-88.
- [10] M. Tamura, K. Kon, A. Satsuma and K. Shimizu, *ACS Catalysis*, 2012, 2, 1904-1909.
- [11] S. Gomez, C. Torres, J. L. G. Fierro, C. R. Apesteguia and P. Reyes, *Journal of the Chilean Chemical Society*, 2012, 57, 1194-1198.
- [12] F. Yang, C. Chi, C. Wang, Y. Wang and Y. Li, *Green Chemistry*, 2016, 18, 4254-4262.
- [13] S. Wu, G. Wen, J. Wang, J. Rong, B. Zong, R. Schlog and D. S. Su, *Catalysis Science & Technology*, 2014, 4, 4183-4187.
- [14] Y. Lin, S. Wu, W. Shi, B. Zhang, J. Wang, Y. A. Kim, M. Endo and D. S. Su, *Chemical Communications*, 2015, 51, 13086-13089.
- [15] C. Liu, P. Tang, A. Chen, Y. Hu, Y. Yu, H. Lv and D. Ma, *Materials Letters*, 2013, 108, 285-288.
- [16] Y. Gao, D. Ma, C. Wang, J. Guan and X. Bao, *Chemical Communications*, 2011, 47, 2432-2434.
- [17] Y. Shiraishi, Y. Togawa, D. Tsukamoto, S. Tanaka and T. Hirai, *ACS Catalysis*, 2012, 2, 2475-2481.
- [18] X. J. Yang, B. Chen, L. Q. Zheng, L. Z. Wu and C. H. Tung, *Green Chemistry*, 2014, 16, 1082-1086.
- [19] R. M. Mohamed and E. S. Aazam, *Journal of Alloys and Compounds*, 2014, 595, 8-13.
- [20] K. Imamura, K. Nakanishi, K. Hashimoto and H. Kominami, *Tetrahedron*, 2014, 70, 6134-6139.
- [21] O. R. Berny, S. O. Flores, I. Cordova and M. A. Valenzuela, *Tetrahedron Letters*, 2010, 51, 2730-2733.
- [22] K. Imamura, K. Hashimoto and H. Kominami, *Chemical Communications*, 2012, 48, 4356-4358.

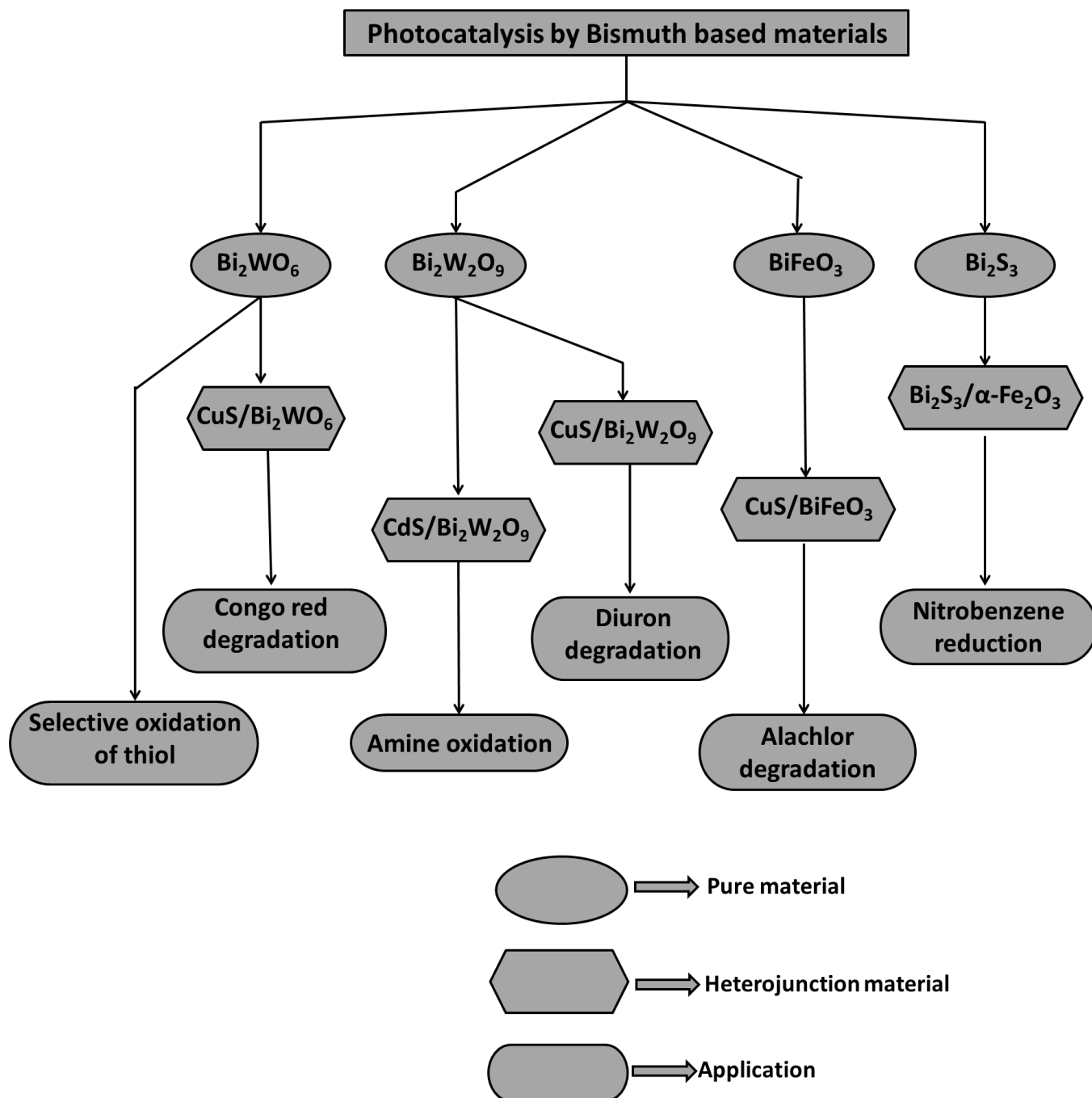
- [23] S. Fuldner, R. Mild, H. I. Siegmund, J. A. Schroeder, M. Gruber and B. Konig, *Green Chemistry*, 2010, 12, 400-406.
- [24] C. Xu, Y. Yuan, R. Yuan and X. Fu, *RSC Advances*, 2013, 3, 18002-18008.
- [25] S. Naraginti, F. B. Stephen and A. Radhakrishnan, A. Sivakumar, *Spectrochimica Acta Part A: Molecular and Biomolecular Spectroscopy*, 2015, 135, 814-819.
- [26] R. M. Mohamed and M. W. Kadi, *Ceramic International*, 2014, 40, 6597-6604.
- [27] X. Ning, S. Meng, X. Fu, X. Ye and S. Chen, *Green Chemistry*, 2016, 18, 3628-3639.
- [28] S. Liu and Y. J. Xu, *Nanoscale*, 2013, 5, 9330-9339.
- [29] A. H. Qustia, R. M. Mohamed, M. A. Salam, *Ceramic International*, 2014, 40, 5539-5546.
- [30] R. M. Mohamed and F. M. Ibrahim, *Journal of Industrial and Engineering Chemistry*, 2015, 22, 28-33.
- [31] W. Wu, R. Lin, L. Shen, R. Liang, R. Yuan and L. Wu, *RSC Advances*, 2013, 3, 10894-10899.
- [32] M. Q. Yang, B. Weng and Y. J. Xu, *Journal of Materials Chemistry A*, 2014, 2, 1710-1720.
- [33] T. Toyao, M. Saito, Y. Horiuchi, K. Mochizuki, M. Iwata, H. Higashimura and M. Matsuoka, *Catalysis Science & Technology*, 2013, 3, 2092-2097.
- [34] J. L. T. Chen, V. Nalla, G. Kannaiyan, V. Mamidala, W. Ji and J. J. Vittal, *New Journal of Chemistry*, 2014, 38, 985-992.
- [35] C. Liu, Y. Yang, W. Li, J. Li, Y. Li and Q. Chen, *Chemical Engineering Journal*, 2016, 302, 717724.
- [36] P. Han, A. Mihi, J. Ferreborrull, J. Pallares and L. F. Marsal, *The Journal of Physical Chemistry C*, 2015, 119, 10693-10699.
- [37] X. Li, Y. Li, J. Shenn and M. Ye, *Ceramics International*, 2016, 42, 3154-3162.
- [38] H. Cheng, B. Huang, X. Qin, X. Zhang and Y. Dai, *Chemical Communications*, 2012, 48, 97-99.
- [39] Z. Wu, L. Chen, C. Xing, D. Jiang, J. Xie and M. Chen, *Dalton Transactions*, 2013, 42, 12980-12988.
- [40] Y. Shi, Y. Chen, G. Tian, H. Fu, K. Pan, J. Zhou and H. Yan, *Dalton Transactions*, 2014, 43, 12396-12404.
- [41] Y. Huang, W. Fan, B. Long, H. Li, F. Zhao, Z. Liu, Y. Tong and H. Ji, *Applied Catalysis B: Environmental*, 2016, 185, 68-76.
- [42] J. Kim and M. Kang, *International Journal of Hydrogen Energy*, 2012, 37, 8249-8256.
- [43] L. Chen, J. He, Q. Yuan, Y. Liu, C. T. Au and S. F. Yin, *Journal of Materials Chemistry A*, 2015, 3, 1096-1102.
- [44] D. A. Wheeler, G. Wang, Y. Ling, Y. Li and J. Z. Zhang, *Energy & Environmental Science*, 2012, 5, 6682-6702.
- [45] X. Mou, X. Wei, Y. Li and W. Shen, *CrystEngComm*, 2012, 14, 5107-5120.

- [46] D. Zhang, Y. Li, M. Yan and Y. Jiang, *ChemElectroChem*, 2014, 1, 1155-1160.
- [47] E. Kalamaras, V. Dracopoulos, L. Sygellou and P. Lianos, *Chemical Engineering Journal*, 2016, 295, 288-294.
- [48] A. G. Tamirat, J. Rick, A. A. Dubale, W. N. Su and B. J. Hwang, *Nanoscale Horizons*, 2016, 1, 243-267.
- [49] X. J. Wen, C. Zhang, C. G. Niu, L. Zhang, D. W. Huang, X. Y. Wang, X. G. Zhang and G. M. Zeng, *RSC Advances*, 2016, 6, 4035-4042.
- [50] X. Liu, Q. Lu, C. Zhu and S. Liu, *RSC Advances*, 2015, 5, 4077-4082.
- [51] J. Zhao, Q. Lu, Q. Wang and Q. Ma, *Superlattices and Microstructures*, 2016, 91, 148-157.
- [52] Y. Guo, G. Zhang, J. Liu and Y. Zhang, *RSC Advances*, 2013, 3, 2963-2970.
- [53] J. P. Dhal, B. G. Mishra and G. Hota, *RSC Advances*, 2015, 5, 58072-58083.
- [54] L. Alfonso, T. Gomez and R. Sabbah, *Thermochimica Acta*, 1982, 57, 67-81.
- [55] Z. D. Wang, M. Yoshida and B. George, *Computational and Theoretical Chemistry*, 2013, 1017, 91-98.
- [56] J. Madarasz, P. Bombicz, M. Okuya and S. Kaneko, *Solid State Ionics*, 2001, 141, 439-446.
- [57] M. P. Deshpande, P. N. Sakariya, S. V. Bhatt, N. H. Patel, K. Patel and S. H. Chaki, *Bulletin of Materials Science*, 2015, 38, 83-88.
- [58] R. B. Lanjewar and A. N. Garg, *Polyhedron*, 1993, 12, 1219-2626.
- [59] X. Zhang, Y. Niu, X. Meng, Y. Li and J. Zhao, *CrystEngComm*, 2013, 15, 8166-8172.

CHAPTER 7

Summary and Conclusions

The summary of the research work carried out in this thesis is schematically presented below



In this thesis, effort has been made to explore the photocatalytic potential of bismuth based semiconducting nanomaterials towards complete mineralization of persistent organic pollutants from aqueous sources as well as selective organic transformations. The Bi based semiconducting materials namely Bi_2WO_6 , $\text{Bi}_2\text{W}_2\text{O}_9$, BiFeO_3 and Bi_2S_3 with different morphologies and sizes are prepared by combustion synthesis method. The nature of the fuels, fuel to oxidizer ratio and calcinations temperature are vital factors which influences the phase purity and surface characteristics of the synthesized materials. In order to improve the optical absorption and photocatalytic properties, the Bi-based complex oxide materials are subsequently modified with low band gap metal sulfide nanoparticles (CuS and CdS) having suitable band alignment to prepare novel heterojunction systems. The heterojunction materials exhibited improved visible light absorption and enhanced charge carrier separation compared to the parent semiconducting materials. The heterojunction materials having high positive VB potential were studied as efficient photocatalysts for aqueous phase degradation of recalcitrant Congo red dye and potentially harmful diuron and alachlor pesticides under visible light illumination. In this thesis, an effort has also been made to carry out selective organic transformations by visible light assisted photocatalytic route using the heterojunction materials as photocatalyst. The heterostructure systems with higher negative CB potential such as $\text{Bi}_2\text{S}_3/\alpha\text{-Fe}_2\text{O}_3$ are particularly effective for selective organic transformations. The major conclusions obtained from this thesis are presented below

Major Conclusions

- Well dispersed bismuth tungstate (Bi_2WO_6) nanoparticles are synthesized by combustion synthesis method using different reducible organic compounds as fuel. Phase pure Bi_2WO_6 nanoparticles are obtained when glycine is used as fuel whereas formation of $\text{Bi}_2\text{W}_2\text{O}_9$ and $\text{Bi}_{14}\text{W}_2\text{O}_{27}$ as impurity phases are noticed in case of urea, malonic acid dihydrazide and hexamethylenetetramine fuels.
- The nature of the fuel significantly influences the particle size and morphology. Spherical, flake like and elongated polyhedral particles are obtained by varying the fuel and its content in the combustion mixture. Glycine as fuel is highly effective towards synthesis of uniformly distributed Bi_2WO_6 nanoparticles with size in the range of 5–7 nm.
- The combustion synthesized Bi_2WO_6 material efficiently catalyzes the selective oxidation of thiols to disulfides in aqueous media under visible light irradiation. Particularly, the Bi_2WO_6 nanoparticles prepared using glycine as fuel is highly active and 100 % selective to the formation of disulfides for a variety of substrates containing electron withdrawing and donating functional group.
- The Bi_2WO_6 nanoparticles also prepared by amorphous citrate process contain orthorhombic Russellite crystalline phase having polyhedral sheet shaped and elongated particle morphologies. The CuS nanomaterials are dispersed over the Bi_2WO_6 matrix by using hydrothermal route to form $\text{CuS}/\text{Bi}_2\text{WO}_6$ heterojunction materials.

- During hydrothermal treatment, the Cu^{2+} ions substituted for the W^{6+} ions in the Bi_2WO_6 lattice to form a substitutional solid solution ($\text{Bi}_2\text{Cu}_x\text{W}_{1-x}\text{O}_{6-2x}$). Simultaneously, morphological reorganization of the Bi_2WO_6 phase took place leading to the formation of flower like hierarchical nanostructures.
- The $\text{CuS}/\text{Bi}_2\text{WO}_6$ heterojunction materials possess characteristic features of a type-II heterojunction exhibiting narrow band gap, enhanced visible light absorption and efficient charge separation properties. The heterojunction materials efficiently catalyze the degradation of Congo red dye from aqueous solution under visible light irradiation. Compared to earlier studies, the photocatalytic protocol developed in this work is advantageous in terms of minimum use of catalyst and oxidant, less irradiation time and its applicability for aqueous effluents containing higher concentration of the dye.
- Phase pure $\text{Bi}_2\text{W}_2\text{O}_9$ with orthorhombic crystal structure and plate like particle morphology is synthesized by combustion synthesis route using urea as a fuel. The $\text{Bi}_2\text{W}_2\text{O}_9$ material is subsequently modified with CdS and CuS nanoparticles to form $\text{CdS}/\text{Bi}_2\text{W}_2\text{O}_9$ and $\text{CuS}/\text{Bi}_2\text{W}_2\text{O}_9$ heterojunction systems.
- The $\text{CdS}/\text{Bi}_2\text{W}_2\text{O}_9$ heterojunction materials contain ultrafine CdS nanoparticles with diameter in the range of 8-15 nm well dispersed over the BWO plates. The two crystalline phases exhibited microscopic close contact across grain boundaries facilitating transfer of excitons. The $\text{CdS}/\text{Bi}_2\text{W}_2\text{O}_9$ heterojunction materials displayed improved visible light absorption, enhanced charge carrier separation and suitable band alignment characteristic of a type-II heterojunction.
- The $\text{CdS}/\text{Bi}_2\text{W}_2\text{O}_9$ heterojunction by virtue of its favorable band position used as a visible light active photocatalyst for aerobic oxidation of amines to imines. Structurally and functionally diverse amine molecules were oxidized to the corresponding imines with excellent selectivity in a short span of time.
- In case of $\text{CuS}/\text{Bi}_2\text{W}_2\text{O}_9$ heterojunction systems, the desegregation of the $\text{Bi}_2\text{W}_2\text{O}_9$ plates to nanosheets and the concurrent formation of CuS nanorods occurred during hydrothermal synthesis. The nanosheets and nanorods organize themselves in a hierarchical manner to form microspherical structures. Partial substitution of Cu^{2+} ions in to the $\text{Bi}_2\text{W}_2\text{O}_9$ lattice is also observed leading to the formation of $\text{Bi}_2\text{Cu}_x\text{W}_{2-x}\text{O}_{9-2x}$ as a nonstoichiometric solid solution phase. The $\text{CuS}/\text{Bi}_2\text{W}_2\text{O}_9$ material exhibited characteristic features of a Type-II heterojunction with significant improvement in visible light absorption and enhanced separation of excitons.
- The $\text{CuS}/\text{Bi}_2\text{W}_2\text{O}_9$ materials exhibit excellent photocatalytic activity towards degradation of diuron pesticide under visible light irradiation achieving 95% mineralization within 3 h. Mechanistic study indicated that the mineralization of diuron occurred in a cascade manner over the catalyst surface involving dechlorination, alkyl oxidation and oxidative ring-opening steps.
- A sustainable visible light promoted photocatalytic route has been developed for mineralization of alachlor pesticide using $\text{CuS}/\text{BiFeO}_3$ heterojunction materials. The

heterojunction materials prepared by a two-step process contain BiFeO₃ nanoplates with high aspect ratio and CuS nanorods. The heterojunction materials exhibited enhanced visible light absorption, greater charge carrier separation and improved charge mobility, which are vital factors for their improved photocatalytic performance.

- The CuS/BiFeO₃ materials displayed excellent photocatalytic performance for mineralization of alachlor pesticide. The study of photocatalytic mechanism suggested that the degradation of alachlor occur in a series of steps over the catalyst surface with the identification of seven metabolites. The VB holes and hydroxyl radicals have been identified as the major transient species responsible for oxidation of alachlor.
- A novel combustion synthesis procedure is developed for single step synthesis of Bi₂S₃/α-Fe₂O₃ heterojunction materials using thiourea as a fuel as well as sulfur source. The presence of well dispersed α-Fe₂O₃ nanorods of 30–50 nm in diameter and 120–150 nm in length in a continuous Bi₂S₃ matrix is noticed for the composite materials. Favorable band alignment of the two semiconductors facilitates electrons transfer from the conduction band of α-Fe₂O₃ to Bi₂S₃ whereas migration of holes occurs in the reverse direction yielding a type-II heterojunction.
- The α-Fe₂O₃-Bi₂S₃ heterojunctions exhibit excellent photocatalytic activity for nitroarenes reduction under hydrogen transfer condition. Structurally diverse nitroarenes moieties could be reduced to the corresponding amines in high yield and purity. The developed photocatalytic protocol is highly selective to the reduction of nitro group in presence of other reducible functional groups.

Visible Research Output

Refereed Journals

1. **Y. P. Bhoi** and B.G. Mishra, Synthesis, characterization and photocatalytic application of type II CdS/Bi₂W₂O₉ heterojunction nanomaterials towards aerobic oxidation of amines to imines. *European Journal of Inorganic Chemistry*, **2018**, 2648-2658.
2. **Y. P. Bhoi** and B.G. Mishra, Photocatalytic degradation of alachlor using Type-II CuS/BiFeO₃ heterojunctions as novel photocatalyst under visible light irradiation. *Chemical Engineering Journal*, **2018**, 344, 391-401.
3. **Y. P. Bhoi**, C. Behera, D. Majhi, Sk. Md. Equeenuddin and B. G. Mishra, Visible light-assisted photocatalytic mineralization of diuron pesticide using novel type II CuS/Bi₂W₂O₉ heterojunctions with a hierarchical microspherical structure. *New Journal of Chemistry*, **2018**, 42, 281-292.
4. **Y. P. Bhoi** and B. G. Mishra, Photocatalytic application of Bi₂S₃/BiFeO₃ heterojunction material for the degradation of carbendazim pesticide under visible light. *Catalysis Communications*, **2018**, 114, 114-119.
5. D. Majhi, **Y.P. Bhoi**, P. K. Samal and B.G. Mishra, Morphology controlled synthesis and photocatalytic study of novel CuS-Bi₂O₂CO₃ heterojunction system for chlorpyrifos degradation under visible light illumination. *Applied Surface Science*, **2018**, 455, 891-902.
6. **Y. P. Bhoi** and B. G. Mishra, Single step combustion synthesis, characterization and photocatalytic application of α -Fe₂O₃-Bi₂S₃ heterojunctions for efficient and selective reduction of structurally diverse nitroarenes. *Chemical Engineering Journal*, **2017**, 316, 70-81.
7. **Y. P. Bhoi**, S. R. Pradhan, C. Behera and B. G. Mishra, Visible light driven efficient photocatalytic degradation of Congo red dye catalyzed by hierarchical CuS-Bi₂Cu_xW_{1-x}O_{6-2x} nanocomposite system. *RSC Advances*, **2016**, 6, 35589-35601.
8. **Y. P. Bhoi**, D. P. Rout and B. G. Mishra, Photocatalytic chemoselective aerobic oxidation of thiols to disulfides catalyzed by combustion synthesized bismuth tungstate nanoparticles in aqueous media. *Journal of Cluster Science*, **2016**, 27, 267-284.
9. P. Kar, A. Nayak, **Y. P. Bhoi** and B. G. Mishra, Preparation and catalytic application of sulfonated PVA-Zr-pillared clay nanocomposite materials towards one pot synthesis of hexahydropyrimidines. *Microporous and Mesoporous Materials*, **2016**, 223, 176-186.

Manuscript under review/preparation

10. S. Pradhan, **Y. P. Bhoi**, D. Majhi, G. Hota, B. G. Mishra, Al-pillared α -ZrP as efficient heterogeneous catalyst for synthesis of structurally diverse 1,4-dihydropyridines under mild conditions (Communicated)
11. **Y. P. Bhoi** and B. G. Mishra, Photocatalytic application of $\text{Bi}_2\text{S}_3/\text{BiW}_2\text{O}_9$ heterojunction material for the degradation of phenolic compounds under visible light. (to be communicated)
12. **Y. P. Bhoi** and B. G. Mishra, One pot synthesis, characterization and photocatalytic applications of $\alpha\text{-Fe}_2\text{O}_3/\text{CuS}$ heterojunction for aerobic oxidation of benzyl alcohol under visible light. (to be communicated)
13. **Y. P. Bhoi** and B. G. Mishra, combustion synthesis, characterization and photocatalytic applications of cesium tungstate nanomaterial for the degradation of 2,4-dinitro phenol under UV light (to be communicated).

Poster and paper presented in conference/symposium

1. **Y. P. Bhoi** and B. G. Mishra, "Single step combustion synthesis, characterization and photocatalytic application of $\alpha\text{-Fe}_2\text{O}_3\text{-Bi}_2\text{S}_3$ heterojunctions for efficient and selective reduction of structurally diverse nitroarenes", 21st CRSI National Symposium in Chemistry, 14th – 16th July 2017, CSIR- Indian Institute of Chemical Technology, Hyderabad, India.
2. **Y. P. Bhoi** and B. G. Mishra, "Type II $\text{CuS}/\text{Bi}_2\text{W}_2\text{O}_9$ heterojunction photocatalyst for degradation of diuron pesticide and congo red dye under visible light", International Conference on Recent Advances in Materials Chemistry (RAMC 2017), 24th – 26th February 2017, Department of Chemistry, Utkal University, Bhubaneswar, Odisha, India.
3. **Y. P. Bhoi** and B. G. Mishra, "Visible light driven efficient photocatalytic degradation of congo red dye catalyzed by hierarchical $\text{CuS-Bi}_2\text{Cu}_x\text{W}_{1-x}\text{O}_{6-2x}$ heterojunction system", Conference on Emerging Materials (CEMAT-2016), , 18th – 19th July 2016, Indian Institute of Science, Bangalore.
4. **Y. P. Bhoi** and B. G. Mishra, "Chemoselective aerobic oxidation of thiols to disulfides catalyzed by combustion synthesized bismuth tungstate nanoparticles in aqueous media", 3rd International Conference on Nanostructured Materials and Nanocomposites (ICNM-2015), 12th – 14th December 2015, Hindustan College of Science and Technology, Farah, Mathura, Uttar Pradesh, India.
5. **Y. P. Bhoi** and B. G. Mishra, "Visible light driven photocatalytic decomposition of 4-chloro phenol from aqueous sources using combustion synthesized Bi_2WO_6 nanoparticles as heterogeneous catalyst", 17th CRSI National Symposium in Chemistry, 6th – 8th February, 2015, CSIR- National Chemical Laboratory, Pune, India
6. **Y. P. Bhoi** and B. G. Mishra, "Visible light driven photocatalytic applications of combustion synthesized Bi_2WO_6 nanoparticles", National Conference on Recent Trends in Chemical Sciences (RETICS-2014), 14th – 15th November 2014, School of Chemistry, Sambalpur University, Jyoti Vihar, Burla, Odisha, India.